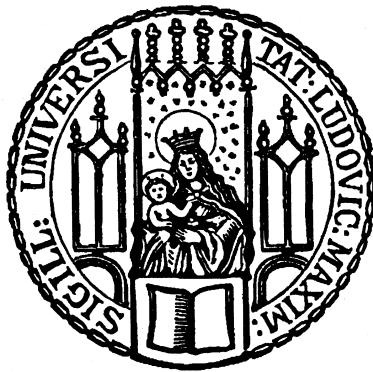

The Lamb shift of the muonic helium-3 ion and the helion charge radius

Julian Krauth



Munich 2017

Die Lamb Verschiebung in myonischen Helium-3 Ionen und der Helion Ladungsradius

Julian Krauth

Dissertation
an der Fakultät für Physik
der Ludwig-Maximilians-Universität
München

vorgelegt von
Julian Krauth
aus Pforzheim

München, den 20. Januar 2017

Erstgutachter: Prof. Dr. Theodor W. Hänsch

Zweitgutachter: Prof. Dr. Randolph Pohl

Tag der mündlichen Prüfung: 15. März 2017

Zusammenfassung

Diese Arbeit befasst sich mit der erstmaligen Messung der Lamb-Verschiebung in myonischen Helium-3 Ionen. Desweiteren liefert diese Arbeit den bisher genauesten Wert des Ladungsradiuses des Helium-3 Kerns. Die Messungen wurden von der CREMA Kollaboration im Jahr 2014 am Paul Scherrer Institut in Villigen, Schweiz, durchgeführt.

Da Myonen ungefähr zweihundertmal schwerer sind als Elektronen, sind Wasserstoff-ähnliche myonische Atome sehr sensitiv auf Strukturen des Atomkerns, wie zum Beispiel auf seine Polarisierbarkeit, oder eben auf den Ladungsradius. Die Bestimmung des Letzteren hat seit Entstehung des sogenannten Protonenradius Puzzles eine besondere Aufmerksamkeit erfahren. Im Jahr 2010 hat ein Vorgängerexperiment der CREMA Kollaboration den Ladungsradius des Protons vermessen. Dieser Wert war zehn mal genauer, als das Mittel der bisherigen Werte aus Messungen an elektronischem Wasserstoff. Allerdings lag der Wert auch mehr als 5 Standardabweichungen davon entfernt. Nach über sechs Jahren ist dieses Problem weiterhin ungelöst. Die Messungen an myonischem Helium-3 reihen sich damit in viele weitere Experimente ein, welche auf der Suche nach einer Lösung des besagten Puzzles sind.

Das Experiment funktioniert folgendermaßen: Langsame Myonen werden in einem Gefäß gestoppt, welches bei niedrigem Druck mit Helium-3 Gas gefüllt ist. Sobald die Myonen gestoppt sind, formen sie hoch angeregte myonische Helium-3 Ionen, welche sogleich in den Grundzustand kaskadieren. Ungefähr 1% dieser Ionen enden allerdings nicht im 1S Grundzustand, sondern im metastabilen 2S Zustand. Diese werden ungefähr $1\text{ }\mu\text{s}$ später mit einem Laser beschossen, dessen Frequenz so lange justiert wird, bis er genau die Übergangsenergie trifft. Daraufhin springt das myonische Atom in den 2P Zustand, um gleich darauf in den 1S Grundzustand zu fallen. Hierbei wird ein verspätetes K_α Röntgenquant emittiert. Das gesuchte Signal erhält man, wenn die Anzahl der detektierten Röntgenquanten in Abhängigkeit der Laserfrequenz bestimmt wird.

Die gemessenen Übergangsfrequenzen der Lamb-Verschiebung lauten

$$\nu(2S_{1/2}^{F=1} - 2P_{3/2}^{F=2}) = 347\,212(20) \text{ GHz}$$

$$\nu(2S_{1/2}^{F=0} - 2P_{3/2}^{F=1}) = 312\,830(21) \text{ GHz}$$

$$\nu(2S_{1/2}^{F=1} - 2P_{1/2}^{F=1}) = 310\,814(20) \text{ GHz}$$

mit einer relativen Unsicherheit von unter 70 ppm.

Mithilfe einer ausführlichen Analyse und Zusammenfassung der bisher gerechneten Theorieterme ergibt sich der Helion Ladungsradius zu

$$r_h = 1.96861(12)^{\text{exp}}(128)^{\text{theo}} \text{ fm}$$

mit einer relativen Unsicherheit von 7×10^{-4} .

Zusammen mit dem "myonischen" Ladungsradius des α -Teilchens, kann die (quadratische) Radiusdifferenz bestimmt werden. Das Ergebnis stimmt mit einer von drei sich unterscheidenden Messungen der Isotopieverschiebung in den elektronischen Helium Isotopen überein.

The Lamb shift of the muonic helium-3 ion and the helion charge radius

Julian Krauth

Dissertation
Faculty of Physics
Ludwig-Maximilians-Universität München

presented by
Julian Krauth
born in Pforzheim, Germany

Munich, January 20, 2017

1st Referee: Prof. Dr. Theodor W. Hänsch

2nd Referee: Prof. Dr. Randolph Pohl

Date of oral exam: March 15, 2017

*Before I came here I was confused about
this subject. Having listened to your lecture
I am still confused. But on a higher level.*

Enrico Fermi

Abstract

This thesis reports on the first ever measurement of several Lamb shift transitions in the muonic helium-3 ion and on the hitherto most precise extraction of its nuclear charge radius. The measurements have been performed in 2014 by the CREMA collaboration at the Paul Scherrer Institute in Villigen, Switzerland.

Due to the large muon mass, hydrogen-like muonic atoms are highly sensitive to nuclear structure contributions like the polarizability. A special attraction to this topic has been created by the so-called proton radius puzzle. In 2010, a predecessor experiment performed by the CREMA collaboration measured the proton charge radius to be more than 5 standard deviations smaller than the average of all previous measurements on electronic hydrogen. After more than six years this problem remains still unresolved. The measurement on muonic helium-3 is therefore a decisive experiment on the way to solve this puzzle.

The experiment described in this thesis has the following working principle. Low-energy muons are stopped in a low-pressure gas target filled with ^3He gas. Once stopped, a muonic atom in a highly excited state is formed whereupon the muon cascades down to the ground state. Only about 1% of the muons end up in the meta-stable 2S state. After a delay of 1 μs a laser is scanned over the transition frequency and, if on resonance, excites these atoms to the 2P state. The 2P state immediately decays to the ground state, emitting a delayed K_α X-ray. The signal is obtained determining the number of delayed K_α X-rays versus the laser frequency.

The frequencies of the measured transitions result in

$$\begin{aligned}\nu(2S_{1/2}^{F=1} - 2P_{3/2}^{F=2}) &= 347\,212(20) \text{ GHz} \\ \nu(2S_{1/2}^{F=0} - 2P_{3/2}^{F=1}) &= 312\,830(21) \text{ GHz} \\ \nu(2S_{1/2}^{F=1} - 2P_{1/2}^{F=1}) &= 310\,814(20) \text{ GHz}\end{aligned}$$

with a relative precision better than 70 ppm.

By means of an extensive theory compilation, the helion charge radius is found to be

$$r_h = 1.96861(12)^{\text{exp}}(128)^{\text{theo}} \text{ fm}$$

with a relative precision of 7×10^{-4} .

In combination with the “muonic” radius of the α particle, the (squared) charge radius difference is obtained. This result is in excellent agreement with one amongst three isotope shift measurements in ordinary helium which measured discrepant values.

Contents

Contents	xv
1. Introduction	1
1.1. Historical introduction of the Lamb shift	5
1.2. Muons	6
2. Experimental setup	9
2.1. Principle of the experiment	9
2.2. Proton accelerator and pion generation	9
2.3. Low energy muon beamline	10
2.3.1. Cyclotron trap	11
2.3.2. Muon extraction channel	12
2.3.3. Nondestructive muon detection	13
2.4. The gas target and its inner workings	14
2.4.1. Multipass cavity	16
2.4.2. Detection of X-rays and electrons	19
2.5. Laser system	20
3. Systematics	25
3.1. Characterization of the laser	26
3.2. Quantum interference in the CREMA experiments	27
3.3. Estimation of other systematic effects	34
3.3.1. Asymmetries in the recorded data	36
3.3.2. Zeeman effect	36
3.3.3. Doppler broadening	39
3.3.4. Collisional effects	40
3.3.5. Power broadening	40

4. Data analysis	41
4.1. APD trace analysis, energy spectrum and cut	44
4.2. Electron identification via coincidences	46
4.3. Delayed electron cut (creation of XDele events)	48
4.4. Second muon cut	50
4.5. Laser performance	52
4.6. Laser time window	54
4.7. Fit the data	58
5. Theory summary of the $n=2$ levels in $\mu^3\text{He}^+$	63
5.1. Lamb shift	65
5.1.1. Nuclear structure-independent contributions	65
5.1.2. Nuclear structure-dependent contributions	66
5.1.3. Total Lamb shift contribution	69
5.2. 2S hyperfine structure	69
5.3. 2P levels (fine and hyperfine structure)	70
5.4. Summary and properties of the Lamb shift transitions	72
6. Results	73
7. Conclusions	77
A. Calibration	79
A.1. Time calibration	79
A.1.1. X-ray and electron detectors	79
A.1.2. Photodiodes and light in APD B9	79
A.2. Energy calibration	81
A.2.1. APD energy calibration	81
A.2.2. Laser pulse energy calibration	84
B. The Lamb shift transitions of the muonic helium-3 ion	87
C. ^3He circulation system	89
D. Theory of the $n=2$ levels in muonic helium-3	91
E. Theory of the $n=2$ levels in muonic deuterium	123

F. Abbreviations	153
List of Figures	155
List of Tables	157
Bibliography	159

1. Introduction

It has been the simplest of all atoms which led to the major improvements in atomic physics, the hydrogen atom. The effort to understand the hydrogen spectrum led to the Bohr model in 1913 which for the first time could motivate the experimental observations by a theory using fundamental physical constants. It contained the first “quantum rule” where electrons have been restricted to discrete energy levels, where they orbit around the nucleus without emitting radiation. The Bohr model was a large step towards a quantum mechanical description of atoms. In 1926, Schrödinger succeeded to explain the hydrogen spectrum with his wave equation. The Schrödinger equation, as it is called today set the foundations of quantum mechanics. In 1928, by introducing a relativistic wave equation compatible with both, quantum mechanics and special relativity, Dirac was able to explain the fine and hyperfine structure in the hydrogen atom, which arises due to the spin of the electron and the nucleus, respectively.

The discovery of the Lamb shift [1] and the anomalous magnetic moment of the electron [2], both in 1947, opened the door to quantum electrodynamics, in short QED (a short historical overview on the Lamb shift is given in Sec. 1.1). By means of QED, the interaction of light and matter can finally be fully described using a quantum field theory. Since the development of QED, physicists try to test this highly successful theory by more and more precise measurements and calculations. On the way to the ultimate precision, ingenious tools enabling laser spectroscopy and optical frequency measurements, have been developed. The latter has been essentially simplified by the invention of the frequency comb at the chair of Prof. Hänsch [3]. The fundamental physical constants involved in QED have been measured to unprecedented precision. One of the cornerstones of this precision career is the measurement of the $1S - 2S$ transition frequency in atomic hydrogen which currently is known with a stunning relative uncertainty of few times 10^{-15} [4, 5]. The uncertainty in the theoretical prediction of this transition frequency is currently dominated by the measured values of the Rydberg constant and the proton charge radius. The $1S - 2S$ measurement, in combination with a measurement of a $2S - nl$ transition (for $n > 2$), is used to determine both of these constants. From these measurements the Rydberg constant is known to a relative uncertainty of few times 10^{-12} , which is three orders of magnitude away from the uncertainty

in the above mentioned $1S - 2S$ measurement. The full potential of the precision in the $1S - 2S$ measurement can only be tapped with better $2S - nl$ measurements, or using an improved value of the proton charge radius obtained elsewhere.

It is not ordinary hydrogen, but an exotic version of it, muonic hydrogen, which has been used to further reduce the uncertainty in the value of the proton charge radius. The muon is about 200 times heavier than the electron, but also interacts via the Coulomb potential (a short introduction to muons is given in Sec. 1.2). Its larger mass implies a Bohr radius which is reduced by the ratio of the reduced muon mass to the reduced electron mass

$$\frac{m_\mu m_p}{m_\mu + m_p} \bigg/ \frac{m_e m_p}{m_e + m_p} \approx 186. \quad (1.1)$$

The increased overlap of the muon wavefunction with the nucleus makes the Lamb shift an ideal candidate for the measurement of the charge radius. The Lamb shift is the energy difference between the $2S_{1/2}$ and the $2P_{1/2}$ state. Whereas the $2S$ wavefunction has a large overlap with the nucleus, the $2P$ wavefunction's probability to be at the nucleus is very small. The difference of a Lamb shift measurement to the theoretical prediction using a point-like nucleus, is attributed to its finite charge distribution. This measurement has been performed by the CREMA collaboration in 2010 and yields a proton root-mean-square (rms) charge radius of [6, 7]

$$r_p = 0.84087(39) \text{ fm} \quad (1.2)$$

This value is more than ten times more precise than the current “literature” value of $r_p = 0.8751(61) \text{ fm}$ provided by the CODATA least-squares adjustment [8], which compiles the results from laser spectroscopy experiments in ordinary hydrogen as well as the values obtained by electron scattering. Remarkably the precise “muonic” value of the proton charge radius is not only ten times more precise but also more than five standard deviations away from the “electronic” one. It is alarming that the hydrogen atom has been studied without any big surprises in the last decades and as soon as someone measures something “exotic” a discrepancy appears. Of course, all protons should have the same size, no matter which experimental method is used to determine it. The so-called *proton radius puzzle* has caused a sensation and has been discussed extensively in literature [9, 10, 11]. Several ideas to solve the puzzle have been discussed, but the solution to the puzzle remains still unknown [12].

Recently, the CREMA collaboration has provided a value of the rms charge radius of the deuteron [13]

$$r_d = 2.12562(78) \text{ fm} \quad (1.3)$$

from a Lamb shift measurement in μd . This value again is more precise than but results to be 5 sigma away from the “accepted” value of $r_{\text{d}} = 2.1413(25) \text{ fm}$ [8].

A second, independent, and even more precise value of r_{d} is obtained by combining Eq. (1.2) with the deuteron-proton charge radius difference of [14]

$$r_{\text{d}}^2 - r_{\text{p}}^2 = 3.82007(65) \text{ fm}^2 \quad (1.4)$$

which is obtained by the measurement of the electronic isotope shift. So, combining Eq. (1.2) and (1.4), the resulting deuteron rms charge radius is [13]

$$r_{\text{d}}(\mu\text{p} + \text{iso}) = 2.12771(22) \text{ fm} \quad (1.5)$$

The deuteron radii from Eqs. (1.3) and (1.5) are compatible within 2.6σ .

After measuring nuclei with one and two nucleons, the CREMA collaboration has performed measurements of the Lamb shift in the hydrogen-like muonic helium-4 ion and in the muonic helium-3 ion [15]. These measurements are used to determine precise values of the charge radii of the alpha particle and the helion. Isotope shift measurements on ordinary helium atoms can be tested and used to obtain accurate values of the nuclear radii of helium-6 and -8. The values of these nuclear charge radii will be a benchmark for nuclear *ab initio* calculations which are essential to understand the internal structure of nuclei. Furthermore the measurement in muonic helium will set constraints on beyond standard model solutions proposed for the proton radius puzzle. Last but not least, a future measurement of the $1\text{S} - 2\text{S}$ transition in He^+ in combination with the measurement of the Lamb shift in muonic helium ions, will be able to test higher order bound-state QED and to extract an additional precise value of the Rydberg constant.

In this thesis the measurement of three different Lamb shift transitions in muonic helium-3 ions is described. The energy level structure as well as the measured transitions are shown in Fig. 1.1. The experiment has been performed in 2014 during a three months long data taking period at the Paul Scherrer Institute in Villigen, Switzerland. It is the first measurement of its kind and therefore no comparison to previous measurements is possible. However, the helion charge radius which is extracted in this work can be compared with several values obtained from electron scattering [16, 17, 18] (a complete list is found in [19]). Unfortunately their uncertainties are very large. The most recent value from electron scattering is provided by Sick [20] and amounts to

$$r_{\text{h}} = 1.959(34) \text{ fm}. \quad (1.6)$$

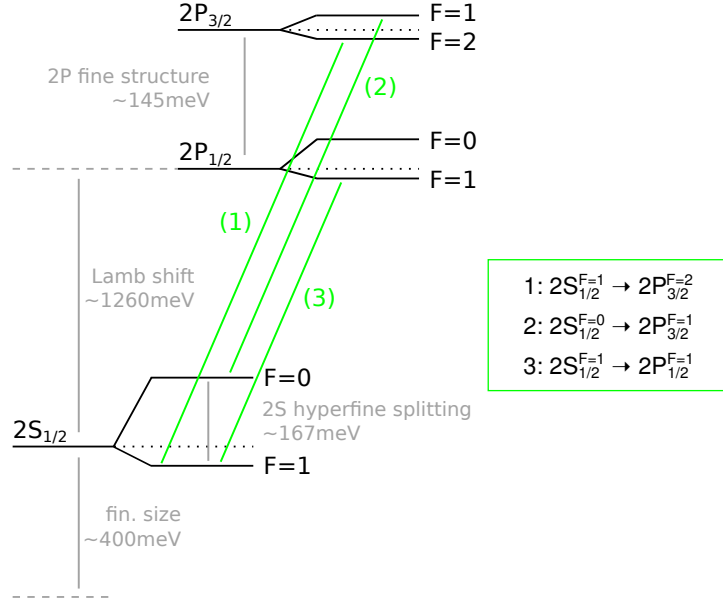


Figure 1.1.: $n=2$ states of muonic helium-3. The *green* lines indicate the measured transitions, numbered 1, 2, and 3. They are also listed in the box on the right side and in Tab. B.1. The Lamb shift is defined as the energy difference of the $2S_{1/2}$ and the $2P_{1/2}$ state. However, these states are no physical states and a measurement of the Lamb shift in muonic helium-3 always includes the hyperfine structure and, depending on the respective transition, the fine structure. The finite size effect is a part of the Lamb shift.

The most precise value of the helion charge radius available is given in Angeli *et al.* [21]. They obtain this value by a compilation of charge radius measurements in helium-4 and combine it with an isotope shift measurement from Shiner *et al.* [22]. It is important to note that the helium-4 charge radius compilation is dominated by a wrong measurement from Carboni *et al.* [23] as shown in [24]. Therefore the Angeli value does not serve as a comparison.

In the meantime the isotope shift value from Shiner *et al.* has not only been reevaluated with updated theory, but also additional isotope shift measurements have been performed and these measurements differ by several standard deviations. Hence, a further motivation of the measurement in this thesis is to provide a “muonic” isotope shift measurement, together with the alpha particle charge radius obtained from muonic helium-4 [24].

This thesis is structured as follows. Sec. 2 explains the experimental setup which has been used for the Lamb shift measurement. Sec. 3 estimates the systematics which are found to play a minor role. The measurement has produced about 4 TB of data. The analysis of this data, its calibration and cuts, are described in Sec. 4. At the end of this

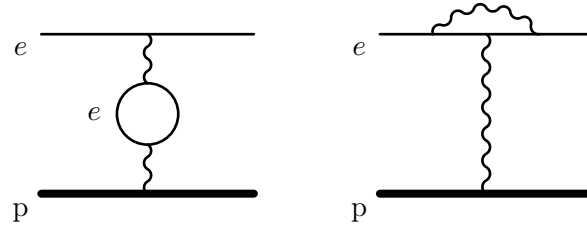


Figure 1.2.: The one-loop electron vacuum polarization, also referred to as *Uehling term* (left) and the electron self-energy correction (right). In ordinary hydrogen-like atoms, the self-energy is the leading contribution, followed by the vacuum polarization. The two contributions have opposite sign.

section the data is fitted with a line shape model. In order to compare the measurement with theory, the current knowledge of QED contributions to the Lamb shift transitions has to be compiled. This has been done in App. D which is summarized in Sec. 5. App. D is a draft of a paper which is about to be submitted. It is written in the same manner as a paper about the theory in muonic deuterium which has already been published [25]. As the paper about muonic deuterium theory also was an important part of my work it is attached to this thesis as App. E. Finally, Sec. 6 provides the results and discusses their impact.

1.1. Historical introduction of the Lamb shift

By means of their *microwave method* Willis E. Lamb, Jr. and Robert C. Retherford discovered in 1947 [1] that the $2S_{1/2}$ and the $2P_{1/2}$ levels in the hydrogen atom are not degenerate as predicted by the Dirac equation, but are separated by roughly 1 GHz. This so-called *shift* appeared when driving the $2S_{1/2} - 2P_{3/2}$ transition which differed from the expected frequency derived from the $2P_{1/2} - 2P_{3/2}$ energy difference. Furthermore they could depopulate the $2S_{1/2}$ state also via an incident frequency of 1 GHz driving directly the $2S_{1/2} - 2P_{1/2}$ transition.

The effect of finite size of the proton or the electron had already been estimated before [26] and was found to be far too small for serving as an explanation of the discovered $2S_{1/2} - 2P_{1/2}$ energy difference.

The effect of the *polarization of the vacuum*¹ (see Fig. 1.2) calculated by E. A. Uehling [27] could also not explain the effect. It was again too small and additionally had the wrong sign [28].

¹Note, that the so-called Uehling term results to be the leading contribution in muonic atoms. There the electron vacuum polarization is much enhanced due to the heavier mass of the muon.

The result of Lamb and Retherford was discussed extensively at the famous Shelter Island Conference. In order to explain this measurement Schwinger, Weisskopf, and Oppenheimer suggested an effect due to the permanent absorption and emission of virtual photons. This interaction with the radiative field results in an effective spread of the point-like electric charge over a finite volume, generating a correction to the Coulomb potential. This correction is called *self-energy* (see Fig. 1.2). The self-energy had not been considered before because it resulted in infinite shifts of the energy levels. Kramers' idea was to solve this problem by renormalization, which means that he would use the physically observed mass of the electron and not the bare mass (when uncoupled from the radiative field) which appeared in the equations. Hereby the self-energy of a free particle which is also infinite is subtracted from the one of a bound electron. During the conference no one knew how to perform this calculation. Bethe finally succeeded to calculate it and his result agreed well with the measured value of the *Lamb shift* as it is called today. His work set the foundations of future quantum electrodynamics (QED). [29]

Since its discovery, the Lamb shift has provided an ideal playground to test QED, for both experimentalists and theorists.

Nowadays the Lamb shift is calculated up to order α^6 and several measurements [30, 31, 32] have improved the value from Lamb and Retherford. Another group in Toronto is now working on a new measurement of the Lamb shift aiming for an unrivaled precision of 10^{-5} of the transition line width.

At the current level of accuracy in the $2S_{1/2} - 2P_{1/2}$ energy difference, the Lamb shift can not be explained by pure QED any more. Several nuclear effects are becoming more and more important. Especially the above mentioned finite size effect, proposed in 1933 [26], has become significant. Hence, the nucleus can not be treated as a point-like particle anymore. Its spatial charge distribution affects the energy levels of the bound lepton. The finite size effect in ordinary atoms only contributes on the 10^{-4} level to the $2S_{1/2} - 2P_{1/2}$ energy difference. However, due to the large muon mass, this effect is strongly enhanced for muonic atoms, which are very well suited to measure this quantity.

1.2. Muons

The muon has been discovered in 1937 [33], when Neddermeyer and Anderson studied the energy loss of particles occurring in the cosmic-ray showers. The unexpected discovery of a second charged lepton has provoked Rabi's famous exclamation "Who ordered

that?”. A justified question, as the muon was the first particle to be observed which is not a building block of ordinary atoms.

The muons are created in the upper atmosphere by collisions of cosmic high-energy protons which collide with the atomic nuclei in the air. In these collisions pions are created, which after a short lifetime decay into muons. The mass of the muon is about 200 times the mass of the electron. Muons have a lifetime of $2.2\,\mu\text{s}$ before they decay into electrons and neutrinos. Even though they travel with relativistic speed only the effect of time dilation makes it possible that they reach the Earth’s surface. The rate of muons reaching the surface is roughly $1\,\text{min}^{-1}\text{cm}^{-2}\text{sr}^{-1}$.

In order to use muons for physics experiments, their natural source is not well suited. A much more convenient way is to use proton accelerators where muons can be produced with increased rates and well defined energy and momentum. Nowadays muons are involved in numerous experiments which search for rare phenomena and measure precisely fundamental physical constants. Rare phenomena would be e.g. not yet discovered decay channels of the muon ($\mu \rightarrow eee$, $\mu \rightarrow e\gamma$), implying lepton flavor violation. The measurement of fundamental physical constants using muons (e.g. the muon g-2 experiment) test the standard model of particle physics. There are also several experiments using muonic atoms (like muonium or muonic hydrogen) for tests of bound-state QED. In 2010, the CREMA collaboration succeeded to measure the Lamb shift in muonic hydrogen and by that determined the proton charge radius. This thesis describes their follow-up experiment with muonic helium-3.

2. Experimental setup

2.1. Principle of the experiment

The measurement of the Lamb shift in $\mu^3\text{He}^+$ ions is achieved in the following way.

Low energy (5 keV) muons are stopped in a low pressure (2 mbar¹) gas target at room temperature filled with ^3He atoms. In collisions with the helium atoms the muon kicks out electrons. With each ionization the muon loses an energy of ≥ 24.6 eV, which corresponds to the ionization energy of the helium atom. After roughly $5 \text{ keV} / 24.6 \text{ eV} \approx 200$ collisions the muon remains bound to a nucleus, forming a highly excited $\mu^3\text{He}$ atom. From an initial state of $n \approx 14$ ² the muon cascades down towards the 1S ground state emitting several *prompt* X-rays. The second electron of the helium atom is emitted as an Auger electron. About one percent of the muons end up in the metastable 2S state. A good description of the muonic atom formation and the muonic cascade process is found in [34].

A certain time delay after the formation of the muonic atom, a laser pulse illuminates the target and its frequency is tuned over the Lamb shift transition. The laser, when having the correct frequency, excites the ion from the 2S to the 2P state from where it immediately (~ 0.5 ps) decays to the ground state emitting an 8 keV K_α X-ray. The resonance line is obtained by plotting these *delayed* X-rays against the laser frequency.

The sections in this chapter describe the production of low-energy muons by means of a proton accelerator and the muon beamline, then the heart of the experiment which is the target, containing a special multipass cavity and the detection system, and finally the laser system.

2.2. Proton accelerator and pion generation

The muonic Lamb shift experiment is situated at the Paul Scherrer Institute (PSI) in Switzerland. PSI provides a high intensity proton accelerator (HIPA) [35] which is

¹The pressure throughout this thesis is given in units of mbar. Note that 1 mbar = 1 hPa.

²The muon arrives at just that excited state n which has the largest overlap with the electron wavefunction. The corresponding quantum number n scales with the square root of the reduced mass ratio: $\sqrt{\tilde{m}_\mu / \tilde{m}_e} = \sqrt{186} = 13.6$.

needed as a first step for the low-energy muon production. The proton accelerator as well as the Lamb shift experiment is located in the so-called *Experimentierhalle*.

The acceleration process of the protons is extended over three stages. The first part is an 870 keV Cockcroft-Walton pre-injector [36], housing also the proton source. The second and third part are two ring cyclotrons in succession accelerating the protons up to 72 MeV, and finally 590 MeV. The final kinetic energy of the protons corresponds to a velocity of 80% of the speed of light. The resulting proton beam has a current of 2.2 mA which makes it the currently most powerful (~ 1.3 MW) proton beam in the world.

The high intensity proton beam is transferred to a graphite target (target E). In collisions of the high-energy protons with the nucleons of the carbon atoms pions are produced. For the Lamb shift experiment only negative pions are needed which are obtained via the strong interaction channel

$$np \rightarrow pp\pi^- . \quad (2.1)$$

From target E the low-momentum ($40 - 120$ MeV/ c) negative pions which are obtained from a backward scattering angle of 175° to the proton beam are guided via the pion beamline to the outlet at the π E5 area. The pion beamline supports pions with a momentum of ~ 100 MeV/ c (width 6% FWHM). They enter the first part of the Lamb shift experiment, the cyclotron trap (Sec.2.3) with a rate of 10^8 s $^{-1}$. There are also muons and electrons of similar momentum in the beam, and a considerable background flux of neutrons.

2.3. Low energy muon beamline

The purpose of the muon beamline (see Fig.2.1) is to convert the pion beam into a momentum-filtered low-energy negative muon beam, free of background from pions, neutrons, and electrons.

The muon beamline consists of a cyclotron trap (CT) [37, 38], a muon extraction channel (MEC) and the PSC ³. It is located in the π E5 area of PSI and is connected to the pion beamline mentioned in the previous section.

³The PSC is a huge solenoid which before had been used as part of a phase-space compression scheme. This is where the name PSC originates from.

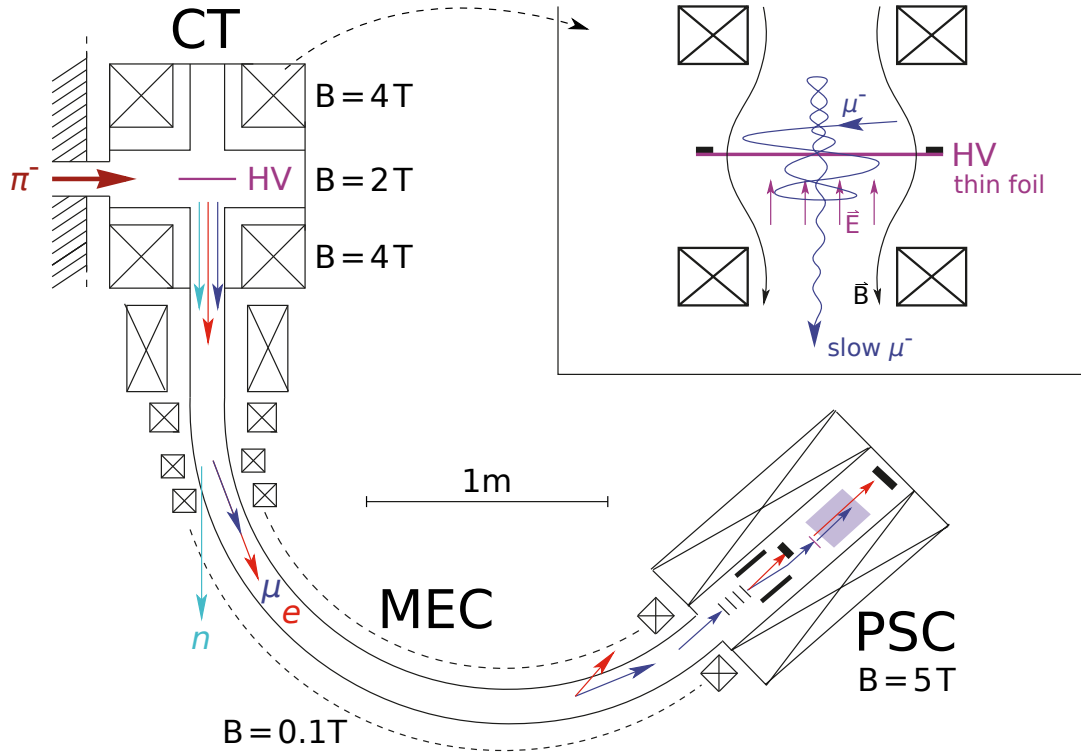


Figure 2.1.: The muon beamline. Pions from the PSI proton accelerator facility arrive at the cyclotron trap (CT) where they are moderated and decay into muons. The muons are slowed down and transferred to a large solenoid (PSC) via the muon extraction channel (MEC), which separates the muons from background radiation and at the same time serves as a momentum filter. In the PSC the muons are detected non-destructively before they enter the gas target where they are stopped and form muonic atoms.

2.3.1. Cyclotron trap

The CT [37, 38] is made out of two superconducting coils which create a 4 T magnetic field at their respective center. The resulting magnetic potential has the form of a magnetic bottle with a 2 T magnetic field at the center of the plane between the two magnetic coils. The pions from the PSI proton accelerator facility arrive at the CT with a momentum of $\sim 100 \text{ MeV}/c$. They enter the magnetic field of the CT from a transverse direction where they pass a moderator which slows them down to $40 - 60 \text{ MeV}/c$ ⁴. The moderator is chosen such that the pions pass it once and after that perform cyclotron motion without a second hit on the moderator. After a lifetime of $\tau_{\pi^\pm} = 26 \text{ ns}$ [40],

⁴40 MeV/c is the “magic” laboratory momentum $p_\pi = (m_\pi^2 - m_\mu^2)/2m_\mu \approx 40 \text{ MeV}/c$ near which pions decaying in flight yield (primarily transverse to their line of flight) very slow muons [39].

which for most of them is during the first few round-trips, about 30% of the pions decay in flight into muons via weak interaction

$$\pi^- \rightarrow \mu^- + \bar{\nu}_\mu, \quad (2.2)$$

the others hit the target walls or get stuck in the moderator hitting it a second time.

Most of the muons have kinetic energies above the acceptance of the trap and are lost, only a few percent remain trapped. These few percent are the ones where the muon is emitted predominantly at kinetic energies below a few MeV. Spiraling in the magnetic bottle potential forth and back along the magnetic field lines these muons are further slowed down by passing repeatedly a 160 nm Formvar foil installed between the two coils perpendicular to the magnetic field (see inset in Fig. 2.1). The Formvar foil is coated with a conductive 3 nm Ni layer and mounted on a high negative voltage (−20 kV) copper ring which accelerates the muons axially towards the magnetic bottle necks on both sides of the CT. In that way the ratio of longitudinal to transverse momentum increases. As soon as the ratio is large enough (~ 1) the muons leave the CT through the bottle neck. Half of the muons is lost by leaving the CT opposite to the MEC. Muons which leave the CT through the bottle neck entering the MEC have kinetic energies of 20 – 50 keV.

2.3.2. Muon extraction channel

The MEC transfers the muons from the CT to the target region, which is protected from neutron radiation originating from the pion beam outlet by a 1 m thick massive concrete block. Furthermore the MEC serves as a momentum filter for muons in the energy range of 20–40 keV. It consists of 17 identical magnetic coils mounted in such a way that the resulting magnetic field has a toroidal form spanning over a segment of 130° . Its magnetic field measures 0.15 T. The momentum filter is achieved due to the toroidal shape of the magnetic field which leads to a slight magnetic field gradient in the horizontal plane. Particles with charge q and momentum $p = \sqrt{p_\parallel^2 + p_\perp^2}$ in a homogeneous magnetic field B perform a cyclotron motion with radius a_c of

$$a_c = \frac{p_\perp}{|q|B}. \quad (2.3)$$

If there is a magnetic field gradient the cyclotron radius varies spatially. It is larger in the region of a lower magnetic field and vice versa. Hence, in the case of a horizontal gradient a vertical drift results. Muons with higher momenta p_\perp have larger cyclotron radii a_c and therefore experience larger magnetic field differences which results in an

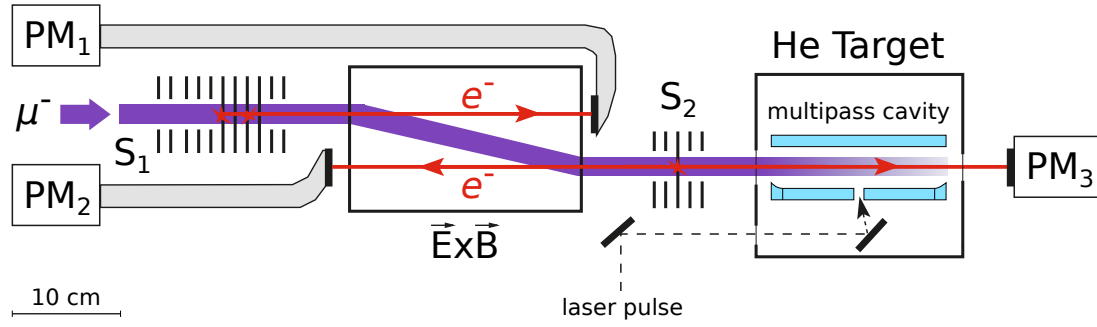


Figure 2.2.: Muon detection. Before the muons enter the target they pass two stacks (S_1 and S_2) of conducting rings, which are kept on negative high voltage. Some of them also serve as support for thin carbon foils. Passing S_1 , the muons kick out electrons which hit a scintillator connected to a photomultiplier (PM_1). The muons are separated from these electrons in an $\vec{E} \times \vec{B}$ filter and pass a second stack (S_2) where they again kick out electrons detected by the photomultipliers PM_2 or PM_3 . A coincidence of signals from S_1 and S_2 triggers the laser. This configuration at the same time also serves to frictionally cool the muons. After the detection system the muons enter the target where they are stopped and form muonic atoms.

increased vertical drift. Using collimators at the end of the MEC muons with a certain momentum range can be chosen. In order to keep the required muons (~ 20 keV) on a horizontal plane the individual magnetic coils are tilted from the vertical plane by about 4° . A weak toroidal magnetic field of the MEC yields a large cyclotron radius and so increases the vertical drift of the muons. Exiting the MEC the muons enter the PSC, a 1 m long solenoid which creates a 5 T homogeneous magnetic field in its inner 20 cm spanning bore hole. Inside the target, the muons need to be stopped in a small volume (given by the size of the multipass cavity) which requires a small cyclotron radius. This is the reason for the strong 5 T field in the PSC which shrinks the muon beam to a diameter of a few millimeters. The bore hole in the PSC contains a device for non-destructive muon detection as well as a gas target with the multipass cavity described in the next sections.

2.3.3. Nondestructive muon detection

The principle of the nondestructive muon detection system (see Fig. 2.2) is the following. Before entering the target the muons pass thin carbon foils. In collisions with the carbon atoms of these foils the muons kick out electrons. The electrons are separated from the muons and detected via a plastic scintillator connected to a photomultiplier (PM_1 , PM_2 , PM_3). The muons continue towards the target.

This basic principle is realized by two stacks (S_1 and S_2) of stainless steel rings. Between

the two stacks there is an $\mathbf{E} \times \mathbf{B}$ (velocity) filter. S1 contains 15 rings, where the rings 8 to 12 (counting in muon direction) carry ultra-thin ($d = 4 \mu\text{g cm}^{-2}$) carbon foils. S2 contains 5 rings with only the third ring carrying a carbon foil. As the muons have very low energies in the keV range they are slowed down significantly by the carbon foils. In order to prevent absorption of the muon the rings are connected via resistances and kept at high negative voltage. Hence, after each foil the muons are accelerated along the magnetic field lines. An advantage of this configuration is that the muons are also slightly frictionally cooled [41]. After passing S1 the muons enter the $\mathbf{E} \times \mathbf{B}$ filter. Here, the magnetic field (5 T) stems from the solenoid (PSC) and the electric field is produced via a capacitor with a distance of 2 cm between the conducting plates. Charged particles experience a drift in the filter, anti-proportional to their velocity and perpendicular to the electric and magnetic fields. As the electrons have much higher velocities than the muons they are hardly affected by the filter. In this way a separation of muons and electrons is achieved. Whereas the electrons are absorbed in the scintillator, the muons continue to S2 where they again produce fast electrons which hit scintillators connected to the photomultipliers PM2 and PM3. Subsequently the muons enter the target with an energy of $\sim 5 \text{ keV}$. A coincidence of the signals from S1 and S2 ⁵ produces the T1 signal which (if the laser and the DAQ are ready) leads to the fire laser (FL) signal which triggers the laser.

2.4. The gas target and its inner workings

After a muon is detected by the nondestructive muon detection system it enters the helium target (see Fig. 2.2). The target is filled with ordinary ^3He atoms and kept at room temperature at a pressure of $\sim 2 \text{ mbar}$. It houses the multipass cavity and several optical elements which allow for the alignment of the laser beam entering the cavity as well as for the characterization of the light distribution inside the cavity. Outside of the target several LAAPDs and plastic scintillator paddles are installed for the detection of X-rays and electrons, respectively. Pictures of the target and its inner parts are shown in Fig. 2.3.

The target is an aluminum box which extends over 220 mm along the muon beam axis. It has an entrance and an exit window which measure $19 \times 8 \text{ mm}^2$ centered around the beam axis. The window, a thin Formvar foil ($4 \mu\text{g cm}^{-2}$), has to keep the helium gas inside the target but still be transparent to the incoming muons. It has to stand a pressure difference of 2 mbar from the target to the vacuum in the muon beamline

⁵a signal from S2 can be either a happening in PM2 or in PM3. Here no coincidence is required.

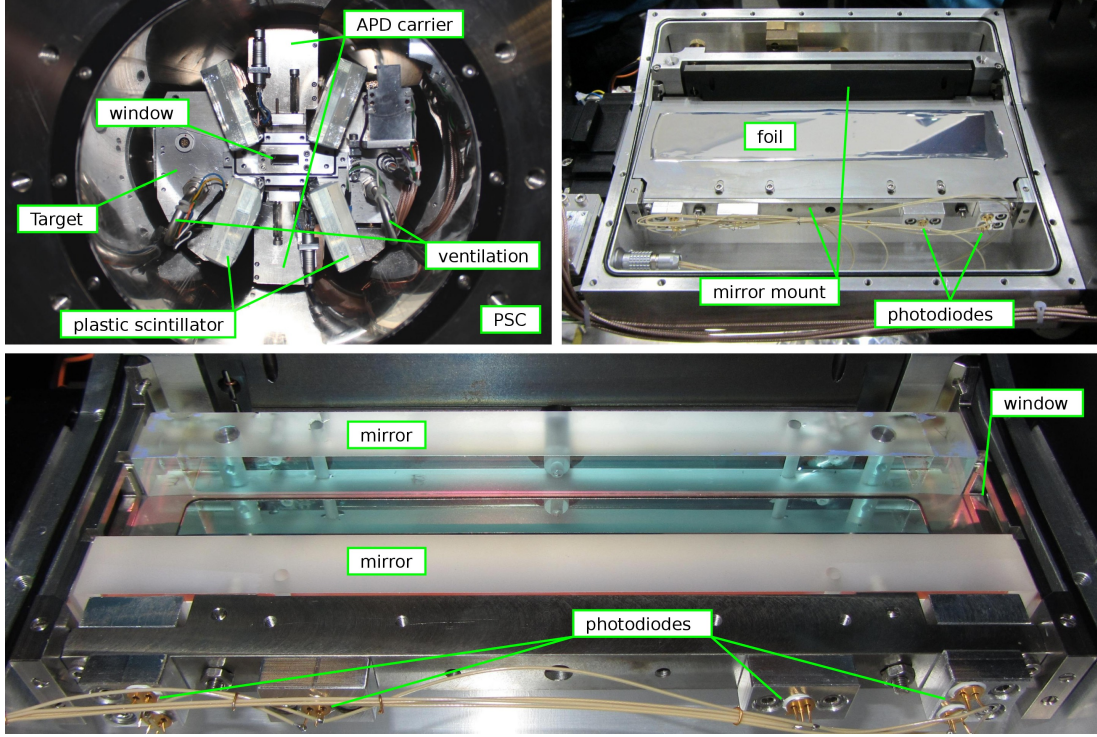


Figure 2.3.: Pictures of target, cavity, and detection system. The first image (*top left*) shows the target inside the bore hole of the solenoid, with the exit window of the target in the center. Right above and below this window the carrier for the LAAPDs is seen. The plastic scintillators are recognized by their X shape around the muon stop volume. The small tubes visible at the left and right side are part of the helium ventilation. The second image (*top right*) shows the opened target carrying the mirror cavity in its middle. The cavity is covered with an aluminum coated foil in order to protect the APDs (not visible here) from light. The third image (*bottom*) shows the uncovered cavity in the target. At the left and right side reside the target windows. The muons enter from the right side. At the backside of the cylindrical mirror photodiodes are installed to monitor the light distribution inside the cavity.

and is therefore reinforced with gold-plated tungsten wires ($15\text{ }\mu\text{m}$ diameter, 0.4 mm distance). The helium gas in the target is continuously exchanged in order to keep it as pure as possible. As ^3He resources are limited a circulation system was built which also contains a helium purification mechanism. More information about the circulation system is found in App. C. The volume defined by the muon beam inside the target is called *muon stop volume*. The cross section of the muon beam is adjusted by collimators which are placed between the $\mathbf{E} \times \mathbf{B}$ filter and S2. The muon stop volume is enclosed horizontally by the multipass cavity and vertically by thin, aluminum coated foils which protect the LAAPDs arranged behind from laser light. The plastic scintillators are collocated in an X shape around the muon beam.

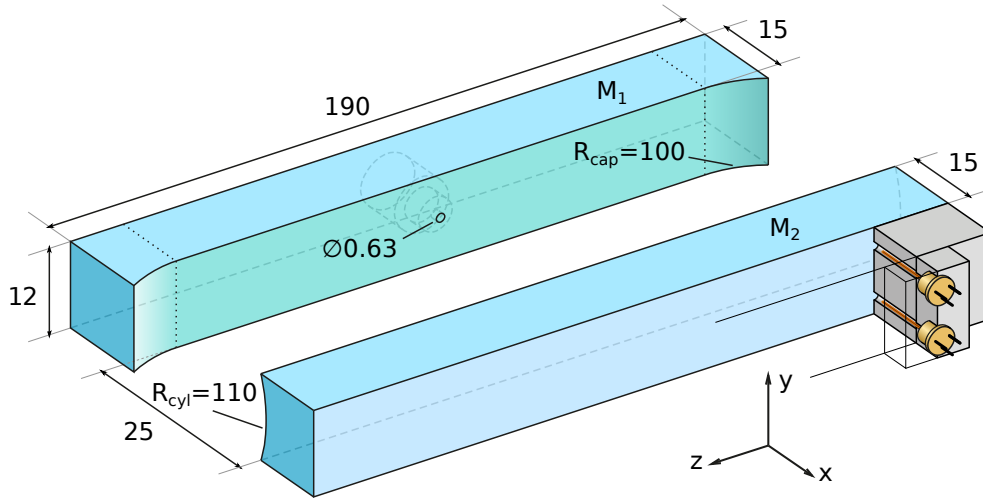


Figure 2.4.: The multipass cavity. The muon beam enters the cavity through the muon entrance window along the z axis. The laser beam is injected via the hole in the center of the flat mirror (M_1). Two end caps with cylindrical shaped surface are connected tightly to the flat substrate. They confine the laser light along the z axis in the horizontal plane. The other mirror (M_2) is of cylindrical shape and therefore confines the light along the y axis in the vertical plane. The illuminated stop volume measures $25 \times 7 \times 176 \text{ mm}^3$. On the back side of mirror M_2 the online monitoring system for the light distribution inside the cavity is sketched (shown are two from a total of six photodiodes). Small pieces of fiber in front of the photodiodes reduce the incidence angle and so increase the sensitivity on the mirror alignment. The dimensions in this figure are given in mm .

In the following the cavity and the detection system of X-rays and electrons is described more in detail.

2.4.1. Multipass cavity

The multipass cavity [42] (see Fig. 2.4) has been especially designed for the experiments of the CREMA collaboration, but in principle is well suited for all kinds of particle beam experiments. Its concept provides a nearly arbitrary large overlap with the particle beam without the need of blocking it by a mirror. Still it does not occupy too much space, so there remains a large free solid angle where detectors can be placed. Additionally it is robust against misalignment and so fulfills the requirement of long term stability (a beamtime extends over several months) without any need of active stabilization.

It is composed of two elongated mirrors which are placed in the horizontal plane along the muon beam axis. As substrate material fused silica is used. The mirrors have a reflectivity of 99.98% in the required range of 800 to 1000 nm. The coated surface measures $190 \times 12 \text{ mm}^2$. One of the mirrors is flat (M_1) and has at its center a hole

of 630 μm diameter for the injection of the laser pulse. The other mirror (M2) is of cylindrical shape (110 mm radius of curvature) confining the light in the vertical plane. The pulse is injected through the hole in a slightly tilted way. Thereby the light is hindered to exit the cavity through the injection hole right after the first reflection. In order to avoid that the light leaves the cavity in the horizontal plane two cylindrical end caps (100 mm radius of curvature) are connected tightly to the flat mirror. By this configuration the light is confined in all directions. Tilting the entering laser beam defines the size of the illuminated volume. A useful tilt of the laser beam makes sure that the light is distributed fast over the stopping volume but still stays confined between the mirrors. The laser beam has its focus of 100 μm at the mirror hole. About 95% of the light is coupled into the cavity. The cavity confines the light for $\tau_c \approx 110 \text{ ns}$ corresponding to 1300 reflections. Its lifetime is constrained by the reflectivity of the coating, by the gaps (50 μm) between the cylindrical end caps and the flat mirror, and by the size of the injection hole.

Having an average pulse energy of 4.5 mJ for the first measured transition line (line 1 in Fig. 1.1) the fluence F in the cavity yields

$$F_1 = 4.5 \text{ mJ} \frac{1300}{7 \times 176 \text{ mm}^2} \approx 0.5 \text{ J cm}^{-2}. \quad (2.4)$$

For lines 2 and 3 the average pulse energy is 5.9 mJ which results in a fluence of

$$F_{2\&3} = 0.6 \text{ J cm}^{-2}. \quad (2.5)$$

The saturation fluences of the helium transitions are given in Tab. B.1. They amount to 1.3 J cm^{-2} , 1.1 J cm^{-2} , and 3.3 J cm^{-2} , for lines 1, 2 and 3, respectively. For line 2 the pulse energy is already close to saturation. As the matrix element for line 3 is very small, here, a higher fluence would be desirable. The laser pulse energy, however, is limited by the optical surface damage threshold of the mirrors where the diameter during the first reflections of the beam is small.

The light distribution inside the multipass cavity (Fig. 2.5) can be measured by a thin (25 μm diameter) vertically spanned wire which is moved along the muon beam axis. The light inside the cavity is reflected from the wire and recorded by a CCD camera. The thickness of the wire is chosen such that it does not significantly alter the light distribution. Fig. 2.5 shows that the intensity distribution has its maxima at the outer edges of the light-filled volume. This can be explained in a ray optics picture where the light bounces forth and back between the two mirrors with a small, but finite reflection angle, “slowly” approaching the border of the mirror surface. The curvature of the mirror slows down the process of approaching the border and causes a turning

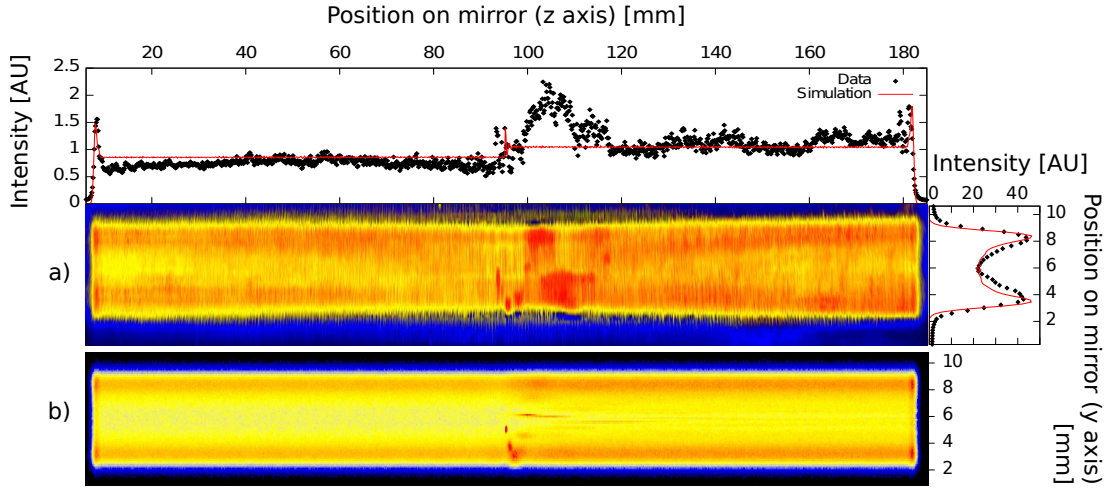


Figure 2.5.: Light distribution inside the multipass cavity [42]. This is a comparison of the measured (a) and the simulated (b) light distribution in the multipass cavity when it is well aligned. The light which reaches the outer edges (vertically and horizontally) is turning back towards the cavity center. At the turning point it spends more time which is where the intensity maxima are observed. Close to the injection hole the laser beam cross section is still quite small and therefore intensity peaks are observed.

point from where the light moves back towards the center. The light spends more time at the turning point, which increases the intensity which is then reflected by the thin wire.

The light intensity is distributed rather homogeneously ($\pm 30\%$) in the cavity volume. However the method using a thin wire can not be applied during measurement and therefore is used only for characterization and alignment of the cavity, which is done outside the target (*offline*). Once the cavity is aligned and placed in the target a different method is used to monitor the light distribution *online*.

The online method is necessary because of two reasons. First, the space inside the target, especially above and below the cavity is very tight. If something is not placed correctly it is possible that by closing the target mechanical forces lead to a misalignment. Second, the laser pulses might damage the entrance hole or one of the cavity mirrors. In both cases the fluence inside the cavity can be drastically reduced. Via the online system it can be observed if anything like this has happened.

The online system is realized by six photodiodes which are placed with some distance behind the mirror substrate. Short pieces of an optical fiber ($600\text{ }\mu\text{m}$, multi-mode) guide the light which is transmitted through the cavity mirror to the photodiodes. The photodiodes therefore only see the transmitted light at a certain position and under a certain incidence angle.

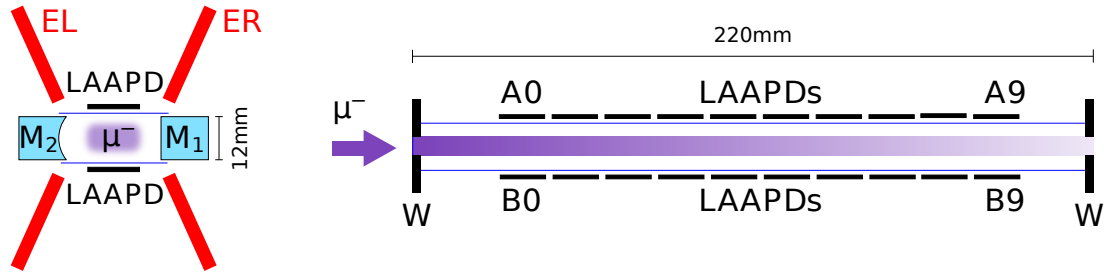


Figure 2.6.: X-ray and electron detection system. *left:* A cross section of the detection scheme in the target. The APDs are located above and below the muon beam. The electron paddles are ordered in X shape around the cavity to capture as many electrons as possible, which perform cyclotron motion in the magnetic field. *right:* Side view of the muon stop section.

Four of the six photodiodes are located at the outer edge of the light distribution. Their vertical position is chosen in a way that only the light from the intensity maxima (in vertical direction) reaches the photodiodes. Hence, a vertical misalignment, which shifts up or down the light-filled volume, leads to an immediate decrease of the detected intensity. The exact horizontal position of the photodiodes is not very important as a slight (horizontal) misalignment leads to a loss in intensity throughout a wide region. They are placed with a horizontal distance of ± 75 mm from the center of the mirror. The other two photodiodes are located on the axis of the cavity, where most of the atoms are, with a distance of ± 45 mm from the center of the mirror.

A sketch of the installed online system is shown in Fig. 2.4. The online system is described more in detail in Ref. [43].

2.4.2. Detection of X-rays and electrons

When a muonic atom is formed prompt X-rays from the muonic cascade are emitted. A successful excitation of the Lamb shift transition is indicated via a delayed 8.1 keV X-ray. Finally, the muon decays into an electron and two neutrinos. A specialized detection system records all these events which are needed in order to determine the transition energy of the Lamb shift. The arrangement of the detectors is shown in Fig. 2.6.

For the detection of the X-rays 20 large area avalanche photo diodes (LAAPDs, or short APDs) [44, 45] are used. They are located outside of the target 8 mm above and below the muon beam center. The single APDs are labeled A0-A9 (B0-B9) above (below) the cavity counting along the muon beam direction. The individual APDs have an active surface of $14 \times 14 \text{ mm}^2$ and are mounted very close to each other reducing

the size of the gap (~ 1 mm) between them. In total the APDs cover roughly 30% of the entire solid angle into which X-rays are emitted. The APDs are cooled via a closed ethanol circuit down to -30°C and actively stabilized on a level of less than 0.1 K. They are biased with a high reverse voltage of 1600-1690 V (depending on the individual APD) which results in a gain of 200. Under these conditions an average energy resolution of about 15% (FWHM) for the 8.1 keV K_α X-rays is achieved. The signal is amplified by a factor of about 100 in preamplifiers which are located right next to the APDs and further amplified ($4\times$) by post-amplifiers outside the vacuum of the PSC. The final signal amplitude is about 200 mV. It is then recorded on a circular memory buffer of a waveform digitizer ⁶ (WFD) and a time-to-digital converter ⁷ (TDC), each APD being related to one channel respectively. The signals are labeled with the names of the individual APDs (A0 to B9) they are originating from.

Muon decay electrons have kinetic energies in the MeV range. In the strong magnetic field of the PSC they perform cyclotron motion crossing all kinds of solid material (like target walls, APDs, mirrors). Four plastic scintillator paddles (also termed electron paddles) with dimensions of $250 \times 60 \times 5 \text{ mm}^3$ are located outside the target in an X shape around the muon beam axis. The four electron paddles are connected to two photomultiplier tubes (PMTs). The recorded signals are therefore only distinguishable between right and left (but not top and bottom) paddles, creating the signals ER and EL. Before they are recorded on a TDC they are discriminated into signals of four different amplitudes as there are *low*, *m1*, *m2*, and *high*. The decay electrons might also deposit energy (10-20 keV) in the APDs. Signals in the APDs with an energy in that range are therefore also treated as electrons in the analysis. The detection of a decay electron after an X-ray signal ensures that the X-ray signal itself was not created by the muon decay electron.

2.5. Laser system

The lifetime of a muon is about $2.2 \mu\text{s}$. Hence, the temporal distance between the detection of a muon right before entering the target and the arrival of a laser pulse in the target should be kept as short as possible. The muons arrive with an average rate of about 300 Hz but at random times. Thus the laser cannot be driven with a fixed repetition rate, but rather has to be stochastically triggerable. Once the pulse entered

⁶CAEN V1720 8 Channel 12bit - 250MS/s Digitizer

⁷CAEN V767 128 Channel Multihit TDC (800 ps)

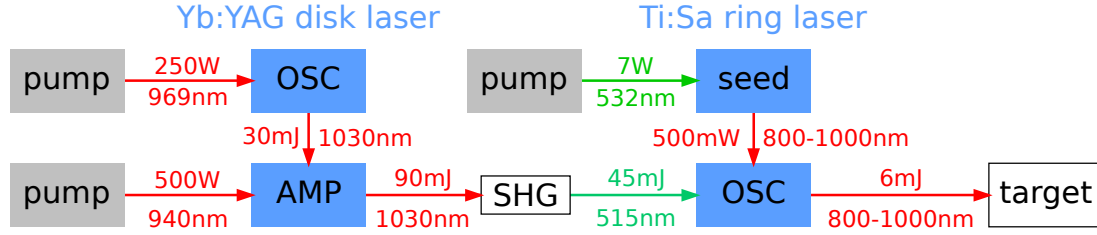


Figure 2.7.: The laser system. A Ti:Sa oscillator is pumped by a frequency-doubled Yb:YAG thin disk laser. The disk laser is composed of an oscillator and an amplifier, both pumped by high-power diode lasers. The frequency of the Ti:Sa oscillator is adjusted and controlled by a continuous wave (cw) single frequency Ti:Sa ring laser. The ring laser is pumped by a cw Yb:YVO₄ laser and controlled by a wavemeter.

the multipass cavity it is distributed over a large volume, demanding high pulse energies in order to reach optimal excitation probabilities.

The requirements for this laser system are then, a stochastic trigger with an average repetition rate of up to 500 Hz⁸, pulse energies of 12 mJ⁹, and 500 ns delay between the trigger and the laser pulse. Additionally the laser has to run under the conditions typical for accelerator experiments. This means it has to provide long-term stability over months. It is placed in a temperature stabilized room, termed *laser hut* (LH). The LH sits right next to the area π E5. The laser beam path from the LH to the target cavity measures about 20 m.

The laser system in the $\mu^3\text{He}^+$ experiment has already been used for the Lamb shift measurement in $\mu^4\text{He}^+$ [24] and with some minor differences in the predecessor experiments with μp and μd [46]. It is sketched in Fig. 2.7. A Ti:Sa oscillator tunable in the required range of 850-960 nm (for the LS transition energies, see Tab. B.1) is pumped by a frequency-doubled Yb:YAG thin disk laser [47, 48, 49]. In order to precisely tune its frequency the Ti:Sa oscillator is injection seeded by a frequency controlled continuous wave (cw) Ti:Sa ring laser. The different parts of the laser are explained in more detail in the following.

The concept of a thin disk laser [50] is chosen, because it is ideally suited for high pump power densities with reduced thermal distortions. The pump laser consists out of a Q-switched thin disk oscillator followed by an 8 pass¹⁰ thin disk amplifier. The Yb:YAG thin disk of the oscillator is 345 μm thick with a 7% doping, the Yb:YAG thin

⁸The repetition rate needs to be higher than the average muon rate due to the statistical distribution of the muons.

⁹Due to damage thresholds of the optics inside the target the pulse energy was limited to 6 mJ.

¹⁰The meaning of a *pass* varies in literature. In this work one *pass* refers to one reflection, which means that the disk is actually traversed twice.

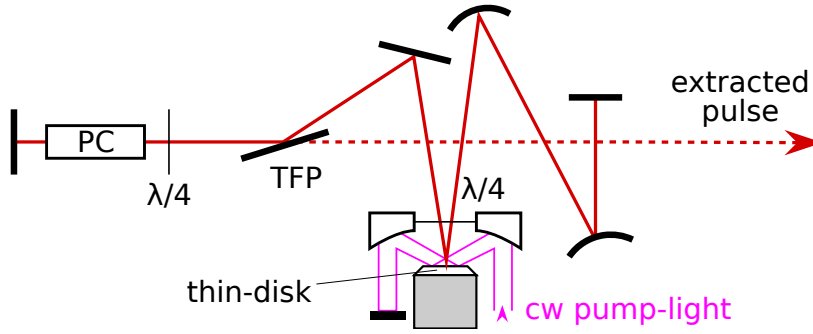


Figure 2.8.: The Q-switched Yb:YAG thin disk oscillator. The cavity of the thin disk oscillator is 1 m long. The disk is water-cooled to 10°C. It is continuously pumped by 250 W of 969 nm light. By default the cavity is open and the linear polarized 1030 nm light exits through the thin film polarizer (TFP). Upon the laser trigger the Pockels cell (PC) turns the polarization which makes the TFP highly reflective and therefore closes the cavity for pulse build-up. After 250 ns the polarization is turned again and a laser pulse with an energy of 30 mJ and a pulse duration of 100 ns exits the oscillator.

disk of the amplifier is 456 μm thick with a 5% doping. Both are anti-reflection (AR) coated on the front side, high-reflection (HR) coated on the backside, and contacted to water cooled CVD¹¹ diamond heat sinks.

The disk of the oscillator is cw pumped by a fiber-coupled diode laser (969 nm) with 250 W. The cavity of the oscillator is shown in Fig. 2.8. It is 1 m long and composed of a Pockels cell (PC), two $\lambda/4$ plates, a thin film polarizer (TFP), and the already mentioned disk. One $\lambda/4$ plate is located right in front of the thin disk in order to reduce interference effects of the incoming and back-reflected light. The second $\lambda/4$ plate is placed between the PC and the TFP. The combination of PC, $\lambda/4$ plate, and TFP allows to close and open the cavity. The second $\lambda/4$ plate is also used to adjust the intra-cavity power. By default the cavity is open and runs in pre-lasing mode with an intra cavity power of ~ 1 W. This ensures a short delay between the fire laser (FL) signal and the extraction of a laser pulse. The FL signal triggers the HV of the first electrode of the PC closing the cavity for the pulse build-up. After a delay of 250 ns the second electrode is set to HV and the cavity opens again. The emitted pulse (30 mJ, 100 ns) enters the multipass amplifier.

The 8 pass thin disk amplifier is pumped by a second fiber-coupled diode laser (940 nm) with 500 W. In the amplifier the light traverses the Yb:YAG disk 16 times. A sketch of the beam trace is shown in Fig. 2.9. The amplifier consists of several concatenated optically stable elements. A single element is composed of a flat end mirror,

¹¹CVD for chemical vapor deposition, a technique to grow artificial diamonds, which provide high thermal conductivity and mechanical stability.

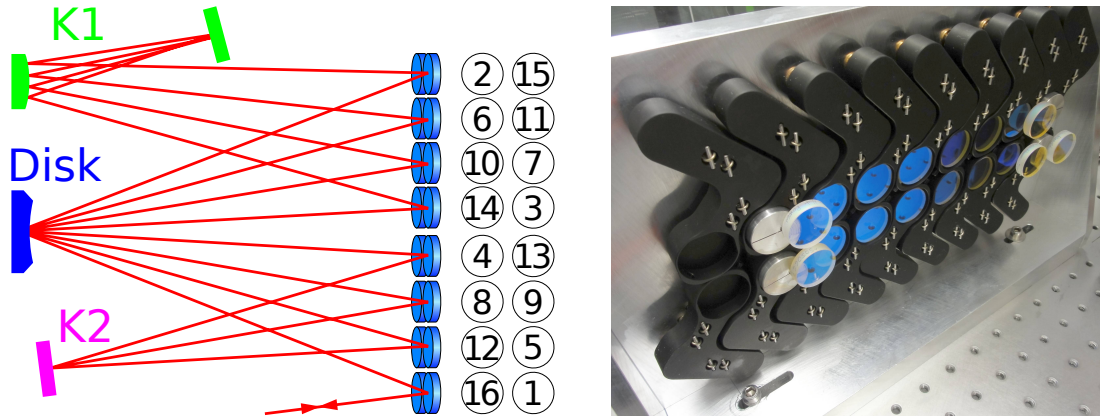


Figure 2.9.: A sketch of the beam trace (*left*) and the mirror array (*right*) of the thin disk amplifier. The laser pulse experiences 8 reflections at the Yb:YAG thin disk, hence the light traverses the disk 16 times. The way between the mirrors K1 and K2 is a stable optical element which is repeated 8 times. The numbers from 1 to 16 indicate the order in which the mirrors of the array are reflecting the light. In total the pulse is amplified by a factor of 5. On the right side a picture of the mirror array with the L shaped mirror mounts is shown. They were developed in order to place the mirrors as close to each other as possible, keeping the feature of aligning them individually.

a convex mirror, the thin disk (focusing the light), and another flat end mirror. This element is multiplied and strung together. So in each element the beam shape is reproduced. The end mirrors for each round-trip are the same. The mirrors between the end mirrors and the thin disk are mounted on a special mirror array where each mirror is adjusted individually. Special L-shaped mounts have been developed in order to place these mirrors very close to each other and still maintain the degrees of freedom for individual alignment. This design was chosen because it minimizes thermal lens effects and is rather insensitive to pointing instabilities. During the beamtime the amplifier was running for months without any need of realignment. In each round-trip (path of one stable optical element) the laser pulse traverses the disk four times (2 passes). The total gain of the amplifier depends on various parameters as there are the pump power density, temperature, thickness of disk, etc. After 8 passes a gain of 3 is achieved. The gain of a single pass is then ~ 1.15 . Pulses exiting the disk amplifier have energies of 90 mJ at 1030 nm. The pulses are then frequency-doubled to 515 nm in an LBO¹² crystal. The pulses at 515 nm with an energy of 45 mJ are then used to pump the Ti:Sa crystal of the Ti:Sa oscillator.

The Ti:Sa oscillator is an injection-seeded ring laser. Its frequency is adjusted by seeding it with a cw single-frequency Ti:Sa ring laser through the out-coupling mir-

¹²Lithium triborate (LiB_3O_5)

ror. This so-called seed laser is tunable in an interval between 800 and 1000 nm which encloses most of the Lamb shift transitions in $\mu^3\text{He}^+$. It is pumped continuously with 7 W at 532 nm provided by a frequency-doubled Nd:YVO₄¹³ diode laser. The seed laser contains several optical intra-cavity elements (several Lyot filters and a solid etalon) for the selection of the wavelength. Two galvo plates used to adjust the effective cavity length which widens the mode-hopping free tuning range. The cavity is locked to a wavemeter which has been calibrated via several transition lines in Cs and Kr [51].

The cavity of the Ti:Sa oscillator contains a prism in order to adjust the gain-maximum to the seed wavelength. The final pulses exiting the Ti:Sa oscillator are sent to the non-resonant multipass cavity in the target. For that a roughly 20 m long distance has to be covered. The beam pointing over that distance is controlled by an active pointing stabilization system. The pulses entering the multipass cavity are about 90 ns long and have energies in the range of 6 mJ. A photodiode (E0) behind the in-coupling mirror right before the multipass cavity records a signal proportional to the pulse energy. The multipass cavity has already been described in Sec. 2.4.1.

¹³Neodymium-doped yttrium orthovanadate

3. Systematics

In muonic systems a precise measurement of the charge radius requires to split the transition line only on a level of a few percent (with a linewidth of 320 GHz this is on the order of 10 GHz). Due to this rather gross splitting of the line in combination with the strong binding energies in a muonic atom the experiment is quite insensitive to systematic effects. The effects on the Lamb shift experiment have already been described for the case of $\mu^4\text{He}^+$ in [24]. Most of these effects apply in the same way to the $\mu^3\text{He}^+$ experiment. For the sake of completeness they will be briefly discussed in this thesis. However, there are also some differences between these two isotopes, which are amongst others the nuclear mass and the nuclear spin (^4He has nuclear spin $I = 0$, whereas ^3He has $I = 1/2$). A non-zero nuclear spin gives rise to a hyperfine splitting (HFS) leading to energetically close states. This enhances an effect called *quantum interference* which was not considered for the CREMA experiments until recently and which is treated more in detail in Sec. 3.2. A summary of the estimated effects is found in Tab. 3.1.

Table 3.1.: Systematic effects in the $\mu^3\text{He}^+$ experiment. This table shows the shifts and the broadenings due to effects estimated in this section. The total value is the quadratic sum of the above. The AC and DC Stark effect is not listed as their contribution is much smaller than even the collisional effects. The given uncertainty for the quantum interference (QI) is a conservative upper limit. The details are given in Tab. 3.3. The power broadening depends strongly on the respective transition. It is discussed in Sec. 3.3.5 and is included in the line shape model in Sec. 4.7.

	Shift (Uncertainty) [GHz]	Broadening [GHz]
Laser	0.12	0.84
QI	0.2	0
Zeeman effect	0	0.5
Doppler broadening	0	2.4
Collisional effects	$< 5 \times 10^{-4}$	$< 2 \times 10^{-4}$
Power broadening	0	(16 – 48)
Total (w/o Pow.broad.)		2.6
Total	0.2	16 – 48

The total broadening effect (added quadratically) is completely dominated by the power broadening. As the power broadening (see Sec. 3.3.5) is taken care of in the line shape model introduced later in Sec. 4.7, it is interesting to know what the remaining broadening is. The remaining broadening effects (not included in the line shape model) are dominated by the Doppler broadening. Added quadratically they amount for all three measured transition lines to

$$\Delta\nu_{\text{broadening}} = 2.6 \text{ GHz.} \quad (3.1)$$

Compared to the linewidth of $\sim 320 \text{ GHz}$ and the low statistics of the measurement this broadening effect is negligible.

The total shift, given in Tab. 3.1, is not corrected and included as a systematic uncertainty. It depends on the specific transition. An upper limit which is valid for all three lines is given by

$$\Delta\nu_{\text{uncertainty}} = 0.2 \text{ GHz.} \quad (3.2)$$

Compared to the statistical uncertainty in the range of 20 GHz (to be discussed in Sec. 4.7), the systematical uncertainty again is negligible.

3.1. Characterization of the laser

The systematics arising from the laser have been discussed in detail in [51] and [24].

The dominating effect originating from the laser is its bandwidth. The FWHM amounts to

$$\Delta\nu_{\text{FWHM}} = 0.84(10) \text{ GHz,} \quad (3.3)$$

which results in a broadening of the Lorentzian transition line. The broadening effect is somewhat in between a Lorentzian and a Gaussian. As this effect is small compared to the natural transition line width ($\sim 320 \text{ GHz}$), no further investigation is needed.

A contribution to the uncertainty of the frequency originates from the laser frequency calibration. The cavity is locked to a wavemeter with an accuracy of 60 MHz . The wavemeter in turn has been calibrated by transition lines in Kr and Cs.

A part contributing to a frequency shift arises from chirp. The laser chirp has been measured in the context of [51] and contributes a shift of $-60 \pm 30 \text{ MHz}$. As this is too small to correct for, a conservative uncertainty of 100 MHz is taken into account.

The total “laser uncertainty” which enters the value for the transition frequencies is then given by the quadratic sum of 60 MHz from the wavemeter and 100 MHz from the chirp

$$\Delta\nu_{\text{laser}} = 0.12 \text{ GHz} \quad (3.4)$$

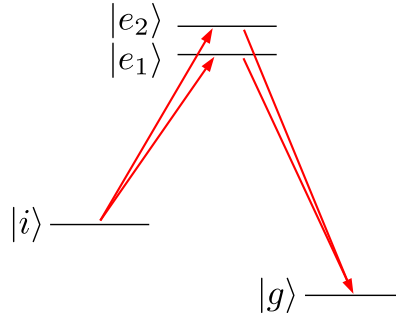


Figure 3.1.: Interfering paths in an atomic system. Interference happens if different paths over ≥ 2 excited states exist and only if initial and final state is the same for all paths. This is the case if e.g. a resonant laser excites the transition from $|i\rangle$ to $|e_1\rangle$ and non-resonant excitation to $|e_2\rangle$ is possible.

A possible distortion of the transition line arises from asymmetries in the pulse energy when scanning the very broad transitions (320 GHz, corresponding to nearly 1 nm). The pulse energy of each run is discussed in Sec. 3.3.1 and the power fluctuations are then taken into account by a line shape model, which is used to fit the transition lines (see Sec. 4.7). This effect, however, has to be very small, because the results of the line shape model agree very well ($\sim 0.1\sigma$) with the results from a simple Lorentzian fit which does not account for the variations in laser pulse energy (see Sec. 4.7).

3.2. Quantum interference in the CREMA experiments

The effect of quantum interference (QI) can be understood considering an atomic energy level system as seen in Fig. 3.1, with one initial state $|i\rangle$, ≥ 2 excited states $|e_n\rangle$, and one final (ground) state $|g\rangle$. A laser excites the atomic system from $|i\rangle$ to $|e_1\rangle$. The successful excitation is detected via the emission of a photon when decaying to the ground state. The possibility that the atom is excited to another (not $|e_1\rangle$) close lying excited state is finite and if the possible paths have the same initial and final states (as shown in Fig. 3.1) they are indistinguishable and therefore they interfere. The QI results in an additional anisotropy in the emission pattern, which means that the line shape of the detected signal depends on the detection angle referred to the quantization axis of the atomic system¹. Fitting a Lorentzian function to an asymmetrically deformed line results in a shift of the extracted line center. Several references [52, 53, 54, 55] describe and calculate this effect for atomic precision physics experiments. A rule of thumb to find out if the QI effect matters is given by [52]:

¹The quantization axis in the CREMA experiments is given by the horizontal polarization of the linear polarized laser.

Table 3.2.: Quantum interference: rule of thumb applied to CREMA measurements. Listed are the transitions of μp , μd , and $\mu^3\text{He}^+$ which were measured by the CREMA collaboration. u is the total uncertainty given in units of the linewidth Γ , d is the distance from the excited state to the closest allowed energy level, also given in units of Γ . If the inverse uncertainty u^{-1} is larger than d , a significant QI effect is expected. The transitions marked with a cross are therefore candidates for being affected by QI. The crosses which are marked with brackets are very close to fulfill the rule of thumb and should also be investigated. Of course, also farther separated states do contribute, but their influence is less significant.

	$\Gamma_{2\text{P}}$ [GHz]	meas. trans.	u [$\Gamma_{2\text{P}}$]	d [$\Gamma_{2\text{P}}$]	
μp	18.5	$2\text{S}_{1/2}^{\text{F}=1} - 2\text{P}_{3/2}^{\text{F}=2}$	1/28	42	
		$2\text{S}_{1/2}^{\text{F}=0} - 2\text{P}_{3/2}^{\text{F}=1}$	1/18	59	
μd	19.5	$2\text{S}_{1/2}^{\text{F}=3/2} - 2\text{P}_{3/2}^{\text{F}=5/2}$	1/21	9	x
		$2\text{S}_{1/2}^{\text{F}=1/2} - 2\text{P}_{3/2}^{\text{F}=3/2}$	1/10	5	x
		$2\text{S}_{1/2}^{\text{F}=1/2} - 2\text{P}_{3/2}^{\text{F}=1/2}$	1/9	5	x
$\mu^3\text{He}^+$	318.7	$2\text{S}_{1/2}^{\text{F}=1} - 2\text{P}_{3/2}^{\text{F}=2}$	1/16	18	(x)
		$2\text{S}_{1/2}^{\text{F}=0} - 2\text{P}_{3/2}^{\text{F}=1}$	1/15	18	(x)
		$2\text{S}_{1/2}^{\text{F}=1} - 2\text{P}_{1/2}^{\text{F}=1}$	1/16	44	

"If the precision measurement has an accuracy of one part in N of the natural linewidth, a neighboring resonance within N natural linewidths of the resonance leads to a significant shift."

This effect has recently been studied [55] for the CREMA experiments as the given rule of thumb applies in some parts to the measurements which have been performed, see Tab. 3.2. In the case of μp QI seems to be negligible whereas for μd a deeper investigation is necessary. Also $\mu^3\text{He}^+$ is quite close to the rule of thumb. As calculation and cross checking of this effect was part of this thesis (see also [55]) the QI effect is studied here in more detail. The effect is treated similar to Refs. [53, 56]. For that several formulas are used which have been derived in [57] and [58]. It should be mentioned already here that the following treatment will show the QI effect to be irrelevant because of the large solid angle which is covered by the APDs in the CREMA setup.

In order to understand the full line shape in the QI regime one needs to have a closer look at Fermi's golden rule

$$\frac{dR_{i \rightarrow f}}{d\Omega_s} = \frac{2\pi}{\hbar} |M_{fi}|^2 \rho_s, \quad (3.5)$$

where M is the scattering matrix with initial and final state i and f and ρ_s the density of scattered photon states into the solid angle $d\Omega_s$. It was derived by Dirac in 1927 [59] and describes in first order perturbation theory the transition rate of a perturbed system with an initial and a final state. From a generalized golden rule (up to second order processes) the Kramers-Heisenberg formula can be derived, which is e.g. done in chapter 8.7 of [60]. It was used in the way written down by Brown *et al.* [53]

$$\frac{dR_{i \rightarrow f}}{d\Omega_s} = \frac{\pi E_L^2 \omega_s^3}{h^3 c^3 \epsilon_0} \left| \sum_e \frac{(\hat{\epsilon}_s^* \cdot \mathbf{D}_{fe})(\mathbf{D}_{ei} \cdot \hat{\epsilon}_L)}{\omega_{ei} - \omega_L - i\Gamma_e/2} \right|^2. \quad (3.6)$$

Here, E_L , ω_s , and ϵ_0 are the amplitude of the electric field of the laser, the frequency of the scattered light, and the permittivity of free space, respectively. \mathbf{D} is the dipole operator which is projected onto the polarization vector of the incident and scattered light, $\hat{\epsilon}_L$ and $\hat{\epsilon}_s$. ω_{ei} is the transition frequency from the initial state i to the excited state e and ω_L is the laser frequency. The scattering matrix contains the sum over all possible excited states e with decay rate Γ_e . Eq. (3.6) shows the origin of QI-induced shifts: The square modulus is not the incoherent sum of Lorentzians, but cross-terms occur which distort the lines.

The matrix elements of the dipole operator with the polarization of the incident ($\mathbf{D}_{ei} \cdot \hat{\epsilon}_L$) and with the polarization of the scattered light ($\hat{\epsilon}_s^* \cdot \mathbf{D}_{fe}$) will in the following be written as $d_p^{i \rightarrow e}$ and $d_q^{e \rightarrow f}$. Now the polarization p of the incident light and q of the scattered light is given in spherical components with the values $(-1, 0, 1)$. The matrix element from state 1 to state 2 is then given in a good basis for a hydrogen-like atom with non-zero nuclear spin as

$$d_q^{1 \rightarrow 2} = \langle n I J F m_F | d_q | n' I J' F' m'_F \rangle. \quad (3.7)$$

It can be reduced decoupling it from the polarization by taking advantage of the Wigner-Eckart theorem and introducing the Wigner $3j$ symbol, as shown in equation 4.120 of Ref. [58]. The matrix element becomes then

$$\langle n I J F m_F | d_q | n' I J' F' m'_F \rangle = (-1)^{F-m_F} \begin{pmatrix} F & 1 & F' \\ -m_F & q & m'_F \end{pmatrix} \langle n I J F | d | n' I J' F' \rangle. \quad (3.8)$$

This matrix element can be further reduced in two steps considering that the spin I of the nucleus as well as the spin S of the lepton are not associated with the electric dipole

moment. This is done according to equation 4.175 of the same Ref. [58], extracting two times a Wigner 6j symbol. For the nuclear spin I this is

$$\begin{aligned} \langle n I J F | d | n' I J' F' \rangle &= (-1)^{I+J+F'+1} \sqrt{(2F+1)(2F'+1)} \\ &\times \begin{Bmatrix} J & F & I \\ F' & J' & 1 \end{Bmatrix} \langle n J | d | n' J' \rangle \end{aligned} \quad (3.9)$$

and finally for the leptonic spin S , with $J = L + S$

$$\begin{aligned} \langle n (SL) J | d | n' (S' L') J' \rangle &= (-1)^{S+L+J'+1} \sqrt{(2J+1)(2J'+1)} \\ &\times \begin{Bmatrix} L & J & S \\ J' & L' & 1 \end{Bmatrix} \langle n, L | d | n', L' \rangle. \end{aligned} \quad (3.10)$$

In total the matrix element is then given by

$$\begin{aligned} d_q &= \langle n, L | d | n', L' \rangle \\ &\times (-1)^{S+L+J'+1} \sqrt{(2J+1)(2J'+1)} \begin{Bmatrix} L & J & S \\ J' & L' & 1 \end{Bmatrix} \\ &\times (-1)^{I+J+F'+1} \sqrt{(2F+1)(2F'+1)} \begin{Bmatrix} J & F & I \\ F' & J' & 1 \end{Bmatrix} \\ &\times (-1)^{F-m_F} \begin{pmatrix} F & 1 & F' \\ -m_F & q & m'_F \end{pmatrix} \end{aligned} \quad (3.11)$$

This electric dipole matrix element can be used either for the excitation (absorbing) process with initial and excited state ($d_p^{i \rightarrow e}$) or for the decay (emitting) process ($d_q^{e \rightarrow f}$) with polarization p and q , respectively. The term $\langle n, L | d | n', L' \rangle$ is evaluated via the Schrödinger hydrogen wavefunctions. As d has only radial dependence the wavefunction

$$\psi_{nlm}(r, \theta, \phi) = R_{nl}(r) Y_{lm}(\theta, \phi) \quad (3.12)$$

can be separated into a radial $R_{nl}(r)$ and a spherical part $Y_{lm}(\theta, \phi)$. The reduced matrix element then becomes

$$R_{nl}^{n'l'} = \langle n, L | d | n', L' \rangle = \int \psi_{n'l'm'}^*(r, \theta, \phi) r \psi_{nlm}(r, \theta, \phi) dr d\Omega \quad (3.13)$$

$$= \int R_{n'l'}^*(r) r R_{nl}(r) r^2 dr, \quad (3.14)$$

where the integral over the spherical part is 1. The general result of this integral is given in equation 63.2 of Ref. [57] and can be simplified for the absorbing process where

the principle number n does not change (CREMA experiment: 2S – 2P transition) to (equation 63.5 in [57])

$$R_{nl}^{n,l-1} = \frac{3n}{2} \sqrt{n^2 - l^2} \stackrel{n=2, l=1}{\approx} 5.196 \quad (3.15)$$

and for the emitting process with 2P– n S (CREMA experiment: 2P–1S transitions) to (equation 63.4 in [57])

$$R_{21}^{n0} = \sqrt{\frac{2^{15} n^9 (n-2)^{2n-6}}{3(n+2)^{2n+6}}} \stackrel{n=1}{\approx} 1.290. \quad (3.16)$$

Now the scattering matrix element, which appears in Eq. (3.6),

$$M_{fi}^{qp} = \sum_e S_{i \rightarrow e \rightarrow f}^{qp} = \sum_e \frac{d_q^{e \rightarrow f} \times d_p^{i \rightarrow e}}{\omega_{ei} - \omega_L - i\Gamma_e/2} \quad (3.17)$$

with polarizations p and q for incident and scattered light and the sum over all possible excited states is determined. In the CREMA case the detector does not distinguish between the different scattered polarizations, so it detects a combination of the different spherical components. As the different spherical components are not emitted isotropically the ratio of the different detected polarizations and therefore the detected interference pattern depends at which angle the detector is placed (for now the detector is assumed to be point-like). As shown later, the large CREMA detector makes the QI effect much smaller.

The emitted intensity pattern up to here is only given in the spherical basis. However, for a better understanding this should be rewritten for spherical coordinates. This will also help to later integrate over the given detector surface in the experiment. A scattering matrix M , known in the spherical basis, can be expressed in the Cartesian basis by

$$\vec{M} = \begin{pmatrix} -\frac{1}{\sqrt{2}}(M^1 - iM^{-1}) \\ \frac{i}{\sqrt{2}}(M^1 + iM^{-1}) \\ M^0 \end{pmatrix} \quad (3.18)$$

Here, $M^{q=-1,0,1}$ are the matrix elements from Eq. 3.17. For simplicity the only index written down is the spherical component q which represents the polarization of the emitted light.

The unit vectors of the spherical coordinates can also be expressed in the Cartesian basis by

$$\vec{e}_r = \begin{pmatrix} \sin \theta \cos \phi \\ \sin \theta \sin \phi \\ \cos \theta \end{pmatrix} \quad \vec{e}_\theta = \begin{pmatrix} \cos \theta \cos \phi \\ \cos \theta \sin \phi \\ -\sin \theta \end{pmatrix} \quad \vec{e}_\phi = \begin{pmatrix} -\sin \phi \\ \cos \phi \\ 0 \end{pmatrix} \quad (3.19)$$

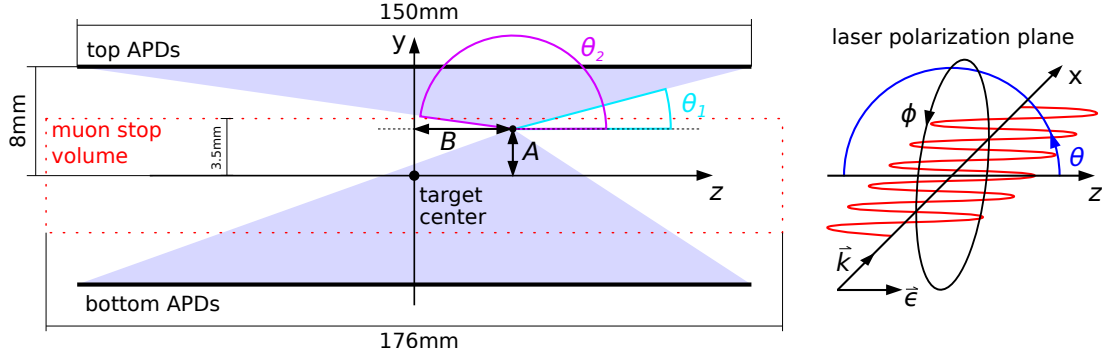


Figure 3.2.: Detection geometry for the QI effect. Shown is the transverse cross section of the target where the muons enter from the left side and are stopped along the z axis inside the muon stop volume (dotted red line). The violet surface shows the opening angle $\Delta\theta = \theta_2 - \theta_1$ where the scattered light of the atom at position (A, B) is detected. On the right side the laser propagation and polarization in the $x - z$ plane is shown.

The scattering matrix is then projected onto the unit vectors². The emission probability (intensity) is finally given by the sum of the squares. Ordering the terms by the values of q yields

$$\begin{aligned}
 I_i^p(\theta) &= |M_i^p|^2 \propto |\vec{e}_\phi \cdot \vec{M}|^2 + |\vec{e}_\theta \cdot \vec{M}|^2 \\
 &\propto \sum_f \left(\frac{1}{2} (\cos^2(\theta) + 1) \left| \sum_e S_{p,-1}^{i \rightarrow e \rightarrow f} \right|^2 \right. \\
 &\quad \left. + \frac{1}{2} (\sin^2(\theta)) \left| \sum_e S_{p,0}^{i \rightarrow e \rightarrow f} \right|^2 \right. \\
 &\quad \left. + \frac{1}{2} (\cos^2(\theta) + 1) \left| \sum_e S_{p,+1}^{i \rightarrow e \rightarrow f} \right|^2 \right)
 \end{aligned} \tag{3.20}$$

For each spherical component q all (close lying) excited states are summed coherently. Pulling out the sums over the excited states would make them incoherent, in consequence the different paths would not interfere and the QI would disappear. Between the different spherical components, no interference exists. Additionally the sum is taken over all possible final states. The sum over f is incoherent and can be pulled out³. With Eq. (3.20) the lineshape for a point-like detector placed under an angle θ is given. Note that Eq. (3.20) is independent of ϕ .

²The projection along \vec{e}_r is neglected because only the directions along \vec{e}_θ and \vec{e}_ϕ are of interest here.

³Paths with different final state do not interfere.

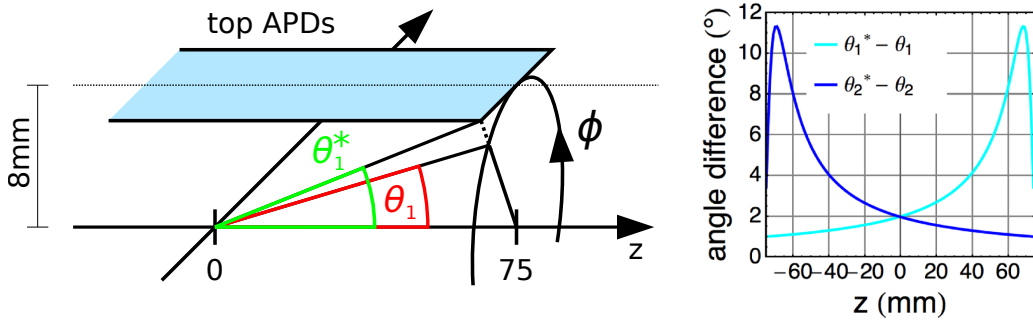


Figure 3.3.: The top APDs are shown in the CREMA coordinate system. Neglecting the ϕ dependence by assuming cylindrically shaped APDs, the integration interval $\Delta\theta = \theta_2 - \theta_1$ (θ_2 not shown) results actually larger than it is in reality. The influence of this effect depends strongly on the z position of the muonic atom, see figure on the *right*.

For the last step the coordinate system has to be placed into the geometry of the CREMA experiment (see Fig. 3.2). The LAAPDs detect the intensity $I_i^{p=0}$ ⁴ of the scattered light of a muonic atom located at position (A, B) in the muon stop volume. Now the specific line shape has to be calculated which is dependent on the geometry of the detection with respect to the quantization axis. For that at first a two dimensional system as shown in Fig. 3.2 is considered and $I_i^{p=0}$ is integrated from $\theta_1(A, B)$ to $\theta_2(A, B)$ for the top APDs and in the corresponding range $[\theta'_1, \theta'_2]$ for the bottom APDs.

$$I_{\text{total}}(A, B) = \int_{\theta_1}^{\theta_2} I(\theta) d(\cos \theta) + \int_{\theta'_1}^{\theta'_2} I(\theta) d(\cos \theta) \quad (3.21)$$

The reduction to two dimensions seems reasonable, because the emission intensity is not dependent on ϕ . However, the arrangement of the LAAPDs is not symmetric in ϕ , because the LAAPDs have no cylindrical shape. Hence, the opening angle $\Delta\theta = \theta_2 - \theta_1$ varies slightly for different ϕ (see Fig. 3.3). Ignoring this effect would result in a situation as shown in the figure by the starting angle θ_1 (red). The same applies to the end angle θ_2 (not shown in the figure). Thus the opening angle is in total reduced by $(\theta_1^* - \theta_1)$ and $(\theta_2^* - \theta_2)$, respectively. The effect is position dependent and exemplary shown as a function of the z coordinate. In the worst case the opening angle can be reduced by up to $(11+1)^\circ$ at a position of $(A = 0, B = z = 68 \text{ mm})$. However, this is only at the outer edge of the APDs and has to be averaged with those ϕ directions where the effect is smaller. Doubling the QI shift which is calculated in the two dimensional model will give a conservative estimate.

⁴ $p = 0$, for the laser polarization pointing in z direction.

Table 3.3.: QI effect in the CREMA experiments. In this table conservative estimates for the QI effect in the CREMA experiments are given. Shown are only the relevant transitions. The effect can shift the result when fitting a purely Lorentzian line shape to a distorted line. As comparison the statistical uncertainty u on the line center given by the Lorentzian fit is shown. The uncertainty values are taken from Refs. [7, 13] and from this work for μp , μd , and $\mu^3\text{He}^+$, respectively. The shifts result to be too small to be significant and can therefore be neglected.

	meas. trans.	shift [% Γ]	shift [MHz]	u [GHz]
μp	$2\text{S}_{1/2}^{\text{F}=1} - 2\text{P}_{3/2}^{\text{F}=2}$	0.009	+1.7	0.57
	$2\text{S}_{1/2}^{\text{F}=0} - 2\text{P}_{3/2}^{\text{F}=1}$	0.011	+2.0	1.00
μd	$2\text{S}_{1/2}^{\text{F}=3/2} - 2\text{P}_{3/2}^{\text{F}=5/2}$	0.025	+4.8	0.84
	$2\text{S}_{1/2}^{\text{F}=1/2} - 2\text{P}_{3/2}^{\text{F}=3/2}$	-0.084	-16.4	2.0
	$2\text{S}_{1/2}^{\text{F}=1/2} - 2\text{P}_{3/2}^{\text{F}=1/2}$	0.112	+21.8	2.2
$\mu^3\text{He}^+$	$2\text{S}_{1/2}^{\text{F}=1} - 2\text{P}_{3/2}^{\text{F}=2}$	0.004	+12.7	19.6
	$2\text{S}_{1/2}^{\text{F}=0} - 2\text{P}_{3/2}^{\text{F}=1}$	0.051	+162.5	20.9
	$2\text{S}_{1/2}^{\text{F}=1} - 2\text{P}_{1/2}^{\text{F}=1}$	-0.009	-28.7	19.5

Finally the intensity I is calculated by integrating $I_{\text{total}}(A, B)$ over the whole muon stop volume, i.e. all possible positions $[A, B]$ within the muon stop volume (red dotted rectangle in Fig. 3.2). As the stopping distribution is quite homogeneous, no further function weighing the intensities from different origins (A, B) is necessary. The resulting lineshape from intensity I is then fitted with an incoherent sum of Lorentzians. The final QI shift is the difference of the position resulting from the fit to the theoretical transitions implemented before. An example for μd which shows the incoherent fit to the coherent line shape is given in Fig. 3.4. The shifts calculated for all transitions in μp , μd , and $\mu^3\text{He}^+$ are listed in Tab. 3.3. The results have been compared with the calculations of a group in Lisbon, led by J. P. Santos, which calculated the shifts independently. The results agreed very well, and have been published by Amaro *et al.* [55]. Later a follow-up paper has been published by the same group, investigating the effect of elliptically polarized laser light [61].

3.3. Estimation of other systematic effects

In contrast to the QI effect which has not been considered in atomic laser spectroscopy until recently there are many well known systematic effects which are studied in the

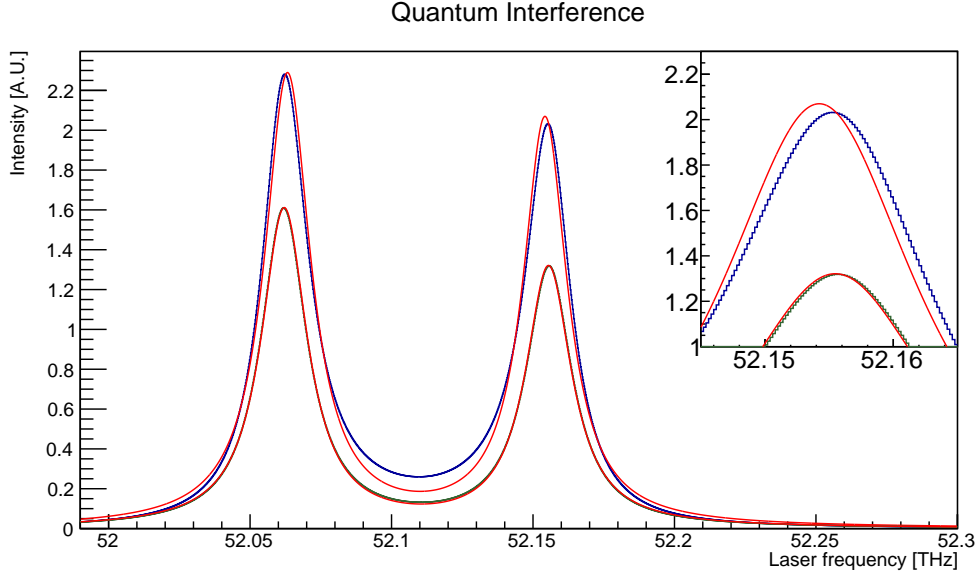


Figure 3.4.: The quantum interference effect. Shown are two transitions (pseudo data) in muonic deuterium, where the effect is maximal. Both transitions have the same initial state $2S_{1/2}^{F=1/2}$ which is excited to the close lying hyperfine states $2P_{3/2}^{F=3/2}$ and $2P_{3/2}^{F=1/2}$. The excitation happens with linear polarized light (in the horizontal plane) (see Fig.3.2). The muonic atom is located at the origin ($x,y,z = 0$). The *blue* and the *green* line are detected with different detection geometries (for better visibility the two cases are presented with different amplitudes). The *blue* line shows the coherent line shape seen by a point-like detector at an angle of $\theta = 0^\circ$. The *green* line shows the coherent line shape seen by the APD detectors in the CREMA geometry. The red lines are the respective fits with an incoherent sum of two Lorentzians. The inset on the right top shows clearly the effective shift of the extracted resonance lines. Maximizing this effect with a (unrealistic) point-like detector (*blue* line), the shift can get as large as 8% of the linewidth. However, in the real setup (*green* line) the shift is roughly 0.1% of the width, which is negligible in our case.

following. They have been considered previously for μp , μd , and $\mu^4\text{He}^+$. The estimation of the various effects is described in literature and here follows in large parts Ref. [62]. The effects which are estimated below are possible shifts due to the Zeeman effect, Doppler broadening, and collisional effects. Power broadening is treated later in Sec. 4.7. The AC and DC Stark effect are not treated here. This has been done in detail in Ref. [46] for μp and is several orders of magnitude below the required precision. As shown in [46], the main reason for the AC Stark shift to vanish is the very short (0.5 ps) lifetime of the 2P state. It leads to a decay rate which is larger than the Rabi oscillation. In consequence overdamping occurs which leads to a suppression of the AC Stark shift. The DC Stark effect is negligible mainly due to the 200 times smaller Bohr radius.

3.3.1. Asymmetries in the recorded data

There are different parameters which could lead to an asymmetry in the recorded data that would shift the fitted line center. A trivial reason for a shift would be if one side of the line is measured much longer than the other. This is accounted for by normalizing the number of counts of the data points to the measurement times.

Another origin of an asymmetry might arise from fluctuations in the laser pulse energy. The fitted line center could so be distorted by systematical variations of the pulse energy with respect to the laser frequency. This 'laser asymmetry' can have different origins. Temperature drifts which e.g. could lead to mirror misalignment might impose shifts on a time scale of days or weeks. This kind of asymmetry has been avoided by measuring randomly at different frequencies, switching between the two sides of a line. Intrinsic properties of the laser can also shift the line. The laser is tuned over several hundreds of GHz and its efficiency or beam pointing might easily change over that range. For that the laser pulse energy is recorded on a pulse-per-pulse basis with photodiodes and after each run calibrated using a commercial pyroelectric detector (see also App. A.2.2).

The pulse energy plotted against frequency is shown in Fig. 3.5. For the first line (top of Fig. 3.5) the laser has an average power of 4.5 mJ. The line center is roughly at 347.2 THz. In total the power fluctuations are not very strong. However, during the final days of measurement some data at the peak of the line were recorded at much higher pulse energy. This could lead to an overestimated signal to noise ratio and an underestimated width.

The average pulse energy of the second and the third line is 5.9 mJ. In this energy and frequency range the pulse energy fluctuates much more than in the first case. The rough positions of the line centers are 310.8 THz and 312.8 THz.

In order to avoid possible line shifts one should consider these power fluctuations in the fit.

Possible shifts are taken care of by a line shape model where the individual events are binned in terms of the pulse energy and so fitted with a different amplitude. The fitting procedure is described more in detail in Sec. 4.7.

3.3.2. Zeeman effect

The muon stop volume is placed in a strong homogeneous $B = 5\text{ T}$ magnetic field where the diameter of the incoming muon beam is small. By that the muons are concentrated in a small stop volume which is illuminated by means of a multipass cavity. The strong

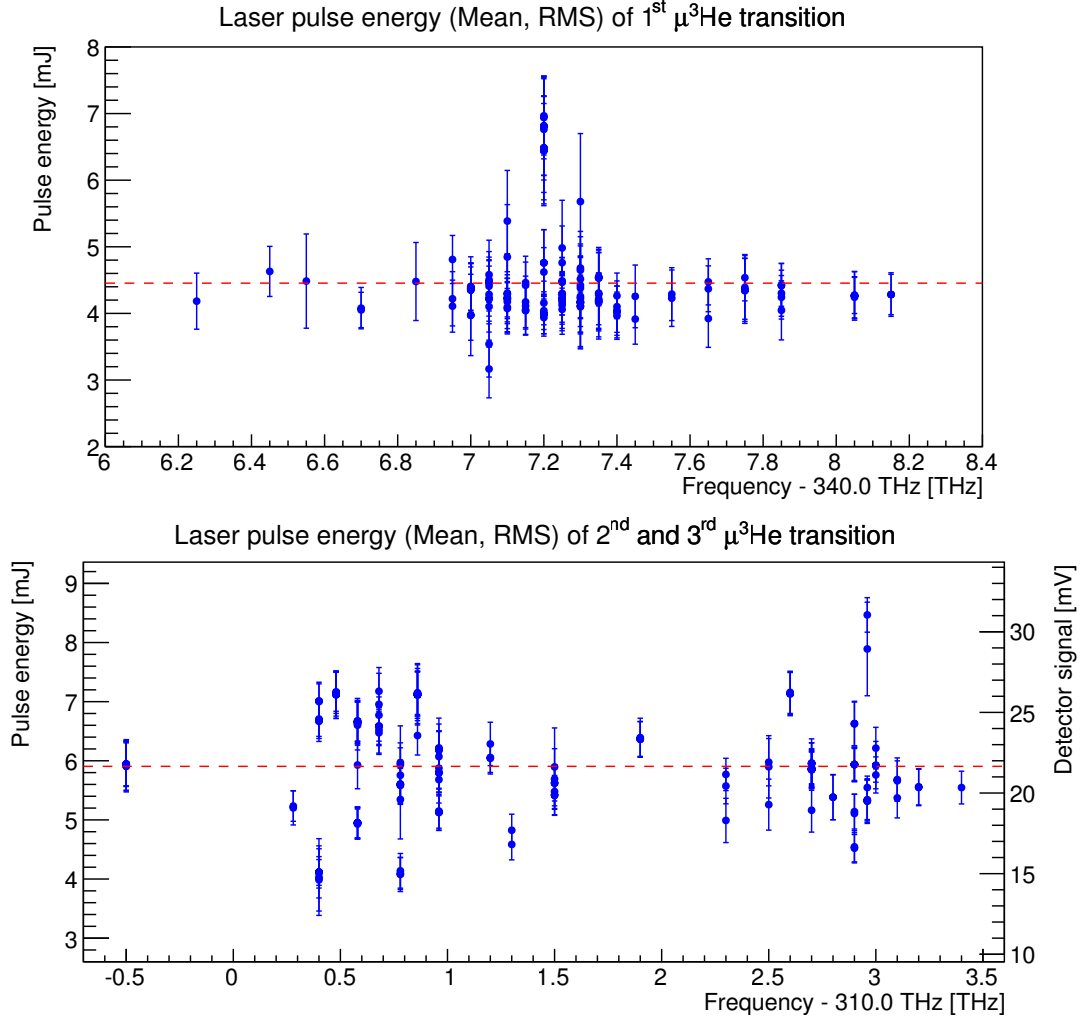


Figure 3.5.: Laser pulse energy plotted against frequency for the first (*top*) and the second and third (*bottom*) measured transition lines. Each data point represents a single run. The red dashed line indicates the mean of the total data set, respectively. The runs with noticeably high pulse energies at 347.2 THz (*top*) and 312.7 THz (*bottom*) are the reason for the high lying data points in the resonance plots which are shown later in Sec. 4.7. Note the mV scale of the bottom plot. During the measurement of the first line a calibrated Gentec energy detector was used which displays the energy in mJ, for the second and third line the pulses were measured with a different pyroelectric detector which was connected to an oscilloscope. The mJ axis of the bottom plot is obtained by an average conversion factor and shown for comparison with the top plot.

magnetic field couples to the atom and changes the energy level structure which is described by the Hamiltonian

$$H = g_J \mu_B^\mu \mathbf{J} \cdot \mathbf{B} + g_I \mu_N^h \mathbf{I} \cdot \mathbf{B} = \mu_B^\mu \left(g_J \mathbf{J} + g_I \frac{\mu_N^h}{\mu_B^\mu} \mathbf{I} \right) \cdot \mathbf{B} \quad (3.22)$$

with the fine structure Landé g-factor g_J and the nuclear g-factor g_I , the muon Bohr magneton $\mu_B^\mu = 67.690 \text{ MHz/T}$, and the helion nuclear magneton μ_N^h . Despite the magnetic field being strong, the Zeeman energy in a muonic atom is still best described in the IJ -coupling scheme where the induced Zeeman shift is small compared to the hyperfine splitting (weak field approximation). The Zeeman energy in that regime is given by

$$\Delta E = g_F \mu_B^\mu B m_F \quad (3.23)$$

where g_F is the hyperfine structure Landé g-factor, and m_F the projection of the total atomic angular momentum F , which in the weak field regime is a good quantum number. The Landé factor is given by [46]

$$g_F = g_J \frac{F(F+1) - I(I+1) + J(J+1)}{2F(F+1)} + g_I \frac{\mu_N^h}{\mu_B^\mu} \frac{F(F+1) + I(I+1) - J(J+1)}{2F(F+1)} \quad (3.24)$$

with the helion nuclear magneton to muon Bohr magneton ratio $\mu_N^h/\mu_B^\mu = 0.038$ and the fine structure Landé factor [57]

$$g_J = g_L \frac{J(J+1) - S(S+1) + L(L+1)}{2J(J+1)} + g_S \frac{J(J+1) + S(S+1) - L(L+1)}{2J(J+1)}. \quad (3.25)$$

The orbital g-factor g_L is equal to 1 in the approximation of infinite nuclear mass. However, with a bound muon instead of an electron, recoil effects are enhanced and the correct value of $g_L = M/(m+M) \simeq 0.964$ (see Sec. 47 β in [57]) should be inserted. The g-factor values are for the muon $g_S \simeq 2.002$ and for the nucleus (helion) $g_I = 4.255$.

The effect of the Zeeman shift calculated with Eq. (3.23) is given in Tab. 3.4. As the m_F levels are equally populated, there is no shift but a broadening effect. The laser of the Lamb shift experiment is π polarized. In order to account for the windows of the vacuum system and the target, an admixture of 10% σ polarized light is considered a conservative upper limit. The largest broadening effect for purely π polarized light is in the $2S_{1/2}^{F=1} - 2P_{1/2}^{F=1}$ transition with $2 \times 234 \text{ MHz} = 468 \text{ MHz}$. Including the admixture of σ polarized light a conservative estimate for the line broadening for all transitions is given by 500 MHz. This is 0.2% of the linewidth and therefore negligible.

Table 3.4.: Zeeman shift in the $\mu^3\text{He}^+$ Lamb shift transitions due to the 5 T magnetic field. Given are the shifts of the single m_F states which are involved in the respective Lamb shift transition (see also the level scheme in Fib.B.1), as well as the resulting shift of a transition starting from a certain m_F state excited by laser light with linear (π) and circular (σ^\pm) polarization. States with $m_F < 0$ experience the inverted shift, compared to the ones with $m_F > 0$. States with $m_F = 0$ are not shifted and therefore not indicated here. As the m_F states are populated equally and the laser light is polarized linearly, no shift, but only a broadening happens in the experiment. This broadening effect, however, is not significant. All numbers are given in MHz.

	2S shift	2P shift		total shift	
	$m_F = 1$	$m_F = 1$	$m_F = 2$	π	σ^\pm
$2S_{1/2}^{F=1} - 2P_{3/2}^{F=2}$	366	346	692	0, ± 20	$\pm 326, \pm 346, \pm 366$
$2S_{1/2}^{F=0} - 2P_{3/2}^{F=1}$	–	540	–	0	± 540
$2S_{1/2}^{F=1} - 2P_{1/2}^{F=1}$	366	132	–	0, ± 234	$\pm 132, \pm 366$

3.3.3. Doppler broadening

When atoms have a velocity \mathbf{v} with a component parallel to the laser propagation \mathbf{k} the Doppler effect leads to a shift of the effective laser frequency experienced by the atom. In the lab frame the observed transition frequency ω' is then given by

$$\omega' = \omega + \mathbf{k} \cdot \mathbf{v}. \quad (3.26)$$

with ω being the transition frequency of the atom at rest.

In the Lamb shift experiment the muons are stopped in the gas target and form a muonic atom. After a delay time of $t \simeq 1 \mu\text{s}$ the laser pulse enters the multipass cavity. At that time the muonic ion is thermalized at a temperature of $T = 293 \text{ K}$. The thermalized atoms move isotropically which leads to a pure broadening effect of the line. The most probable thermal velocity is given by [63]

$$v_{th} = \sqrt{\frac{2k_B T}{m}} \simeq 1250 \text{ ms}^{-1} \quad (3.27)$$

with the mass of $\mu^3\text{He}^+$ m , the Boltzmann constant k_B , and the temperature T .

The Doppler width is given by [63]

$$\Delta\nu_D = \nu_0 \sqrt{\frac{8k_B T \ln 2}{mc^2}} \simeq 2.4 \text{ GHz} \quad (3.28)$$

using $\nu_0 \simeq 347 \text{ THz}$ of the $2S_{1/2}^{F=1} - 2P_{3/2}^{F=2}$ transition which has the largest transition frequency among the measured transitions. The obtained broadening of $\Delta\nu_D = 2.4 \text{ GHz}$ is only 0.8% of the linewidth and is therefore negligible.

3.3.4. Collisional effects

The muonic atoms are created in a helium gas at a pressure of ~ 2 mbar. Hence, during the interaction of the electromagnetic field of the laser with the muonic atom it may collide with the surrounding target gas. This leads to a shift and a broadening effect in the transition lines.

The effect of collisions of the muonic atom with the surrounding helium gas has been treated in Ref. [64]. Therein collisional effects at a gas pressure of 100 mbar were treated. In that case the collision rate is enhanced. Their value therefore serves as a conservative upper limit. The calculation in Ref. [64] yields a shift of up to 50 MHz and a broadening effect of maximal 13.6 MHz for $\mu^3\text{He}^+$ ions. At lower target pressures of ~ 2 mbar the collision rate decreases and the effects are expected to be much (two orders of magnitude) smaller and negligible.

3.3.5. Power broadening

Laser energies close to saturation distort the line shape. This is taken into account by a line shape model which is used to fit the transition lines (see Sec. 4.7). The power broadening is still calculated here. The saturation fluences F_{sat} are given in Tab. B.1. The actual fluences F for the different transition lines are given in Sec. 2.4.1. For simplicity they are listed here again:

transition	1	2	3
F [J cm ⁻²]	0.5	0.6	0.6
F_{sat} [J cm ⁻²]	1.3	1.1	3.3

The line shape model used in Sec. 4.7 is an exponentially saturating Lorentzian (see Eq. (4.6)). Plugging the numbers given in the above table into the Lorentzian yields broadenings of 9, 15, and 5% of the linewidth for the three lines, respectively. For a width of 320 GHz this results in a broadening of 29, 48, and 16 GHz and is therefore by far the largest broadening effect in this experiment. As mentioned above, the broadening is taken into account by the fit model.

4. Data analysis

The data obtained from the Lamb shift measurement in $\mu^3\text{He}^+$ are separated into two sets, A and B. Set A contains the data of the $2S_{1/2}^{F=1} - 2P_{3/2}^{F=2}$ transition (14 days of measurement) which was recorded first. Set B contains the data of the $2S_{1/2}^{F=0} - 2P_{3/2}^{F=1}$ and $2S_{1/2}^{F=1} - 2P_{1/2}^{F=1}$ transition (19 days of measurement). The data of the latter two transitions are combined because their transition energy only differs by 2 THz. Having a linewidth of 320 GHz these two transitions sit on each others tails and should therefore be fitted at once to avoid errors due to incoherent line pulling effects. All three transitions are analyzed with the same software. The main difference between set A and set B originates from the laser which performed differently in the region of 350 THz (set A) compared to the region of 310 THz (set B). This resulted in a different laser time window (LTW) between the two data sets. Also the pulse energies were higher for set B.

In the data analysis a lot of terms and expressions are used which can only be understood knowing about the data acquisition (DAQ). In the following the DAQ, the construction of events, and the terms used in this context shall be explained.

The time in which the measurements at the accelerator take place is called *beamtime*. During a beamtime the Lamb shift experiment has to be mounted, the measurements have to be performed, and, before the beamtime ends, the experiment has to be dismounted again.

The measurement time, i.e. the time during which data is recorded, is split into many single *runs*. These runs take about one hour and the data of each run is written into a single file on the hard disk drive (HDD) of the backend (BE) computer. Between two sequential runs it is possible to change the laser frequency, to control the target pressure, to refill the superconducting magnets with liquid helium (if necessary), etc. There are two different kinds of runs, one is the laser-off (LOFF) run and the other the laser-on (LON) run. In LOFF runs the *fire laser* trigger (FL) is switched off permanently and only the background (muons stopping in ^3He gas) is studied, in LON runs the actual excitation of the Lamb shift transition takes place. Both types of runs are used for the fit of the resonance line.

A single run is composed out of many *events*. An event is the detection of a muon by a coincidence of the signals $S1 \wedge S2$ ¹ which creates the T1 signal. T1 is the trigger for starting an *event gate* (EVG). T1 can only start an EVG if the frontend (FE) computer is *ready*. The status of the laser system (ready or not ready) sets the signals termed TBILE (*LON event*, it leads to the FL signal which triggers the laser) or TBINLE (*LOFF event*, no laser is fired). Thus, the events can be sorted later in the analysis and not only complete LOFF runs can be used for background studies, but also individual LOFF events in LON runs. An EVG is 20 μs long. The single *happenings* (single hits on the detectors) detected in this time interval are written on a ring buffer of the VME modules (TDC, WFD).

If during the EVG an X-ray is detected in the APDs, the APD GATE opens. The X-ray indicates that the muon which entered the target indeed formed a bound state with a helium nucleus. Electrons which originate from muon decay are detected by plastic scintillators, labeled ER and EL (see Sec. 2.4.2). The signals from these so-called electron paddles are sorted by their amplitude into four categories and labeled as *low*, *m1*, *m2*, and *high*.

After 20 μs the end-of-event gate (EEVG) signal closes the EVG. However, the ring buffers are only read out by the FE if the APD GATE is active. The APD GATE in combination with the EEVG signal then creates the STROBE signal. The STROBE stops the data record of WFDs and TDCs so their data can be read out and saved on the memory of the FE. From there the data is sent to the HDD at the BE. After that the FE is again *ready* for a new event. The arrangement of data into events has the advantage that it drastically reduces the amount of recorded data without losing the important events.

The software used for the DAQ is MIDAS². The software used for the analysis and the visualization of the recorded data is ROOT³.

In order to summarize the above explanations, the way of a muon from its detection until its decay is sketched and the respective detectors and signals are mentioned. The example shows the ideal case, the so called “golden event”. The indented text explains what happens in the DAQ.

A muon is detected in the nondestructive muon detection system (described in Sec. 2.3.3), right before the target.

¹S1 and S2 are introduced in Sec. 2.3.3.

²Maximum Integration Data Acquisition System (MIDAS), a data acquisition system developed at PSI, Switzerland and TRIUMF, Canada.

³ROOT, a data analysis software developed at CERN, Switzerland.

The coincidence of $S1 \wedge S2$ triggers T1 which, if the FE is ready, triggers the EVG. The EVG is now open for 20 μs . In this example the laser is ready (TBILE is set) and the FL signal triggers the laser. Hence, this event appears in the analysis as a LON event.

The muon enters the target and is stopped in the helium-3 gas. It forms a highly excited muonic atom and cascades down to the 2S state. About 1 μs after the muon enters the target, the laser pulse (triggered by FL) enters the multipass cavity, illuminates the muon stop volume, and excites the muonic atom to the 2P state.

Several photodiodes detect the time and the amplitude of the laser pulse.

The 2P state immediately decays to the 1S ground state emitting a delayed $^4 K_\alpha$ X-ray which is again detected by an APD. A few hundred nanoseconds later, the muon decays into an electron and two neutrinos. The highly energetic electron when passing an APD deposits energy in the APD and is then additionally detected by the plastic scintillators which are installed around the target.

By the detection of X-rays the APD GATE is opened. After 20 μs the event gate is closed by the EEVG signal which in coincidence with the opened APD GATE creates the STROBE signal. The STROBE triggers the read out of the WFDs and TDCs. All data are saved and can be used in the analysis.

The main purpose of the analysis is to find events as described above. This event is one “good” event among about 10 000 “bad” events. In most of the events no excitation of the muonic atom takes place, or the excitation is not detected. These events are considered background events. In order to obtain a good signal to noise ratio of the recorded Lamb shift transition, all events are characterized and several cuts are introduced which filter out unwanted “bad” events and so reduce the background.

A very important tool for the characterization of events is to create coincidences. A coincidence means that two happenings on different detectors have to happen in a small time window. In this way the probability that these happenings have the same physical origin is strongly enhanced and effective cuts can be performed. For example, electrons can be identified reliably if the signal they caused by passing an APD appears at the same time as a signal from the plastic scintillator.

Eventually, the energy of the Lamb shift transition is then determined by fitting a saturated Lorentzian to a plot of the delayed K_α X-rays versus the laser frequency (as shown in the end of this chapter, in Sec. 4.7).

In the following the different steps in the analysis of the recorded data are explained.

⁴The term “delayed” means delayed with respect to the prompt X-rays. The delayed K_α X-ray is in coincidence with the laser.

4.1. APD trace analysis, energy spectrum and cut

Waveform Digitizers (WFD) record every happening from an APD during an EVG. The recorded waveforms have a wide variety of shapes and it is crucial to characterize them in order to obtain useful time and energy spectra. The method used to obtain amplitude and timing as well as the characteristic slope of a signal is described in Diepold *et al.* [65] and summarized in the following.

There are mainly three different categories of happenings from the APDs. Two of them are caused by X-rays which are absorbed by the APDs, the third is caused by muon decay electrons, depositing energy, but passing through the APDs. The two X-ray categories differ depending on the APD region, where the X-ray is stopped. As explained in [65], APDs consist out of a drift region, a conversion region and an avalanche region. X-rays typically should stop in the conversion region, which leads to high charge collection efficiency and fast amplification. The signals which originate from these X-rays have a short rise time (called *fast* X-rays in the analysis). Due to the large opening angle in the experiment, the fraction of X-rays which stop in the drift layer is increased. If X-rays are stopped in this region the charge collection efficiency is slow as is the amplification. This results in long rise times and smaller amplitudes (called *slow* X-rays, accordingly). The signal from electrons results to have a rise time which is in between the two types of X-rays. This seems feasible as they pass all three APD regions.

The characterization of the APD signals works as follows. An edge-finder locates the beginning of a pulse by scanning a step function over the signal. After that an integrator yields the amplitude of a signal. The slope of the leading edge is fitted with a function and normalized by the pulse integral. A plot which shows the slope plotted versus the integral is shown in Fig. 4.1. The four different contributions in this plot originate from slow and fast 8 keV K_α X-rays, from electrons, and only one contribution from the 1.5 keV L_α X-rays.

By an adequate cut of the different APD signal classes seen in Fig. 4.1, the respective events can be separated and labeled accordingly. A selection of the respective signals is used to create a numerically averaged standard waveform trace for the two X-ray classes and the electrons. In the analysis of the data, each standard waveform trace is then fitted to every signal. The only free parameter is the timing of the trace. The amplitude is fixed by the integral of the signal. Finally the best χ^2 of the fits with the different standard traces decides whether the fitted signal in the analysis appears as a slow or a fast X-ray, or an electron. The slow and fast X-ray amplitudes are then

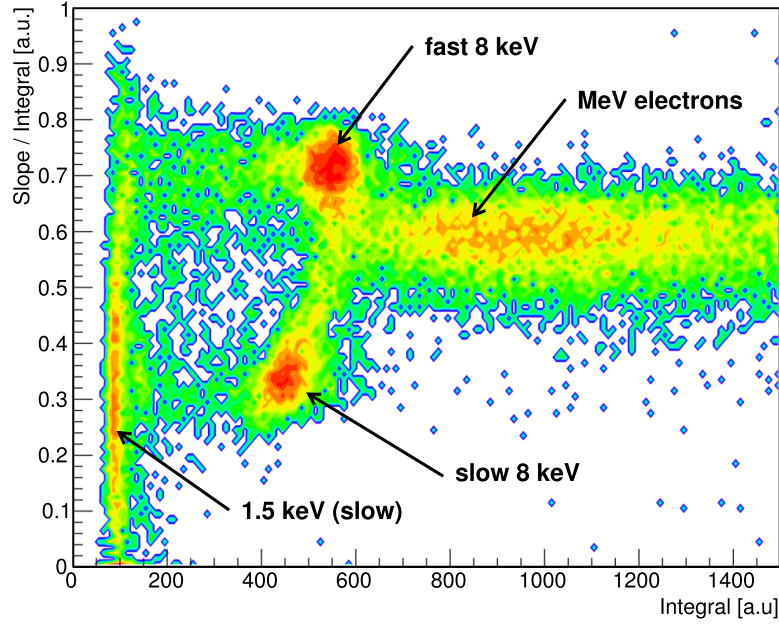


Figure 4.1.: Particle identification via waveform trace analysis (figure and caption from Ref [65]). Plotted is the normalized slope of the rising edge versus the integral of the pulse. Integrals are roughly proportional to the deposited energies of the registered X-rays. Four contributions are visible: Low energy 1.5 keV X-rays show integrals below 200. The recorded 8.2 keV X-rays create two different responses in the APD, one with slow rise time (slope ≈ 0.3), and one with significantly faster rise time (slope ≈ 0.7). The last contribution with an integral above 700 arises from MeV electrons depositing keV energies in the APD.

calibrated individually to the 8.13 keV K_α energy of the muonic helium-3 ion. The so obtained X-ray spectrum is shown in Fig. 4.2.

The “golden event” which is mentioned at the beginning of this chapter is characterized by a delayed 8 keV X-ray, emitted after a successful excitation of the Lamb shift transition. In consequence, a first effective cut to reduce background events is, that only events which include the detection of an 8 keV X-ray are further processed in the analysis. This cut is called energy cut and it selects only events with X-ray energies larger 7.3 keV but smaller 8.9 keV. This interval was chosen aiming for a balance of a good signal-to-noise ratio without losing too much statistics. The interval is marked in blue color in Fig. 4.2.

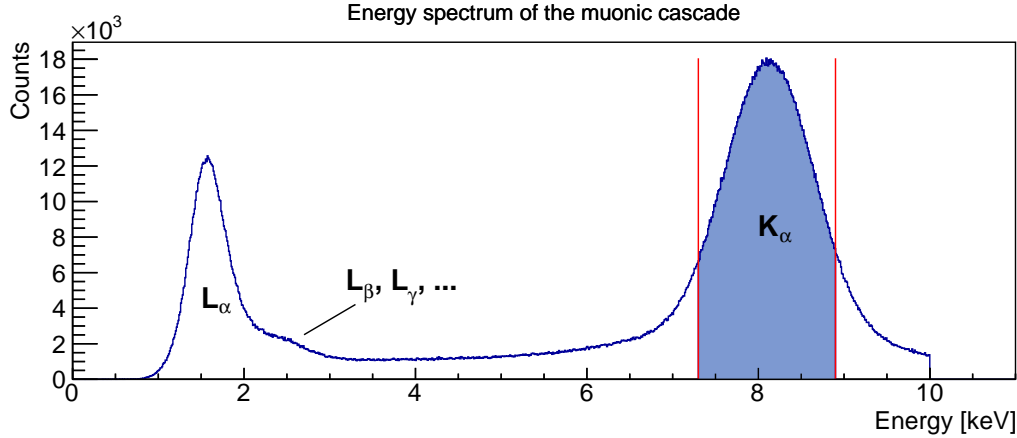


Figure 4.2.: APD spectrum of the data set used for the second and third $\mu^3\text{He}^+$ resonance. The first peak at 1.5 keV is the L_α transition of the Balmer series. The tiny elevation at the right tail of the L_α peak is due to the higher transitions of the Balmer series which are not resolved. At 8.1 keV the K_α transition of the Lyman series is located. The two lines at 7.3 keV and 8.9 keV indicate the energy cut. In order to find the delayed K_α X-rays only the events in this interval are used for the analysis. The background originates from muon decay electrons.

4.2. Electron identification via coincidences

The purpose of this section is to explain the various methods of identifying muon decay electrons. The events where muon decay electrons have been detected are then labeled with a quality factor (termed *tidiness* TDS1,...,TDS8), depending on which method is used to identify the electron. The determination of the origin of a happening (X-ray or electron) is essential for further background reduction. First, it helps to have a clean X-ray energy spectrum and therefore improves the X-ray energy cut, mentioned above. Second, the identification of delayed muon decay electrons ensures that the detected X-rays are not faked by decay electrons ⁵.

In the previous section (Sec. 4.1), a first method to detect electrons has already been introduced. Sec. 4.1 explains how signals in the APDs can be traced back to either electrons or X-rays, depending on the shape of the waveform. Events with an electron identified by the waveform trace analysis are labeled with a tidiness of TDS8 = true.

Another method which can be derived from Fig. 4.1 is, that every signal above a certain energy (integral) is very probable an electron. Thus all events with APD signals above 10 keV are labeled with TDS7 = true.

⁵During an EVG, usually only one muon is inside the target. A special cut introduced for the case of a second muon entering the target during the EVG of a first, is presented later in Sec. 4.4.

Another useful tool to identify electrons apart from the waveform trace analysis in the APDs, is the detection of electrons by the plastic scintillators, which are installed around the target for this purpose. As explained in Sec. 2.4.2, there are four plastic scintillators connected to two photomultiplier tubes (ER and EL). The signals from ER and EL are further discriminated by their amplitude in four categories termed *low*, *m1*, *m2*, and *high*. This creates in total eight signal classes from the plastic scintillators, four from ER and another four from EL. They are recorded in eight different TDC channels. The amplitude of the signal is therefore given by the respective TDC channel, the timing is provided by the TDC itself.

The *high* and the *m2* signals are the cleanest, i.e. the probability that the signal is actually caused by a muon decay electron is trivially larger than for the categories *low* and *m1*. The *high* and *m2* signals are therefore directly identified with electrons. Events with *high* signals are labeled with $\text{TDS1} = \text{true}$.

The other signals (*low*, *m1*, and *m2*) are only further processed if they coincide with a happening from another detector within a certain time interval. This “coincidence” further increases the probability that the signal is indeed caused by an electron. The coincidences are a powerful tool only because of the 5 T magnetic field in which the electrons perform cyclotron motion and therefore may hit several detectors in a short time interval. For a proper determination of the coincidences a time calibration (see A.1) is needed which introduces one single timescale for all detectors, mainly compensating the length of cables to their respective TDCs, but also intrinsic transient times of the various detectors (e.g. PMTs). After the time calibration, the time of the single happenings can be compared. This is done by time difference histograms as exemplary shown in Fig. 4.3. The red lines indicate the defining interval in which a coincidence is indeed treated as a coincidence.

The different coincidences are listed in the following. The respective tidiness is then set to true.

First, the coincidences between plastic scintillator signals: A coincidence between a *low* or *m1* signal with another *low* or *m1* signal ($\text{TDS2} = \text{true}$). A coincidence between a *m2* or *high* and a *low* or *m1* signal ($\text{TDS3} = \text{true}$). A coincidence between a *m2* or *high* and another *m2* or *high* signal ($\text{TDS4} = \text{true}$).

Then, the coincidences between plastic scintillator signals and APD signals: A coincidence between any APD signal and a *low* or *m1* signal ($\text{TDS5} = \text{true}$). A coincidence between any APD signal and a *m2* or *high* signal ($\text{TDS6} = \text{true}$).

Finally there are also coincidences between different APD signals. These are mostly caused by the prompt X-rays from the muonic cascade, but some also originate from the

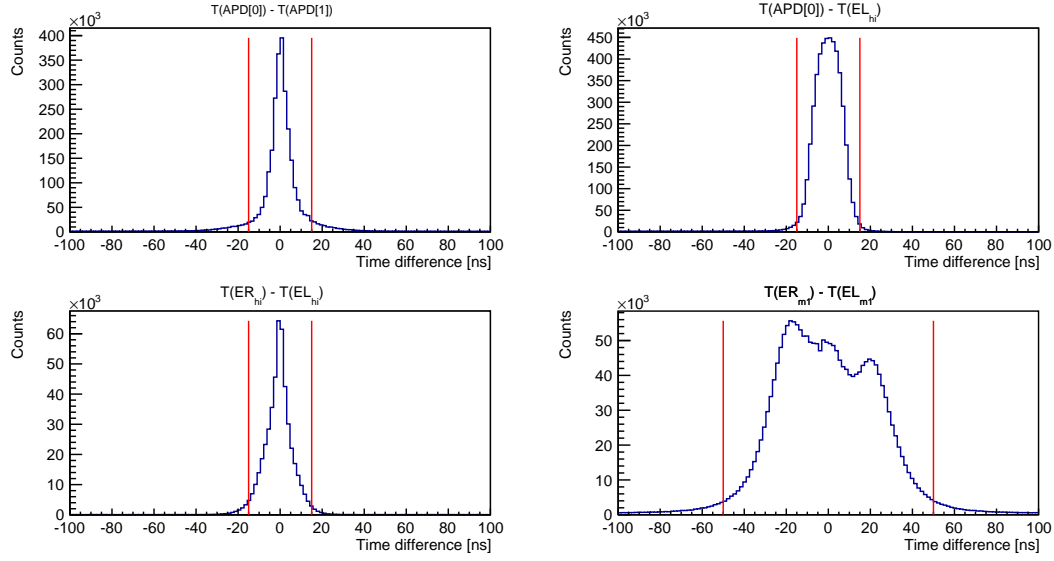


Figure 4.3.: Coincidences. Different happenings from the APDs or plastic scintillators have to happen inside certain time intervals in order to be *coincident*. This is displayed here via time difference histograms. Coincidences between different APDs are mainly traced back to X-rays from the muonic cascade. Coincidences between different plastic scintillator signals or between APD and plastic scintillator signals are indications for electrons. The structure in the peak of the lower histogram on the right side has also appeared in the previous experiments and is not understood. It might originate from crosstalk between the cables transferring the signal from the detector to the TDCs. The data shown here are from set B. The data from set A look the same.

two-photon decay of the 2S state. They are not further interesting for the measurement of the Lamb shift transition.

The time interval which defines if a coincidence is treated as such in the analysis may vary depending on the specific type of coincidence. The different time intervals are listed in Tab. 4.1. They are chosen in a way optimizing the signal to noise ratio of the resonance line and vary due to the data spread in the time difference histograms.

4.3. Delayed electron cut (creation of XDele events)

In the previous section, all events which contain the detection of an electron have been labeled with a parameter called tidiness (TDS). It has been mentioned that it is useful to detect a *delayed* muon decay electron after the detection of an X-ray, because the electron ensures that the previous X-ray indeed originated from a muonic atom.

Table 4.1.: Coincidence cuts of the signals from APDs and electron paddles. The cuts are applied to the absolute values of the time differences. Left (EL) and right (ER) paddles are treated equally and simply called E.

APD – APD	15 ns
APD – E _{low/m1}	20 ns
APD – E _{m2/high}	15 ns
E _{low/m1} – E _{low/m1}	50 ns
E _{m2/high} – E _{low/m1}	45 ns
E _{m2/high} – E _{m2/high}	15 ns

A strong background reduction is therefore achieved if such a delayed electron is *required*. In order to find such events, it is useful to look at time difference histograms (electron time – X-ray time) as shown in Fig. 4.4, sorted by their tidiness.

The two histograms shown there are separated in terms of their tidiness. In Fig. 4.4, the events with TDS1 and TDS7 are shown as an example. Events where the time difference is negative are clearly background events. It is important to note that the background level varies for different parameters TDS. In events where the time difference is zero the two happenings might have a common origin and are not due to an X-ray and a subsequent electron. These events should not be used. In order to avoid these events

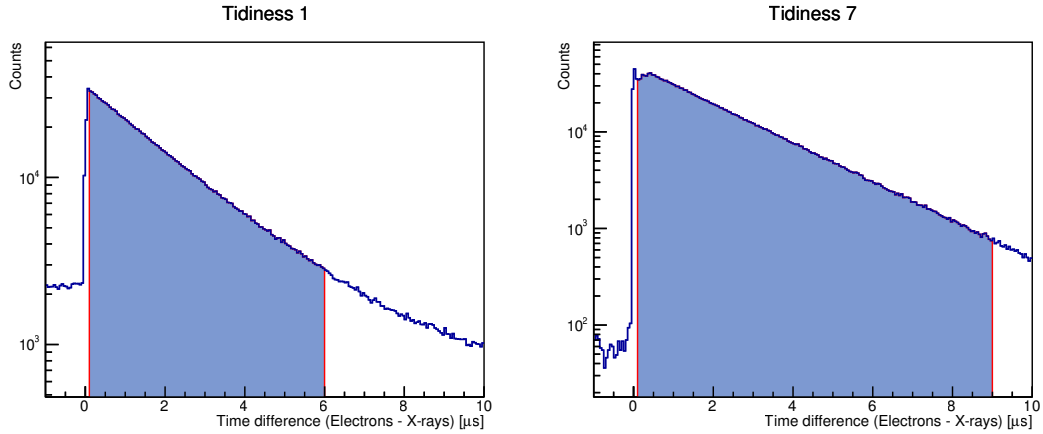


Figure 4.4.: Exemplary delayed electron cuts for tidiness TDS1 and TDS7. The data shown here is from data set A. The figures show maximum and minimum of the allowed time difference between muon and electron detection. *left:* The electron signal is a *high* or a *m2* signal in the paddles. *right:* The electron signal is a signal from the APDs with an energy larger than 10 keV. The cuts are chosen depending on the background level. Higher background requires shorter time differences. To ensure that different signals have different origins, a minimal time difference of 0.15 μs is required.

Table 4.2.: XDele cuts for all eight different electron classes TDS. Signals where the time delay between an X-ray and a decay electron is longer than the respective cut time are not used in the analysis. For longer delays the signal to noise ratio is too low. The minimal allowed time difference for all classes TDS is 150 ns. See also Fig. 4.4.

TDS	1	2	3	4	5	6	7	8
cut after [μs]	6	3	9	9	5	9	9	5

a minimal time difference is required which is set to 150 ns. The events with a larger time difference are marked with a blue color in Fig. 4.4. For very large time differences the signal to noise ratio decreases (mainly corresponding to the muon life time) and it is useful to also require a maximally allowed time difference. The maximally allowed time difference depends on how clean the result of the various coincidences is, which is indicated by the background level at negative time differences, and furthermore it depends on how many events fulfill the respective coincidence. The best TDS classes have a maximal time difference of 9 μs , which is chosen as the upper limit.

The selection of events due to the allowed time difference interval is called XDele cut. The XDele cut for each tidiness class is given in Tab. 4.2. The events which fulfill the condition of the XDele cut (time difference inside the blue area) are termed XDele events in the following. For the extraction of the Lamb shift transition energy only XDele events are used.

Many events agree with several definitions, in such a case they are assigned to the highest tidiness class ⁶. All tidiness classes are used for the analysis, however, the advantage of this classification lies in the possibility of introducing individual XDele cuts.

4.4. Second muon cut

A muon which is detected via a coincidence signal of the detectors S1 and S2 at time t_{S1} triggers the laser and starts the event gate (EVG). About 170 – 350 ns later (depending on the kinetic energy of the incoming muon), the muon stops in the target and forms a muonic atom whereupon at time t_X prompt X-rays from the muonic cascade are emitted. In 99% of the cases the atom ends up in the 1S ground state, emitting a prompt 8.1 keV

⁶The fact that events are only assigned to one single tidiness class (even if they fulfill the definition of several classes) stems from the analysis of the $\mu^4\text{He}^+$ data. It hasn't been changed for $\mu^3\text{He}^+$. However, flagging the events with all applicable tidiness definitions would allow to look at coincidences between the different classes and might reduce the background even better.

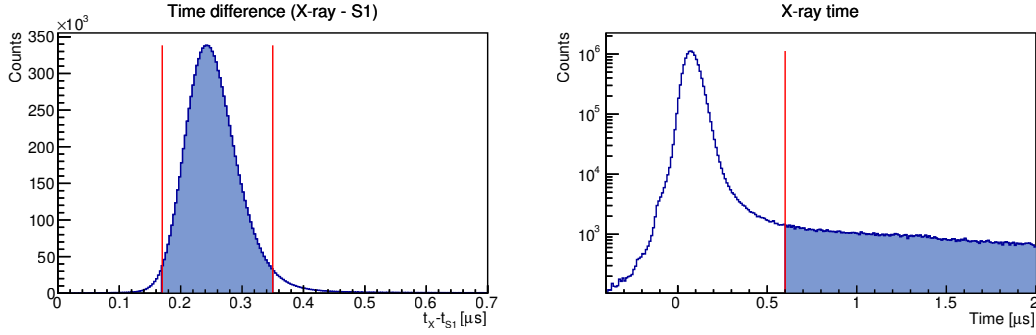


Figure 4.5.: Second muon identification. Muons are identified as *second* muons if they release a muonic cascade in a certain time interval after their detection in S1 (*left*) AND if the muonic cascade of these *second* muons happens later than a certain time after the prompt X-ray peak (*right*). The events fulfilling these two conditions are filtered off as they contribute to noise.

X-ray. In the remaining 1%, the muonic cascade ends in the 2S state and the 8.1 keV X-ray is emitted as a delayed X-ray after the successful excitation to the 2P state by the resonant laser pulse.

If now a *second* muon enters the target and forms another muonic atom during the laser time window, its muonic cascade fakes delayed X-ray signals from the *first* muon, i.e. a signal appears which imitates a successful excitation of the Lamb shift transition. This case creates unwanted XDele events which are additional background that can be eliminated with a corresponding cut. The idea of this cut is to exploit the fact that 99% of the muons have a fix time window between their detection (S1) and the emission of a prompt 8.1 keV X-ray (t_X).

The second muon cut discards all events with the following two conditions. First, X-rays with time t_X have to happen in a certain, typical time window after t_{S1} (see Fig. 4.5 left)

$$\Delta t_{\min} < (t_X - t_{S1}) < \Delta t_{\max}, \quad (4.1)$$

where the interval is defined by $\Delta t_{\min} = 0.17 \mu\text{s}$ and $\Delta t_{\max} = 0.35 \mu\text{s}$. This is the time the muons need from their detection to the formation of a muonic atom.

Second, t_X has to be larger than a certain time threshold $t_{\min} = 0.6 \mu\text{s}$ (see Fig. 4.5 right),

$$t_{\min} < t_X, \quad (4.2)$$

which is about when the first prompt X-ray peak ends.

This means, that if X-rays from a muonic cascade are detected at a time $t_X > 0.6 \mu\text{s}$, where the muonic cascade should already have happened AND they are correlated to a S1 signal via the first condition, they are very likely caused by a second muon.

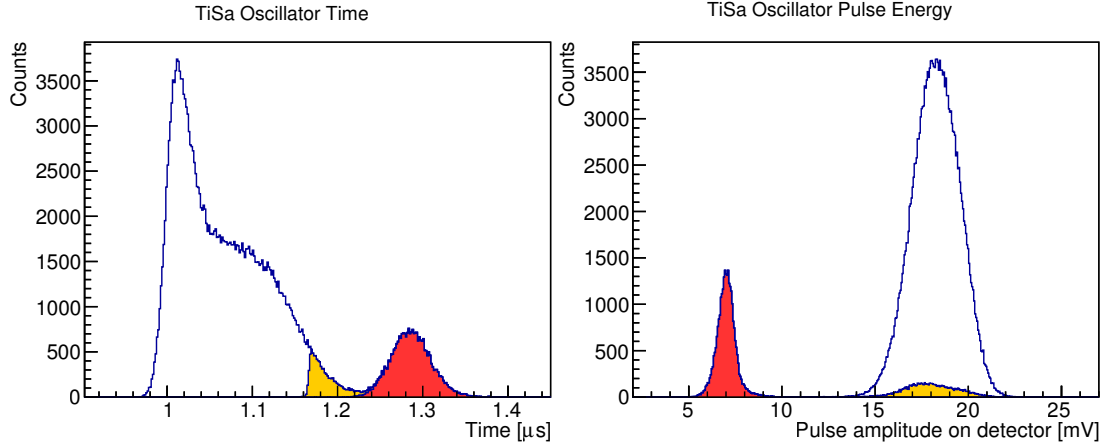


Figure 4.6.: Laser time (*left*) and energy (*right*) in Run 2079 of data set B. The events marked in *red* are events where the laser was out of lock (see also Fig. 4.7). The “unlocked” pulses arrive later and have about 60% less energy. These events are not used in the analysis. The very late *yellow* colored events are also excluded from the analysis. Including these events widens the LTW which leads to a decrease in signal to noise ratio.

In this way about 0.5% of the events with a delayed electron (XDele events) are identified as second muon events.

4.5. Laser performance

Additionally to the laser characterization in Sec. 3.1, in the analysis the laser performance has been studied on a pulse per pulse basis. Several photodiodes are measuring the pulse energy and the time of the pulses at different positions of the laser setup. The recorded data helps to sort out events where the laser did not work well. What that means is shown in Fig. 4.6 using the example of run 2079 of data set B. Here, the pulsed Ti:Sa laser was not very well locked to the cw Ti:Sa laser. As a result, the pulsed Ti:Sa was probably lasing at a wrong wavelength (determined by the pulsed cavity, not by the cw seed). Because no “cw photons” were present, the pulse build-up time was longer, and these bad laser shots can be excluded by a time cut.

The unseeded events where the laser is not locked are identified easily via Fig. 4.7. These are the same events which are marked in a red color in Fig 4.6. As the frequency of pulses from the unlocked laser is not well determined, these pulses are discarded from the analysis with a cut called *LowLaser*. The origin of the shoulder on the right side of the left peak in the left histogram of Fig 4.6 is not clear. This shoulder only appears in data set B (for transitions 2 and 3).

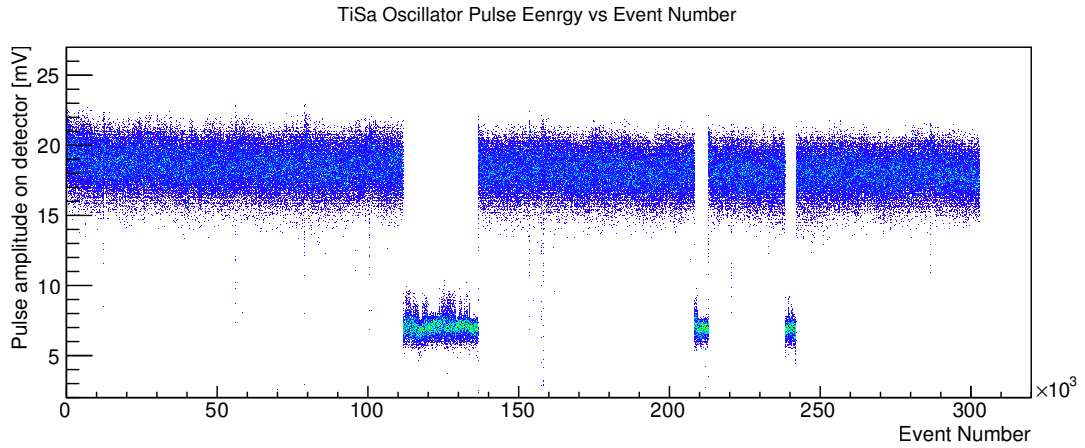


Figure 4.7.: Pulse energy vs. event number in Run 2079 of data set B. In this histogram the events where the laser is out of lock are very well visible and characterized by a loss in pulse power of roughly 60%. Note that the pulse energy over this run also changes slightly. This run is about 50 minutes long.

A possible cause for these delayed pulses might originate from the temporal distance to the previous LON event, e.g. if two laser shots are too close to each other, problems with the lock might arise. Fig. 4.8 shows the laser pulse time plotted versus the time delay to the previous LON event. However, the recovery time of 3 ms between two events is large enough and no correlation between the laser time and the time delay is visible.

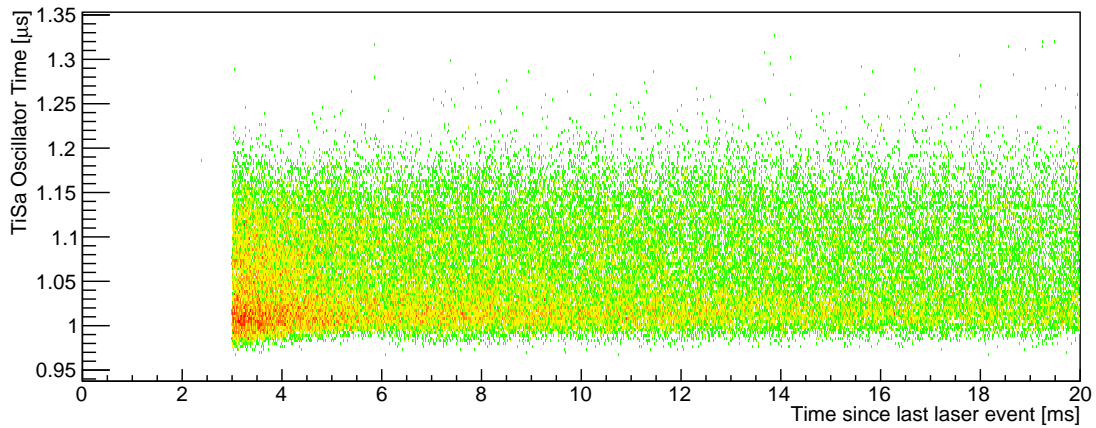


Figure 4.8.: Laser time vs. delay to previous LON event. After each LON event there is a 3 ms recovery delay for the laser. A shorter delay would lead to lower pulse energy and delayed pulse detection. Note, that the events where the laser was not locked are not shown. The “shoulder” next to the peak (see also Fig. 4.6) is visible in the whole range up to 20 ms.

In some runs the tails of the shoulders reach out up to 400 ns (compare to 90 ns pulse length) from the peak, which also shifts the events to very late times and therefore decreases the signal-to-noise ratio. These very late events are discarded via the *LateLaser* cut. It is adjusted in such a way that those events are not used, where the entries in the histogram amount to less than 20% of the peak ⁷. These events are shown in Fig. 4.6 in an yellow color.

4.6. Laser time window

The final cut before creating the resonance plot is performed by only using those XDele events where the K_α X-ray has been detected during the laser time window (LTW). It is only during the laser time window that X-rays may be caused by a successfully driven Lamb shift transition. The LTWs chosen for the two data sets are

$$\text{LTW(A)} = [0.98 \mu\text{s} - 1.22 \mu\text{s}] \quad (4.3)$$

$$\text{LTW(B)} = [1.12 \mu\text{s} - 1.46 \mu\text{s}]. \quad (4.4)$$

The delayed events in the X-ray time spectrum are clearly visible (see Figs. 4.9 and 4.10) and the laser time window is chosen accordingly. A fine tuning of the LTWs has been done optimizing for the signal to noise ratio and the significance of a Lorentzian fit to the data compared to fitting a flat line.

The difference between these two windows originates from the timings of the laser pulses which differed between the different data sets. Fig. 4.11 shows the laser time. Each data point reflects the mean and the rms value of a single run. The pulses from Set B arrive later and are spread over a larger time interval which explains the broader and later placed LTW. The bottom plot of Fig. 4.11 suggests a frequency dependence of the laser timing. Considering the mean value of the second or third resonance only, a gap of 30 ns is created. This gap, however, is small compared to the LTW interval and can be neglected. The data in Fig. 4.11 is spread over 180 ns (270 ns) for data set A (B). The larger LTW of 240 ns (340 ns) is due to the lifetime of the multipass cavity.

In order to fit the correct line position, the delayed events at each frequency have to be normalized with the number of prompt events at each frequency. The prompt events are the ones originating from the muonic cascade. They are defined to be prompt if the

⁷The 20% are not exactly reflected in Fig. 4.6, because the definition of the cut has been done with a photodiode right before the multipass cavity. However, the signal shown in Fig. 4.6 stems from a photodiode next to the Ti:Sa Oscillator.

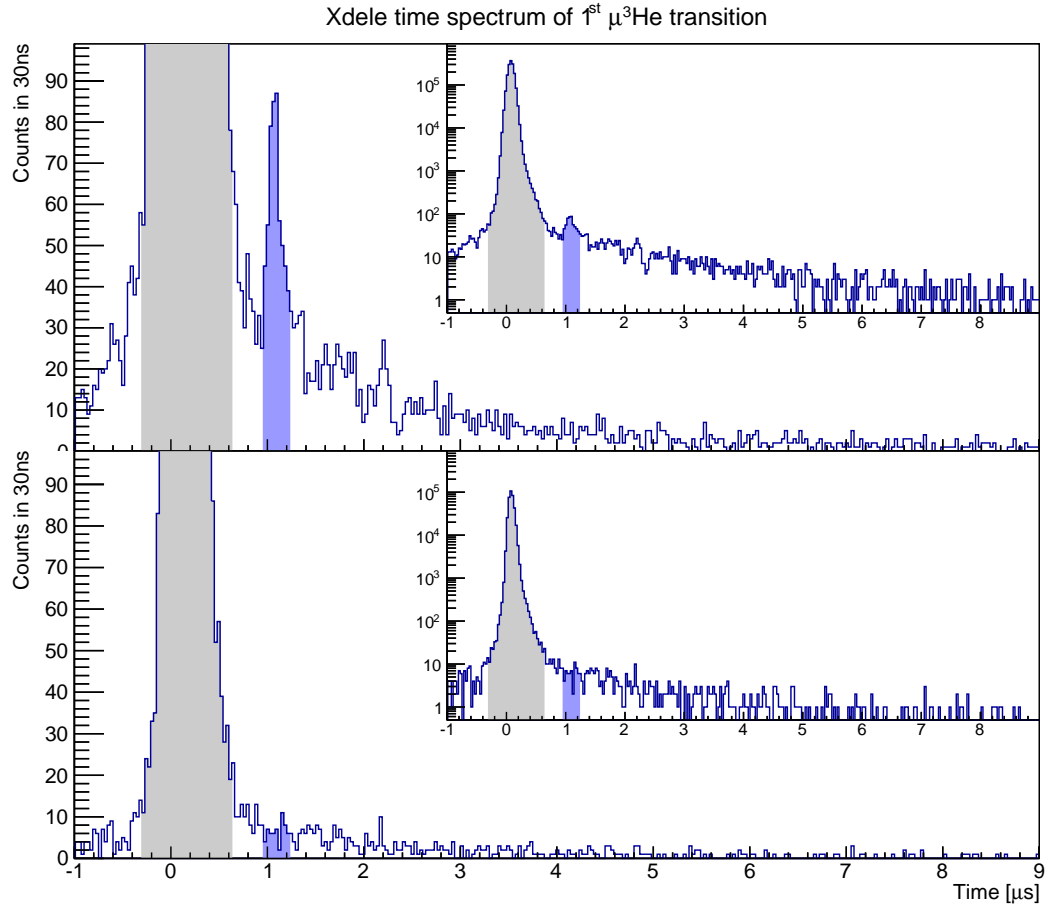


Figure 4.9.: Prompt events (*gray*) and laser time window (*blue*) shown in the Xdele time spectrum of the 1st $\mu^3\text{He}^+$ transition. The laser induced delayed events in the laser-on data (*top*) are clearly visible. As comparison the laser-off data (*bottom*) are shown where no delayed peak exists.

X-rays are detected between -0.3 and $+0.6 \mu\text{s}$. LTW (blue) and prompt events (gray) are indicated in Fig. 4.9 and 4.10 for data set A and B, respectively.

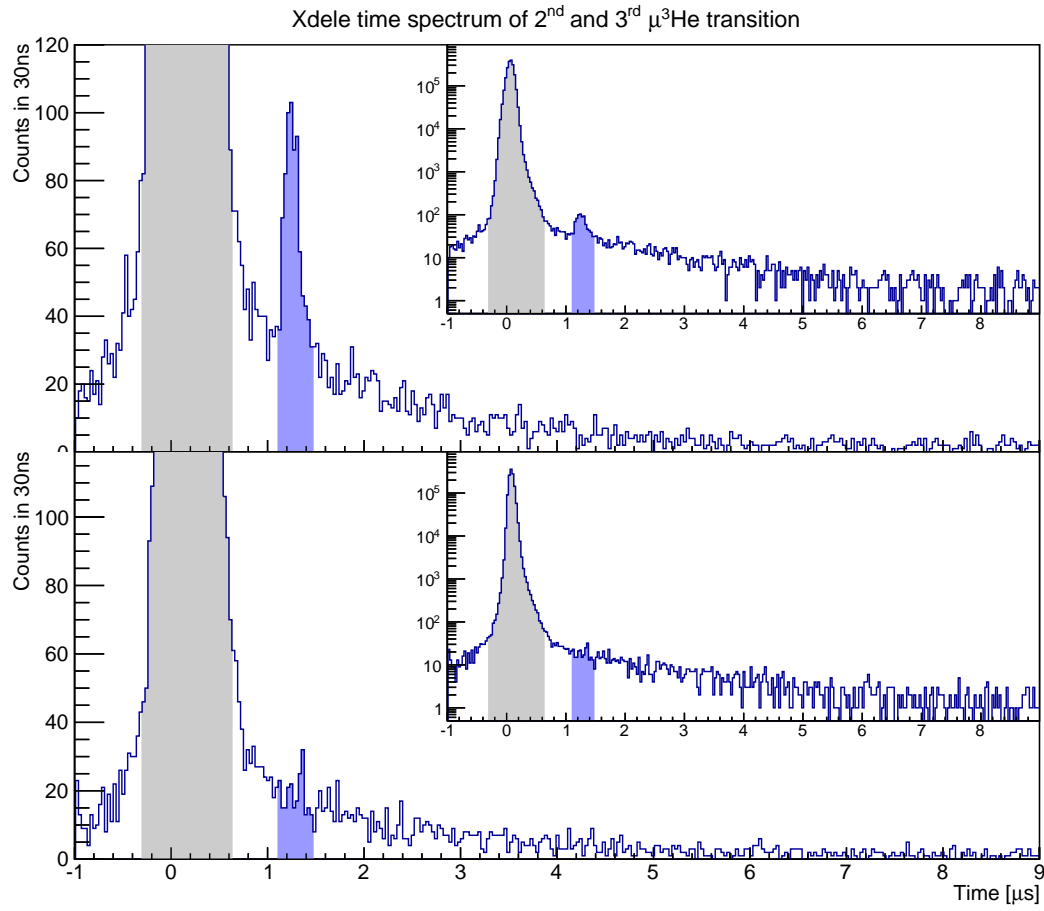


Figure 4.10.: Prompt events (*gray*) and laser time window (*blue*) shown in the Xdele time spectrum of the 2nd and 3rd $\mu^3\text{He}^+$ transition. The laser induced delayed events in the laser-on data (*top*) are clearly visible. As comparison the laser-off data (*bottom*) are shown where no delayed peak exists.

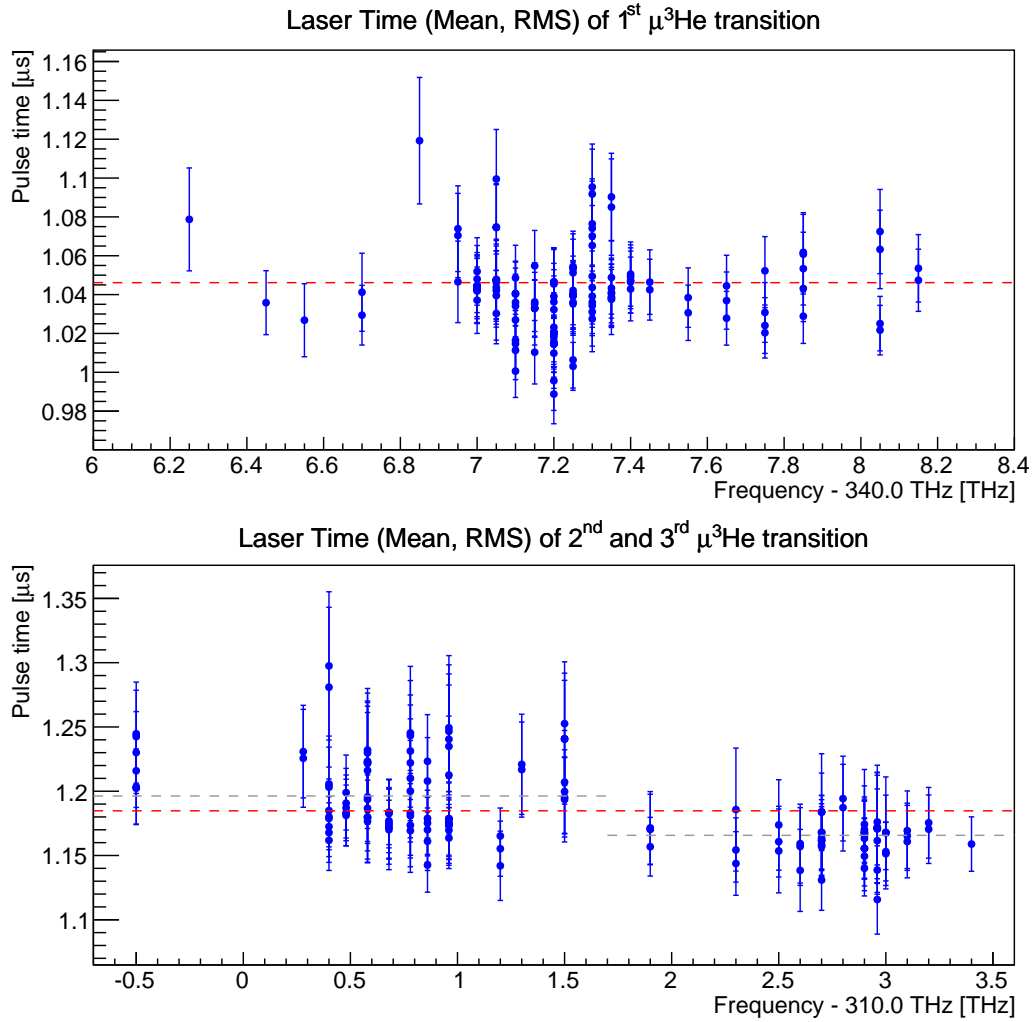


Figure 4.11.: Laser time plotted against frequency for the first (*top*) and the second (*bottom, right*) and third (*bottom, left*) measured transition lines. Each data point represents a single run. The red dashed line at $1.046\ \mu\text{s}$ and $1.185\ \mu\text{s}$ indicates the mean of the total data set, respectively. In the bottom plot the average laser timings of the second line are about $30\ \text{ns}$ earlier than the one of the third line (gray dashed lines). Note the different y-axis scaling, the total spread is about 70% larger for the bottom plot.

4.7. Fit the data

After calibrating the data (see App. A) and after applying the cuts (described in this chapter) the resonance can finally be fitted.

The natural atomic transition line is described by a Lorentzian function

$$L(\nu) = \frac{1}{\pi} \frac{\left(\frac{1}{2}\Gamma\right)^2}{(\nu - \nu_0)^2 + \left(\frac{1}{2}\Gamma\right)^2}. \quad (4.5)$$

This function can be derived from the power spectrum of the Fourier transform of a spontaneously emitted wave. The width of the Lorentzian in this case is given by the life time of the 2P state of ~ 0.5 ps. Several systematic effects usually lead to a Gaussian broadening of the line. Others, as the QI effect, may distort the line in a more complex way. However, Sec. 3 describes that these effects are negligible compared to the very broad (318.7 GHz [55]) transition and therefore a Lorentzian function can be used to fit the data.

There are only two things which are important to consider.

The first is the laser asymmetry, which has been discussed in Sec. 3.3.1.

The second is power broadening. The fraction of saturation reached for the individual lines is obtained from the saturation fluences given in Tab. B.1 in App. B and the actually realized fluences given in Eqs. 2.4 and 2.5 in Sec. 2.4.1. The fractions yield 36%, 56%, and 19% for the lines 1, 2, and 3, respectively. Thus the broadening due to saturation might be significant and should be considered in the fit, at least for line 2.

In order to tackle these effects, the CREMA collaboration has developed a line shape model (LSM) which has proven successful already for μp and μd . In preparation for the fit, the time spectra shown in Figs. 4.9 and 4.10 are sorted by the applied laser frequency and plotted in two dimensional histograms where the laser pulse energy is the second dimension.

Additionally the events in the LTW are normalized by the number of events in the prompt peak. This normalization accounts for different statistics at different frequencies. The variations in statistics occur due to different measurement times and fluctuations in the proton beam current of the accelerator.

The LSM which is used to fit these histograms is an exponentially saturating Lorentzian on top of a flat background

$$L(\nu) = B + A \left[1 - \exp \left(- \frac{I(\nu)}{I_{\text{sat}}} \frac{\left(\frac{1}{2}\Gamma\right)^2}{(\nu - \nu_0)^2 + \left(\frac{1}{2}\Gamma\right)^2} \right) \right] \quad (4.6)$$

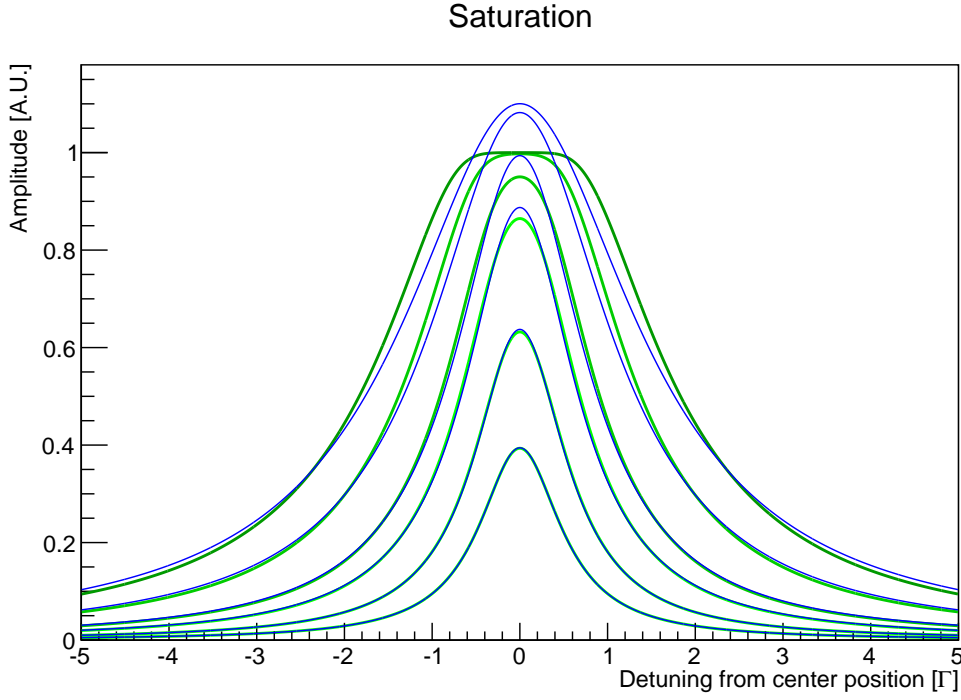


Figure 4.12.: *Green:* The line shape of an exponentially saturating Lorentzian transition. With increasing intensities of 0.5, 1, 2, 3, 6, 10 times the saturation intensity. *Blue:* A Lorentzian fit to the respective line with respective widths of 1.13, 1.26, 1.52, 1.78, 2.46, 3.22 times Γ .

with $I(\nu)$, the average pulse energy at a certain frequency ν and I_{sat} , the saturation intensity for the respective transition. The behavior of the fit function for several laser intensities is shown in Fig. 4.12.

Two parameters in the LSM are fixed. One is the full width at half maximum (FWHM) Γ which is fixed at the calculated value of 318.7 GHz, taken from [55]. The other is the saturation, which is adjusted by the percentages given above, and all other fit parameters are free.

A fit with free width results in a width of $\Gamma = 307.4(76.4)$ GHz for transition 1, and $\Gamma = 312.0(40.5)$ GHz for transitions 2 and 3, in agreement with the theoretical one. The LOFF data is fitted with a flat line which at the same time is the background parameter BG in the fit function for the LON data.

The fit is a Poissonian maximum log-likelihood fit. The optimization is done via the ROOT MINUIT package.

Table 4.3.: Results of the measured Lamb shift transition frequencies, applying a line shape model with an exponentially saturating Lorentzian (see Eq. (4.6)). Fixed parameters are indicated with bold letters.

Transition	1	2	3
Position [GHz]	347 211.5(19.6)	312 829.6(20.9)	310 814.3(19.5)
Width [GHz]	318.7	318.7	318.7
Amplitude [A.U.]	9.84(1.03)	10.24(1.12)	11.90(1.01)
I/I_{sat} [%]	36	56	19
BG [A.U.]	1.48(15)	1.60(10)	
χ^2	158	177	
DOF	201	232	
$\chi^2(\text{flat line})$	254	429	
σ above BG	9.8	15.9	

The fit results are listed in Tab. 4.3. The χ^2 of the Poissonian fit is given by [66]

$$\chi^2 = -2 \ln W = 2 \sum_i L(\nu_i) - D(\nu_i) - D(\nu_i) \ln \left(\frac{L(\nu_i)}{D(\nu_i)} \right) \quad (4.7)$$

with W the product of the probabilities of the single channels i . $D(\nu_i)$ is the number of events at the respective frequency ν_i and $L(\nu_i)$ is the value of the fit function at the same frequency ν_i . The reason that the LSM fit function, shown in Figs. 4.13 and 4.14, doesn't look like a Lorentzian, is that it can only be evaluated at the frequencies, where data points exist. At each of these data points the amplitude depends on the pulse energy. For better visibility the values of the LSM at the various frequencies are connected with straight lines.

In order to determine the significance of the measured transition lines, the fit is repeated for an amplitude $A = 0$. The χ^2 of the flat fit is shown in Tab. 4.3. The resulting significance is 9.8σ for transition 1 and 15.9σ for transitions 2 and 3.

Compared with the fit of a simple Lorentzian (see Eq. (4.5)) the results of the LSM (see Eq. (4.6)) agree very well. The fit of a simple Lorentzian results in 347 210(16) GHz, 312 832(19) GHz, and 310 811(19) GHz for the lines 1, 2, and 3, respectively. These positions are all within about 0.1σ from the positions of the LSM, given in Tab. 4.3.

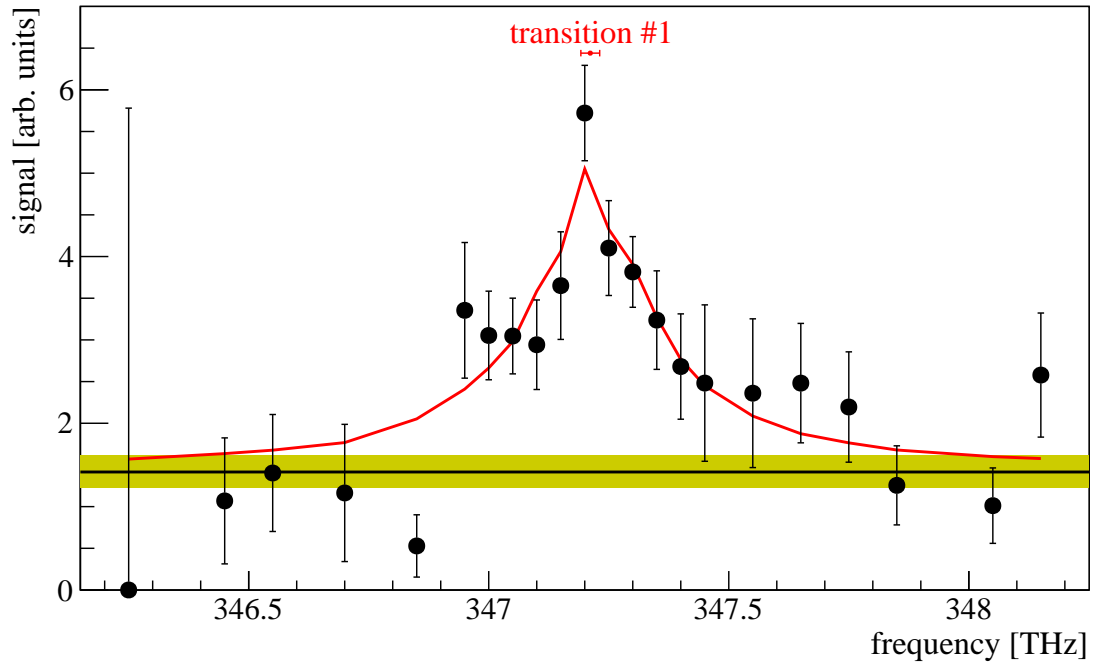


Figure 4.13.: LSM fit to the $2S_{1/2}^{F=1} - 2P_{3/2}^{F=2}$ transition (also termed transition 1). The signal is given by the normalized events in the LTW. The black data points are recorded LON events. The LOFF events are indicated via the flat black line. The yellow band shows the uncertainty of the LOFF events. The little red data point at the top indicates the fitted center position including its uncertainty. Note that the high data point at $\nu = 347.2$ THz is caused mainly by an increased laser pulse energy (see Fig. 3.5). This effect is taken into account by the line shape model explained in Sec. 4.7.

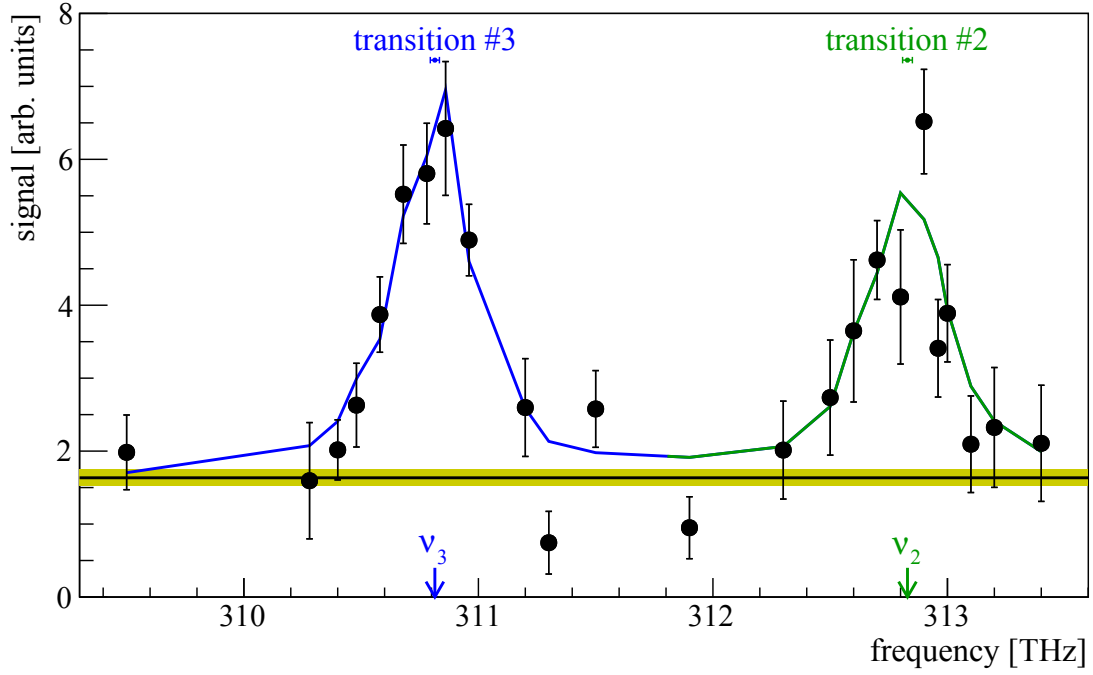


Figure 4.14.: LSM fit to the $2S_{1/2}^{F=0} - 2P_{3/2}^{F=1}$ and $2S_{1/2}^{F=1} - 2P_{1/2}^{F=1}$ transition (also termed transition 2 and 3, respectively). The signal is given by the normalized events in the LTW. The black data points are recorded LON events. The LOFF events are indicated via the flat black line. The yellow band shows the uncertainty of the LOFF events. The little blue and green data points at the top indicate the fitted center positions including their uncertainty. Again, pulse energy variations (see Fig. 3.5) cause significant deviations of the fit function from simple Lorentzians.

5. Theory summary of the $n=2$ levels in $\mu^3\text{He}^+$

According to the Dirac theory, the $2S_{1/2}$ and the $2P_{1/2}$ states should be degenerate. It appears that they are not, which mainly is explained by means of quantum electrodynamics (QED). The energy difference between those two states is called the Lamb shift. As pointed out already in Sec. 1, the effect of a finite nuclear charge distribution is also included in the Lamb shift. Hence, a good description of the $n=2$ energy levels together with a measurement of the same can be used to test QED and to extract a nuclear charge radius.

In practice, measuring the Lamb shift always means to measure a combination of the Lamb shift (LS), the fine structure (FS), and the hyperfine structure (HFS)¹. The total energy of a measured transition from an initial state i to a final state f is therefore given by

$$\Delta E_{\text{tot}}(i \rightarrow f) = \Delta E_{\text{LS}} + E_{2\text{P}}(f) + E_{2\text{SHFS}}(i). \quad (5.1)$$

The first term is the pure Lamb shift energy E_{LS} , the second term $E_{2\text{P}}(f)$ represents the energy of the involved 2P hyperfine level f with respect to the virtual $2P_{1/2}$ level², and the third term $E_{2\text{SHFS}}(i)$ represents the energy of the involved 2S hyperfine state i with respect to the virtual $2S_{1/2}$ level. It depends on the splitting $\Delta E_{2\text{SHFS}}$ of the two 2S hyperfine levels.

ΔE_{LS} can be divided into three parts

$$\Delta E_{\text{LS}} = \Delta E_{\text{LS}}^{\text{r-indep.}} + \Delta E_{\text{LS}}^{\text{r-dep.}}(r_E^2) + \Delta E_{\text{LS}}^{\text{TPE}} \quad (5.2)$$

A radius-independent and a radius-dependent part, as well as a two-photon exchange (TPE) part. Here, r_E is the rms nuclear charge radius.

$\Delta E_{2\text{SHFS}}$ can be divided into two parts

$$\Delta E_{2\text{SHFS}} = \Delta E_{\text{HFS}}^{\text{r-indep.}} + \Delta E_{\text{HFS}}^{\text{TPE}}. \quad (5.3)$$

¹The hyperfine structure only exists for nonzero nuclear spin. Helium-3 has a nuclear spin of 1/2.

The $2S_{1/2}$ and $2P_{1/2}$ states are therefore virtual states, i.e. the center of gravity of the hyperfine states.

² $E_{2\text{P}}(f)$ might also include the fine structure splitting ΔE_{FS} , depending on the angular momentum j of the final state f .

where $\Delta E_{\text{HFS}}^{\text{r-indep.}}$ again is the radius-independent part and $\Delta E_{\text{HFS}}^{\text{TPE}}$ is the two-photon exchange (TPE) part. It will later be of importance that the TPE term of the 2S HFS can again be split into a part dependent on the Zemach radius r_Z and a polarizability part

$$\Delta E_{\text{HFS}}^{\text{TPE}} = \Delta E_{\text{HFS}}^{\text{r-dep.}}(r_Z) + \Delta E_{\text{HFS}}^{\text{pol.}} \quad (5.4)$$

In $\mu^3\text{He}^+$ three transitions have been measured (see Fig. 1.1). They are used to extract two parameters and to additionally have a cross-check via the third measurement. The two parameters usually are the Lamb shift ΔE_{LS} and the 2S hyperfine structure $\Delta E_{2\text{SHFS}}$, which are the least well known parts in the theory. The extracted Lamb shift can then either be used to extract the nuclear charge radius r_E or the two-photon exchange of the Lamb shift $\Delta E_{\text{LS}}^{\text{TPE}}$, whereas the extracted 2S hyperfine structure can be used to extract the Zemach radius r_Z or the two-photon exchange in the 2S hyperfine structure $\Delta E_{\text{HFS}}^{\text{TPE}}$.

In this chapter the result of a theory compilation is presented which summarizes and compares all calculated terms of the most recent publications from theorists all over the world on a term-by-term basis. The compilation is given in detail in App. D. Such a compilation has become necessary already for muonic hydrogen [67] in 2013. Later this has been repeated for muonic deuterium [25] and muonic helium-4 [68]. The reason is that the different theory groups calculated and sorted the calculated terms in different ways. Independent calculations are indeed very important, however, the outcome sometimes differed and there is no way to compare the calculations and identify missing or wrongly calculated terms other than by the mentioned compilation. Besides, this practice has successfully proven to stimulate fruitful discussions among theorists and therefore contributed to theory in a very constructive way. The compilation for $\mu^3\text{He}^+$ also will be published [69] and will constitute the theoretical basis for the extraction of the helion charge radius.

The procedure of this compilation is the following. The individual terms from different authors are compared and for each term a value (termed *our choice*) is obtained by taking the average of the most outlying calculations. The assigned uncertainty to the averaged *our choice* is then half the spread. If an uncertainty for an individual term is given by one of the authors it is included via Gaussian propagation of uncertainty.

For some terms the average is not taken but rather a single value is adopted. This is the case only if there is a reason to not take the other available values into account, e.g. if a calculation is incorrect or not complete.

The experimental uncertainty is on the order of 20 GHz ($\sim 0.08 \text{ meV}$ ³). Ideally, a theoretical uncertainty on the order of 0.01 meV is therefore desirable. With that an accuracy of the helion charge radius of 10^{-4} can be achieved. The theory groups (with their authors in alphabetical order) contributing to $\mu^3\text{He}^+$ theory are

- Karlsruhe: E. Borie
- Mainz – Williamsburg (MAWI): Carl E. Carlson, Mikhail Gorchtein, Marc Vanderhaeghen
- Missouri – Heidelberg (MIHE): U. D. Jentschura, B. J. Wundt.
- Samara – Moscow (MOSA): E. N. Elekina, R. N. Faustov, A. A. Krutov, A. P. Martynenko, and G. A. Martynenko
- St. Petersburg (SAPE): V. G. Ivanov, S. G. Karshenboim, E. Yu. Korzinin, V. A. Shelyuto
- TRIUMF – Hebrew University (TRHE): S. Bacca, N. Barnea, O. J. Hernandez, C. Ji, N. Nevo Dinur

5.1. Lamb shift

The Lamb shift (LS) has historically been introduced in Sec. 1.1. Following Eq. (5.2) the Lamb shift can be divided into three parts. The first part is the QED part which is not dependent on nuclear structure. In contrast, the second and third part do depend on nuclear structure and are in turn separated by the number of exchanged photons. The one-photon exchange (OPE) is parameterized with the square of the nuclear charge radius and the two-photon exchange (TPE) includes nuclear excitations and therefore has a nontrivial dependence on the nuclear structure.

5.1.1. Nuclear structure-independent contributions

All known nuclear structure-independent contributions are listed in Tab. 1 of App. D. The groups which have calculated terms in this table are Borie, MOSA, MIHE, and SAPE. The leading term in the charge radius independent Lamb shift contributions is the so-called Uehling term, which is the one-loop electron vacuum polarization (eVP) (see Fig. 5.1). It scales with $\alpha(Z\alpha)^2 m$ (where m is the muon mass) and accounts for

³1 meV = 241.7989 GHz

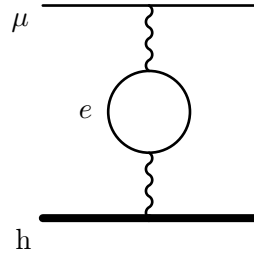


Figure 5.1.: The leading order 1-loop electron vacuum polarization (eVP), also called Uehling term. It accounts for 99.5% of the structure-independent part of the Lamb shift.

99.5% of the structure-independent part. The Uehling term which is strongly enhanced due to the large muon mass is responsible for the large distance from the 2S to the 2P levels, a characteristic of muonic hydrogen-like atoms.

The second largest term is the so-called Källén-Sabry term, which is the two-loop eVP contribution (order $\alpha^2(Z\alpha)^2m$). The third largest term is composed out of the contributions from muon self-energy and muon vacuum polarization (order $\alpha(Z\alpha)^4m$). It is the third largest term which is of leading order in the case of ordinary hydrogen-like atoms.

Including all terms given in Tab. 1 of App. D, the total radius-independent contribution to the Lamb shift is

$$\Delta E_{\text{LS}}^{\text{r-indep.}} = 1644.3466 \pm 0.0146 \text{ meV} \quad (5.5)$$

where the uncertainty mainly comes from hadronic vacuum polarization and higher order radiative recoil corrections.

5.1.2. Nuclear structure-dependent contributions

In this section, we distinguish between one-photon exchange (OPE) contributions and two-photon exchange (TPE) contributions (see Fig. 5.2).

The finite size effect originates from the OPE terms (also called *radius-dependent contributions*) which are parameterizable with a constant times the charge radius squared. These contributions are pure QED interactions with nuclear form factor insertions. The finite size effect is by far the largest part of the nuclear structure contributions.

The polarizability of a nucleus is described by the TPE terms. These involve QCD and therefore are very complicated to evaluate, which explains the dominant uncertainty originating from the TPE part. The TPE contributions are discussed in more detail below, after the discussion of the OPE terms.

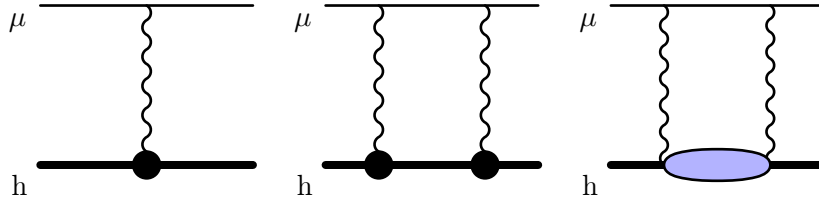


Figure 5.2.: *Left:* One-photon exchange. This is the leading finite size term. *Center and right:* elastic and inelastic two-photon exchange. One has to add also the diagrams with crossed photons. The black dot indicates a form factor insertion at the helion vertex. The blue blob on the *right* indicates all possible excitations of the helion.

One-photon exchange contributions

All known finite size contributions are listed in Tab. 2 of App. D. The groups which have calculated terms in this table are Borie, MOSA, and SAPE.

The contributions in this section can be written with an explicit dependency of the squared nuclear electric charge radius r_E^2 which is given by [10]

$$r_E^2 = -6 \left. \frac{dG_E}{dQ^2} \right|_{Q^2=0} \quad (5.6)$$

where G_E is the Sachs electric form factor (FF) of the nucleus and Q^2 is the negative of the square of the four-momentum transfer to the nucleus. This is the term which appears in the calculations of the electron-nucleus scattering process, as well as in the bound-state calculations with nuclear FF insertions. In the following the nuclear charge radius r_E will be denoted as r_h , which stands for the nuclear charge radius of the helion particle.

The leading order (LO) in the charge radius dependent Lamb shift contributions is the finite nuclear size term. It scales with $(Z\alpha)^4 m^3 r_h^2$ and is given by [10]

$$\Delta E_{\text{fin.size}}^{\text{LO}} = \frac{2}{3} \pi (Z\alpha) |\Psi(0)|^2 r_h^2 \quad (5.7)$$

where $\Psi(0)$ is the lepton wavefunction at the origin. In leading order only S states are affected, because only these are nonzero at their origin, where the nucleus resides⁴. The mass dependence to the power of three is what makes muonic atoms so sensitive to the finite size effect. This contribution is the second largest in the Lamb shift of muonic atoms right after the Uehling term.

Including higher order corrections as given in Tab. 2 of App. D, the total radius-dependent contribution amounts to

$$\Delta E_{\text{LS}}^{\text{r-dep.}}(r_h^2) = -103.5184(98) r_h^2 \text{ meV fm}^{-2} + 0.1177(33) \text{ meV}. \quad (5.8)$$

⁴This is true in a nonrelativistic approximation, which suffices for this argument.

Here, the second term has a nontrivial radius dependence which is prohibitively difficult to evaluate in a model independent way [70]. Therefore an exponential charge distribution is used for the calculation and no explicit radius dependence is given.

Two-photon exchange contributions

The two-photon exchange (TPE) describes the polarizability of the nucleus and therefore involves hadronic physics. Its scaling with the fourth power of the lepton mass raises its contribution in muonic atoms to a significant level. It can be divided in an *elastic* (third Zemach moment, also labeled Friar moment) and an *inelastic* (polarizability) part. The TPE is a heavily discussed contribution as it carries the largest uncertainty and dominantly limits the accuracy in the extraction of the charge radius. This is the case for muonic deuterium [25], muonic helium-4 [68], and it will also limit the extraction of the helion charge radius. For quite a while an underestimation of the TPE in μp had been discussed [71, 10] as a possible solution to the proton radius puzzle. However in order to solve the puzzle this term would have to be wrong by several multiples of its value, which finally has been considered to be very unlikely [72, 73].

The studies of the TPE calculations in μd in [25] have shown, that the available values for the TPE in μd scattered a lot. In different publications different single contributions have been omitted and only recently the compilation in [25] could explain the differences between the published values and find what maybe could be called a reliable value. Still, this value does not agree well with the experimental extraction (2.6σ between theory and experiment [13]). However, in spite of the difficulty of these calculations 2.6σ are satisfying as a start.

In the case of $\mu^3\text{He}^+$ the TPE exchange contribution is much larger than in the μd case. Here, it is even more important to identify missing terms. However for $\mu^3\text{He}^+$ not many calculations are available.

Fortunately in 2016, TRHE published the total TPE contribution in $\mu^3\text{He}^+$ where they took all previous inconsistencies into account. Performing *ab initio* calculations using nuclear potentials they obtain a total value of the nuclear and nucleon TPE of 15.46(39) meV [74, 75]. A second paper has been put on the arXiv in the finals of 2016 by MAWI [76]. Using dispersion relations they obtain a value of 15.14(49) meV.

For the extraction of the nuclear charge radius we will take the average of those two available values and as a conservative uncertainty we use the larger one from MAWI and add half the spread in quadrature:

$$\Delta E_{\text{LS}}^{\text{TPE}} = 15.30(52) \text{ meV}, \quad (5.9)$$

5.1.3. Total Lamb shift contribution

Summarizing the structure-independent contributions from Eq. (5.5), the finite size contributions from Eq. (5.8), and the TPE contribution from Eq. (5.9) results in a total energy difference for the Lamb shift of

$$\begin{aligned}
 \Delta E(2S_{1/2} - 2P_{1/2}) &= 1644.3466(146) \text{ meV} \\
 &+ 0.1177(33) \text{ meV} \quad - 103.5184(98) r_h^2 \text{ meV/fm}^2 \\
 &+ 15.3000(5200) \text{ meV} \\
 &= 1659.76(52) \text{ meV} \quad - 103.518(10) r_h^2 \text{ meV/fm}^2.
 \end{aligned} \tag{5.10}$$

5.2. 2S hyperfine structure

All known 2S hyperfine structure (HFS) terms are given in Tab. 3 of App. D. Contributions to the 2S HFS have been calculated by Borie and MOSA.

The leading contribution in the 2S HFS is the Fermi energy. The Fermi term for the 1S levels is in analytical form given by [77] and can be expressed for general n by

$$\Delta E_{\text{Fermi}} = \frac{8}{3} \frac{(Z\alpha)^4}{n^3} (1 + \kappa) \frac{m}{M} \left(\frac{m_r}{m} \right)^3 mc^2 \tag{5.11}$$

where κ is the nucleus anomalous magnetic moment and M (m) the mass of the nucleus (lepton).

Similar to the Lamb shift, the 2S hyperfine structure (2S HFS) can be divided into a radius-independent part, a radius-dependent part ⁵, and a polarizability part (see Eqs. (5.3) and (5.4)). The radius in this case is the Zemach radius of the nucleus [79]

$$r_Z = \int d^3r \int d^3r' r' \rho_E(\mathbf{r}) \rho_M(\mathbf{r} - \mathbf{r}') \tag{5.12}$$

$$= - \frac{4}{\pi} \int_0^\infty \frac{dq}{q^2} (G_E(q^2) G_M(q^2) - 1) \tag{5.13}$$

which is a convolution of the charge $\rho_E(\mathbf{r})$ and the magnetization $\rho_M(\mathbf{r})$ distribution.

From the muonic Lamb shift measurements not only the charge radius can be extracted, the final equations can also be solved for a parameter in the 2S HFS which can be either the Zemach radius or the polarizability in the 2S HFS.

In contrast to the Lamb shift, no calculations are available for the polarizability contribution in the 2S HFS. However, the value has been estimated by Kottmann [80] calculating the ratio of the 2S HFS polarizability to the Zemach term in $^3\text{He}^+$ and

⁵This part is also known as the Bohr-Weisskopf effect [78].

transferring it to $\mu^3\text{He}^+$. The required values are found calculating the Zemach term for electronic(!) $^3\text{He}^+$ in the 1S ground state, parameterized as [79]

$$\Delta E_{\text{HFS}}^{\text{r-dep.}}(r_Z) = -\Delta E_{\text{Fermi}} \times 2(Z\alpha)m_r r_Z. \quad (5.14)$$

With the Zemach radius r_Z from [81] a value of 1717 kHz is obtained. In order to obtain the total sum (polarizability + Zemach) of 1442 kHz [81], a polarizability term of order -300 kHz is missing. The ratio is then roughly -1/6. For muonic helium-3 ions in the 2S state, by means of Eq. (5.14) and with the helion Zemach radius [82], a Zemach term of $\Delta E_{\text{HFS}}^{\text{r-dep.}}(r_Z = 2.528(16)\text{fm}) \approx 6.5\text{ meV}$ is obtained. The estimate for the polarizability consequently follows with $\Delta E_{\text{HFS}}^{\text{pol.}} \approx -1.0 \pm 1.0\text{ meV}$, including a conservative 100% uncertainty.

However, as only one parameter from the 2S HFS can be extracted and the helion Zemach radius is available with good precision, it is clear that the Zemach radius will be used to experimentally determine the 2S HFS polarizability. $\Delta E_{\text{HFS}}^{\text{pol.}}$ will therefore remain as a fit parameter.

Including all other higher order contributions, the sum of the 2S HFS is

$$\Delta E_{2\text{SHFS}} = -172.7457(89)\text{ meV} + \Delta E_{\text{HFS}}^{\text{TPE}} \quad (5.15)$$

$$= -172.7457(89)\text{ meV} + 6.5312(413)\text{ meV} + \Delta E_{\text{HFS}}^{\text{pol.}} \quad (5.16)$$

$$= -166.2145(423)\text{ meV} + \Delta E_{\text{HFS}}^{\text{pol.}} \quad (5.17)$$

$$= -167.2(1.0)\text{ meV} \quad (5.18)$$

The second term (Zemach term) in Eq. (5.16) includes the Zemach radius [81] $r_Z = 2.528(16)\text{ fm}$. Eq. (5.17) will be the equation used to extract $\Delta E_{\text{HFS}}^{\text{pol.}}$ experimentally.

5.3. 2P levels (fine and hyperfine structure)

The structure of the 2P energy levels is determined by the 2P fine structure (FS), which is the $2P_{3/2} - 2P_{1/2}$ energy difference, and the hyperfine structure (HFS) of the $2P_{1/2}$ and $2P_{3/2}$ levels.

All known fine structure terms are given in Tab. 4 of App. D. Contributions to the FS have been calculated by Borie, MOSA, and SAPE.

The FS arises due to the interaction of the electron or muon spin with the induced magnetic field of the nucleus and the HFS due to the interaction of the nuclear spin with the induced magnetic field of the electron or muon. They are described by the spin-orbit and spin-spin terms in the Breit Hamiltonian [77, 83].

The leading contribution to the FS scales with $(Z\alpha)^4 m$. Including all higher order contributions, the total 2P FS yields

$$\Delta E_{\text{FS}} = 144.7993(101) \text{ meV.} \quad (5.19)$$

Below, the total 2P level geometry for $\mu^3\text{He}^+$ is determined by following the procedure of Pachucki [83] for μp and applying it for $\mu^3\text{He}^+$. The Breit Hamiltonian in matrix representation is given by [83]

$$M_{\text{Breit}} = \begin{matrix} & \begin{matrix} 2P_{1/2}^{F=0} & 2P_{1/2}^{F=1} & 2P_{3/2}^{F=1} & 2P_{3/2}^{F=2} \end{matrix} \\ \begin{matrix} 2P_{1/2}^{F=0} \\ 2P_{1/2}^{F=1} \\ 2P_{3/2}^{F=1} \\ 2P_{3/2}^{F=2} \end{matrix} & \begin{pmatrix} -\frac{3}{4}\beta_1 & & & \\ & \frac{1}{4}\beta_1 & \beta_2 & \\ & \beta_2 & -\frac{5}{8}\beta_3 + \gamma & \\ & & & \frac{3}{8}\beta_3 + \gamma \end{pmatrix} \end{matrix} \quad (5.20)$$

where γ is the 2P fine structure ΔE_{FS} from Eq. (5.19) above and

$$\beta_1 = \frac{1}{3}(Z\alpha)^4 \frac{\mu^3}{m_\mu m_h} (1 + \kappa) \left(\frac{1}{3} + \frac{a_\mu}{6} + \frac{1}{12} \frac{m_\mu}{m_h} \frac{1 + 2\kappa}{1 + \kappa} \right) \quad (5.21)$$

$$\beta_2 = \frac{1}{3}(Z\alpha)^4 \frac{\mu^3}{m_\mu m_h} (1 + \kappa) \left(1 + \frac{m_\mu}{m_h} \frac{1 + 2\kappa}{1 + \kappa} \right) \left(-\frac{\sqrt{2}}{48} \right) \quad (5.22)$$

$$\beta_3 = \frac{1}{3}(Z\alpha)^4 \frac{\mu^3}{m_\mu m_h} (1 + \kappa) \left(\frac{2}{15} - \frac{a_\mu}{30} + \frac{1}{12} \frac{m_\mu}{m_h} \frac{1 + 2\kappa}{1 + \kappa} \right). \quad (5.23)$$

Furthermore Pachucki adds corrections due to vacuum polarization in his Eq. (89) and (90)

$$\delta\beta_1 = \frac{1}{3}(Z\alpha)^4 \frac{\mu^3}{m_\mu m_h} (1 + \kappa) 0.00022 \quad (5.24)$$

$$\delta\beta_3 = \frac{1}{3}(Z\alpha)^4 \frac{\mu^3}{m_\mu m_h} (1 + \kappa) 0.00008. \quad (5.25)$$

where the Z scaling is now included.

The diagonal elements in Eq. (5.20) represent the energies of the 2P levels with respect to the virtual $2P_{1/2}$ level, excluding the mixing of states with same quantum number F . Diagonalizing the matrix yields the final energies where the $F = 1$ states are shifted.

The result of the 2P hyperfine structure energies calculated here are listed in Tab. 5 of App. D. Therein, also values published by Borie and MOSA are considered. The final values which also consider the scatter between the different authors are given in Tab. 5.1.

Table 5.1.: 2P levels from fine- and hyperfine splitting. All values are in meV relative to the $2\text{P}_{1/2}$ level. Uncertainties arise from differences between the published values and from the uncertainty in the fine structure value ΔE_{FS} .

$\Delta E(2\text{P}_{1/2}^{\text{F}=1})$	-14.7979(102)
$\Delta E(2\text{P}_{1/2}^{\text{F}=0})$	43.8754(296)
$\Delta E(2\text{P}_{3/2}^{\text{F}=2})$	135.7554(27)(101) _{FS}
$\Delta E(2\text{P}_{3/2}^{\text{F}=1})$	160.0452(42)(101) _{FS}

5.4. Summary and properties of the Lamb shift transitions

In the above sections the different theory parts which are involved in the Lamb shift transitions have been discussed. In order to compare the theoretical predictions with the measurement the above numbers have to be combined in the following way.

The theoretically predicted energy for the Lamb shift transition is obtained by inserting Eqs. (5.5), (5.17), and the corresponding value of Tab. 5.1 into the equations below.

For $2\text{S}_{1/2}^{\text{F}=1} - 2\text{P}_{3/2}^{\text{F}=2}$ this is

$$\Delta E(2\text{S}_{1/2}^{\text{F}=1} - 2\text{P}_{3/2}^{\text{F}=2}) = \Delta E_{\text{LS}} - \frac{1}{4}\Delta E_{2\text{SHFS}} + \Delta E(2\text{P}_{3/2}^{\text{F}=2}). \quad (5.26)$$

In the same manner the transition energies can be expressed for the $2\text{S}_{1/2}^{\text{F}=0} - 2\text{P}_{3/2}^{\text{F}=1}$ transition

$$\Delta E(2\text{S}_{1/2}^{\text{F}=0} - 2\text{P}_{3/2}^{\text{F}=1}) = \Delta E_{\text{LS}} + \frac{3}{4}\Delta E_{2\text{SHFS}} + \Delta E(2\text{P}_{3/2}^{\text{F}=1}), \quad (5.27)$$

and the $2\text{S}_{1/2}^{\text{F}=1} - 2\text{P}_{1/2}^{\text{F}=1}$ transition

$$\Delta E(2\text{S}_{1/2}^{\text{F}=1} - 2\text{P}_{1/2}^{\text{F}=1}) = \Delta E_{\text{LS}} - \frac{1}{4}\Delta E_{2\text{SHFS}} + \Delta E(2\text{P}_{1/2}^{\text{F}=1}) \quad (5.28)$$

Eqs. (5.26), (5.27), and (5.28) form the system of equations which together with the measured transition energies (see Tab. 4.3) also can be used in order to obtain experimentally determined values of ΔE_{LS} and $E_{2\text{SHFS}}$. This is done in the next section.

6. Results

In 2014, three Lamb shift transitions in muonic helium-3 have been measured by the CREMA collaboration for the first time. In this thesis the experiment is described and the process of data analysis documented comprehensively. The experiment has been described in Sec. 2 and the data analysis, including the final fit of the transition lines by means of a line shape model, in Sec. 4. The frequencies of the measured transitions are found to be

$$\Delta E(2S_{1/2}^{F=1} - 2P_{3/2}^{F=2}) = 347.2115(196)^{\text{stat}}(2)^{\text{sys}} \text{ THz} \quad (6.1)$$

$$\Delta E(2S_{1/2}^{F=0} - 2P_{3/2}^{F=1}) = 312.8296(209)^{\text{stat}}(2)^{\text{sys}} \text{ THz} \quad (6.2)$$

$$\Delta E(2S_{1/2}^{F=1} - 2P_{1/2}^{F=1}) = 310.8143(195)^{\text{stat}}(2)^{\text{sys}} \text{ THz}. \quad (6.3)$$

Here, the uncertainties arise from the fit (see Tab. 4.3 in Sec. 4.7) and the systematics described in Sec. 3 and summarized in Tab. 3.1.

By means of the Lamb shift theory, these measurements are now used to extract several other values. For that an extensive theory compilation has been written (see App. D) which compares the calculated contributions from different authors, identifying missing and wrongly calculated terms. This compilation is summarized in Sec. 5 of this thesis.

As there are three measured transitions, maximally three free parameters can be fitted for their positions. If only two free parameters are evaluated the third transition can be used to test the theory. The equations which transform the individual theory contributions into the total transition energies are Eqs. (5.26)-(5.28). These are compared with the measured transition frequencies, given by Eqs. (6.1)-(6.3) using the conversion $1 \text{ THz} = 4.314084 \text{ meV}$. The statistical and systematic uncertainties from Eqs. (6.1)-(6.3) are in the following summarized and labeled as experimental uncertainty.

In order to obtain the best values for the Lamb shift (LS) energy ΔE_{LS} and the 2S hyperfine structure (HFS) energy $\Delta E_{2\text{SHFS}}$, Eqs. (5.26)-(5.28) are used as the function which is fitted to the data points given by Eqs. (6.1)-(6.3). This yields

$$\Delta E_{\text{LS}} = 1258.58566(480)^{\text{exp}}(105)^{\text{theo}} \text{ meV} \quad (6.4)$$

$$\Delta E_{2\text{SHFS}} = -166.495(104)^{\text{exp}}(1)^{\text{theo}} \text{ meV}. \quad (6.5)$$

The only theoretical values which are needed for the extraction of the LS and the HFS are the values of the 2P level structure (see Tab.5.1). The theory value of the fine structure (see Eq. (5.19)) is included therein. Its uncertainty is by far dominating the theoretical uncertainty in Eq. (6.4). An additional fit, where the FS is a free parameter yields perfect agreement with theory. However, the experimental uncertainty is too large to improve the value of the fine structure.

As a second step, the experimentally determined value of ΔE_{LS} (r_{h}) from Eq. (6.4) can be used to extract a charge radius by means of Eq. (5.10). Solving this equation for the rms charge radius of the helion results in

$$\boxed{r_{\text{h}} = 1.96861(12)^{\text{exp}}(128)^{\text{theo}} \text{ fm}} \quad (6.6)$$

with a total relative uncertainty of 7×10^{-4} . The uncertainty of the charge radius is clearly dominated by the theoretical value of the TPE in the Lamb shift. It is trivial that the given value of the charge radius is only as good as the theoretical value of the TPE which is still under discussion.

The helion charge radius from Eq. (6.6) can be compared with measurements from electron scattering as shown in Fig. 6.1 [16, 84, 85, 17, 18] (a complete list is found in [19]). However, the available values have very large uncertainties (>10 times the muonic uncertainty). The most recent value directly obtained from scattering data in helium-3 is given by Sick [20] and amounts to $r_{\text{h}} = 1.959(34) \text{ fm}$. This value is in excellent agreement with our result.

The most precise (not necessarily accurate, see next paragraph) value of the helion charge radius available is $r_{\text{h}} = 1.9661(30) \text{ fm}$ from Angeli *et al.* [21]. It is in agreement with our measurement, but it is not useful as a comparison for two reasons.

First, Angeli *et al.* use an average of previous r_{α} measurements which is dominated by the $\mu^4\text{He}^+$ results from Carboni *et al.* [23]. This measurement has been proven wrong by a recent measurement of r_{α} from the CREMA collaboration. The only reason that the values agree is that the theory which has been used to extract the Carboni value, was missing some terms which compensated for the wrong measurement.

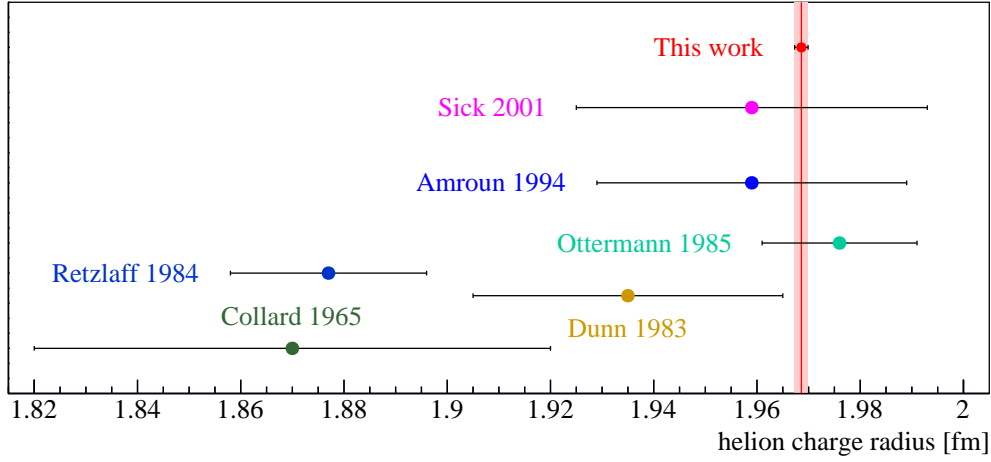


Figure 6.1.: Direct measurements of the helion charge radius. Except the “muonic” value from this thesis (red data point at the top) all others are obtained by electron scattering. The pink bar shows the total uncertainty of the muonic value, given in Eq. 6.6. Its position is in excellent agreement with the three most recent values from electron scattering.

Second, Angeli *et al.* use the isotope shift measurement from Shiner *et al.* [22]. By doing this, they ignore that there are two other isotope shift measurements with a large scatter. In consequence, this leads to an underestimation of their uncertainty.

Considering the difference of charge radii from ${}^3\text{He}$ and ${}^4\text{He}$, we can compare the muonic result with quite precise results from spectroscopy where the isotope shift has been measured to much better precision than comparable values from electron scattering. However, different measurements [22, 86, 87] of the isotope shift have resulted in discrepant values (see Fig. 6.2) which is why an additional and independent determination of it is needed. The measurement of the Lamb shift in $\mu^4\text{He}^+$ resulted in a charge radius of the alpha particle of [24]

$$r_\alpha = 1.67829(14)^{\text{exp}}(52)^{\text{theo}} \text{ fm}, \quad (6.7)$$

which can now be used to calculate a *muonic* value of the charge radius difference between these two isotopes. The charge radius difference from measurements in muonic helium-3 (Eq. (6.6)) and -4 (Eq. (6.7)) results in

$$\boxed{\Delta r^2(\mu^3\text{He}^+ - \mu^4\text{He}^+) = 1.0588(7)^{\text{exp}}(53)^{\text{theo}} \text{ fm}^2.} \quad (6.8)$$

This value is in excellent agreement with the value from Shiner *et al.* [22]. It is furthermore 2.6σ away from van Rooij *et al.* [86] and in rough agreement (1.7σ) with Cancio

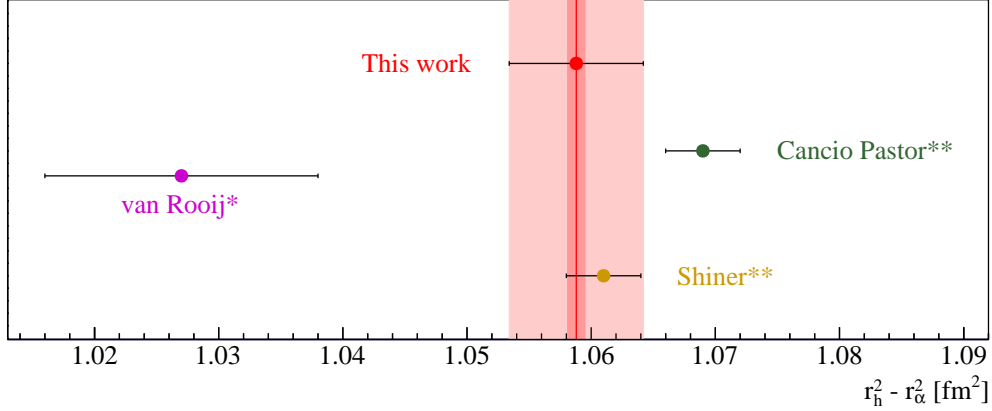


Figure 6.2.: The charge radius difference of the He isotopes -3 and -4. The value of van Rooij *et al.* [86] flagged with * has been reevaluated in [89]. The values of Cancio Pastor *et al.* [87] and Shiner *et al.* [22] flagged with ** have been reevaluated in [88]. The red data point shows the value from Eq. (6.8) which is obtained in this thesis. The pink error bar reflects the total uncertainty, whereas the red uncertainty band shows the purely experimental uncertainty. The value extracted in this work is in excellent agreement with the Shiner measurement, in rough agreement (1.7σ) with Cancio Pastor, and in 2.6σ distance to the van Rooij value.

Pastor *et al.* [87]. Note, that all values of the three given references have been reevaluated. The most recent values are found in Patkos *et al.* [88, 89].

A detailed study of the correlations between the theoretical uncertainties of the two muonic values (Eqs. (6.6) and (6.7)) might likely be able to further improve the theoretical uncertainty in Eq. (6.8).

In principle, the same procedure as done for the LS can be repeated for the 2S HFS, which means to take a theoretical value of the polarizability in the 2S HFS and extract an experimental value for the Zemach radius. However, as in Sec. 5.2 explained, no calculation of the polarizability in the 2S HFS exists and the existing estimate's uncertainty is too large to obtain a useful result. Instead it is more reasonable to use the most recent value of the Zemach radius of $r_Z = 2.528(16)$ fm [82] and obtain the polarizability of the 2S HFS via Eq. (5.17) which results in

$$\Delta E_{\text{HFS}}^{\text{pol.}} = -0.281(104)^{\text{exp}}(1)^{\text{theo}} \text{ meV}, \quad (6.9)$$

or with rounded numbers $\Delta E_{\text{HFS}}^{\text{pol.}} = -0.28(10) \text{ meV}$. The uncertainty is dominated by statistics. The largest part of the theoretical uncertainty originates from the Zemach term. This number for the polarizability in the 2S hyperfine structure fulfills the expectation of a value with inverted sign compared to the Zemach term, and furthermore fits perfectly to the rough estimate from Kottmann ($-1.0 \pm 1.0 \text{ meV}$, see Sec. 5.2).

7. Conclusions

This work reports on the first ever measurement of the Lamb shift in the muonic helium-3 ion. The experiment has been performed by the CREMA collaboration, which has measured three different transitions with a precision of $< 70\text{ppm}$. The uncertainty is dominated completely by statistics.

The reported measurement allows the extraction of the helion charge radius with a relative uncertainty of 7×10^{-4} , limited by the uncertainty in the polarizability of the helion. Its value provides a useful observable to check theories of few nucleons nuclei using nucleon-nucleon (NN), three-nucleon (NNN), or four-nucleon (NNNN) potentials.

Together with the CREMA charge radius of the alpha particle, a charge radius difference is obtained which is in excellent agreement with an isotope shift measurement from Shiner *et al.*.

The results of this measurement are ideally suited to test bound-state QED calculations. Together with an upcoming $1S - 2S$ measurement in He^+ [90, 91] and with an improvement of the theoretical prediction of the TPE, interesting QED terms like e.g. B_{60} (two-loop contribution in the Lamb shift theory in H and He^+), can be tested to high accuracy and the value of the Rydberg constant can be improved.

In terms of the proton radius puzzle, it is interesting to see that the muonic values of the nuclear charge radii of the helium isotopes agree with the results from electron scattering. An interesting question is, how large would the effect of a smaller value of the proton radius inside the helium nucleus be. This effect might still be hidden in the current uncertainty.

Despite the muonic helium results which do not disagree with values obtained by electron scattering, there are still some ideas applying beyond standard model physics to solve the proton problem, see e.g. Ref. [92].

The questions around the proton radius puzzle have motivated many other experiments and their future results will provide significant contributions to this problem.

One of the upcoming experiments is MUSE [93] which will measure muon and electron scattering on nuclei in the same setup. The feature of having muons and electrons in

the same setup increases the sensitivity for any differences in the couplings of electrons and muons with the nucleus.

Another highly interesting experiment is the $2S - 4P$ measurement in hydrogen at MPQ [94], which is close to publication. Together with the very accurate $1S - 2S$ measurement they will provide a proton charge radius which is proposed to be as precise as the average of all previous laser spectroscopy measurements on ordinary hydrogen combined. It will therefore also be able to give further insight into the puzzle and tell whether the value of the Rydberg constant should be changed to a value which is obtained when using the CREMA value of the proton charge radius.

A. Calibration

A.1. Time calibration

A.1.1. X-ray and electron detectors

Muon decay electrons spiral in the 5 T magnetic field of the PSC and make coincidences in the electron paddles and APDs. Thus, a common time scale for all APDs and electron paddles is crucial for the analysis. The timings of the different detectors in the raw data are given in TDC bins (32 bins/25 ns) and may vary due to the length of cables from the detector to the TDCs or due to different discriminator thresholds. As a common reference, the *high* signal in the left electron paddle is used. The time differences from this signal to the signals of the other detectors are computed and fitted. These differences provide the offset for the calibration of all X-ray and electron detectors with the left *high* paddle. The time is then converted to seconds via the factor 25 ns/32 bins ¹. With this calibration all coincidence plots between the X-ray and electron paddle detectors have their peak at zero (see Fig. 4.3).

A.1.2. Photodiodes and light in APD B9

During the measurement of line 1 (the $2S_{1/2}^{F=1} - 2P_{3/2}^{F=2}$ transition) the light shield of the APDs did not work properly for APD B9, which is the last APD in the bottom array heading downstream. Other APDs were not affected. The neighboring APD B8 did not work and in B7 no laser is visible anymore. The histogram on the right side in Fig. A.1 shows the laser light at roughly 1 μ s and 1.5 keV. This peak can be cut away, but it also can be used because it allows to compare the time of the APDs with the time of the photodiodes (Fig. A.2). Between photodiode E0 and the laser signals in B9 is a 225 ns delay. This time difference is used to calibrate the scale of Fig. 4.11.

¹Furthermore an offset is added which shifts the beginning of the prompt peak of the X-rays in the time histograms to zero. With that the common time scale starts approximately with the muon stopping in the target gas.

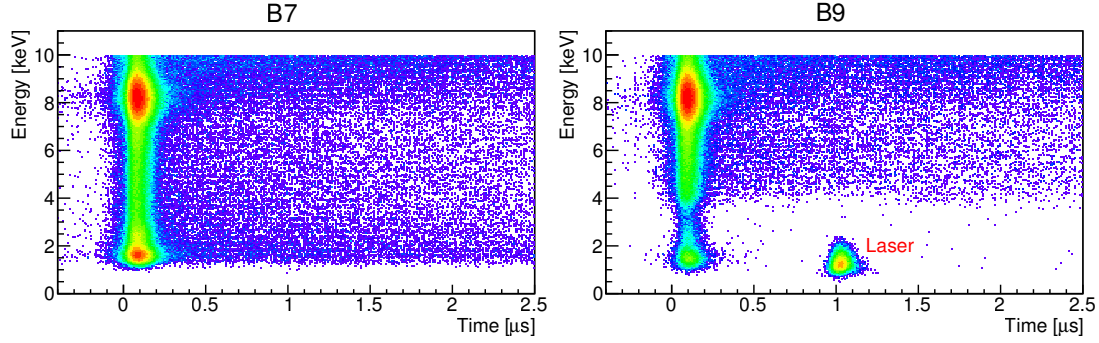


Figure A.1.: Laser light in APD B9. During the measurements of the $2S_{1/2}^{F=1} - 2P_{3/2}^{F=2}$ transition, some laser light passed the light shield of APD B9 (*right*). The signal from the laser is seen at about $1\text{ }\mu\text{s}$ and an energy below 2 keV . As APD B8 did not work during these runs, the next APD to see laser light would be B7. For APD B7, however, the light shield worked well (*left*). Note, that there is less background visible in APD B9. This is due to a higher threshold of the discriminator before the TDC to minimize laser induced overflow.

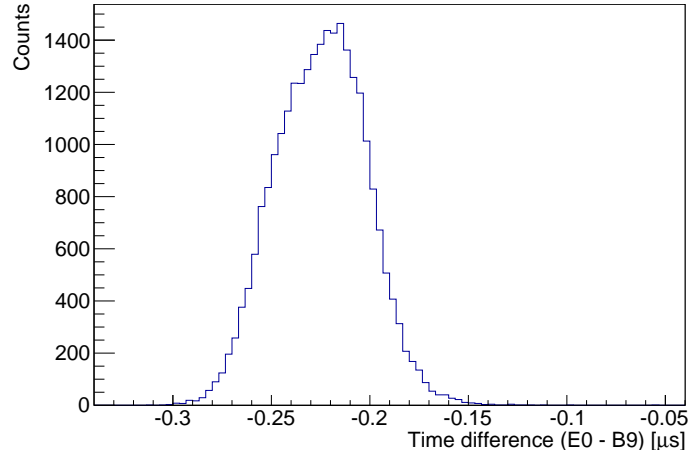


Figure A.2.: Offset between laser light in APD B9 and photodiode E0. The mean of this histogram is -225 ns . The physical delay should be below 5 ns , the rest originates from cable delays. For this histogram a cut around the laser peak in Fig. A.1 has been applied.

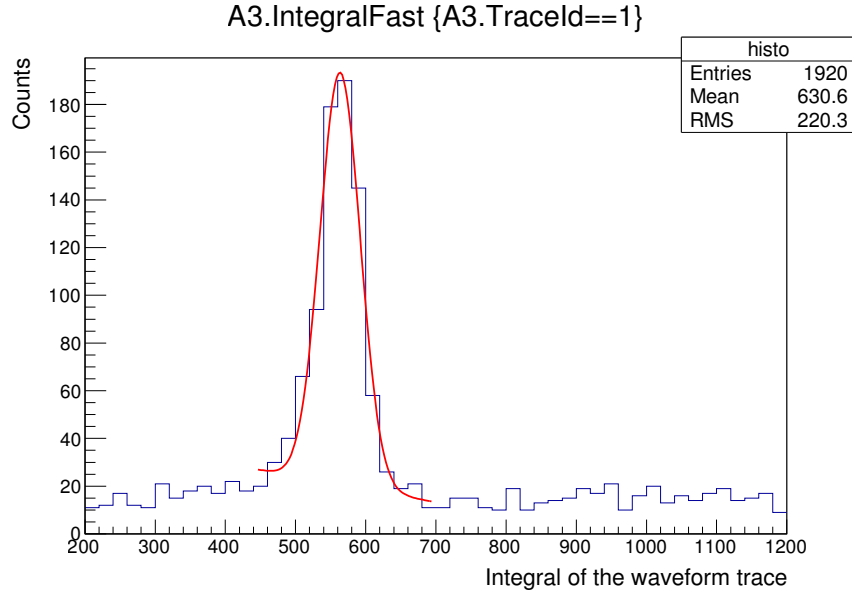


Figure A.3.: Raw energy spectrum of APD A3 in run 1944. Shown is the K_{α} peak roughly fitted by a Gaussian. The calibration procedure shifts this peak to 8.13 keV. Depending on the trace ID, different Integrals are used. This is described in Sec. 4.1 and more in detail in Ref. [65].

A.2. Energy calibration

A.2.1. APD energy calibration

The APD energy calibration has been explained in Sec. 4.1 which summarizes Ref. [65]. In short:

20 APDs inside the target are detecting the X-rays originating from the muonic atoms. 10 APDs are located above, and another 10 below the muon stop volume. In order to perform a clear cut of the 8 keV (K_{α}) X-rays, a good energy calibration of the APD data is mandatory.

The APD signals are recorded via WaveForm Digitizers (WFDs). In order to obtain the energy of an X-ray, the waveform trace of each signal is integrated. This procedure requires an edge-finder which is needed to determine the time where the signal begins and an elaborate method which depends on the different standard waveform traces appearing in the APDs. For further information see [65].

The so obtained histogram (see Fig. A.3) shows the energy spectrum of the X-rays. The position of the center of the K_{α} peak (which is the highest peak in the APD spectrum) of each APD in each run is obtained by a Gaussian fit. With a conversion factor for each APD and each waveform trace, the scale is then converted in such a way

that the K_α peak actually appears at 8.13 keV. However during the measurements there have been some problems with the high voltage power supply for the APDs, which led to jumps in the raw data. By means of an additional algorithm these jumps have been corrected successfully. This is described below.

The calibrated spectrum is shown in Fig. 4.2.

APD jumps

During the measurements of $\mu^3\text{He}^+$ the high voltage power supply for the APDs did not work properly. The malfunction manifested itself by sudden jumps in the bias voltage, which in turn have been observed in the energy vs. time histograms of the APDs (Fig. A.4). The origin of this effect was not found at that time and a replacement for the power supply was not available during the measurement time. In order to make an effective energy cut (see Sec. 4.1) on the 8.1 keV Ly- α X-rays seen in the APD spectra a good calibration of the X-ray data is required. Therefore the jumps which already exist in the un-calibrated raw data have to be corrected. This is done by a macro which identifies the jumps, locates them within an interval of 500 events (corresponds roughly to a time window of 8 s) and rescales the distorted data. The result is seen in Fig. A.5.

Besides the jumps in Fig. A.4, there is also a small continuous drift visible. However, this drift is not important as it is far below the Ly- α linewidth seen by the APDs and therefore does not affect the cut significantly.

In the following the process of correcting for the jumps is described more in detail. The data is plotted with 500 events per bin on the x-axis, whereas the y-axis contains the energy information. The position of a jump (bin b') is roughly picked by eye (bin b_0) and written in a file. In order to find the true position of the jump, a kind of step function is used. The file is read out by a macro which scans a 40 bin wide interval (≈ 5 min of measurement time) around bin b_0 . The y-projection of every single of these 40 bins is fitted to find the energy peak p of the Ly- α X-rays. So for every single of these 40 bins b_i there is a fitted value $p(b_i)$ of the Ly- α energy. Scanning the data around a certain bin b_i with $i \in [-20, 20]$ the macro takes the average difference D_i of the two neighboring bins on each side:

$$D_i = \frac{1}{2} (p(b_{i-2}) + p(b_{i-1})) - \frac{1}{2} (p(b_{i+1}) - p(b_{i+2})). \quad (\text{A.1})$$

If D_i passes a threshold of 0.3 keV, bin b_i is defined to be the bin b' where the jump happens in. The event in the middle of bin b' is then maximally 250 events away from the true position of a jump. 250 is therefore the number of events per jump which after running the macro still might have a wrong calibration. This is sufficient.

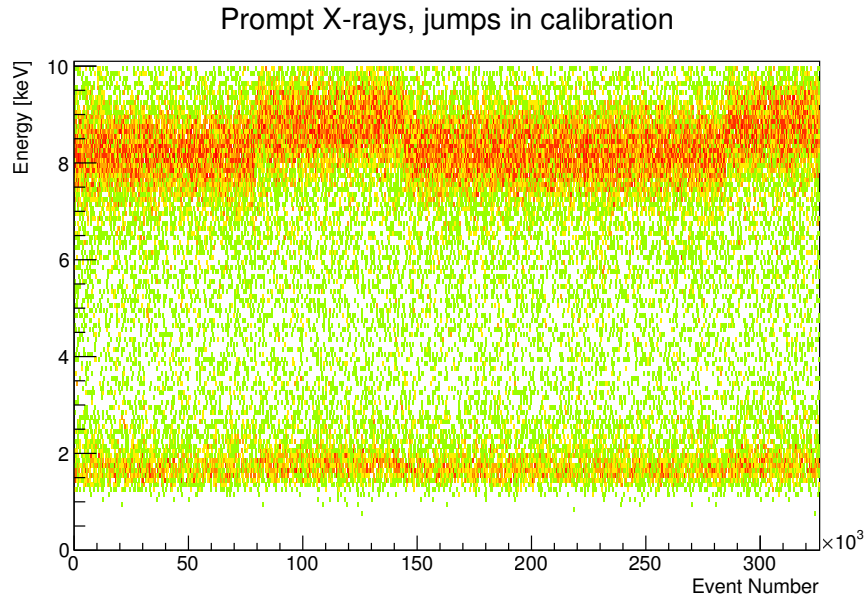


Figure A.4.: Prompt X-ray spectrum of run #1961 plotted versus event number. The calibration of the 8 keV Ly- α line jumps three times due to sudden changes in the bias voltage of the APDs. The jumps are located around event number 79250, 144250, and 285250. Correcting the spectrum for these jumps results in Fig. A.5.

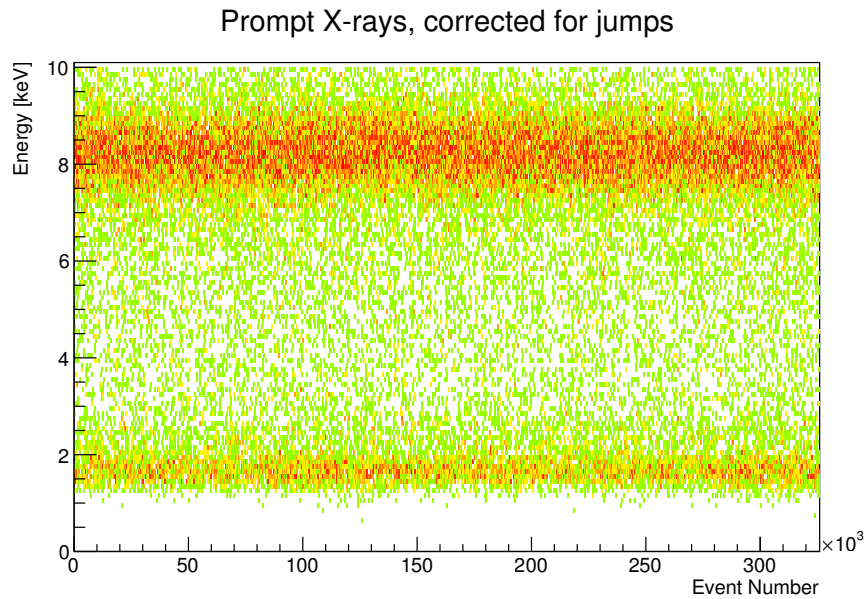


Figure A.5.: Prompt X-ray spectrum of run #1961 after correcting for jumps in the calibration (compare Fig. A.4). The energy of the events in the interval between number 7925 and 144250 is rescaled with a factor of 0.940, the energy of the events after event 285250 with 0.944.

Now having found the position of the jump, the average Ly- α energy of 4 bins before and 4 bins after the jump, respectively, is evaluated. Their ratio determines the correction factor to the calibration of the events after the jump. Trivially the calibration for these events is only changed until the position of a possible second jump where the calibration is reset.

A.2.2. Laser pulse energy calibration

The laser pulse energy is detected by several photodiodes. The photodiodes only need a small fraction of the pulse and thus can be operated during the actual measurement. In consequence they record the pulse energy on a pulse-per-pulse basis. The photodiodes are measuring the pulse energy at the thin disk oscillator, at the thin disk amplifier, at the Ti:Sa oscillator, behind the in-coupling mirror inside the target, and another six photodiodes are located behind the cylindrical multipass cavity mirror. The signals of all photodiodes are highly correlated, as they should be. The data is recorded by several Analog-to-Digital Converters (ADCs). However, the photodiodes still have to be calibrated. So, before each run, the laser pulse energy is measured on an absolute scale by a calibrated pyroelectric detector. This detector has to be placed into the beam and therefore cannot be operated during the measurement. For the first transition a calibrated detector from the company Gentec-EO has been used, which indicates the laser pulse energy in mJ. During the measurement of the second transition line the calibrated Gentec detector died and another pyroelectric detector has been used. Due to some overlapping measurements the second detector could be calibrated by the first one.

Later, in the analysis the average pulse energies per single photodiode per single run are evaluated by a simple Gaussian fit (see Fig. A.6) and then calibrated with the data from the pyroelectric detectors. The evaluation on a single run basis eliminates possible systematics due to long-term shifts of the photodiodes.

The average calibrated pulse energies for each run are summarized in Fig. 3.5.

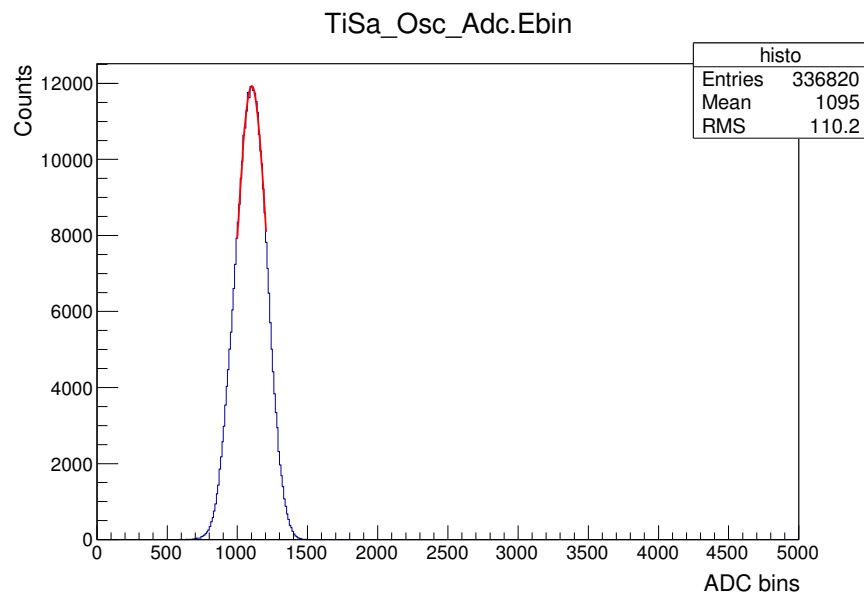


Figure A.6.: Raw pulse energies at the output of the Ti:Sa oscillator in run 2054. A Gaussian function is used to fit the peak. The fitted center position is used for the calibration with the data of the pyroelectric detector.

B. The Lamb shift transitions of the muonic helium-3 ion

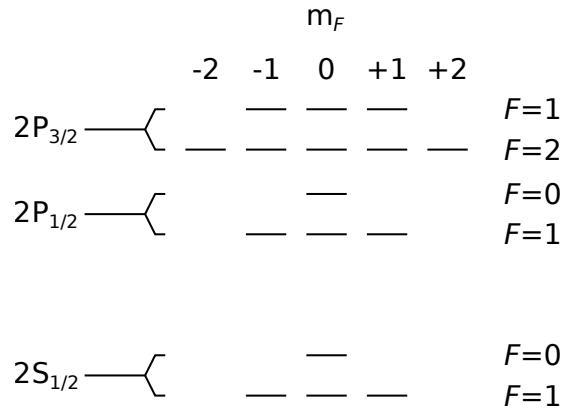


Figure B.1.: $n = 2$ energy levels of the helium-3 ion. Not to scale.

Table B.1.: The Lamb shift transitions in $\mu^3\text{He}^+$. There are six allowed Lamb shift transitions in $\mu^3\text{He}^+$. Transitions #1, #2, and #3 have been measured during this thesis. Transition #6 is not reachable with the current laser system. From left to right the following transition properties are given: transition frequency ν , wavelength λ , energy E , population η , matrix element M , and saturation fluence F_{sat} . The values of the transition energies are obtained from theory and rounded here to serve as rough estimates.

#	Transition	ν [THz]	λ [nm]	ΔE [meV]	Pop. η	M [a_μ^2]	F_{sat} [J/cm ²]
1	$2S_{1/2}^{F=1} - 2P_{3/2}^{F=2}$	347	864	1435	3/4	5	1.3
2	$2S_{1/2}^{F=0} - 2P_{3/2}^{F=1}$	313	959	1295	1/4	6	1.1
3	$2S_{1/2}^{F=1} - 2P_{1/2}^{F=1}$	311	965	1285	3/4	2	3.3
4	$2S_{1/2}^{F=1} - 2P_{3/2}^{F=1}$	353	849	1460	3/4	1	5.9
5	$2S_{1/2}^{F=1} - 2P_{1/2}^{F=0}$	325	923	1345	3/4	1	6.4
6	$2S_{1/2}^{F=0} - 2P_{1/2}^{F=1}$	270	1109	1120	1/4	3	2.1

C. ^3He circulation system

Helium-3 is a very rare isotope and only very little stocks of it exist. Fortunately PSI provided a bottle of it filled with about $10 \text{ bar} \cdot l$. In order to save this very expensive isotope, a circulation system has been developed at PSI where the helium gas could be purified continuously and be re-used several times. With that the experiment could run for several months, spending only a small part of the bottle. Furthermore a cold trap has been included where other gases than helium are condensed. It consists of two concentric stainless steel pipes, about 1 m long, inserted vertically into a standard liquid-helium dewar.

The working principle of the circulation system is shown in Fig.C.1. The actual helium gas flow is indicated by orange arrows. From the buffer, the helium gas goes to the cold trap where it is purified. From there it proceeds to the inlet (IN) of the target. The distance to the target is few meters. After the target (OUT) it is pumped again into the buffer. A small loss of helium through the thin target windows requires to re-fill the buffer from time to time using the helium bottle. The pressure at IN is about $p_{\text{IN}} = 2.5 \text{ mbar}$ and at OUT about $p_{\text{OUT}} = 1.5 \text{ mbar}$, leading to a pressure difference of $\Delta p = 1 \text{ mbar}$ and therefore a slow constant ventilation. The ventilation is used to remove the contamination from outgassing (mainly water and hydrocarbon molecules). The helium gas is then purified again in the cold trap, mentioned above.

Before the circuit has been used for helium-3 it has been tested with helium-4 during the measurement of the second Lamb shift transition in $\mu^4\text{He}^+$.

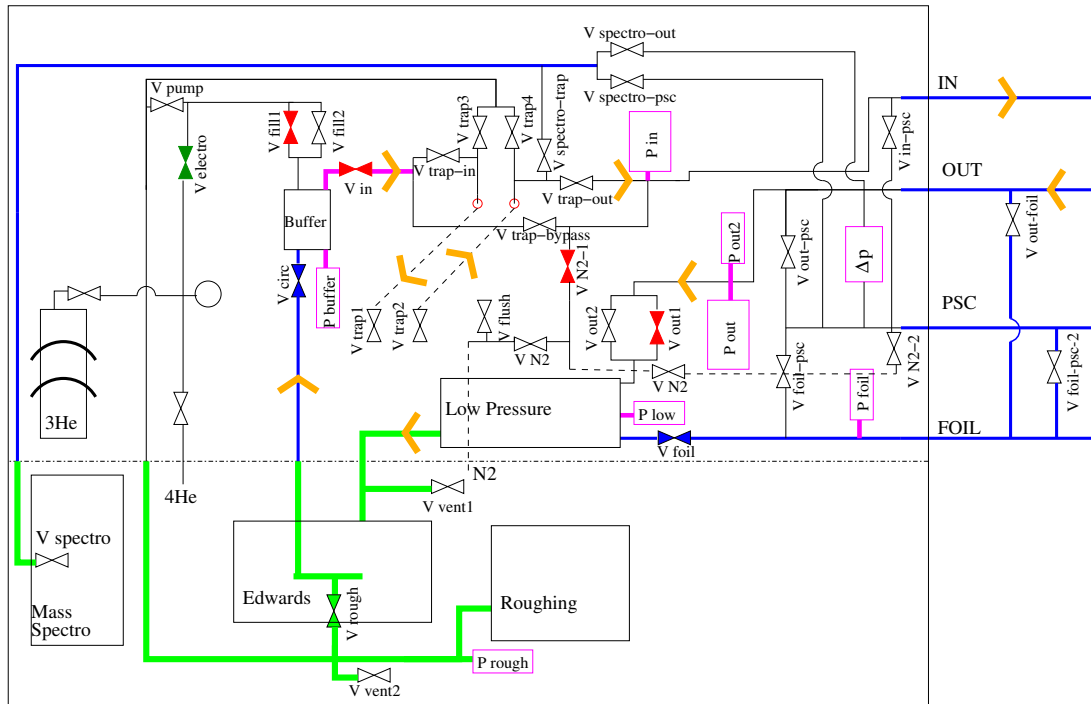


Figure C.1.: The ^3He circulation system. The usual flow of the helium-3 gas is indicated via the orange arrows. On the right side the connection to the inlet (IN) and to the outlet (OUT) of the gas target is indicated. Below there is also a connection to the vacuum of the PSC and to a differential pumping section between the target window and an additional foil, which could have been used to reduce the helium-3 loss through the windows. However, the target windows turned out to be more tight than previously assumed, and the additional foil was therefore not installed during data-taking. The helium-3 bottle is indicated on the left and connected to the buffer. The helium gas starts the circuit from the buffer, passes the cold trap and flows towards the target. From there it comes back, driven by the low pressure and is then pumped into the buffer again by a scroll pump from Edwards.

Theory of the $n = 2$ levels in muonic helium-3 ions

Beatrice Franke^{a,b,*}, Julian J. Krauth^{a,c,*}, Aldo Antognini^{d,e}, Marc Diepold^a, Franz Kottmann^d,
Randolf Pohl^{c,a}

^a*Max-Planck-Institut für Quantenoptik, 85748 Garching, Germany.*

^b*TRIUMF, 4004 Wesbrook Mall, Vancouver, BC V6T 2A3, Canada*

^c*Johannes Gutenberg-Universität Mainz, QUANTUM, Institut für Physik & Exzellenzcluster PRISMA, 55099 Mainz, Germany*

^d*Institute for Particle Physics, ETH Zurich, 8093 Zurich, Switzerland.*

^e*Paul Scherrer Institute, 5232 Villigen, Switzerland.*

Abstract

The present knowledge of Lamb shift, fine-, and hyperfine structure of the 2S and 2P states in muonic helium-3 ions is reviewed in anticipation of the results of a first measurement of several $2S \rightarrow 2P$ transition frequencies in the muonic helium-3 ion, $\mu^3\text{He}^+$. This ion is the bound state of a single negative muon μ^- and a bare helium-3 nucleus (helion), $^3\text{He}^{++}$.

A term-by-term comparison of all available sources, including new, updated, and so far unpublished calculations, reveals reliable values and uncertainties of the QED and nuclear structure-dependent contributions to the Lamb shift and the hyperfine splitting. These values are essential for the determination of the helion rms charge radius and the nuclear structure effects to the hyperfine splitting in $\mu^3\text{He}^+$. With this review we continue our series of theory summaries in light muonic atoms; see Antognini *et al.*(2013) [1], Krauth *et al.*(2016) [2], and Diepold *et al.*(2016) [3].

Keywords: muonic helium-3 ions, Lamb shift, hyperfine structure, fine structure, QED, proton radius puzzle

1. Introduction

Laser spectroscopy of light muonic atoms and ions, where a single negative muon orbits a bare nucleus, holds the promise for a vastly improved determination of nuclear parameters, compared to the more traditional methods of elastic electron scattering and precision laser spectroscopy of regular atoms.

The CREMA collaboration has so far determined the charge radii of the proton and the deuteron, by measuring several transitions in muonic hydrogen (μp) [4, 5, 1] and muonic deuterium (μd) [6, 2]. Interestingly, both values differ by as much as six standard deviations from the respective CODATA-2014 values [7]. This discrepancy has been coined "proton radius puzzle" [8, 9], although the discrepancy exists for the deuteron, too.

*authors contributed equally

Email addresses: bfranke@triumf.ca (Beatrice Franke), jkrauth@uni-mainz.de (Julian J. Krauth), pohl@uni-mainz.de (Randolf Pohl)

The respective radii are

$$r_p(\mu p) = 0.84087(26)^{\text{exp}}(29)^{\text{th}} = 0.84087(39) \text{ fm} \quad [4, 5] \quad (1)$$

$$r_p(\text{CODATA} - 2014) = 0.8751(61) \text{ fm} \quad [7] \quad (2)$$

$$r_d(\mu d) = 2.12562(13)^{\text{exp}}(77)^{\text{th}} = 2.12562(78) \text{ fm} \quad [6] \quad (3)$$

$$r_d(\text{CODATA} - 2014) = 2.1413(25) \text{ fm} \quad [7]. \quad (4)$$

Very recently, the CREMA collaboration has measured a total of five transitions in muonic helium-3 and -4 ions, which have been analyzed now. These measurements will help to improve our understanding of nuclear model theories [10, 11] and help to solve a discrepancy between several measurements of the helium isotope shift [12, 13, 14, 15, 16]. Furthermore they will shed more light on the proton radius puzzle.

Interestingly, for the proton and the deuteron, the muonic isotope shift is compatible with the electronic one from the 1S-2S transition in H and D [17, 18]. A new measurement of the Rydberg constant in hydrogen will soon shed new light on the discrepancies [19].

Similar to muonic hydrogen [1], deuterium [2], and helium-4 ions [3], we feel therefore obliged to summarize the current knowledge on the state of theory contributions to the Lamb shift, fine-, and hyperfine structure in muonic helium-3 ions. The accuracy to be expected from the experiment will be on the order of 20 GHz, which corresponds to $\sim 0.08 \text{ meV}^1$. In order to exploit the experimental precision, theory should, ideally, be accurate to a level of

$$\sigma_{\text{theory}} \sim \mathcal{O}(0.01 \text{ meV}). \quad (5)$$

This would result in a nearly hundred-fold better accuracy in the helion charge radius compared to the value from electron scattering of

$$r_h = 1.959(34) \text{ fm}, \quad (6)$$

deduced by Sick [20].

We anticipate here that the total uncertainty in the theoretical calculation of the Lamb shift transition amounts to 0.52 meV, neglecting the charge radius contribution to be extracted from the $\mu^3\text{He}^+$ measurement. This value is completely dominated by the two-photon exchange contributions which are difficult to calculate but have seen wonderful progress in recent years [11, 21, 22]. The total uncertainty of the pure QED contributions (without the two-photon exchange) amounts to 0.04 meV and is thus in the desired range. Note that while the theory uncertainty from the two-photon exchange in r_p is of similar size as the experimental uncertainty (Eq. (1)), already for μd the theory uncertainty is vastly dominant (Eq. (3)). Experiments with muonic atoms can be used to determine the two-photon exchange contributions.

2. Overview

The $n = 2$ energy levels of the muonic helium-3 ion are sketched in Fig. 1. The helion has nuclear spin $I = 1/2$, just as the proton. Hence the level scheme is very similar to the one of muonic hydrogen. However, the helion magnetic moment $g = -2.127\,625\,308(25)$ [7] (here given in units of the nuclear magneton) is negative, which swaps the ordering of the hyperfine levels.

¹1 meV \cong 241.799 GHz

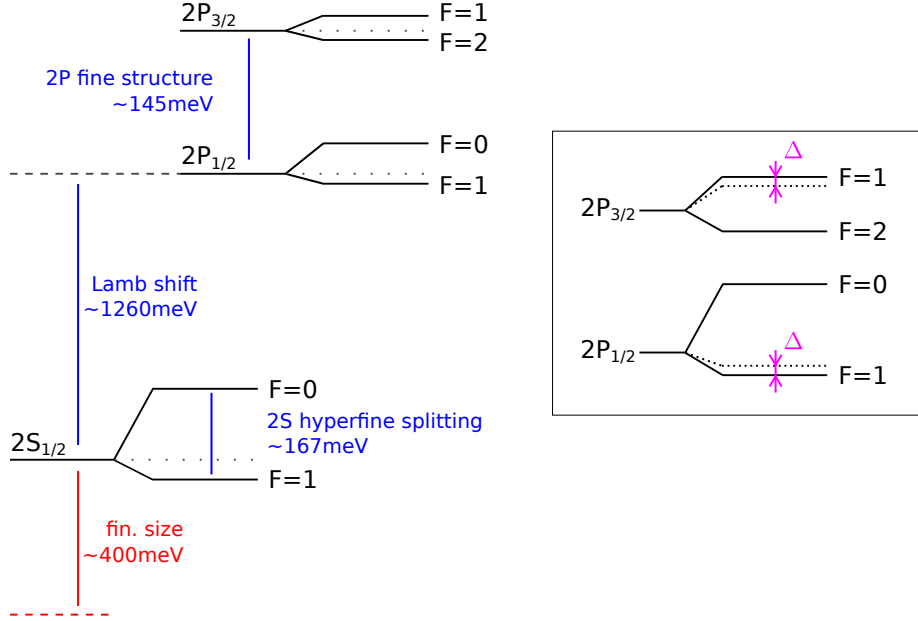


Figure 1: The 2S and 2P energy levels in the muonic helium-3 ion. The inset on the right displays the shift Δ of the 2P levels due to the mixing of levels with same quantum number F , as described in Sec. 5. The figure is not to scale.

A note on the sign convention of the Lamb shift contributions used in this article: The 2S level is shifted below the 2P levels due to the Lamb shift. This means that, fundamentally, the 2S Lamb shift should be given a *negative* sign.

However, following long-established conventions we assign the *measured* $2S_{1/2} \rightarrow 2P_{1/2}$ energy difference a *positive* sign, i.e. $E(2P) - E(2S) > 0$. This is in accord with almost all publications we review here and we will mention explicitly when we have inverted the sign with respect to the original publications where the authors calculated level shifts.

Moreover, we obey the traditional definition of the Lamb shift as the terms beyond the Dirac equation and the leading order recoil corrections, i.e. excluding effects of the hyperfine structure. In particular, this means that the mixing of the hyperfine levels (Sec. 5) does *not* influence the Lamb shift.

The Lamb shift is dependent on the rms charge radius of the nucleus and is treated in Sec. 3. We split the Lamb shift contributions into *nuclear structure-independent* contributions and *nuclear structure-dependent* ones. The latter are composed out of one-photon exchange diagrams which represent the finite size effect and two-photon exchange diagrams which contain the polarizability contributions.

In Sec. 4, we treat the 2S hyperfine structure, which depends on the Zemach radius. It also has two-photon exchange contributions. However, these have not been calculated yet and can only be estimated with a large uncertainty.

In Sec. 5, we compile the 2P level structure which includes fine- and hyperfine splitting, and the mixing of the hyperfine levels [23].

For the theory compilation presented here, we use the calculations from many sources mentioned in the following. The names of the authors of the respective groups are ordered alphabetically.

The first source is E. Borie who was one of the first to publish detailed calculations of many terms involved in the Lamb shift of muonic atoms. Her most recent calculations for μp , μd , $\mu^4\text{He}^+$, and $\mu^3\text{He}^+$

are all found in her Ref. [24]. Several updated versions of this paper are available on the arXiv. In this work we always refer to [25] which is version-7, the most recent one at the time of this writing.

The second source is the group of Elekina, Faustov, Krutov, and Martynenko *et al.* (termed “Martynenko group” in here for simplicity). The calculations we use in here are found in Krutov *et al.* [26] for the Lamb shift, in Martynenko *et al.* [27, 28] and Faustov *et al.* [29] for the 2S hyperfine structure, and Elekina *et al.* [30] for the 2P fine- and hyperfine structure.

Jentschura and Wundt calculated some Lamb shift contributions in their Refs. [31, 32]. They are referred to as “Jentschura” for simplicity.

The group of Ivanov, Karshenboim, Korzinin, and Shelyuto is referred to “Karshenboim group” for simplicity. Their calculations are found in Korzinin *et al.* [33] and in Karshenboim *et al.* [34] for Lamb shift and fine structure contributions.

The group of Bacca, Barnea, Hernandez, Ji, and Nevo Dinur, situated at TRIUMF and Hebrew University, has performed *ab initio* calculations on two-photon exchange contributions of the Lamb shift. Their calculations are found in Nevo Dinur *et al.* [11] and Hernandez *et al.* [21]. For simplicity we refer to them as “TRIUMF-Hebrew group”.

A recent calculation of the two-photon exchange using scattering data and dispersion relations has been performed by Carlson, Gorchtein, and Vanderhaeghen [22].

Item numbers # in our tables follow the nomenclature in Refs. [1, 2]. In the tables, we usually identify the “source” of all values entering “our choice” by the first letter of the (group of) authors given in adjacent columns (e.g. “B” for Borie). We denote as average “avg.” in the tables the center of the band covered by all values v_i under consideration, with an uncertainty of half the spread, i.e.

$$\begin{aligned} \text{avg.} &= \frac{1}{2} [\text{MAX}(v_i) + \text{MIN}(v_i)] \\ &\pm \frac{1}{2} [\text{MAX}(v_i) - \text{MIN}(v_i)]. \end{aligned} \tag{7}$$

If individual uncertainties are provided by the authors we add these in quadrature. We would like to point out that uncertainties due to uncalculated higher order terms are often not indicated explicitly by the authors. In the case some number is given, we include it in our sum. But in general our method can not account for uncertainty estimates of uncalculated higher order terms.

Throughout the paper, Z denotes the nuclear charge with $Z = 2$ for the helion and alpha particle, α is the fine structure constant, $m_r = 199 m_e$ is the reduced mass of the muon-nucleon system. “VP” is short for “vacuum polarization”, “SE” is “self-energy”, “RC” is “recoil correction”. “Perturbation theory” is abbreviated as “PT”, and SOPT and TOPT denote 2nd and 3rd order perturbation theory, respectively.

3. Lamb shift in muonic helium-3

3.1. Nuclear structure independent contributions

Nuclear structure independent contributions have been calculated by Borie, Martynenko group, Karshenboim group, and Jentschura. The contributions are listed in Tab. 1, labeled with # i . The leading contribution is the one-loop electron vacuum polarization (eVP) of order $\alpha(Z\alpha)^2$, the so-called Uehling term (see Fig. 2). It accounts for 99.5% of the radius-independent part of the Lamb shift, so it is very important that this contribution is well understood. There are two different approaches to calculate this term.

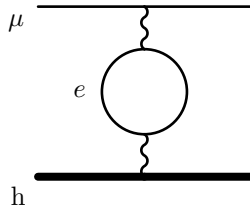


Figure 2: Item #1, the leading order 1-loop electron vacuum polarization (eVP), also called Uehling term.

Borie [25] (p. 4, Tab.) and the Karshenboim group [33] (Tab. I) use relativistic Dirac wavefunctions to calculate a relativistic Uehling term (item #3). A relativistic recoil correction (item #19) has to be added to allow comparison to nonrelativistic calculations (see below). Borie provides the value of this correction explicitly in [25] Tab. 6, whereas the Karshenboim group only gives the total value which includes the correction, thus corresponding to (#3 + #19).

Nonrelativistic calculations of the Uehling term (item #1) exist from the Martynenko group [26] (No. 1, Tab. 1) and Jentschura [32], which are in very good agreement. Additionally, a relativistic correction (item #2) has to be applied. This relativistic correction already accounts for relativistic recoil effects (item #19). Item #2 has been calculated by the Martynenko group [26] (No. 7+10, Tab. 1), Borie [25] (Tab. 1), Jentschura [32, 31] (Eq. 17), and Karshenboim *et al.* [34], which agree well within all four groups, however do not have to be included in Borie's and Korzinin *et al.*'s value because their relativistic Dirac wavefunction approach already accounts for relativistic recoil effects.

Both approaches agree well within the required uncertainty. As *our choice* for the Uehling term with relativistic correction (#1 + #2) or (#3 + #19) we take the average

$$\Delta E(\text{Uehling} + \text{rel. corr.}) = 1642.3962 \pm 0.0018 \text{ meV}. \quad (8)$$

Item #4, the second largest contribution in this section, is the two-loop eVP of order $\alpha^2(Z\alpha)^2$, the so-called Källén-Sabry term [35] (see Fig. 3). It has been calculated by Borie [25] (p. 4, Tab.) and the Martynenko group [26] (No. 2, Tab. 1) which agree within 0.0037 meV. As *our choice* we take the average.

Item #5 is the one-loop eVP in two Coulomb lines of order $\alpha^2(Z\alpha)^2$ (see Fig. 4). It has been calculated by Borie [25] (Tab. 6), the Martynenko group [26] (No. 9, Tab. 1), and Jentschura [31] (Eq. 13) of whom the latter two obtain the same result, which differs from Borie by 0.0033 meV. As *our choice* we adopt the average.

The Karshenboim group [33] (Tab. I) has calculated the sum of item #4 and #5, the two-loop eVP (Källén-Sabry) and one-loop eVP in two Coulomb lines (Fig. 3 and 4). Good agreement between all groups is observed.

Item #6+7 is the third order eVP of order $\alpha^3(Z\alpha)^2$. It has been calculated by the Martynenko group [26] (No. 4+11+12, Tab. 1) and the Karshenboim group [33] (Tab. I). Borie [25] (p. 4) adopts the value from Karshenboim *et al.*. Martynenko *et al.* and Karshenboim *et al.* differ by 0.004 meV, which is in agreement considering the uncertainty of 0.003 meV given by the Martynenko group. As *our choice* we adopt the average and obtain an uncertainty of 0.0036 meV via Gaussian propagation of uncertainty.

Item #29 is the second order eVP of order $\alpha^2(Z\alpha)^4$. It has been calculated by the Martynenko group [26] (No. 8+13, Tab. 1) and the Karshenboim group [33] (Tab. VIII). Their values did agree in the case of μd ,

however for $\mu^3\text{He}^+$ they differ by 0.004 meV. This difference is twice as large as the value from Martynenko *et al.* but this contribution is small, so the uncertainty is not at all dominating. We reflect the difference by adopting the average as *our choice*.

Items #9, #10, and #9a are the terms of the Light-by-light (LbL) scattering contribution (see Fig. 5). The sum of the LbL terms is calculated by the Karshenboim group [33] (Tab. I). Borie [25] also lists the value from Karshenboim *et al.*. Item #9 is the *Wichmann-Kroll* term, or “1:3” LbL, which is of order $\alpha(Z\alpha)^4$. This item has also been calculated by Borie [25] (p. 4) and the Martynenko group [26] (No. 5, Tab. 1) who obtain the same result. Item #10 is the *virtual Delbrück* or “2:2” LbL, which is of order $\alpha^2(Z\alpha)^3$. Item #9a is the *inverted Wichmann-Kroll* term, or “3:1” LbL, which is of order $\alpha^3(Z\alpha)^2$. The sum of the latter two is also given by the Martynenko group [26] (No. 6, Tab. 1). As *our choice* we use the one from Karshenboim *et al.*, who are the first and only group to calculate all three LbL contributions. The groups are in agreement when taking into account the uncertainty of 0.0006 meV given by Karshenboim *et al.*.

Item #20 is the contribution from muon self-energy (μSE) and muon vacuum polarization (μVP) of order $\alpha(Z\alpha)^4$ (see Fig. 6). This item constitutes the third largest term in this section ². This item has been calculated by Borie [25] (Tab. 2, Tab. 6) and the Martynenko group [26] (No. 24, Tab. 1). They differ by 0.001 meV. As *our choice* we adopt the average.

Items #11, #12, #30, #13, and #31 are all corrections to VP or μSE and of order $\alpha^2(Z\alpha)^4$.

Item #11 is the μSE correction to eVP (see Fig. 7). It has been calculated by all four groups. Martynenko *et al.* calculate this term (Eq. 99) in [26], however in their table (No. 28) they use the more exact calculation from Jentschura. Jentschura [31] (Eq. 29), and the Karshenboim group [33] (Tab. VIII a) are in excellent agreement. Borie [25] (Tab. 16) differs significantly because she only calculates a part of this contribution in her App. C. This value does not enter her sum and thus is also not considered in here. On p. 12 of [25] she states that this value should be considered as an uncertainty. As *our choice* we adopt the number from Jentschura and Karshenboim *et al.*.

Item #12 is the eVP in μSE (see Fig. 8). This item has been calculated by the Martynenko group [26] (No. 27, Tab. 1) and the Karshenboim group [33] (Tab. VIII d), which are in perfect agreement. On p. 10 of [25] Borie mentions that she included the “fourth order electron loops” in “muon Lamb shift, higher order” term, which is our item #21. As we include item #21 from Borie, we will not on top include item #12.

Item #30 is the hadronic vacuum polarization (hVP) in μSE (see Fig. 9). This item has only been

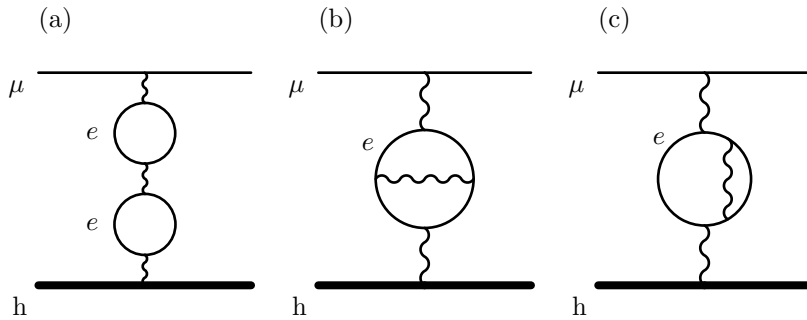


Figure 3: Item #4, the two-loop eVP (Källen-Sabry) contribution. This is Fig. 1 (b,c,d) from the Martynenko group [26].

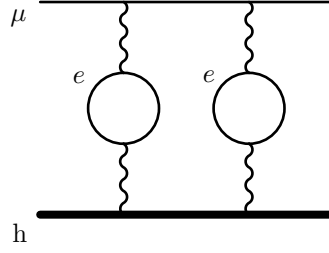


Figure 4: Item #5, the one-loop eVP in 2-Coulomb lines.

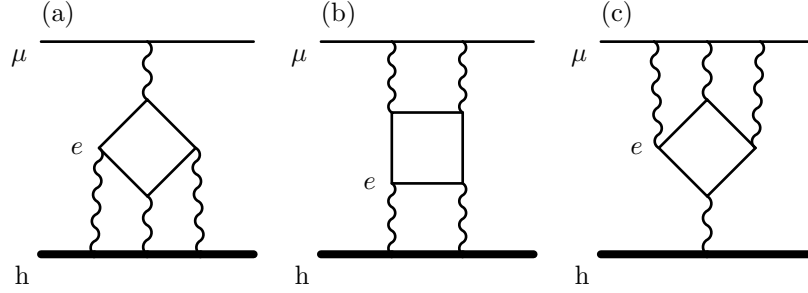


Figure 5: The three contributions to Light-by-light scattering: (a) Wichmann-Kroll or “1:3” term, item #9, (b) Virtual Delbrück or “2:2” term, item #10, and (c) inverted Wichmann-Kroll or “3:1” term, item #9a[†].

calculated by the Karshenboim group [33] (Tab. VIII e) which we adopt as *our choice*.

Item #13 is the mixed $eVP + \mu VP$ (see Fig. 10). The calculations from Borie [25] (p. 4) and the Martynenko group [26] (No. 3, Tab. 1) roughly agree, whereas the value from the Karshenboim group [33] (Tab. VIII b) is 0.002 meV larger. As *our choice* we take the average.

Item #31 is the mixed $eVP + hVP$ (see Fig. 11) which has only been calculated by the Karshenboim group [33] (Tab. VIII c). We adopt their value as *our choice*.

Item #32, the muon VP in SE correction shown in Fig. 12 is not included as a separate item in our Tab. 1. It should already be automatically included in the QED contribution which has been rescaled from the QED of electronic ${}^3\text{He}^+$ by a simple mass replacement $m_e \rightarrow m_\mu$ [38]. This is the case only for QED contributions where the particle in the loop is the same as the bound particle - like in this case, a muon VP correction in a muonic atom. The size of this item #32 can be estimated from the relationship found by Borie [39], that the ratio of hadronic to muonic VP is 0.66. With the Karshenboim group’s value of item #30 [33] one would obtain a value for item #32 of $-0.0004/0.66 \text{ meV} = -0.0006 \text{ meV}$. This contribution is contained in our item #21, together with the dominating item #12 (see also p. 10 of Ref. [25]).

Item #21 is a higher-order correction to μSE and μVP of order $\alpha^2(Z\alpha)^4$ and $\alpha^2(Z\alpha)^6$. This item has only been calculated by Borie [25] (Tab. 2, Tab. 6). On p. 10 she points out that this contribution includes the “fourth order electron loops”, which is our item #12. It also contains our item #32. We adopt her value as *our choice*.

Item #14 is the hadronic VP of order $\alpha(Z\alpha)^4$. It has been calculated by Borie [25] (Tab. 6) and the Martynenko group [26] (No. 29, Tab. 1). Borie assigns a 5% uncertainty to their value. However, in her Ref. [25] there are two different values of item #14, the first on p. 5 (0.219 meV) and the second in Tab. 6 on p. 16 (0.221 meV). Regarding the given uncertainty this difference is not of interest. In our Tab. 1, we report the larger value which is further from that of the Martynenko group in order to conservatively reflect the

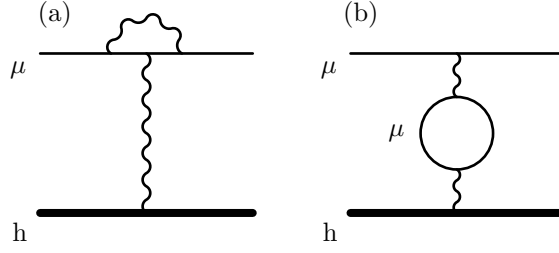


Figure 6: Item #20, the muon-self energy (a) and the muon vacuum polarization (b), $\alpha(Z\alpha)^4$.

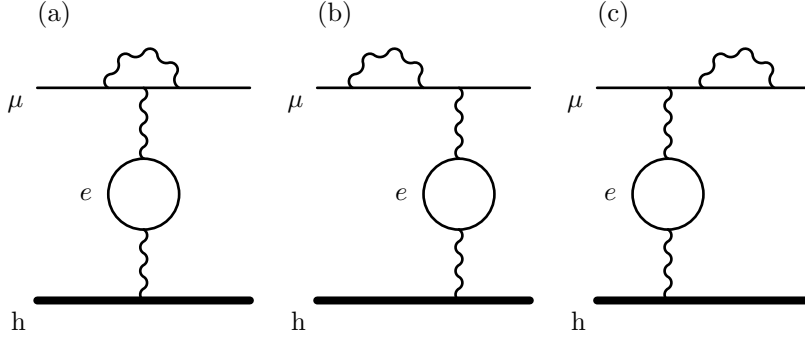


Figure 7: Item #11, muon self-energy corrections to the electron vacuum polarization $\alpha^2(Z\alpha)^4$. This figure is Fig. 2 from Jentschura [36]. It corresponds to Fig. 6(a) from Karshenboim [33].

scatter. Martynenko *et al.* did not assign an uncertainty to their value. However, for μd [40] they estimated an uncertainty of 5%. As *our choice* we take the average of their values and adopt the uncertainty of 5% (0.011 meV).

Item #17 is the Barker-Glover correction [41]. It is a recoil correction of order $(Z\alpha)^4 m_r^3/M^2$ and includes the nuclear Darwin-Foldy term that arises due to the Zitterbewegung of the nucleus. As already discussed in App. A of [2], we follow the atomic physics convention [42], which is also adopted by CODATA in their report from 2010 [43] and 2014 [7]. This convention implies that item #17 is considered as a recoil correction to the energy levels and not as a part of the rms charge radius. This term has been calculated by Borie [25] (Tab. 6), the Martynenko group [26] (No. 21, Tab. 1), and Jentschura [32] and [31] (Eq. A.3). As *our choice* we use the number given by Borie and Jentschura as they give one more digit.

Item #18 is the term called “recoil, finite size” by Borie. It is of order $(Z\alpha)^5 \langle r \rangle_{(2)}/M$ and is linear in the *first* Zemach moment. It has first been calculated by Friar [44] (see Eq. F5 in App. F) for hydrogen and has later been given by Borie [25] for μd , $\mu^4\text{He}^+$, and $\mu^3\text{He}^+$. We discard item #18 because it is considered to be included in the elastic TPE [45, 46]. It has also been discarded in μp [1], μd [2], and $\mu^4\text{He}^+$ [3]. For the muonic helium-3 ion, item #18 in [25] (Tab. 6) amounts to 0.4040 meV, which is ten times larger than the experimental uncertainty of about 0.04 meV (see Eq. 5), so it is important that the treatment of this contribution is well understood.

Item #22 and #23 are relativistic recoil corrections of order $(Z\alpha)^5$ and $(Z\alpha)^6$, respectively. Item #22 has been calculated by Borie [25] (Tab. 6), the Martynenko group [26] (No. 22, Tab. 1), and Jentschura [31] (Eq. 32). They agree perfectly. Item #23 has only been calculated by the Martynenko group [26] (No. 23, Tab. 1) whose value we adopt as *our choice*.

Item #24 are higher order radiative recoil corrections of order $\alpha(Z\alpha)^5$ and $(Z^2\alpha)(Z\alpha)^4$. This item has

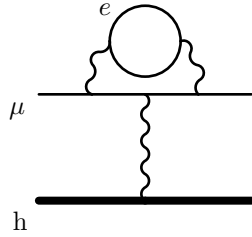


Figure 8: Item #12, eVP loop in SE are radiative corrections with VP effects. This is Fig. 11(b) from a publication by the Martynenko group [26] which is the same as Fig. 4 in Pachucki [37]. It is Karshenboim's Fig. 6(d) in Ref. [33].

been calculated by Borie [25] (Tab. 6) and the Martynenko group [26] (No. 25, Tab. 1). Their values differ by 0.015 meV. As *our choice* we adopt the average.

Item #28 is the radiative (only eVP) recoil of order $\alpha(Z\alpha)^5$. It consists of three terms which have been calculated by Jentschura and Wundt [31] (Eq. 46). We adopt their value as *our choice*. Note that a second value (0.0072 meV) is found in [32]. However, this value is just one of the three terms, namely the seagull term, and is already included in #28 (see [31], Eq. 46).

The total sum of the QED contributions without explicit nuclear structure dependence is summarized in Tab. 1 and amounts to

$$\Delta E_{r\text{-indep.}}^{\text{LS}} = 1644.3466 \pm 0.0146 \text{ meV}. \quad (9)$$

Note that Borie, on p. 15 in Ref. [25] attributes an uncertainty of 0.6 meV to her total sum. The origin of this number remains unclear. Its order of magnitude is neither congruent with the other uncertainties given in Ref. [25] nor with other uncertainties collected in our summary. Thus it will not be taken into account.

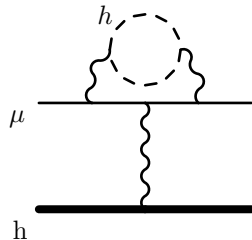


Figure 9: Item #30, hadronic VP in SE contribution, corresponds to Fig. 6(e) in Karshenboim *et al.*'s [33].

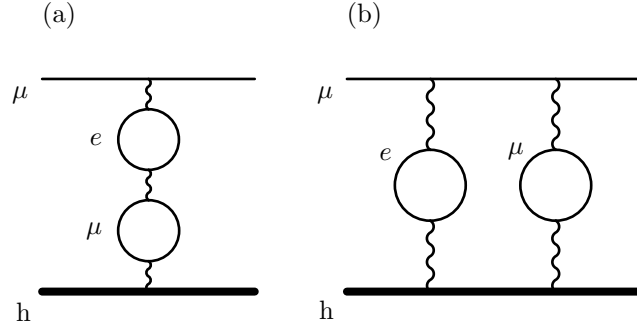


Figure 10: Item #13, the mixed eVP- μ VP contribution.

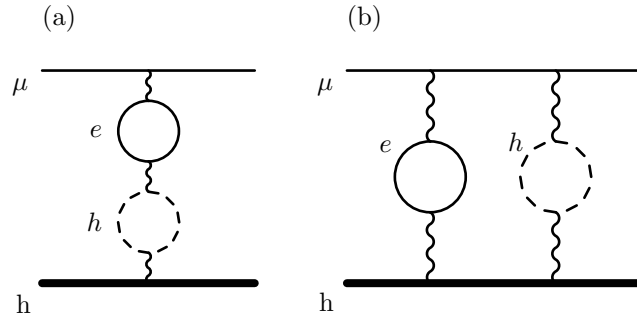


Figure 11: Item #31, the mixed eVP- and hadronic VP contribution, comes from the Uehling correction to the hadronic VP correction. See Fig. 6(c) in Karshenboim *et al.*'s [33].

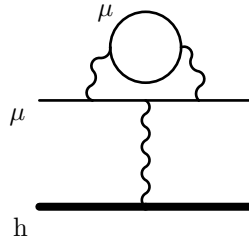


Figure 12: Item #32, muon VP in SE contribution, is automatically included in a rescaled electronic ${}^3\text{He}^+$ QED value of higher order SE contributions (see text).

Table 1: All known **nuclear structure-independent** contributions to the Lamb shift in $\mu^3\text{He}^+$. Values are in meV. Item numbers “#” in the 1st column follow the nomenclature of Refs. [1, 2], which in turn follow the supplement of Ref. [4]. Items “#” with a dagger † were labeled “New” in Ref. [1], but we introduced numbers in Ref. [2] for definiteness. For Borie [25] we refer to the most recent arXiv version-7 which contains several corrections to the published paper [24] (available online 6 Dec. 2011). For Martynenko *et al.*, numbers #1 to #29 refer to rows in Tab. I of Ref. [26]. Numbers in parentheses refer to equations in the respective paper.

#	Contribution	Borie (B) [25]	Martynenko group (M) Krutov <i>et al.</i> [26]	Jentschura (J) Jentschura, Wundt [31] Jentschura [32]	Karshenboim group (K) Karshenboim <i>et al.</i> [34] Korzinin <i>et al.</i> [33]	Our choice value source Fig.
1	NR one-loop electron VP (eVP)		1641.8862 #1	1641.885 [32]		
2	Rel. corr. (Breit-Pauli)	(0.50934) ^a Tab. 1	0.5093 #7+#10	0.509344 [31](17), [32]	(0.509340) [34] Tab. IV	
3	Rel. one-loop eVP	1642.412 Tab. p. 4				
19	Rel. RC to eVP, $\alpha(Z\alpha)^4$	−0.0140 Tab. 1+6				
	Sum of the above	1642.3980 3+19	1642.3955 1+2	1642.3943 1+2	1642.3954 [33] Tab. I	1642.3962 \pm 0.0018 avg. 2
4	Two-loop eVP (Källén-Sabry)	11.4107 Tab. p. 4	11.4070 #2			11.4089 \pm 0.0019 avg. 3
5	One-loop eVP in 2-Coulomb lines $\alpha^2(Z\alpha)^2$	1.674 Tab. 6	1.6773 #9	1.677290 [31](13)		1.6757 \pm 0.0017 avg. 4
	Sum of 4 and 5	13.0847 4+5	13.0843 4+5		13.0843 [33] Tab. I	(13.0846) ^b
6+7	Third order VP	0.073(3) p. 4	0.0689 #4+#12+#11		0.073(3) [33] Tab. I	0.0710 \pm 0.0036 avg.
29	Second-order eVP contribution $\alpha^2(Z\alpha)^4 m$		0.0018 #8+#13		0.00558 [33] Tab. VIII “eVP2”	0.0037 \pm 0.0019 avg.
9	Light-by-light “1:3”: Wichmann-Kroll	−0.01969 p. 4	−0.0197 #5			5a
10	Virtual Delbrück, “2:2” LbL		} 0.0064 #6			5b
9a [†]	“3:1” LbL					5c
	Sum: Total light-by-light scatt.	−0.0134(6) p.5+Tab.6	−0.0133 9+10+9a		−0.0134(6) [33] Tab. I	−0.0134 \pm 0.0006 K
20	μSE and μVP	−10.827368 Tab. 2+6	−10.8286 #24			−10.8280 \pm 0.0006 avg. 6
11	Muon SE corr. to eVP $\alpha^2(Z\alpha)^4$	(−0.1277) ^c Tab. 16	−0.0627 #28	−0.06269 [31](29)	−0.06269 [33] Tab. VIII (a)	−0.06269 J, K 7
12	eVP loop in self-energy $\alpha^2(Z\alpha)^4$	incl. in 21	−0.0299 #27		−0.02992 [33] Tab. VIII (d)	incl. in 21 B 8
30	Hadronic VP loop in self-energy $\alpha^2(Z\alpha)^4 m$				−0.00040(4) [33] Tab. VIII (e)	−0.00040 \pm 0.00004 K 9
13	Mixed eVP + μVP	0.00200 p. 4	0.0022 #3		0.00383 [33] Tab. VIII (b)	0.0029 \pm 0.0009 avg. 10
31	Mixed eVP + hadronic VP				0.0024(2) [33] Tab. VIII (c)	0.0024 \pm 0.0002 K 11
21	Higher-order corr. to μSE and μVP	−0.033749 Tab. 2+6				−0.033749 B
	Sum of 12, 30, 13, 31, and 21	−0.031749 13+21	−0.0277 12+13		−0.0241(2) 12+30+13+31	−0.0288 sum
14	Hadronic VP	0.221(11) Tab. 6	0.2170 #29			0.219 \pm 0.011 avg.
17	Recoil corr. $(Z\alpha)^4 m_r^3/M^2$ (Barker-Glover)	0.12654 Tab. 6	0.1265 #21	0.12654 [31](A.3) [32](15)		0.12654 B, J
18	Recoil, finite size	(0.4040(10)) ^d				
22	Rel. RC $(Z\alpha)^5$	−0.55811 p.9+Tab.6	−0.5581 #22	−0.558107 [31](32)		−0.558107 J
23	Rel. RC $(Z\alpha)^6$		0.0051 #23			0.0051 M
24	Higher order radiative recoil corr.	−0.08102 p.9+Tab.6	−0.0656 #25			−0.0733 \pm 0.0077 avg.
28 [†]	Rad. (only eVP) RC $\alpha(Z\alpha)^5$			0.004941		0.004941 J
	Sum	1644.3916 ^e	1644.3431			1644.3466 \pm 0.0146

^aDoes not contribute to the sum in Borie’s approach.

^bSum of *our choice* of item #4 and #5, written down for comparison with the Karshenboim group.

^cIn App. C of [25], incomplete. Does not contribute to the sum in Borie’s approach, see text.

^dIs not included, because it is a part of the TPE, see text.

^eIncluding item #18 and #r3’ yields 1644.9169 meV, which is Borie’s value from Ref. [25] page 15. On that page she attributes an uncertainty of 0.6 meV to that value. This number is far too large to be correct, so we ignore it.

3.2. Nuclear structure contributions

Terms that depend on the nuclear structure are separated into one-photon exchange (OPE) contributions and two-photon exchange (TPE) contributions.

The OPE terms (also called *radius-dependent contributions*) represent the finite size effect which is by far the largest part of the nuclear structure contributions and are discussed in Sec. 3.2.1. They are parameterizable with a coefficient times the rms charge radius squared. These contributions are QED interactions with nuclear form factor insertions.

The TPE terms can be written as a sum of elastic and inelastic terms, where the latter describe the polarizability of the nucleus. These involve contributions from strong interaction and therefore are much more complicated to evaluate, which explains why the dominant uncertainty originates from the TPE part. The TPE contributions are discussed in more detail in Sec. 3.2.2.

The main nuclear structure corrections to the nS states have been given up to order $(Z\alpha)^6$ by Friar [44] (see Eq. (43a) therein)

$$\Delta E_{\text{fin.size}} = \frac{2\pi Z\alpha}{3} |\Psi(0)|^2 \left(\langle r^2 \rangle - \frac{Z\alpha m_r}{2} \langle r^3 \rangle_{(2)} + (Z\alpha)^2 (F_{\text{REL}} + m_r^2 F_{\text{NREL}}) \right), \quad (10)$$

where $\Psi(0)$ is the muon wave function at the origin, $\langle r^2 \rangle$ is the second moment of the charge distribution of the nucleus, i.e. the square of the rms charge radius, r_E^2 . $\langle r^3 \rangle_{(2)}$ is the Friar moment³, and F_{REL} and F_{NREL} contain various moments of the nuclear charge distribution (see Eq. (43b) and (43c) in Ref. [44]). Analytic expressions for some simple model charge distributions are listed in App. E of Ref. [44].

As the Schrödinger wavefunction at the origin $\Psi(0)$ is nonzero only for S states, it is in leading order only the S states which are affected by the finite size. However, using the Dirac wavefunction a nonzero contribution appears for the $2P_{1/2}$ level [48]. This contribution affects the values for the Lamb shift and the fine structure and is taken into account in the section below.

The Friar moment $\langle r^3 \rangle_{(2)}$ has not been included in μd [2] because of a cancellation [49, 50, 51] with a part of the inelastic nuclear polarizability contributions. However, for $\mu^3\text{He}^+$, it is favorable to calculate each term individually in order to achieve the smallest uncertainty. This has been done by the TRIUMF-Hebrew group [11, 21] and will be discussed in Sec. 3.2.2.

3.2.1. One-photon exchange contributions (finite size effect)

Finite size contributions have been calculated by Borie ([25] Tab. 14), the Martynenko group ([26] Tab. 1), and the Karshenboim group ([34] Tab. III). All of these contributions are listed in Tab. 2, labeled with #ri.

Most of the terms, given in Tab. 2, can be parameterized as $c \cdot r_E^2$ with coefficients c in units of meV fm^{-2} . Borie and Karshenboim *et al.* have provided the contributions in this parameterization, whereas Martynenko *et al.* provide the total value in units of energy. However, the value of their coefficients can be obtained by dividing their numbers by r_E^2 . The value they used for the charge radius r_E is 1.9660 fm ⁴ [53]. In this way the numbers from Martynenko *et al.* can be compared with the ones from the other groups.

Item #r1, the leading term of Eq. (10), is the one-photon exchange with a helion form factor (FF) insertion (see Fig. 13). Item #r1 is of order $(Z\alpha)^4 m_r^3$ and accounts for 99% of the OPE contributions. Borie

³ $\langle r^3 \rangle_{(2)}$ has been called “third Zemach moment” in [44]. To avoid confusion with the Zemach radius r_Z in the 2S hyperfine structure we adopt the term “Friar moment”, as recently suggested by Karshenboim *et al.* [47].

⁴This value has been introduced by Borie [25] as an average of several previous measurements [52, 13, 14].

([25] Tab. 14, b_a), the Martynenko group ([26] No. 14), and the Karshenboim group ([34] Tab. III, $\Delta_{FNS}^{(0)}$) obtain the same result which we adopt as *our choice*. This contribution is much larger than the following terms, but its absolute precision is worse, which we indicate by introducing an uncertainty. For that we take the value from Borie which is given with one more digit than the values of the other authors and attribute an uncertainty of 0.0005 meV, which may arise from rounding.

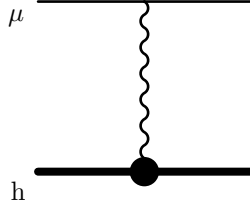


Figure 13: Item (r1), the leading nuclear finite size correction stems from a one-photon interaction with a helion form factor insertion, indicated by the thick dot.

Item #r2 is the radiative correction of order $\alpha(Z\alpha)^5$. The equation used for the calculation of this contribution is given in Eq. (10) of [54]. It has been calculated by Borie [25] (Tab. 14, b_b) and the Martynenko group [26] (No. 26, only Eq. (92)). Both get the same result, which we adopt as *our choice*. Note that the value from the Martynenko group was published with a wrong sign.

Item #r3 and #r3' are the finite size corrections of order $(Z\alpha)^6$. They have first been calculated in Ref. [44]. Item #r3 and #r3' consider third-order perturbation theory in the finite size potential correction and relativistic corrections of the Schrödinger wave functions. There are also corrections in the TPE of the same order $(Z\alpha)^6$, but these are of different origin. Borie [25] (Tab. 14, b_c and Tab. 6) and the Martynenko group [26] (Eq. (91)) follow the procedure in Ref. [44] and then separate their terms into a part with an explicit r_E^2 dependence (item #r3) and another one which is usually evaluated with an exponential charge distribution, since a model independent calculation of this term is prohibitively difficult [25]. Differences in sorting the single terms have already been noticed in the μd case [2], where we mentioned that e.g. the term $\langle r^2 \rangle \langle \ln(\mu r) \rangle$ in F_{REL} of Eq. 10 is attributed to #r3 and #r3' by Martynenko *et al.* and Borie, respectively. The difference in this case amounts to 0.007 meV for #r3'. Note that in Eq. (91) from the Martynenko group [26], the charge radius has to be inserted in units of GeV^{-1} , with $r_E = 1.966 \text{ fm} \hat{=} 9.963 \text{ GeV}^{-1}$.

Item #r4 is the one-loop eVP correction (*Uehling*) of order $\alpha(Z\alpha)^4$. It has been calculated by all three groups, Borie [25] (Tab. 14, b_d), Martynenko *et al.* [26] (No. 16, Eq. (69)), and Karshenboim *et al.* [34] (Tab. III, $\Delta E_{FNS}^{(2)}$). On p. 31 of [25], Borie notes that she included the correction arising from the Källén-Sabry potential in her b_d . This means that her value already contains item #r6, which is the two-loop eVP correction of order $\alpha^2(Z\alpha)^4$. Item #r6 has been given explicitly only by the Martynenko group [26] (No. 18, Eq. 73). The sum of Martynenko *et al.*'s #r4 and #r6 differs by 0.016 meV/fm² from Borie's result. Using a charge radius of 1.9660 fm this corresponds to roughly 0.06 meV and, hence, causes the largest uncertainty in the radius-dependent OPE part. The origin of this difference is not understood, but should be clarified. As *our choice* we take the average of the sum (#r4+#r6) of these two groups. The resulting average does also reflect the value for #r4 provided by Karshenboim *et al.* [34].

Item #r5 is the one-loop eVP correction (*Uehling*) in second order perturbation theory (SOPT) of order $\alpha(Z\alpha)^4$. It has been calculated by all three groups, Borie [25] (Tab. 14, b_e), the Martynenko group [26] (No. 17, Eq. 70), and the Karshenboim group [34] (Tab. III, $\Delta E_{FNS}^{(1)}$). On p. 31 of [25], Borie notes that

she included the two-loop corrections to ϵ_{VP2} in her b_e . This means that her value already contains item #r7, which is the two-loop eVP in SOPT of order $\alpha^2(Z\alpha)^4$. Item #r7 has only been given explicitly by the Martynenko group [26] (No.19). The sum of Martynenko *et al.*'s #r5+#r7 differs by 0.003 meV from Borie's result. As *our choice* we take the average of the sum (#r5+#r7) of these two groups. Again here, *our choice* reflects the value for #r5 provided by Karshenboim *et al.* [34], too.

Item #r8 is the finite size correction to the $2P_{1/2}$ level of order $(Z\alpha)^6$. It has only been calculated by Borie [25] (Tab. 14, $b(2p_{1/2})$). This correction is the smallest in this section and is the only term which affects the $2P_{1/2}$ level. In consequence, the effect on the Lamb shift is inverse, i.e. if the $2P$ level is lifted "upwards", the Lamb shift gets larger. Thus, in contrast to Borie, we include this correction with a positive sign. At the same time this term decreases the fine structure ($2P_{3/2} - 2P_{1/2}$ energy difference) and is hence listed in Tab. 4 as item #f10 with a negative sign.

The total sum of the QED contributions with an explicit dependence of r_E^2 is summarized in Tab. 2 and amounts to

$$\Delta E_{r-\text{dep.}}^{\text{LS}}(r_E^2) = -103.5184(98) \text{ meV fm}^{-2} r_E^2 + 0.1177(33) \text{ meV}. \quad (11)$$

Table 2: Coefficients of the **nuclear structure-dependent** OPE contributions to the Lamb shift of $\mu^3\text{He}^+$. The values from the Martynenko group shown here are the published ones divided by $(1.9660\text{ fm})^2$, which is the radius they used. KS: Källén-Sabry, VP: vacuum polarization, SOPT: second-order perturbation theory. Values are in meV/fm^2 , except for $\#r3'$.

#	Contribution	Borie (B)		Martynenko group (M)		Karshenboim group (K)		Our choice	
		Borie [25] Tab.14		Krutov <i>et al.</i> [26]		Karshenboim <i>et al.</i> [34]		value	source
r1	Leading fin. size corr., $(Z\alpha)^4$	-102.520	b_a	-102.52	#14, (61)	-102.52	$\Delta E_{FNS}^{(0)}$	-102.520 \pm 0.0010	B,M,K
r2	Radiative corr., $\alpha(Z\alpha)^5$	-0.0243 ^a	b_b	-0.0243 ^b	#26, (92)			-0.0243	B,M
r3	Finite size corr. order $(Z\alpha)^6$	-0.1275	b_c	-0.1301	#26, (91)			-0.1288 \pm 0.0013	avg.
r4	Uehling corr. (+KS), $\alpha(Z\alpha)^4$			-0.3310	#16, (69)	-0.323	$\Delta E_{FNS}^{(2)}$		
r6	Two-loop VP corr., $\alpha^2(Z\alpha)^4$			-0.0026	#18, (73)				
sum	r4+r6	-0.3176	b_d	-0.3336				-0.3256 \pm 0.0080	avg.
r5	One-loop VP in SOPT, $\alpha(Z\alpha)^4$			-0.5196	#17, (70)	-0.520	$\Delta E_{FNS}^{(1)}$		
r7	Two-loop VP in SOPT, $\alpha^2(Z\alpha)^4$			-0.0063	#19 ^c				
sum	r5+r7	-0.5217	b_e	-0.5259				-0.5238 \pm 0.0021	avg.
r8	Corr. to the $2P_{1/2}$ level	0.00409 ^d	$b(2p_{1/2})$					0.00409	B
	Sum of coefficients	-103.507(5) ^e		-103.5339		-103.37	ΔE_{FNS}	-103.5184 \pm 0.0098 ^f	
r3'	Remaining order $(Z\alpha)^6$ [meV] ^g	0.121 meV	Tab. 6	0.11445 meV	(91)			0.1177 \pm 0.0033	avg.
	Sum	$-103.507\ r_h^{-2} + 0.121\text{ meV}$		$-103.5368\ r_h^{-2} + 0.11445\text{ meV}$		$-103.37\ r_h^{-2}$		-103.5184(98) $r_h^{-2} + 0.1177(33)\text{ meV}$	

^aBorie uses Eq. (10) of [54] to calculate this term. For further explanations, see text.

^bThe value in Eq. 92 of [26] was published with a wrong sign.

^cThis term is represented by Fig. 9(a,b,c,d) from the Martynenko group [26]. This figure includes equation (76) therein.

^dThe sign is explained in the text.

^eThe summed coefficient is given in Ref. [25] on p. 15, where Borie indicates the uncertainty of 0.005 meV.

^fThis uncertainty is the one obtained from averaging the above values (0.0084 meV) and the one given by Borie in her sum of (0.005 meV) added in quadrature.

^gBelongs to r3. Depends on the charge distribution in a non-trivial way, see text.

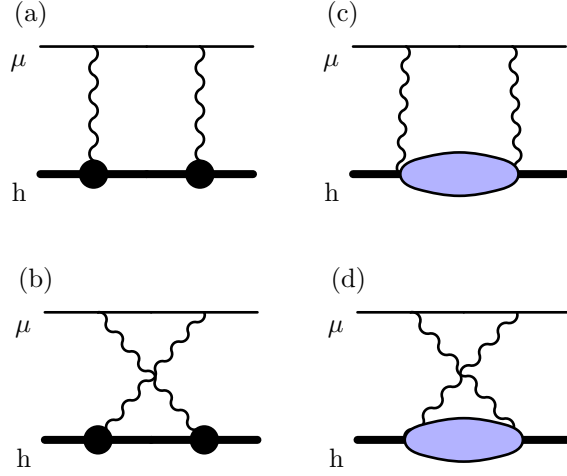


Figure 14: (a)+(b) Elastic $\Delta E_{\text{Friar}}^{\text{LS}}$, and (c)+(d) inelastic $\Delta E_{\text{inelastic}}^{\text{LS}}$ two-photon exchange (TPE) contribution. The thick dots in (a) indicate helion form factor insertions. The blob in (c) and (d) represents all possible excitations of the nucleus.

3.2.2. Two-photon exchange contributions to the Lamb shift

Historically, the two-photon exchange (TPE) contribution to the Lamb shift (LS) in muonic atoms has been considered the sum of the two parts displayed in Fig. 14(a,b) and (c,d), respectively:

$$\Delta E_{\text{TPE}}^{\text{LS}} = \Delta E_{\text{Friar}}^{\text{LS}} + \Delta E_{\text{inelastic}}^{\text{LS}} \quad (12)$$

with the elastic “Friar moment” contribution $\Delta E_{\text{Friar}}^{\text{LS}}$ ⁵ and the inelastic part $\Delta E_{\text{inelastic}}^{\text{LS}}$, frequently termed “polarizability”.

The elastic part, $\Delta E_{\text{Friar}}^{\text{LS}}$ is shown in Fig. 14(a,b). It is sensitive to the shape of the nuclear charge distribution, beyond the leading $\langle r^2 \rangle$ dependence discussed in Sec. 3.2.1. This part is traditionally parameterized as being proportional to the third power of the rms charge radius and it already appeared in Eq. (10) as the second term proportional to $\langle r^3 \rangle_{(2)}$. The coefficient depends on the assumed radial charge distribution.

The inelastic part, $\Delta E_{\text{inelastic}}^{\text{LS}}$ is shown in Fig. 14(c,d). It stems from virtual excitations of the nucleus. The inelastic contributions are notoriously the least well-known theory contributions and limit the extraction of the charge radius from laser spectroscopy of the Lamb shift.

Eq. (12) is valid for the nuclear contributions as well as for the nucleon contributions. This means that elastic and inelastic parts have to be evaluated for both, respectively.

The nuclear parts of $\Delta E_{\text{TPE}}^{\text{LS}}$ are then given as $\delta E_{\text{Friar}}^A$ and $\delta E_{\text{inelastic}}^A$ for a nucleus with A nucleons, and the nucleon parts as $\delta E_{\text{Friar}}^N$ and $\delta E_{\text{inelastic}}^N$.

With that, the total (nuclear and nucleon) TPE is given as⁶

$$\Delta E_{\text{TPE}}^{\text{LS}} = \delta E_{\text{Friar}}^A + \delta E_{\text{Friar}}^N + \delta E_{\text{inelastic}}^A + \delta E_{\text{inelastic}}^N. \quad (13)$$

We refer here to two calculations of the TPE contributions. The first stems from the TRIUMF-Hebrew group, who perform *ab initio* calculations using two different nuclear potentials. They have published two

⁵formerly known as “third Zemach moment”, but see footnote ³ on p.12 for disambiguation.

⁶Compared to the notation of the TRIUMF-Hebrew group [11], the terms in Eq. (13) correspond to δE_{Zem}^A , δE_{Zem}^N , δE_{pol}^A , and δE_{pol}^N , respectively.

papers on the TPE in muonic helium-3 ions, Nevo Dinur *et al.* [11], and Hernandez *et al.* [21]. The second calculation has been performed by Carlson *et al.* [22], who obtain the TPE from inelastic structure functions via dispersion relations.

The two calculations are very different, so that comparisons of any but the total value may be inexact [22]. An attempt to compare the different approaches is given in Tab. II of Ref. [22]. Here, we want to refer to this table only and later compare the total values as suggested. Note that we proceed differently to our previous compilation for μd [2] (Tab. 3), where we listed and compared 16 individual terms (labeled #p1...16) which together yield the sum of the four terms of Eq. (13).

The nuclear Friar moment contribution is calculated by the TRIUMF-Hebrew group to be $\delta E_{\text{Friar}}^A = 10.49(24)$ meV [11, 21]. This value is more reliable than previous values which have been given by Borie [25] (10.258(305) meV) and Krutov *et al.* [26] (10.28(10) meV) using a Gaussian charge distribution and assuming an rms radius of 1.966(10) fm. The value of the TRIUMF-Hebrew group is in agreement with the result of 10.87(27) meV obtained using Eq. (2) in Ref. [11] and the third Zemach moment $\langle r^3 \rangle_{(2)} = 28.15(70)$ fm³ of Sick from electrons scattering off ³He [55].

The nuclear polarizability contribution from the TRIUMF-Hebrew group is $\delta E_{\text{inelastic}}^A = 4.16(17)$ meV [11, 21]. The first calculation of the nuclear polarizability contribution in $\mu^3\text{He}^+$ has been published in 1961 [56]. The recent value from the TRIUMF-Hebrew group replaces a former one of 4.9(1.0) meV from Borie and Rinker [57] which has been used for more than 25 years now.

As mentioned before, the total TPE contribution has a nuclear part and a nucleon part. The nucleon Friar moment contribution from the TRIUMF-Hebrew group amounts to $\delta E_{\text{Friar}}^N = 0.52(3)$ meV. They obtained this value using $\delta E_{\text{Friar}}^N$ from μp and scaling it according to Eq. (17) in their Ref. [11]. This procedure has been done before in [2] for μd . The nucleon polarizability contribution from the TRIUMF-Hebrew group amounts to $\delta E_{\text{inelastic}}^N = 0.28(12)$ meV [11, 21]. This value includes the *proton & neutron subtraction terms* $\delta_{\text{subtraction}}^{p,n}$ taken from Ref. [58].

Summing up all nuclear and nucleon contributions, evaluated by the TRIUMF-Hebrew group [11, 21], yields a total value of the $\Delta E_{\text{TPE}}^{\text{LS}}$ of [11, 21]

$$\Delta E_{\text{TPE}}^{\text{LS}}(\text{nuclear potentials}) = \delta E_{\text{Friar}}^A + \delta E_{\text{Friar}}^N + \delta E_{\text{inelastic}}^A + \delta E_{\text{inelastic}}^N = 15.46(39) \text{ meV}. \quad ^7 \quad (14)$$

Recently, Carlson *et al.* [22] have also calculated the TPE in $\mu^3\text{He}^+$. Their result of

$$\Delta E_{\text{TPE}}^{\text{LS}}(\text{dispersion relations}) = 15.14(49) \text{ meV} \quad (15)$$

is in agreement with the one from the TRIUMF-Hebrew group. As *our choice* we take the average of Eqs. (14) and (15) and remain with

$$\Delta E_{\text{TPE}}^{\text{LS}} = 15.30(52) \text{ meV}. \quad (16)$$

As conservative uncertainty we use the larger one (from Eq. (15)) and add in quadrature half the spread. A weighted average of the two values (Eq. (14) and (15)) which would reduce the total uncertainty is not adequate as certain contributions are effectively fixed by the same data [59].

⁷As explained in the intro, We use a different sign convention, which explains the minus sign in Refs. [11, 21].

3.3. Total Lamb shift in $\mu^3\text{He}^+$

Collecting the radius-independent (mostly) QED contributions listed in Tab. 1 and summarized in Eq. (9), the radius-dependent contributions listed in Tab. 2 and summarized in Eq. (11), and the complete TPE contribution $\Delta E_{\text{TPE}}^{\text{LS}}$ from Eq. (16), we obtain for the $2S \rightarrow 2P$ energy difference in $\mu^3\text{He}^+$

$$\begin{aligned} \Delta E(2S_{1/2} \rightarrow 2P_{1/2}) &= 1644.3466(146) \text{ meV} \\ &+ 0.1177(33) \text{ meV} - 103.5184(98) r_h^2 \text{ meV/fm}^2 \\ &+ 15.3000(5200) \text{ meV} \\ &= 1659.76(52) \text{ meV} - 103.518(10) r_h^2 \text{ meV/fm}^2, \end{aligned} \quad (17)$$

where in the last step we have rounded the values to reasonable accuracies.

One should note that the uncertainty of 0.52 meV from the nuclear structure corrections $\Delta E_{\text{TPE}}^{\text{LS}}$, Eq. (16), is about 30 times larger than the combined uncertainty of all radius-independent terms summarized in Tab. 1, and 13 times larger than the uncertainty in the coefficient of the r_h^2 -dependent term (which amounts to 0.038 meV for $r_h = 1.966$ fm). A further improvement of the two-photon exchange contributions in light muonic atoms is therefore strongly desirable.

4. 2S hyperfine splitting

The 2S hyperfine splitting (HFS) in muonic helium-3 ions has been calculated by Borie [25] and Martynenko [28]. (There is also the more recent paper [27] from Martynenko *et al.*, but it is less detailed and reproduces all numbers from [28], with one exception to be discussed for #h27.) The values are summarized in Tab. 3 and labeled with #hi.

We also adapted the ordering according to increasing order/complexity of the terms and grouped them thematically as: Fermi energy with anomalous magnetic moment and relativistic corrections discussed in Sec. 4.1, vacuum polarization and vertex corrections in Sec. 4.2, nuclear structure contributions and corrections listed in Sec. 4.3, and the weak interaction contribution in Sec. 4.4.

4.1. Fermi energy with muon anomalous magnetic moment and Breit corrections

4.1.1. h1 and h4 Fermi energy and muon AMM correction

Item #h1 is the Fermi energy ΔE_{Fermi} which defines the main splitting of the 2S hyperfine levels. Borie and the Martynenko group have both calculated the Fermi energy, however, their values disagree by 0.055 meV (see Tab. 3). For the calculation Borie uses Eq. (13) in her Ref. [25]. Martynenko uses Eq. (6) in his Ref. [28]. The Fermi energy is calculated using fundamental constants only. Thus we repeated the calculation for both equations, the one from Borie and the one from Martynenko which resulted to be the same: Both equations yield the same result, as they should, which is

$$\Delta E_{\text{Fermi}} = \frac{8(\alpha^4 Z^3) m_r^3}{3n^3 m_\mu m_p} \mu_h = -171.3508 \text{ meV}, \quad (18)$$

where m_μ is the muon mass, m_p is the proton mass, m_r is the reduced mass, and μ_h is the helion magnetic moment to nuclear magneton ratio of $\mu_h = -2.127\,625\,308(25)$ [7]. We use the value in Eq. (18) as *our choice*. This value agrees neither with Borie's value (-171.3964 meV) nor with the one from the Martynenko group (-171.341 meV).

The value for the Fermi energy corrected for the muon anomalous magnetic moment (AMM) a_μ is then also updated to

$$\Delta E_{\text{Fermi,AMM}} = \Delta E_{\text{Fermi}} \cdot (1 + a_\mu) = -171.5506 \text{ meV} \quad (19)$$

with a correction of -0.1998 meV .

All further corrections from Borie given as coefficients ϵ , are applied to this value analogous to

$$\Delta E_{\text{Fermi,AMM}} \cdot (1 + \epsilon). \quad (20)$$

Note, that in Tab. 3, for the contributions given by Borie, we use her coefficients but apply them to our value of the Fermi Energy given in Eq. (19). The value for the Fermi Energy in Eq. (19) is evaluated to a precision of 0.0001 meV . If the number of significant digits from Borie's coefficients is too small to yield this precision we attribute a corresponding uncertainty. For example item #h28* has the coefficient $\epsilon_{2\gamma} = 0.0013$; here the coefficient is only precise up to a level of 0.00005 , which we include as uncertainty. This uncertainty is propagated upon multiplication with the Fermi energy (Eq. (19)) and then yields 0.0086 meV .

4.1.2. *h2 Relativistic Breit correction*

Item #h2 is the relativistic Breit correction of order $(Z\alpha)^6$. It is given congruently by both authors as $\Delta E_{\text{F,rel}}^{\text{B}} = -0.0775 \text{ meV}$ and $\Delta E_{\text{F,rel}}^{\text{M}} = -0.078 \text{ meV}$, respectively. We take the number from Borie as *our choice*, which is given with one more digit and attribute an uncertainty of 0.0001 meV due to the precision in her coefficient.

4.2. *Vacuum polarization and vertex corrections*

4.2.1. *h8 and h9: Electron vacuum polarization in a one-photon one-loop interaction (h8) and in a one-photon two-loop interaction (h9)*

The Feynman diagrams corresponding to #h8 and #h9 are analogous to those shown in Figs. 2 and 3, respectively, and constitute the analogs to the Uehling- and Källén-Sabry contributions in the Lamb shift. #h8 is of order $\alpha(Z\alpha)^4$, #h9 is of order $\alpha^2(Z\alpha)^4$.

Borie calculates the main electron VP contribution ("by modification of the magnetic interaction between muon and nucleus"), which is a one-photon one-loop interaction. It amounts to a correction $\epsilon_{VP1} = 0.00315$, which results in an energy shift of -0.5405 meV (#h8). She also gives $\epsilon_{VP1} = 2.511 \cdot 10^{-5}$ for one-photon two-loop interactions, resulting in -0.0043 meV (#h9). These terms are evaluated on p. 21 of her document [25], using her Eq. (16).

Martynenko calculates these contributions to be -0.540 meV and -0.004 meV , respectively. These values are found in the table in Ref. [28].

Martynenko mentions that his value for our item #h9 consists of his Eqs. (15,16). The numerical result from Eq. (15) corresponds to two separate loops (see our Fig. 3(a)) and is given as -0.002 meV , whereas Eq. (16) describes the two nested two-loop processes where an additional photon is exchanged within the electron VP loop (see our Fig. 3(b,c)). One can conclude that its numerical value is also -0.002 meV .

Both authors give congruent results within their precisions, as *our choice* we write down the numbers by Borie which are given with one more digit. We attribute an uncertainty to item #h8 due to the precision in Borie's coefficient.

4.2.2. *h5 and h7: Electron vacuum polarization in SOPT in one loop (h5) and two loops (h7)*

Items #h5 and #h7 are the SOPT contributions to items #h8 and #h9, respectively.

Borie's value for our item #h5 is given by the coefficient $\epsilon_{VP2} = 0.00506$ and her value for our item #h7 by $\epsilon_{VP2} = 3.928 \cdot 10^{-5}$. This results in energy shifts of $-0.8680(9)$ meV and -0.0067 meV, respectively (those values are for point nuclei; the finite size correction is taken into account in our #h25 and #h26). The uncertainty in item #h5 originates from the precision of ϵ_{VP2} .

The corresponding values from Martynenko are -0.869 meV (#h5) and -0.010 meV (#h7).

Due to slight differences between the two authors, as *our choice* we take the average of items #h5 and #h7, respectively. The uncertainty of item #h5 is the above uncertainty and half the spread between both authors added in quadrature.

4.2.3. *h13 and h14: Vertex correction ($\hat{=}$ self energy happening at the muon-photon vertex)*

Item #h13 is the muon self-energy contribution of order $\alpha(Z\alpha)^5$ (it is the analogue to a part of item #20 in the Lamb shift, see Fig. 6a). It has only been calculated by Borie as

$$\epsilon_{\text{vertex}} = \alpha(Z\alpha) \left(\ln 2 - \frac{5}{2} \right) = -0.9622 \cdot 10^{-4} \cdot Z. \quad (21)$$

Its numerical value is thus 0.0330 meV, however this includes a muon VP contribution of -0.0069 meV (#h12, see Sec. 4.2.4). For our item #h13, we use the value from Borie as *our choice*. We therefore should not include #h12, which is discussed later.

Borie also cites a higher order correction of Brodsky and Erickson [60] which results in a correction of $-0.211 \cdot 10^{-4} \hat{=} -0.0036$ meV (#h14). Very probably the sign of the energy shift is not correct because the coefficient is negative, but the Fermi energy of helium-3 also has a negative sign, thus the energy shift should be positive. (The analogous contributions in muonic hydrogen and deuterium are negative, which is a further hint to a wrong sign since the helium-3 Fermi energy is negative, contrary to hydrogen and deuterium.)

4.2.4. *h12: Muon VP and muon VP SOPT*

Item #h12 is the one-loop muon vacuum polarization. Borie on p.19 (below the equation of ϵ_{vertex}) of Ref.[25] gives the coefficient as $0.3994 \cdot 10^{-4} \cdot Z$. In combination with the Fermi energy this yields -0.0069 meV. Martynenko obtains a value of -0.007 meV which is congruent to Borie's value. However, Borie's value of this contribution is already included in our item #h13, which has been discussed in the previous section. Hence, we do not include it separately in 'our choice'.

4.2.5. *h18 Hadronic vacuum polarization*

Item #h18 is the hadronic vacuum polarization. Borie gives this contribution as $\epsilon_{hVP} = 0.2666 \cdot 10^{-4} \cdot Z$, which amounts to -0.0091 meV on p.19 of her paper. This contribution is analogous to our Fig. 2, but with a hadronic loop in the photon line. Since Martynenko does not provide a value for hadronic VP in muonic helium-3 ions, we use Borie's value as 'our choice'.

4.3. *Nuclear structure and finite size corrections*

Analogously to Sec. 3.2, we categorize the nuclear structure contributions to the 2S HFS as one-photon exchange (OPE) and two-photon exchange (TPE) processes, respectively. We list first the by far dominant contribution to nuclear structure: the Zemach term, which is an elastic TPE process. The following subsections describe the known elastic TPE corrections in the 2S HFS. So far, to our knowledge there are yet no

calculations with respect to the *inelastic* TPE contribution to the 2S HFS. Thus we only give a simplified estimate with a large uncertainty. Later the section is concluded with the one-photon exchange (OPE) corrections to nuclear structure in the 2S HFS.

4.3.1. *h20 Zemach term and h23, h23b*, h28* nuclear recoil*

Item #h20 is the elastic TPE and the main finite size correction to the 2S HFS. This correction arises due to the extension of the magnetization density (Bohr-Weisskopf effect) and is also called the Zemach term [61]. The Zemach term is usually parameterized as [62]

$$\Delta E_{\text{Zemach}}^{\text{HFS}} = -\Delta E_{\text{Fermi,AMM}} 2(Z\alpha)m_r r_Z \quad (22)$$

with m_r being the reduced mass and r_Z the Zemach radius of the nucleus [55]

$$r_Z = -\frac{4}{\pi} \int_0^\infty [G_E(q)G_M(q) - 1] \frac{dq}{q^2}. \quad (23)$$

Here, $G_E(q)$ and $G_M(q)$ are the electric and magnetic form factors of the nucleus, respectively.

The corresponding coefficient to the Fermi energy in Eq. (22) is given by Borie on p. 23 of [25] as $\epsilon_{\text{Zem}} = -2(Z\alpha)m_r r_Z = -0.01506 \text{ fm}^{-1} r_Z$. With our Fermi energy from Eq. (19), item #h20 is

$$\Delta E_{\text{Zemach}}^{\text{HFS}} = 2.5836 r_Z \text{ meV/fm} = 6.5312(413) \text{ meV}, \quad (24)$$

where, in the second step, we inserted the most recent Zemach radius from Sick [55] ($r_Z = 2.528(16) \text{ fm}$).

Note that Borie's published value of $\Delta E_{\text{Zemach}}^{\text{HFS}}$ differs from the one given here, because she uses a different Zemach radius of $r_Z = 2.562 \text{ fm}$, assuming a Gaussian charge distribution.

Martynenko, in his Ref. [28], gives a value of $\Delta E_{\text{str}}^{\text{HFS}} = 6.047 \text{ meV}$. This value contains a recoil contribution and is thus not directly comparable with our item #h20. However, this value has been updated [53] and is now available as two separate values of $\Delta E_{\text{str}}^{\text{HFS}} = 6.4435 \text{ meV} = (6.4085 + 0.0350_{\text{recoil}}) \text{ meV}$. The first can be compared to Eq. (24). The second is the recoil correction and listed in our table as item #h23. Martynenko notes [28] that changing from a Gaussian to a dipole parameterization results in a change of the final number of 2%.

Regarding our item #h20, we do not consider the respective value from Martynenko because it is model-dependent and therefore carries a large uncertainty. This uncertainty can be avoided using the model-independent Zemach radius from Sick and the coefficient given by Borie as stated above.

A new contribution which hasn't been calculated for μp and μd is our item #h23b*. It is an additional recoil contribution which amounts to 0.038 meV . It has only been calculated by Martynenko and we adopt his value as *our choice*. In order to account for the precision given by Martynenko, we write $0.0380(5) \text{ meV}$.

Another contribution which has not been calculated for μp and μd is item #h28*. It is a two-photon recoil correction, calculated by Borie in 1980 [63], who followed the procedure of Grotch and Yennie [64]. This contribution is not listed in Borie's recent Ref. [25], but should be included [65]. It is given by $\epsilon_{2\gamma} = 0.0013$ and therefore results in $-0.2230(86) \text{ meV}$, using our Fermi energy from Eq. (19). The attributed uncertainty originates from the number of significant digits in $\epsilon_{2\gamma}$ (the value of the coefficient is considered to be accurate only to ± 0.00005). Regarding the contributions given by Martynenko, no overlap is found, which is why we list this item separately.

4.3.2. *h24 electron VP contribution to two-photon exchange*

Item #h24, the electron VP contribution to the 2S HFS elastic two-photon exchange in muonic helium-3 ions is only calculated by Martynenko [28]. The corresponding Feynman diagrams are shown in Fig. 4 of his helium 2S HFS paper [28]. These are analogous to our Fig. 14, but with a VP loop in one of the exchange photons. A numerical value of the contribution is given in his Eq. (38) of 0.095 meV and thus enters *our choice*, where we write 0.0950(5) meV and therefore account for the precision given by Martynenko.

4.3.3. *h15, h16, h17 radiative corrections to the elastic two-photon exchange*

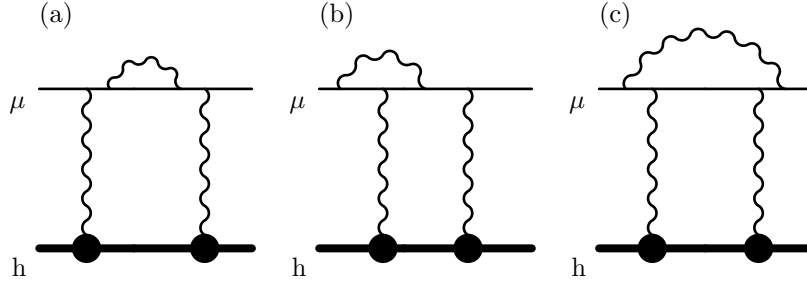


Figure 15: (a) Item #h15, μ SE contribution to the elastic two-photon exchange; (b) item #h16 the vertex correction to the elastic two-photon exchange, which results in two terms (the vertex correction can take place either at one or the other photon); and (c) item #h17, spanning photon contribution to the elastic two-photon exchange, also referred to as jellyfish diagram.

Items #h15, #h16, and #h17 are radiative corrections to the elastic two-photon exchange in the 2S hyperfine structure and represented in Fig. 15. They are partially given in Martynenko's Ref. [28], but have been updated [66] and result to be -0.0101 meV (#h15), 0.0333 meV (#h16), and 0.0074 meV (#h17). These numbers include recoil corrections and are based on Eqs.(24)-(27) from the Martynenko group [29] and use a dipole parameterization of the helion form factor, as well as $r_{\text{helion}}=1.966$ fm. For the moment, we will adapt these preliminary numbers including recoil considerations into *our choice*.

4.3.4. *h22 inelastic two-photon exchange in the hyperfine structure*

In contrast to the Lamb shift, no calculations are available for the inelastic two-photon exchange (polarizability contribution) in the 2S HFS. We give an estimate of this value by calculating the ratio between the polarizability contribution and the Zemach term in the 1S ground state of (electronic) $^3\text{He}^+$ and assume the ratio to be similar for the 2S state in $\mu^3\text{He}^+$.

The 1S Zemach term for electronic $^3\text{He}^+$ is found by using Eq. (22), but with the muon mass replaced by the electron mass and $n = 1$. Using the Zemach radius r_Z from Friar and Payne [67] a value of 1717 kHz is obtained. In order to obtain the total sum (polarizability + Zemach) of 1442 kHz [67], a polarizability term of order -300 kHz is missing. The ratio is then roughly $-1/6$. The Zemach term for muonic helium-3 ions (our item h20), obtained above, yields $\Delta E_{\text{Zem}} \approx 6.5$ meV. The estimate for the polarizability contribution consequently follows with $\Delta E_{\text{pol}}^{\text{HFS}} \approx -1.0 \pm 1.0$ meV, which includes a conservative 100% uncertainty.

4.3.5. *h25 and h26 finite size correction to electron VP*

Borie gives the electron VP contributions #h8 and #h5 (eVP processes in OPE, see Sec. 4.2) which are based on a point nucleus. Additionally, she provides modified contributions which include the finite size effect on electron VP. These are $\epsilon'_{VP1} = 0.00295$ and $\epsilon'_{VP2} = 0.00486$, respectively. The difference between those values and #h8 and #h5 constitute finite size corrections. Multiplied with the Fermi energy

(including the AMM), these yield 0.0343(9) meV each and we attribute them to #h25 and #h26, analogous to the previous CREMA summaries. The uncertainty originates from the precision in Borie's coefficients. Note that these are OPE processes.

4.3.6. $h27$ and $h27b$ nuclear structure correction in leading order and $SOPT$

This correction is only given by Martynenko. The two terms are found in Fig. 5(a) and (b) of Ref. [28], for leading and second order, respectively. This correction is also an OPE process. Care has to be taken here because this contribution is given as 0.272 meV in [28], but as 0.245 meV in a 2010 follow up paper [27] (however, this is the only term that changed between [28] and [27]). As compared to muonic deuterium, Martynenko only gives the sum ($h27+h27b$) and not the single contributions. In [28] the formulas he uses to calculate $h27$ and $h27b$ are explicitly given as

$$\Delta E_{1\gamma, \text{str}}^{\text{HFS}} = -\frac{4}{3}(Z\alpha)^2 m_r^2 r_M^2 \cdot E_{\text{Fermi}} \cdot \frac{1-n^2}{4n^2} \quad (25)$$

$$\Delta E_{\text{str}, \text{SOPT}}^{\text{HFS}}(2S) = \frac{4}{3}(Z\alpha)^2 m_1^2 r_E^2 \cdot E_{\text{Fermi}}(2S) \cdot (\ln(Z\alpha) - \ln 2), \quad (26)$$

where m_r is the reduced mass of the muon, m_1 is the muon mass, and r_E and r_M are the charge and magnetic radii, respectively. Martynenko states to use $r_E \approx r_M = 1.844 \pm 0.045$ fm which is known to be outdated.

However, inserting Martynenko's Fermi energy, the radius he used, and fundamental constants into Eqs. (25) and (26) yields a sum of 0.2251 ± 0.0001 meV which is neither congruent with [28] nor [27].

Using Sick's 2014 values [55] for the charge and magnetic radii yields 0.2577 ± 0.0001 meV.

In the course of some private communications with Martynenko, he provided us his most current value of 0.2421 meV for the sum of $h27+h27b$, and we use this preliminarily as *our choice*.

4.4. $h19$ weak interaction

The contribution of the weak interaction to the 2S HFS of helium-3 is only given by Borie. She cites Eides [68] and provides $\epsilon_{\text{weak}} = 1.5 \cdot 10^{-5} \hat{=} -0.0026$ meV, which we adopt as *our choice*.

4.5. Total 2S HFS contribution

In total, the 2S HFS contributions are given by

$$\begin{aligned} \Delta E^{\text{HFS}}(2S_{1/2}^{\text{F}=1} - 2S_{1/2}^{\text{F}=0}) &= -172.7457(89) \text{ meV} + 2.5836 \text{ meV/fm } r_Z + \Delta E_{\text{pol.}}^{\text{HFS}} \\ &= -166.2145(423) - 1.0(1.0) \text{ meV} \\ &= -167.2(1.0) \text{ meV}. \end{aligned} \quad (27)$$

Here, in the first line, we separated out the Zemach contribution and the estimate of the polarizability contribution. In the second line, the Zemach radius $r_Z = 2.528(16)$ fm [55] is inserted and the estimated value of $\Delta E_{\text{pol.}}^{\text{HFS}}$ is shown. The polarizability is the dominant source of uncertainty in the hyperfine structure and prevents a precise determination of the helion Zemach radius from the measured transitions in the muonic helium-3 ion [69]. A calculation of the polarizability contribution is therefore highly desirable. Until then a precise measurement of the 1S or 2S HFS in muonic helium-3 ions can be used to experimentally determine a value of the polarizability contribution $\Delta E_{\text{pol.}}^{\text{HFS}}$. In essence, the measurement of the 2S HFS by the CREMA collaboration can be used to give the total TPE contribution to the HFS, $\Delta E_{\text{TPE}}^{\text{HFS}} = 2.5836 \text{ meV/fm } r_Z + \Delta E_{\text{pol.}}^{\text{HFS}}$ with an expected uncertainty of 0.1 meV.

Table 3: All contributions to the **2S hyperfine splitting (HFS)**. The item numbers hi in the first column follow the entries in Tab. 3 of Ref. [1]. However, the terms are now sorted by increasing complexity, analogous to their order in the text. For Martynenko, numbers #1 to #13 refer to rows in Tab. I of his Ref. [28], whereas numbers in parentheses refer to equations therein. Borie [25] gives the values as coefficients ϵ to be multiplied with the sum of (h1+h4) of 'our choice' values. We list the resulting values in meV. AMM: anomalous magnetic moment, PT: perturbation theory, VP: vacuum polarization, SOPT: second order perturbation theory, TOPT: third order perturbation theory. All values are in meV. Values in brackets do not contribute to the total sum.

	Contribution	Borie (B) Borie [25]	Martynenko group (M) Martynenko [28]	Our choice value source
h1	Fermi splitting, $(Z\alpha)^4$	(-171.3964) p. 19	-171.341 #1, (6)	-171.3508 ^a
h4	μ AMM corr., $\alpha(Z\alpha)^4$	(-0.1999)	-0.200 #2, (7)	-0.1998
sum	(h1+h4)	-171.5963 p. 19	(-171.541)	
h2	Breit corr., $(Z\alpha)^6$	-0.0775 \pm 0.0001 p. 19	-0.078 #3, (8)	-0.0775 \pm 0.0001 B
h8	One-loop eVP in OPE, $\alpha(Z\alpha)^4$ (ϵ_{VP1})	-0.5404 \pm 0.0009 p. 21	-0.540 #4, (12)	-0.5404 \pm 0.0009 B
h9	Two-loop eVP in OPE, $\alpha^2(Z\alpha)^4$ (ϵ_{VP1})	-0.0043 p. 21	-0.004 #5, (15,16)	-0.0043 B
h5	One-loop eVP in OPE, SOPT, $\alpha(Z\alpha)^4$ (ϵ_{VP2})	-0.8680 \pm 0.0009 p. 21	-0.869 #7, (24)	-0.8685 \pm 0.0010 avg.
h7	Two-loop eVP in OPE, SOPT, $\alpha^2(Z\alpha)^4$ (ϵ_{VP2})	-0.0067 p. 21	-0.010 #8, (29,30)	-0.0084 \pm 0.0017 avg.
h13	Vertex, $\alpha(Z\alpha)^5$	0.0330 p. 19		0.0330 B
h14	Higher order corr. of (h13), part with $\ln(\alpha)$	0.0036 ^b p. 19		0.0036 B
h12	one-loop μ VP in 1γ int., α^6	(-0.0069) incl. in h13 p. 19 & p. 21	-0.007 #6, (12)	incl. in h13 B
h18	Hadronic VP, α^6	-0.0091 p. 19		-0.0091 B
h20	Fin. size (Zemach) corr. to ΔE_{Fermi} , $(Z\alpha)^5$	6.5312 ^c (=2.5836 r_Z /fm) p. 23	6.4085 (\pm 0.1) ^d priv.comm.	2.5836 r_Z /fm B
h23	Recoil of order $(Z\alpha)(m_1/m_2)\ln(m_1/m_2)E_F$		0.0350 priv.comm.	0.0350 M
h23b*	Recoil of order $(Z\alpha)^2(m_1/m_2)E_F$		0.038 #13, (48)	0.0380 \pm 0.0005 M
h28*	Two-photon recoil	-0.2230 \pm 0.0086 [63]		-0.2230 \pm 0.0086 B
h24	eVP in two-photon-exchange, α^6		0.095 #10, (38)	0.0950 \pm 0.0005 M
h15	muon self energy contribution in TPE, w/recoil		-0.0101 priv.comm.	-0.0101 M
h16	vertex correction contribution in TPE, w/recoil		0.0333 priv.comm.	0.0333 M
h17	jelly fish correction contribution in TPE, w/recoil		0.0074 priv.comm.	0.0074 M
h22a	Helion polarizability, $(Z\alpha)^5$			
h22b	Helion internal polarizability, $(Z\alpha)^5$			
sum	(h22a+h22b)			(-1.0 \pm 1.0) ^e
h25	eVP corr. to fin. size in OPE (sim. to ϵ_{VP2})	0.0343 \pm 0.0009 p. 21		0.0343 \pm 0.0009 B
h26	eVP corr. to fin. size in OPE (sim. to ϵ_{VP1})	0.0343 \pm 0.0009 p. 21		0.0343 \pm 0.0009 B
h27+h27b	Nucl. struct. corr. in SOPT, $\alpha(Z\alpha)^5$		0.2421 priv.comm.	0.2421 M
h19	Weak interact. contr.	-0.0026 \pm 0.0001 p. 21		-0.0026 \pm 0.0001 B
	Sum	-166.6988 ^g	-165.1998 ^h	-172.7457 \pm 0.0089 2.5836 r_Z/fm -1.0 \pm 1.0

^acalculated in this work and given in Eq. (18).

^bThe sign from Borie is wrong and has been corrected here, see Sec. 4.2.3.

^cCalculated by combining Borie's coefficient with Sick's r_Z .

^dThis uncertainty reflects the change in this contribution when moving from dipole parameterization to a Gaussian one.

^eIs a preliminary estimate, see text. It is therefore listed separately in the sum below.

^fDifference of two terms in Borie [25], see also Sec. 4.3.5.

^gBorie's sum given in this table differs from her published one of -166.3745 meV [25]. This is because we used an updated value of the Fermi energy (see Sec. 4.1.1), a different value for the Zemach radius r_Z (see Sec. 4.3.1), and included item #h28* which has not been considered in Ref. [25].

^hMartynenko's sum given in this table is different from the (superseded) published one of -166.615 meV [28] because several terms have been changed and added upon private communication.

Table 4: Contributions to the **2P fine structure**. Items # with an asterisk * denote new contributions in this compilation. The items #f7a, #f7d, and #f7e originate from the same graphs as the Lamb shift items #11, #12, and #30, respectively. VP: vacuum polarization, AMM: anomalous magnetic moment, KS: Källén-Sabry. All values are in meV.

#	Contribution	Borie (B) Borie [25] Tab. 7	Martynenko group (M) Elekina <i>et al.</i> [30] Tab. 1	Karshenboim group (K) Karshenboim <i>et al.</i> [34] Korzinin <i>et al.</i> [33]	Our choice
f1	Dirac	144.4157			
f2	Recoil	−0.1898			
f3	Contrib. of order $(Z\alpha)^4$		144.18648 1.1		
f4a	Contrib. of order $(Z\alpha)^6$		0.01994 1.3		
f4b	Contrib. of order $(Z\alpha)^6 m^2/M$		−0.00060 1.4		
sum	(f1+f2) or (f3+f4)	144.2259	144.20582		144.2159 ± 0.0100 avg.
f5a	eVP corr. (Uehling), $\alpha(Z\alpha)^4$		0.12925 1.5		
f5b	eVP corr. SOPT, $\alpha(Z\alpha)^4$		0.14056 1.7		
f13*	eVP corr. SOPT, $\alpha^2(Z\alpha)^4$		0.00028 1.9		
sum	f5+f13*	0.2696	0.27009	0.26920 [34] Tab.IV	0.2696 ± 0.0004 avg.
f6a	two-loop eVP corr. (KS), $\alpha^2(Z\alpha)^4$		0.00098 1.10+11		0.0010 M
f6b	two-loop eVP in SOPT, $\alpha^2(Z\alpha)^4$	0.0021	0.00234 1.12+13	0.00242 [33] Tab.IX “eVP2”	0.0024 K
f7a	$\alpha^2(Z\alpha)^4 m$, like #11			0.000606 [33] Tab.IX (a)	0.0006 K
f7d	$\alpha^2(Z\alpha)^4 m$, like #12			0.00164 [33] Tab.IX (d)	0.0016 K
f7e	$\alpha^2(Z\alpha)^4 m$, like #30*			0.000019(2) [33] Tab.IX (e)	0.0000 K
f11*	$\alpha(Z\alpha)^6$		−0.00055 1.8		−0.0006 M
f12*	one-loop μ VP, $\alpha(Z\alpha)^4$		0.00001 1.6		0.0000 M
f8	AMM (second order)	0.3232			
f9	AMM (higher orders)	0.0012			
sum	Total AMM (f8+f9)	0.3244	0.32446 1.2		0.3244 avg.
f10	Finite size, $(Z\alpha)^6$ ^a	−0.0158			−0.0158 ± 0.0002 B
	Sum	144.8062	144.80315		144.7993 ± 0.0101

^aThis is item #r8, evaluated for a helion radius of 1.966(10) fm [25], see text. The uncertainty is propagated from the charge radius, but is negligible.

5. 2P levels

5.1. 2P fine structure

Fine structure (FS) contributions have been calculated by Borie [25] (Tab. 7), the Martynenko group [30] (Tab. 1), and the Karshenboim group [34] (Tab. 4) and [33] (Tab. 9). All of these contributions are listed in Tab. 4 and labeled with #*fi*.

The leading fine structure contribution of order $(Z\alpha)^4$ has been calculated by Borie using the Dirac wavefunctions (same as in Lamb shift). Her result (our item #f1) has to be corrected by a recoil term (item #f2) in order to be compared with the result from Martynenko *et al.* They use a nonrelativistic approach (our item #f3) and then add relativistic corrections (our item #f4a+b). Their total results differ by 0.02 meV. We take the average as *our choice* and remain with an uncertainty of 0.01 meV. This is by far the dominant uncertainty in the 2P fine structure.

Item #f5a and #f5b are the one-loop eVP of order $\alpha(Z\alpha)^4$ in leading order and SOPT. Item #f13* is the one-loop eVP contribution of order $\alpha^2(Z\alpha)^4$ in SOPT. All three items are given individually by the Martynenko group [30] in lines 5, 7, and 9 of their Tab. 1. In Tab. 7 of [25], Borie's term "Uehling(VP)" presumably contains all these three items. Karshenboim *et al.* [34] (Tab. 4) also calculate the sum of these items. All agree within 0.0009 meV and we take the average as *our choice* which coincides with Borie's value.

Item #f6a and #f6b are the two-loop eVP (*Källén-Sabry*) contribution of order $\alpha^2(Z\alpha)^4$ in leading order and SOPT. These terms have been calculated by Martynenko *et al.* [30] (Tab. 1, line 10+11 and 12+13, respectively). Borie [25] and the Karshenboim group [33] (Tab. IX) only calculated our item #f6b. We therefore adopt the value provided by the Martynenko group for item #f6a and the Karshenboim group's value of #f6b as they included some higher order terms as well.

Items #f7a, #f7d, and #f7e are of order $\alpha^2(Z\alpha)^4$ and have been calculated with high accuracy by the Karshenboim group [33] (Tab. IX). They correspond to the same Feynman diagrams as the Lamb shift items #11, #12, and #30, shown in Figs. 7, 8, and 9, respectively. We adopt the values from the Karshenboim group as *our choice*.

Item #f11* is a contribution of order $\alpha(Z\alpha)^6$ which has been calculated by Martynenko *et al.* [30] (Tab. 1, line 8). Item #f12* is the one-loop μVP of order $\alpha(Z\alpha)^4$ which has been calculated by the Martynenko group as well [30] (Tab. 1, line 6). We adopt both of these values as *our choice*.

The sum of items #f8 and #f9 is the muon anomalous magnetic moment (AMM) contribution of order $(Z\alpha)^4$. These items are labeled by Borie [25] as "second order" and "higher orders", respectively. Martynenko *et al.* [30] (Tab. 1, line 2) provide the sum of these. Both groups agree very well. As *our choice* we adopt the average.

Item #f10 is the finite size correction to the $2P_{1/2}$ level of order $(Z\alpha)^6$ which has only been calculated by Borie [25]. It is the same correction which appears in the radius dependent part of the Lamb shift as #r8, with opposite sign and evaluated with a helion charge radius of 1.966(10) fm [25]. We adopt Borie's value as *our choice* and add the uncertainty which we obtain from the given charge radius.

The total sum of the FS contributions is summarized in Tab. 4 and amounts to

$$\Delta E_{\text{FS}} = 144.7993 \text{ meV} \pm 0.0101 \text{ meV}. \quad (28)$$

It will enter the calculation of the 2P hyperfine structure in the following section. Note, that the uncertainty originates only from differences in the treatment of Dirac term (sum of items #f1 to #f4).

5.2. 2P hyperfine structure

The 2P hyperfine splitting is described by the Breit Hamiltonian. Off-diagonal terms appear in the matrix representation of this Hamiltonian in the basis of $2P_{1/2}^{F=1}$, $2P_{1/2}^{F=0}$, $2P_{3/2}^{F=2}$, and $2P_{3/2}^{F=1}$. These terms lead to a mixing of energy levels with same quantum number F (see Fig. 1). This has first been calculated by Brodsky and Parsons [23] for hydrogen and later has also been evaluated for muonic hydrogen by Pachucki [37]. In previous publications [1, 2], we also discussed the mixing of hyperfine states.

The traditional way [23, 37] is to calculate the FS (without perturbations from the HFS F state mixing) and then include the so obtained FS in the evaluation of the Breit matrix. The centroids of the diagonal elements are now the virtual levels $2P_{1/2}$ and $2P_{3/2}$. *Afterwards* the mixing is included (via diagonalization) which means that the actual centroid is not at the position of the virtual levels anymore.

The 2P hyperfine structure has been calculated by Borie [25] (Tab. 9) and Martynenko *et al.* [30] (Tab. 2). We also calculated the splittings following Pachucki [37], who did the evaluation for μp . The values which are listed in our Tab. 5 are not the published values, but the values which result when including our FS value from Sec. 5.1.

Borie in her Tab. 9 lists the energies of the four 2P hyperfine levels relative to the $2P_{1/2}$ fine structure state where she already included the F state mixing. We reproduced her results using the Eqs. given in her Tab. 9 and then inserted our ΔE_{FS} from our Eq. (28). The result is listed in the second column of Tab. 5. Borie mentions, she used the shielded helion magnetic moment, whereas the (unshielded) magnetic moment should be used. The change, however, appears only on the seventh digit and is therefore negligible.

In their Tab. 2, Martynenko *et al.* provide the total splittings of the hyperfine structure levels, and at the end of their Sec. 3, they list the term $\Delta = 0.173 \text{ meV}$ originating from the mentioned F state mixing. In order to include this term, the numbers in their Tab. 2 first have to be divided according to the weight given by the number of m_F states. Δ has then to be added to the two $F = 1$ states. Furthermore, for the $2P_{3/2}$ states, we add our ΔE_{FS} . The result is listed in the third column of our Tab. 5.

Additionally, following Pachucki [37], we repeat his calculations in μp for $\mu^3\text{He}^+$. The off-diagonal elements are given by Eq. (85) of [37]

$$\langle 2P_{1/2}^{F=1} | V | 2P_{3/2}^{F=1} \rangle = \frac{1}{3} (Z\alpha)^4 \frac{m_r^3}{m_\mu m_h} (1 + \kappa) \left(1 + \frac{m_\mu}{m_h} \frac{1 + 2\kappa}{1 + \kappa} \right) \left(-\frac{\sqrt{2}}{48} \right), \quad (29)$$

where we included the correct Z scaling. m_r is the reduced mass of the muonic helium-3 ion, m_μ (m_h) is the mass of the muon (helion), and $\kappa = -4.18415^8$ is the helion anomalous magnetic moment. The diagonal terms are given by Eq. (86) therein

$$E_{\text{HFS}}(2P_{1/2}) = \frac{1}{3} (Z\alpha)^4 \frac{m_r^3}{m_\mu m_h} (1 + \kappa) \left(\frac{1}{3} + \frac{a_\mu}{6} + \frac{1}{12} \frac{m_\mu}{m_h} \frac{1 + 2\kappa}{1 + \kappa} \right) \quad (30)$$

$$E_{\text{HFS}}(2P_{3/2}) = \frac{1}{3} (Z\alpha)^4 \frac{m_r^3}{m_\mu m_h} (1 + \kappa) \left(\frac{2}{15} - \frac{a_\mu}{30} + \frac{1}{12} \frac{m_\mu}{m_h} \frac{1 + 2\kappa}{1 + \kappa} \right) \quad (31)$$

with the anomalous magnetic moment of the muon $a_\mu = 1.165\,920\,89(63) \times 10^{-3}$ [7].

Furthermore, Pachucki adds corrections due to vacuum polarization in his Eq. (89) and (90). With

⁸The helion anomalous magnetic moment is obtained using the respective equation on p. 17 of Borie's Ref. [25], where this magnitude is denoted as κ_2 .

Table 5: **2P levels from fine- and hyperfine splitting.** All values are in meV relative to the $2P_{1/2}$ level. The columns labeled with Borie and Martynenko include their HFS calculations, but our value of the fine structure ($2P_{3/2}-2P_{1/2}$ energy splitting) $\Delta E_{\text{FS}} = 144.7993(101)$ meV from Eq. (28). The column ‘following [37]’ is calculated in this work following the treatment of Pachucki for $\mu^3\text{He}^+$, also including our value of the fine structure. Uncertainties arise from differences between the published values and from the uncertainty in the fine structure value ΔE_{FS} .

	Borie [25]	Martynenko [30]	following [37]	Our choice
$2P_{1/2}^{F=1}$	-14.7877	-14.8080	-14.7990	-14.7979(102)
$2P_{1/2}^{F=0}$	43.8458	43.9049	43.8797	43.8754(296)
$2P_{3/2}^{F=2}$	135.7580	135.7552	135.7527	135.7554(27)(101) _{FS}
$2P_{3/2}^{F=1}$	160.0410	160.0459	160.0494	160.0452(42)(101) _{FS}

correct Z scaling these are

$$\delta E_{\text{HFS}}(2P_{1/2}) = \frac{1}{3}(Z\alpha)^4 \frac{m_r^3}{m_\mu m_h} (1 + \kappa) \cdot 0.00022 \quad (32)$$

$$\delta E_{\text{HFS}}(2P_{3/2}) = \frac{1}{3}(Z\alpha)^4 \frac{m_r^3}{m_\mu m_h} (1 + \kappa) \cdot 0.00008. \quad (33)$$

They have to be added to Eqs. (30) and (31), respectively. Diagonalizing the matrix given in Eq. (91) of Ref. [37] with entries determined by the above equations yields the values given as *our choice* in Tab. 5. The diagonalization yields an F mixing of $\Delta = 0.1724$ meV. In the same manner as for the sections above, *our choice* in Tab. 5 takes into account the spread of values from the different authors and additionally the uncertainty of our value of the fine structure which we obtained in Sec. 5.1. It is astonishing that the splitting of the $2P_{1/2}$ states differs by as much as 0.04 meV between Borie and Martynenko. These states do not overlap with the nucleus, so it should be possible to determine them to much better precision. A precise calculation of these splittings is therefore highly welcome.

6. Summary

We have compiled all available contributions necessary to extract a charge radius of the helion from the Lamb shift measurement in muonic helium-3 ions, performed by the CREMA collaboration.

The nuclear structure-independent contributions of the Lamb shift, given in Tab. 1, show good agreement within the four (groups of) authors. The uncertainty is dominated by the hadronic VP (#14) and higher order radiative recoil corrections (#24). The total uncertainty in Tab. 1, however, is in the order of 0.01 meV and therefore sufficiently good (see also Eq. 5).

The nuclear structure-dependent part of the Lamb shift completely dominates the theoretical uncertainties. The one-photon exchange (finite size) contributions, where the coefficients are given in Tab. 2, have an uncertainty which corresponds to 0.04 meV, which already is above the “ideal” precision, mentioned in the introduction. This uncertainty is dominated by a disagreement in the terms #r4 and #r6. The much larger uncertainty, however, stems from the two-photon exchange contributions (TPE), given in Eq. (16). Recently, two groups have published new calculations on the TPE with a precision of about 3% which corresponds to roughly 0.5 meV. Improving this uncertainty could directly improve the extraction of the charge radius.

The uncertainty in the 2S HFS is completely dominated by the TPE contribution, where no calculation exists. We have given a very rough estimate. The upcoming results of the CREMA experiment will be able

to extract a value for the TPE experimentally. The second largest uncertainty in the 2S HFS originates from the Zemach radius term (Bohr-Weisskopf effect).

For the 2P levels, we collect all fine structure terms from the various authors which are then used to calculate the hyperfine structure by means of the Breit matrix. The results are compared with two other groups. Here, the largest uncertainty originates from the leading order contributions (#f1 to #f4) in the fine structure (which is still sufficiently good) and from differing published values of the $2P_{3/2}$ splitting. A clarification of this difference would be very welcome.

7. Acknowledgments

We are grateful to E. Borie and A.P. Martynenko for insightful comments and for providing us with previously unpublished results.

We acknowledge valuable contributions from S. Bacca, N. Barnea, M. Birse, E. Borie, C.E. Carlson, M. Eides, J.L. Friar, M. Gorchtein, S. Karshenboim, A.P. Martynenko, J. McGovern, N. Nevo Dinur, K. Pachucki, and M. Vanderhaeghen for their very valuable remarks and insightful discussions in particular of the issues concerning the nuclear polarizability contributions to the Lamb shift discussed in Sec. 3.2.2.

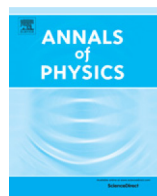
We proactively thank a future generation of motivated theorists for all future critical compilations of theory terms in light muonic atoms/ions.

References

- [1] A. Antognini, F. Kottmann, F. Biraben, P. Indelicato, F. Nez, R. Pohl, Theory of the 2S-2P Lamb shift and 2S hyperfine splitting in muonic hydrogen, *Ann. Phys.* 331 (2013) 127, [arXiv:1208.2637]. doi:10.1016/j.aop.2012.12.003.
- [2] J. J. Krauth, M. Diepold, B. Franke, A. Antognini, F. Kottmann, R. Pohl, Theory of the $n=2$ levels in muonic deuterium, *Ann. Phys.* 366 (2016) 168 – 196, [arXiv:1506.01298]. doi:http://dx.doi.org/10.1016/j.aop.2015.12.006. URL <http://www.sciencedirect.com/science/article/pii/S0003491615004303>
- [3] M. Diepold, J. J. Krauth, B. Franke, A. Antognini, F. Kottmann, R. Pohl, Theory of the Lamb shift and fine structure in $(\mu^4\text{He})^+$ [arXiv:1606.05231].
- [4] R. Pohl, A. Antognini, F. Nez, F. D. Amaro, F. Biraben, J. M. R. Cardoso, D. S. Covita, A. Dax, S. Dhawan, L. M. P. Fernandes, A. Giesen, T. Graf, T. W. Hänsch, P. Indelicato, L. Julien, C.-Y. Kao, P. Knowles, E.-O. L. Bigot, Y.-W. Liu, J. A. M. Lopes, L. Ludhova, C. M. B. Monteiro, F. Mulhauser, T. Nebel, P. Rabinowitz, J. M. F. dos Santos, L. A. Schaller, K. Schuhmann, C. Schwob, D. Taqqu, J. F. C. A. Veloso, F. Kottmann, The size of the proton, *Nature* 466 (2010) 213.
- [5] A. Antognini, F. Nez, K. Schuhmann, F. D. Amaro, F. Biraben, J. M. R. Cardoso, D. S. Covita, A. Dax, S. Dhawan, M. Diepold, L. M. P. Fernandes, A. Giesen, T. Graf, A. L. Gouvea, T. W. Hänsch, P. Indelicato, L. Julien, C.-Y. Kao, P. Knowles, F. Kottmann, E.-O. L. Bigot, Y.-W. Liu, J. A. M. Lopes, L. Ludhova, C. M. B. Monteiro, F. Mulhauser, T. Nebel, P. Rabinowitz, J. M. F. dos Santos, L. A. Schaller, C. Schwob, D. Taqqu, J. F. C. A. Veloso, J. Vogelsang, R. Pohl, Proton structure from the measurement of 2S-2P transition frequencies of muonic hydrogen, *Science* 339 (2013) 417.
- [6] R. Pohl, F. Nez, L. M. P. Fernandes, F. D. Amaro, F. Biraben, J. M. R. Cardoso, D. S. Covita, A. Dax, S. Dhawan, M. Diepold, A. Giesen, A. L. Gouvea, T. Graf, T. W. Hänsch, P. Indelicato, L. Julien, P. Knowles, F. Kottmann, E.-O. Le Bigot, Y.-W. Liu, J. A. M. Lopes, L. Ludhova, C. M. B. Monteiro, F. Mulhauser, T. Nebel, P. Rabinowitz, J. M. F. dos Santos, L. A. Schaller, K. Schuhmann, C. Schwob, D. Taqqu, J. F. C. A. Veloso, A. Antognini, Laser spectroscopy of muonic deuterium, *Science* 353 (6300) (2016) 669–673. arXiv:http://science.sciencemag.org/content/353/6300/669.full.pdf, doi:10.1126/science.aaf2468. URL <http://science.sciencemag.org/content/353/6300/669>
- [7] P. J. Mohr, D. B. Newell, B. N. Taylor, CODATA recommended values of the fundamental physical constants: 2014*, *Rev. Mod. Phys.* 88 (2016) 035009. doi:10.1103/RevModPhys.88.035009. URL <http://link.aps.org/doi/10.1103/RevModPhys.88.035009>
- [8] R. Pohl, R. Gilman, G. A. Miller, K. Pachucki, Muonic hydrogen and the proton radius puzzle, *Ann. Rev. Nucl. Part. Sci.* 63 (2013) 175, [arXiv 1301.0905].
- [9] C. E. Carlson, The proton radius puzzle, *Prog. Part. Nucl. Phys.* 82 (2015) 59 – 77. arXiv:1502.05314, doi:http://dx.doi.org/10.1016/j.pnpnp.2015.01.002. URL <http://www.sciencedirect.com/science/article/pii/S0146641015000034>

- [10] R. Machleidt, D. Entem, Chiral effective field theory and nuclear forces, *Physics Reports* 503 (1) (2011) 1 – 75. doi: <https://doi.org/10.1016/j.physrep.2011.02.001>.
URL <http://www.sciencedirect.com/science/article/pii/S0370157311000457>
- [11] N. Nevo Dinur, C. Ji, S. Bacca, N. Barnea, Nuclear structure corrections to the Lamb shift in $\mu^3\text{He}^+$ and $\mu^3\text{H}$, *Phys. Lett. B* 755 (2016) 380 – 386. doi: <http://dx.doi.org/10.1016/j.physletb.2016.02.023>.
URL <http://www.sciencedirect.com/science/article/pii/S0370269316001192>
- [12] D. Shiner, R. Dixon, V. Vedantham, Three-Nucleon Charge Radius: A Precise Laser Determination Using ^3He , *Phys. Rev. Lett.* 74 (1995) 3553–3556. doi: [10.1103/PhysRevLett.74.3553](https://doi.org/10.1103/PhysRevLett.74.3553).
URL <http://link.aps.org/doi/10.1103/PhysRevLett.74.3553>
- [13] R. van Rooij, J. S. Borbely, J. Simonet, M. D. Hoogerland, K. S. E. Eikema, R. A. Rozendaal, W. Vassen, Frequency metrology in quantum degenerate helium: Direct measurement of the $2^3S_1 \rightarrow 2^1S_0$ transition, *Science* 333 (2011) 196–198.
- [14] P. Cancio Pastor, L. Consolino, G. Giusfredi, P. De Natale, M. Inguscio, V. A. Yerokhin, K. Pachucki, Frequency metrology of helium around 1083 nm and determination of the nuclear charge radius, *Phys. Rev. Lett.* 108 (2012) 143001. doi: [10.1103/PhysRevLett.108.143001](https://doi.org/10.1103/PhysRevLett.108.143001).
URL <http://link.aps.org/doi/10.1103/PhysRevLett.108.143001>
- [15] V. Patkóš, V. A. Yerokhin, K. Pachucki, Higher-order recoil corrections for triplet states of the helium atom, *Phys. Rev. A* 94 (2016) 052508, arXiv:1610.04060 [physics.atom-clus]. doi: [10.1103/PhysRevA.94.052508](https://doi.org/10.1103/PhysRevA.94.052508).
URL <http://link.aps.org/doi/10.1103/PhysRevA.94.052508>
- [16] V. Patkóš, V. A. Yerokhin, K. Pachucki, Higher-order recoil corrections for singlet states of the helium atom, *Phys. Rev. A* 95 (2017) 012508. doi: [10.1103/PhysRevA.95.012508](https://doi.org/10.1103/PhysRevA.95.012508).
URL <https://link.aps.org/doi/10.1103/PhysRevA.95.012508>
- [17] C. G. Parthey, A. Matveev, J. Alnis, R. Pohl, T. Udem, U. D. Jentschura, N. Kolachevsky, T. W. Hänsch, Precision Measurement of the Hydrogen-Deuterium $1S - 2S$ Isotope Shift, *Phys. Rev. Lett.* 104 (2010) 233001.
- [18] U. D. Jentschura, A. Matveev, C. G. Parthey, J. Alnis, R. Pohl, T. Udem, N. Kolachevsky, T. W. Hänsch, Hydrogen-deuterium isotope shift: From the $1S$ - $2S$ -transition frequency to the proton-deuteron charge-radius difference, *Phys. Rev. A* 83 (2011) 042505.
- [19] A. Beyer, J. Alnis, K. Khabarova, A. Matveev, C. G. Parthey, D. C. Yost, R. Pohl, T. Udem, T. W. Hänsch, N. Kolachevsky, Precision spectroscopy of the $2S$ - $4P$ transition in atomic hydrogen on a cryogenic beam of optically excited $2S$ atoms, *Ann. d. Phys. (Berlin)* 525 (2013) 671–679.
- [20] I. Sick, Elastic electron scattering from light nuclei, *Prog. Part. Nucl. Phys.* 47 (1) (2001) 245 – 318. doi: [http://dx.doi.org/10.1016/S0146-6410\(01\)00156-9](http://dx.doi.org/10.1016/S0146-6410(01)00156-9).
URL <http://www.sciencedirect.com/science/article/pii/S0146641001001569>
- [21] O. J. Hernandez, N. Nevo Dinur, C. Ji, S. Bacca, N. Barnea, Update on nuclear structure effects in light muonic atoms, *Hyperfine Interactions* 237 (2016) 158, [arXiv:1604.06496]. doi: [10.1007/s10751-016-1371-9](https://doi.org/10.1007/s10751-016-1371-9).
URL <http://dx.doi.org/10.1007/s10751-016-1371-9>
- [22] C. E. Carlson, M. Gorchtein, M. Vanderhaeghen, Two-photon exchange correction to $2S - 2P$ splitting in muonic ^3He ions, *Phys. Rev. A* 95 (2017) 012506. arXiv:1611.06192v1[nucl-th], doi: [10.1103/PhysRevA.95.012506](https://doi.org/10.1103/PhysRevA.95.012506).
URL <http://link.aps.org/doi/10.1103/PhysRevA.95.012506>
- [23] S. J. Brodsky, R. G. Parsons, Precise theory of the Zeeman spectrum for atomic hydrogen and deuterium and the Lamb shift, *Phys. Rev.* 163 (1967) 134–146.
- [24] E. Borie, Lamb shift in light muonic atoms – Revisited, *Ann. Phys.* 327 (2012) 733.
- [25] E. Borie, Lamb shift in light muonic atoms – Revisited, arXiv: 1103.1772-v7 [physic.atom-ph] (2014).
- [26] A. Krutov, A. Martynenko, G. Martynenko, R. Faustov, Theory of the Lamb shift in muonic helium ions, *J. Exp. Theo. Phys.* 120 (2015) 73.
- [27] A. P. Martynenko, E. N. Elekina, Hyperfine structure of S- and P-wave states in muonic-helium ion, *Phys. At. Nucl.* 73 (12) (2010) 2074–2082. doi: [10.1134/S1063778810120124](https://doi.org/10.1134/S1063778810120124).
URL <http://dx.doi.org/10.1134/S1063778810120124>
- [28] A. P. Martynenko, Hyperfine Structure of the S levels of the muonic helium ion, *J. Exp. Theo. Phys.* 106 (2008) 690.
- [29] R. Faustov, A. Martynenko, G. Martynenko, V. Sorokin, Radiative nonrecoil nuclear finite size corrections of order $\alpha(Z\alpha)^5$ to the hyperfine splitting of S-states in muonic hydrogen, *Physics Letters B* 733 (2014) 354 – 358. doi: <http://dx.doi.org/10.1016/j.physletb.2014.04.056>.
URL <http://www.sciencedirect.com/science/article/pii/S0370269314002962>
- [30] E. N. Elekina, A. P. Martynenko, Fine and Hyperfine Structure of the Muonic ^3He Ion, *Physics of Atomic Nuclei* 73 (11) (2010) 1828–1837. doi: [10.1134/S1063778810110049](https://doi.org/10.1134/S1063778810110049).
URL <http://dx.doi.org/10.1134/S1063778810110049>
- [31] U. D. Jentschura, B. J. Wundt, Semi-analytic approach to higher-order corrections in simple muonic bound systems: vacuum polarisation, self-energy and radiative-recoil., *Eur. Phys. J. D* 65 (2011) 357.
- [32] U. D. Jentschura, Relativistic reduced-mass and recoil corrections to vacuum polarization in muonic hydrogen, muonic deuterium, and muonic helium ions, *Phys. Rev. A* 84 (2011) 012505.
- [33] E. Y. Korzinin, V. G. Ivanov, S. G. Karshenboim, $\alpha^2(Z\alpha)^4m$ contributions to the Lamb shift and the fine structure in light muonic atoms, *Phys. Rev. D* 88 (2013) 125019.
- [34] S. G. Karshenboim, V. G. Ivanov, E. Y. Korzinin, Relativistic recoil corrections to the electron-vacuum-polarization contribution in light muonic atoms, *Phys. Rev. A* 85 (2012) 032509.
- [35] G. Källén, A. Sabry, Fourth order vacuum polarization, *Dan. Mat. Fys. Medd.* 29 (17) (1955) 1–20.
- [36] U. D. Jentschura, Lamb shift in muonic hydrogen – I. Verification and update of theoretical predictions, *Ann. Phys.* 326

- (2011) 500.
- [37] K. Pachucki, Theory of the Lamb shift in muonic hydrogen, *Phys. Rev. A* 53 (1996) 2092–2100.
 - [38] S. G. Karshenboim, private communication (2015).
 - [39] E. Borie, Hadronic vacuum polarization correction in muonic atoms, *Z. Phys. A* 302 (1981) 187.
 - [40] A. A. Krutov, A. P. Martynenko, Lamb shift in the muonic deuterium atom, *Phys. Rev. A* 84 (2011) 052514.
 - [41] W. Barker, F. Glover, Reduction of relativistic two-particle wave equations to approximate forms: III, *Phys. Rev.* 99 (1955) 317.
 - [42] U. D. Jentschura, Proton radius, Darwin-Foldy term and radiative corrections, *Eur. Phys. J. D* 61 (2011) 7.
 - [43] P. J. Mohr, B. N. Taylor, D. B. Newell, CODATA recommended values of the fundamental physical constants: 2010, *Rev. Mod. Phys.* 84 (2012) 1527.
 - [44] J. L. Friar, Nuclear finite-size effects in light muonic atoms, *Ann. Phys.* 122 (1979) 151–196.
 - [45] K. Pachucki, private communication (2015).
 - [46] V. A. Yerokhin, Nuclear recoil in the Lamb shift of hydrogen-like atoms, ECT* Workshop on the Proton Radius Puzzle (2016).
URL <http://www.ectstar.eu/node/1659>
 - [47] S. G. Karshenboim, E. Y. Korzinin, V. A. Shelyuto, V. G. Ivanov, Recoil correction to the proton finite-size contribution to the Lamb shift in muonic hydrogen, *Phys. Rev. D* 91 (2015) 073003.
 - [48] V. G. Ivanov, S. G. Karshenboim, Lamb Shift in Light Hydrogen-Like Atoms, Springer Berlin Heidelberg, Berlin, Heidelberg, 2001, pp. 637–650. doi:10.1007/3-540-45395-4_44.
URL http://dx.doi.org/10.1007/3-540-45395-4_44
 - [49] J. Friar, G. Payne, Higher-order nuclear-size corrections in atomic hydrogen, *Phys. Rev. A* 56 (1997) 5173.
 - [50] K. Pachucki, Nuclear structure corrections in muonic deuterium, *Phys. Rev. Lett.* 106 (2011) 193007.
 - [51] J. L. Friar, Nuclear polarization corrections to μ -d atoms in zero-range approximation, *Phys. Rev. C* 88 (2013) 034003.
 - [52] I. Sick, Precise Radii of Light Nuclei from Electron Scattering, Springer Berlin Heidelberg, Berlin, Heidelberg, 2008, pp. 57–77. doi:10.1007/978-3-540-75479-4_4.
URL http://dx.doi.org/10.1007/978-3-540-75479-4_4
 - [53] A. P. Martynenko, private communication (2016).
 - [54] M. I. Eides, H. Grotch, Radiative correction to the nuclear-size effect and hydrogen-deuterium isotopic shift, *Phys. Rev. A* 56 (1997) R2507–R2509.
 - [55] I. Sick, Zemach radius of ^3He and ^4He , *Phys. Rev. C* 90 (2014) 064002. doi:10.1103/PhysRevC.90.064002.
URL <http://link.aps.org/doi/10.1103/PhysRevC.90.064002>
 - [56] C. Joachain, Polarisation nucléaire dans les atomes mésiques de tritium, d’hélium 3 et d’hélium 4, *Nuclear Physics* 25 (1961) 317 – 327. doi:[http://dx.doi.org/10.1016/0029-5582\(61\)90162-6](http://dx.doi.org/10.1016/0029-5582(61)90162-6).
URL <http://www.sciencedirect.com/science/article/pii/0029558261901626>
 - [57] E. Borie, G. A. Rinker, The energy levels of muonic atoms, *Rev. Mod. Phys.* 54 (1982) 67.
 - [58] M. C. Birse, J. A. McGovern, Proton polarisability contribution to the Lamb shift in muonic hydrogen at fourth order in chiral perturbation theory, *Eur. Phys. J. A* 48 (2012) 120, [arXiv:1206.3030 (hep-ph)].
 - [59] M. Gorchtein, private communication (2016).
 - [60] S. J. Brodsky, G. W. Erickson, Radiative level shifts. III. Hyperfine structure in hydrogenic atoms, *Phys. Rev.* 148 (1966) 26–46.
 - [61] A. C. Zemach, Proton structure and the hyperfine shift in hydrogen, *Phys. Rev.* 104 (1956) 1771–1781.
 - [62] J. L. Friar, I. Sick, Zemach moments for hydrogen and deuterium, *Phys. Lett. B* 579 (2004) 285.
 - [63] E. Borie, Lamb shift in muonic ^3He , *Zeitschrift für Physik A Atoms and Nuclei* 297 (1) (1980) 17–18. doi:10.1007/BF01414239.
URL <http://dx.doi.org/10.1007/BF01414239>
 - [64] H. Grotch, D. R. Yennie, Effective potential model for calculating nuclear corrections to the energy levels of hydrogen, *Rev. Mod. Phys.* 41 (1969) 350–374. doi:10.1103/RevModPhys.41.350.
URL <http://link.aps.org/doi/10.1103/RevModPhys.41.350>
 - [65] E. Borie, private communication (2015).
 - [66] A. P. Martynenko, private communication (2017).
 - [67] J. L. Friar, G. L. Payne, Nuclear corrections to hyperfine structure in light hydrogenic atoms, *Phys. Rev. C* 72 (2005) 014002. doi:10.1103/PhysRevC.72.014002.
URL <http://link.aps.org/doi/10.1103/PhysRevC.72.014002>
 - [68] M. I. Eides, Weak interaction contributions to hyperfine splitting and Lamb shift in light muonic atoms, *Phys. Rev. A* 85 (2012) 034503.
 - [69] CREMA Collaboration, to be published.



Theory of the $n = 2$ levels in muonic deuterium



Julian J. Krauth^{a,*}, Marc Diepold^a, Beatrice Franke^a,
Aldo Antognini^{b,c}, Franz Kottmann^b, Randolph Pohl^a

^a Max-Planck-Institut für Quantenoptik, 85748 Garching, Germany

^b Institute for Particle Physics, ETH Zurich, 8093 Zurich, Switzerland

^c Paul-Scherrer-Institute, 5232 Villigen, Switzerland

ARTICLE INFO

Article history:

Received 28 August 2015

Accepted 22 December 2015

Available online 18 January 2016

Keywords:

Muonic deuterium

Lamb shift

Hyperfine structure

Fine structure

QED

Proton radius puzzle

ABSTRACT

The present knowledge of Lamb shift, fine- and hyperfine structure of the 2S and 2P states in muonic deuterium is reviewed in anticipation of the results of a first measurement of several 2S – 2P transition frequencies in muonic deuterium (μd). A term-by-term comparison of all available sources reveals reliable values and uncertainties of the QED and nuclear structure-dependent contributions to the Lamb shift, which are essential for a determination of the deuteron rms charge radius from μd . Apparent discrepancies between different sources are resolved, in particular for the difficult two-photon exchange contributions. Problematic single-sourced terms are identified which require independent recalculation.

© 2016 Elsevier Inc. All rights reserved.

Contents

1. Introduction.....	169
2. Overview.....	171
3. Lamb shift in muonic deuterium.....	172
3.1. QED contributions.....	172
3.2. Radius-dependent contributions to the Lamb shift.....	177
3.3. Two-photon exchange contribution to the Lamb shift	178
3.3.1. Modern determinations of $\Delta E_{\text{TPE}}^{\text{LS}}$	180
3.3.2. Comparison of terms and further corrections	183

* Corresponding author.

E-mail addresses: julian.krauth@mpq.mpg.de (J.J. Krauth), randolf.pohl@mpq.mpg.de (R. Pohl).

3.3.3.	Our choice	184
3.4.	Total Lamb shift in muonic deuterium	184
4.	2S hyperfine splitting	184
4.1.	Fermi and Breit contributions	184
4.2.	Vacuum polarization (VP) and self-energy (SE) contributions	185
4.3.	Zemach radius	187
4.4.	Nuclear polarizability contributions to the 2S HFS	188
4.5.	Further corrections to the 2S HFS	189
4.6.	Total 2S hyperfine splitting	189
5.	2P fine structure	190
6.	2P levels	190
7.	Summary	193
	Acknowledgments	193
	Appendix. The Darwin–Foldy term	193
	References	194

1. Introduction

Laser spectroscopy of $2S \rightarrow 2P$ Lamb shift transitions in muonic atoms and ions promises a tenfold improvement in our knowledge of charge and magnetic radii of the lightest nuclei ($Z = 1, 2$ and higher). Our recent measurement [1,2] of the 2S Lamb shift and the 2S hyperfine splitting (HFS) in muonic hydrogen, μp , in combination with accurate theoretical calculations by many authors, summarized in Ref. [3], has revealed a proton root-mean-square (rms) charge radius of

$$r_p = 0.84087 (26)^{\text{exp}} (29)^{\text{theo}} \text{ fm} = 0.84087 (39) \text{ fm}. \quad (1)$$

This is an order of magnitude more accurate than the value of $r_p = 0.8775(51) \text{ fm}$ evaluated in the CODATA least-squares adjustment [4] of elastic electron–proton scattering [5,6] and many precision measurements in electronic hydrogen [7].

Most strikingly, however, the two values differ by 7 combined standard deviations (7σ). Despite numerous attempts in recent years to explain this “proton radius puzzle”, it remains a mystery [8,9]. Taken at face value, this 7σ discrepancy constitutes one of the biggest discrepancies in the Standard Model. Further data are clearly required to shed light on this puzzle.

Muonic deuterium, μd , has been measured in the same beam time as μp [1,2], and the data are now nearing publication [10]. We anticipate here that the experimental accuracy of the various $2S - 2P$ transitions is of the order of 1 GHz, or, equivalently, $\sim 0.004 \text{ meV}$.¹ Ideally, theory should be accurate on the level of 0.001 meV to exploit the experimental precision, and to determine the deuteron charge radius, r_d , with tenfold better accuracy, compared to the CODATA value [4]

$$r_d (\text{CODATA}) = 2.1424(21) \text{ fm}. \quad (2)$$

The CODATA value originates from a least-squares adjustment of a huge amount of input values, such as the deuteron charge radius from elastic electron scattering [11,12]

$$r_d (e - d \text{ scatt.}) = 2.130(10) \text{ fm}, \quad (3)$$

but also the proton radius from electron scattering [5,6]. These radii are connected because the CODATA adjustment includes many transition frequencies in hydrogen (H) and deuterium (D) [7,4]. In particular, the squared deuteron–proton charge radius difference,

$$r_d^2 - r_p^2 = 3.82007 (65) \text{ fm}^2 \quad (4)$$

¹ 1 meV \cong 241.799 GHz.

is known with high precision from laser spectroscopy of the isotope shift of the 1S – 2S transition in electronic hydrogen and deuterium [13], and state-of-the-art theory [14]. Using Eq. (4) and the muonic hydrogen proton radius given in Eq. (1) we determined a value of [2]

$$r_d (\text{muonic } r_p) = 2.12771 (22) \text{ fm}. \quad (5)$$

Note that the discrepancy of the deuteron charge radii given in Eqs. (2) and (5) is not a new discrepancy, but rather a result of the proton radius discrepancy: Both values of the deuteron radius depend on the isotope shift in Eq. (4). Hence, discrepant values of the proton radius will result in discrepant values of the deuteron radius.

The upcoming μd data [10], on the other hand, will provide a “muonic” value of the deuteron radius that is *independent* of the proton charge radius. As such, it will shed new light on the proton radius puzzle.

We anticipate here that the theory of the Lamb shift in muonic deuterium is limiting the accuracy of the deuteron charge radius from μd , mainly due to the uncertainty of the deuteron polarizability contribution of 0.020 meV which corresponds to a relative uncertainty of 1%. Nevertheless, the deuteron charge radius from μd [10] will have a nearly three times smaller uncertainty than the current CODATA value (Eq. (2)).

To put this uncertainty of 0.020 meV into another perspective: The “proton radius puzzle” in muonic hydrogen, when expressed as a “missing part” in the theory of muonic hydrogen, amounts to 0.329(47) meV.

This article is organized as follows: We first summarize the current knowledge of the muonic deuterium Lamb shift theory (Section 3) which is required to determine the deuteron rms charge radius r_d from the μd measurement [10]. We separate the Lamb shift theory into “radius-independent” terms that do not depend on the nuclear structure (Section 3.1), terms that depend explicitly on the rms charge radius (Section 3.2), and the deuteron polarizability contribution that constitutes the main theoretical limitation (Section 3.3). In Section 4, we list all contributions to the 2S hyperfine splitting (HFS) in μd . The 2S HFS depends on the magnetic properties of the deuteron through the Zemach radius. Other nuclear structure contributions matter, too, so we separate again terms: Section 4.2 lists the terms that do not depend strongly on the deuteron structure, Section 4.3 is devoted to the Zemach correction, Section 4.4 is concerned with the deuteron polarizability contribution which has recently been calculated for the first time [15]. This term constitutes the main uncertainty for the 2S HFS prediction. Additional contributions to the 2S HFS are mentioned in Section 4.5. The 2P fine structure is summarized in Section 5, and the 2P fine- and hyperfine level structure, including level mixing, is given in Section 6.

The sign convention in this article is such that the final, measured energy difference (Lamb shift, 2S-HFS, fine structure) is always *positive*. For the fine and hyperfine splittings this convention is the natural choice adopted by all other authors, too. For the Lamb shift, however, some authors calculate 2S *level shifts* and their published values have the opposite sign. This is because the 2S level is lower (more bound) than the 2P level (due to the dominant vacuum-polarization term item #1 in Table 1), see Fig. 1, and *positive* level shifts *decrease* the measured 2P – 2S energy difference. The numbers we quote are all matched to our sign convention.

Item numbers # in the first column of Tables 1 and 4 follow the nomenclature in Ref. [3]. In the tables, we usually identify the “source” of all values entering “our choice” by the first name of the (group of) authors given in adjacent columns (e.g. “B” for Borie). We denote as average “avg.” in the tables the center of the band covered by all values v_i under consideration, with an uncertainty of half the spread, i.e.

$$\text{avg.} = \frac{1}{2} [\text{MAX}(v_i) + \text{MIN}(v_i)] \pm \frac{1}{2} [\text{MAX}(v_i) - \text{MIN}(v_i)]. \quad (6)$$

Throughout the paper, Z denotes the nuclear charge with $Z = 1$ for the deuteron, α is the fine structure constant, m_r is the reduced mass of the muon–deuteron system. “VP” is short for “vacuum polarization”, “SE” is “self-energy”, “RC” is “recoil correction”. “Perturbation theory” is abbreviated as “PT”, and SOPT and TOPT denote 2nd and 3rd order PT, respectively.

Table 1

All known **radius-independent** contributions to the Lamb shift in μd . Values are in meV. Item numbers “#” in the 1st column follow the nomenclature of Ref. [3], which in turn followed the Supplement of Ref. [1]. Items “#” with a dagger † were labeled “New” in Ref. [3], but we introduce numbers here for definiteness. Items # with an asterisk * denote new contributions in this compilation. For Borie [22] we refer to the most recent arXiv version-7 (dated 21 Aug. 2014) which contains several corrections to the published paper [21] (available online 6 Dec. 2011). For Martynenko, numbers #1–#31 refer to rows in Tab. I of Ref. [23]. The values in their more recent paper [24] agree exactly with the earlier values [23]. Numbers in parentheses refer to equations in the respective paper.

#	Contribution	Borie [22]	Martynenko [23]	Jentschura	Karshenboim	Our choice value source Fig.
1	NR one-loop electron VP (eVP)		227.6347 #1	227.6346 [27]	227.63467 [29]	
2	Rel. corr. (Breit-Pauli)	(0.02178) ^a Tab. 1	(0.0177) ^b #7+10	0.021781 [54], [28](17)	0.021781 [30] Tab. IV	
3	Rel. one-loop eVP	227.6577 p. 3 Tab.				
19	Rel. RC to eVP, $\alpha(Z\alpha)^4$	−0.00093 Tab. 1+4				
	Sum of the above	227.6568	(227.6524)	227.6564	227.65645	227.65658 ± 0.00020 avg. 2
4	Two-loop eVP (Källén-Sabry)	1.66622 p. 3 Tab.	1.6660 #2			3
5	One-loop eVP in 2-Coulomb lines $\alpha^2(Z\alpha)^2$	0.1718 p. 3	0.1720 #9	0.172023 [28](13)		4
	Sum of #4 and #5	1.8380	1.8380		1.83804 [29] Tab. I	1.83804 K
6+7	Third order VP	0.00842	0.0086 #4+12+13		0.00842(7) [29] Tab. I	0.00842 ± 0.00007 K
29*	Second-order eVP contribution $\alpha^2(Z\alpha)^4 m$		0.0002 #8+11		0.000203 [36] Tab. VIII “eVP2”	0.00020 K
9	Light-by-light “1:3”: Wichmann-Kroll	−0.00111 p. 4	−0.0011 #5		−0.001098(4) [34]	−0.001098 ± 0.00002 K
10	Virtual Delbrick, “2:2” LbL		0.0001 #6		0.00124(1) [34]	0.00124 ± 0.00002 K
9a [†]	“3:1” LbL				−0.00110(1) [34]	−0.00110 ± 0.00002 K
	Sum: Total light-by-light scatt.	−0.00096	−0.0010		−0.00096(2) [34]	−0.00096 ± 0.00002 K
20	μSE and μVP	−0.774616 p. 11 Tab. 2	−0.7747 #28		−0.77462 [36] Tab. VIII (a)	−0.77462 B
11	Meson SE corr. to eVP $\alpha^2(Z\alpha)^4$	(−0.00589) ^c Tab. 16	−0.0047 ^d #30	−0.00306 [28](29)	−0.00306 [36] Tab. VIII (a)	−0.00306 J+K 6
12	eVP loop in self-energy $\alpha^2(Z\alpha)^4$		−0.0018 #29		−0.00177 [36] Tab. VIII (d)	−0.00177 ± 0.00001 avg. 7
30*	Hadronic VP loop in self-energy $\alpha^2(Z\alpha)^4 m$				−0.00002(4) [36] Tab. VIII (e)	−0.00002 ± 0.00001 avg. 9
13	Mixed eVP + μVP	0.00008 p. 4	0.0001 #3		0.000054 [36] Tab. VIII (b)	0.000054 ± 0.00001 avg. 8
31*	Mixed eVP + hadronic VP				0.000097(10) [36] Tab. VIII (c)	0.000097 ± 0.00001 avg. 10
21	Higher-order corr. to μSE and μVP	−0.002001 p. 11 Tab. 2				
	Sum of #12, 30, 31, and 21	−0.00192	−0.0017		−0.00164(1)	−0.00178 ± 0.00014 avg.
14	Hadronic VP	0.013 ± 5% p. 5+Tab. 4	0.0129 ± 5% #31			0.01290 ± 0.00070 M+B
17	Recoil corr. $(Z\alpha)^4 m^2/M^2$ (Barker-Glover)	0.06724 p. 9/10	0.0672 #23	0.06722 [28](A.3) [27](15)		0.06723 ± 0.00001 avg.
22	Rel. RC $(Z\alpha)^5$	−0.02656 p. 9	−0.0266 #24	−0.026561 [28](32)		−0.02656 avg.
23	Rel. RC $(Z\alpha)^6$		0.0001 #25			0.00010 M
24	Higher-order radiative recoil corr.	−0.00302 p. 9	−0.0026 #27 ^f			−0.00302 B
28 [†]	Rad. (only eVP) RC $\alpha(Z\alpha)^5$		0.0002 #26 ^g	0.000093 [28](46)		0.000093 J
	Sum	228.7797 ± 0.04 ^h	228.7683 ⁱ			228.77356 ± 0.00075

^aDoes not contribute to the sum in Borie’s approach, see text.

^bContains a mistake [32], see text.

^cIn Appendix C, incomplete.

^dMartynenko calculates only a part of this item.

^eThis item is part of #21. (and not of #22 as we erroneously wrote in Tab. 1, footnote f of Ref. [3]).

^fThis is only Tab. 9 from Ref. [41], whereas parts of Tab. 8 should be included here, too [22].

^gThis is only the seagull term [27, 23, 28].

^hValue from Ref. [22] page 13. Compared to Tab. 4 therein, we discard our item #18, *recoil finite size*, of 0.019 meV (see text), and list the terms *remaining order* $(Z\alpha)^6$ and *correction to the* $2P_{1/2}$ level as items (r3[†]) and (r8) in our Tab. 2, respectively.

ⁱThe value of 230.4511 meV given at the end of Refs. [23, 24] includes the deuteron polarizability contribution of 1.680 meV from Ref. [55], discussed in our Sec. 3.3, and the item (r3[†]) of 0.0029 meV listed in our Tab. 2.

2. Overview

The $n = 2$ levels in muonic deuterium are sketched in Fig. 1. The Lamb shift, i.e. the splitting between the 2S and the $2P_{1/2}$ state, is sensitive to the rms charge radius of the deuteron, as detailed in Section 3. In contrast, 2S hyperfine splitting (HFS) is caused by the magnetic interaction between the muon spin and the magnetic moment of the deuteron. The finite deuteron size results in a finite magnetization distribution inside the deuteron, and makes the 2S HFS depend on the so-called Zemach radius of the deuteron, as explained in Section 4.

The first calculation of the Lamb shift in muonic deuterium was published by Carboni [16] in 1973. More elaborate calculations of QED effects in muonic atoms were introduced with the seminal paper by Borie and Rinker [17] in 1982.

Later, Pachucki [18] and Borie [19] presented very detailed calculations of many terms for muonic hydrogen. Borie then extended her μp calculations [19] to the case of muonic deuterium [20]. After our measurements in muonic hydrogen [1,2] and deuterium, Borie revisited the theory of the $n = 2$ energy levels in light muonic atoms (μp , μd , $\mu^3\text{He}$, and $\mu^4\text{He}$) in Ref. [21]. The published paper [21] (available online 6 Dec. 2011) has subsequently been superseded by the arXiv version of the paper [22]. At the time of this writing, Borie’s paper on the arXiv has reached version 7 (dated 21 Aug. 2014). This is the first source of knowledge on μd summarized in here.

The second source is the group around Faustov, Krutov, Martynenko et al., termed “Martynenko” in here for simplicity. They have published an impressive set of papers on theory of energy levels in light muonic atoms. At the time of this writing, the 2011 paper [23] was the most recent one on the

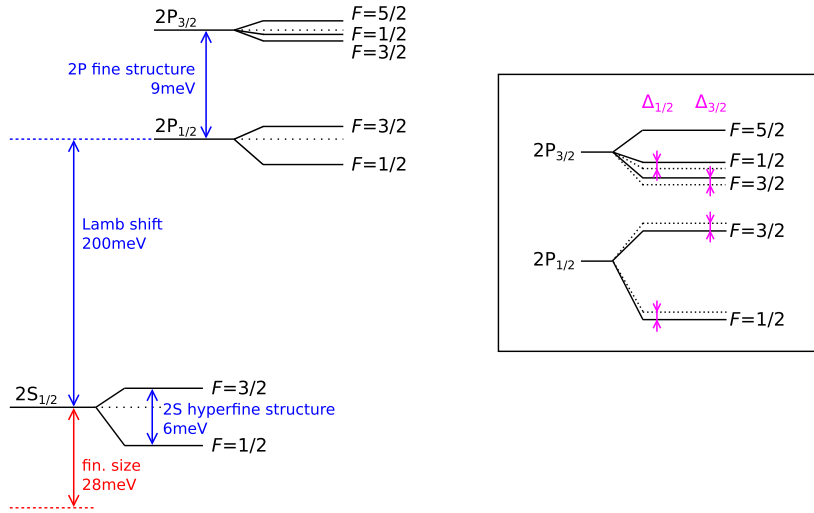


Fig. 1. The 2S and 2P energy levels in muonic deuterium. The inset on the right displays the shifts $\Delta_{1/2}$ and $\Delta_{3/2}$ of the $2P(F = 1/2)$ and $2P(F = 3/2)$ levels due to the mixing of the $F = 1/2$ and $F = 3/2$ states, respectively, as described in Section 6. The figure is not to scale.

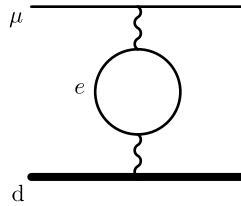


Fig. 2. Item #1, the leading order 1-loop electron vacuum polarization (eVP), also called Uehling term.

Lamb shift in μd , and we based our summary on this paper. Later, Ref. [24] from the Martynenko group appeared, with only minor differences in the results compared to Ref. [23]. For simplicity, we still base our compilation of Lamb shift contributions on the earlier, more detailed, paper [23]. In particular, equation numbers and table entries refer to Ref. [23], unless otherwise noted. For the 2S HFS, Ref. [15] is the main source of numbers from the Martynenko group.

After the advent of the proton radius puzzle from muonic hydrogen, many groups have revisited and improved the theory on muonic hydrogen in an (unsuccessful) attempt to identify wrong or missing theory terms large enough to solve the puzzle (see our compilation [3] for a detailed overview). Thankfully, two groups have (re-)calculated many terms not only for the case of muonic hydrogen, but also for muonic deuterium (and $\mu^3\text{He}$ and $\mu^4\text{He}$): Jentschura, and Karshenboim's group with Ivanov, Korzinin, and Shelyuto, have published many papers on muonic deuterium which are included in the present compilation.

3. Lamb shift in muonic deuterium

3.1. QED contributions

One-loop electron vacuum polarization (eVP) (Fig. 2), the so-called Uehling term [25], accounts for 99.5% of the nuclear-structure-independent part of the Lamb shift in μd . It is therefore mandatory to double-check this term as thoroughly as possible.

Borie has argued [17,20–22] that the Uehling term should ideally not be treated perturbatively. Instead, the Dirac equation should be solved numerically after adding the Uehling potential to the

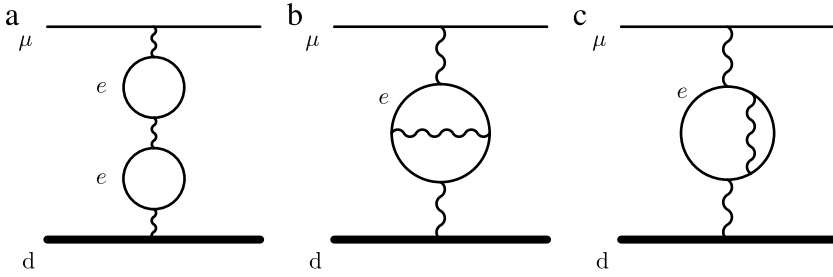


Fig. 3. Item #4, the two-loop eVP (Källén–Sabry) contribution.

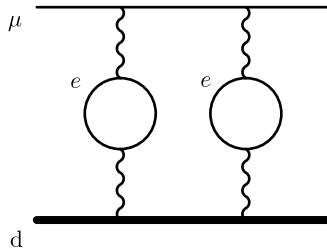


Fig. 4. Item #5, the one-loop eVP in 2-Coulomb lines.

electrostatic Coulomb potential. For light muonic atoms such as muonic deuterium, however, both approaches should give accurate results [22]. This has been demonstrated for muonic *hydrogen*, where the nonperturbative result of Indelicato [26] is in excellent agreement with the perturbative results of Pachucki [18] and Borie [19], see Ref. [3].

For muonic *deuterium*, only perturbative calculations exist, albeit with two slightly different approaches:

Martynenko et al. [23], Jentschura [27,28] and Karshenboim et al. [29,30] calculate the leading order eVP nonrelativistically (item #1 in Table 1), and apply a relativistic correction (item #2). The most important item #1 is in excellent agreement for all three authors, as well as with the value of 227.635 meV obtained by Carboni [16] in 1973. For item #2 see below.

Borie, in contrast, uses relativistic Dirac wave functions to evaluate the relativistic Uehling term (item #3). The relativistic recoil correction to eVP of order $\alpha(Z\alpha)^4$ (item #19) has to be added, to be able to compare all four results.

It is very reassuring that these results are in excellent agreement, with one exception: Item #2, *rel. corr. (Breit–Pauli)*, from Martynenko [23], 0.0177 meV, differs from the value of 0.02178 meV, calculated by the other three groups, who agree: Borie [22] Tab. 1, Jentschura [27] Tab. I and [28] Eq. (17), and Karshenboim [30] Tab. IV. This item #2 should be the sum of Martynenko’s rows 7 and 10 (*relativistic and VP corrections of order $\alpha(Z\alpha)^2$ in first and second order PT*). For muonic helium-3 and -4 ions [31] the sum agrees exactly with the numbers given by Jentschura in Ref. [27] Eq. (17) and by Karshenboim in Ref. [30] Tab. IV. Martynenko confirmed that their value for our item #2 for muonic deuterium (their rows 7 and 10 in Tab. I of Ref. [23]) contains an error [32].

The average of items #1 + #2 or #3 + #19 is thus calculated from the other three sources only, with excellent agreement:

$$\Delta E (\text{one-loop eVP with rel. corr.}) = 227.65658 \pm 0.00020 \text{ meV.} \quad (7)$$

Our item #4, the *two-loop electron-VP correction*, usually called “Källén–Sabry” contribution [33], displayed in Fig. 3, is the second largest “purely QED” contribution to the Lamb shift. Borie [22] and Martynenko [23] give values which are in very good agreement.

Our item #5, the *one-loop eVP insertion in 2 Coulomb lines* shown in Fig. 4, has been calculated with very good agreement by Borie [22], Martynenko [23], and Jentschura [28].

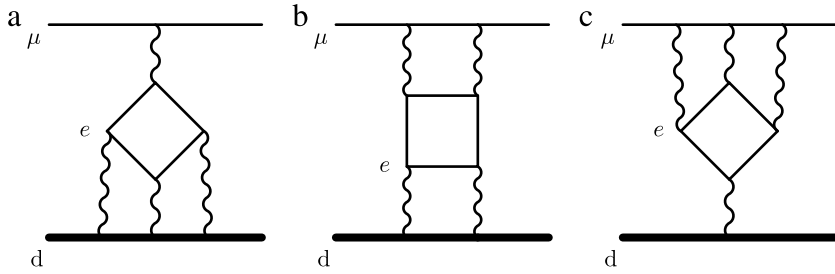


Fig. 5. The three contributions to Light-by-light scattering: (a) Wichmann–Kroll or “1:3” term, item #9, (b) Virtual Delbrück or “2:2” term, item #10, and (c) inverted Wichmann–Kroll or “3:1” term, item #9a[†].

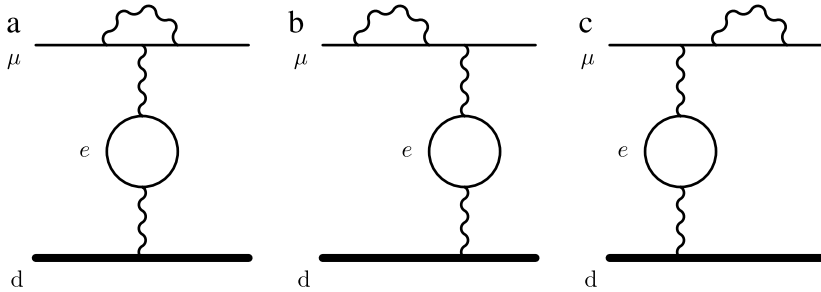


Fig. 6. Item #11, muon self-energy corrections to the electron vacuum polarization $\alpha^2(Z\alpha)^4$. This figure is Fig. 2 from Jentschura [35]. It corresponds to Fig. 6(a) from Karshenboim [36].

Karshenboim et al. [29] give the sum of items #4 and #5. It is in agreement with the sums from Borie and Martynenko. We use Karshenboim’s value because it is given with more significant digits.

Light-by-light (LbL) scattering (see Fig. 5) contains 3 terms, Wichmann–Kroll, or “1:3” LbL (item #9 in [3]), Virtual Delbrück, or “2:2” LbL (item #10 in [3]), and the “inverted Wichmann–Kroll” or “3:1” LbL (called “new” item in [3]). For definiteness, we label this term “item #9a” from now on. Considerable cancellations occur in the sum of all three terms which has been evaluated in Ref. [34]. Both Borie and Martynenko calculate only #9, and adopt the full result from Karshenboim [34]. We use Karshenboim’s result [34].

Item #11 *muon self-energy (SE) correction to electron vacuum polarization (eVP)* $\alpha^2(Z\alpha)^4$ is displayed in Fig. 6. Jentschura [28] (Eq (29b), Fig. 2) and Karshenboim [36] (Tab. VIII (a), Fig. 6a) agree in the result for the complete calculation, -0.00306 meV. Martynenko [23] Eq. (80) calculates only the contribution from Fig. 6(a), following Pachucki’s Eq. (39) in Ref. [18]. Also Borie [22] calculates part of this term in her Appendix C.

Higher-order corrections to the muon self-energy and vacuum polarization are denoted items #12, #13, #21, #30* and #31* in Table 1. For muonic hydrogen [3] we used Borie’s value of item #21, noting that this includes item #12. Afterwards, Karshenboim et al. [36] have recalculated many of these small terms. We construct the corresponding sum from each source, which we average.

Item #12 is shown in Fig. 7. It is Martynenko’s item 29. This contribution has been confirmed by Karshenboim [36] Tab. VIII (d). As mentioned in Ref. [3], item #12 is included in Borie’s value for item #21.

Item #13, *mixed muon–electron VP* is depicted in Fig. 8. Borie and Martynenko calculated only the contribution from Fig. 8(a), see Fig. 3 in Ref. [37]. This is Martynenko’s item 3, “VP and MVP contribution in one-photon interaction”. Karshenboim gives the sum of both diagrams in Fig. 8 in Ref. [36] Tab. VIII (d).

Item #30* (#31*) is somewhat similar to item #12 (#13), with the electron (muon) loop replaced by a hadronic VP loop, see Fig. 9 (Fig. 10). It has only been calculated by Karshenboim [36], Tab. VIII item (e) ((c)).

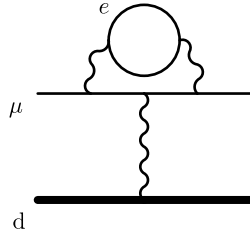


Fig. 7. Item #12, *eVP loop in SE* are radiative corrections with VP effects. This is Fig. 11 from Martynenko [23] which is the same as Fig. 4 in Pachucki [18]. It is Karshenboim's Fig. 6(d) in Ref. [36].

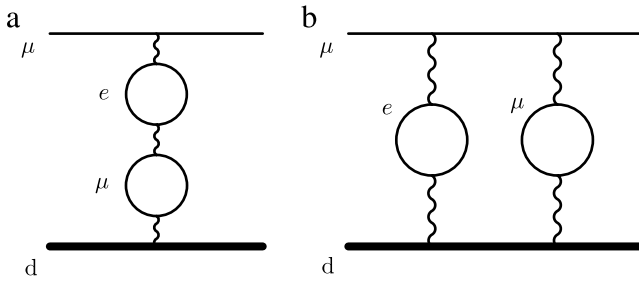


Fig. 8. Item #13, the mixed *eVP-μVP* contribution.

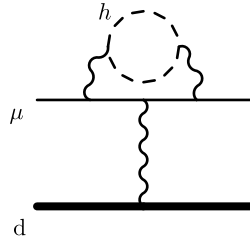


Fig. 9. Item #30*, hadronic VP in SE contribution, corresponds to Fig. 6(e) in Karshenboim [36].

Item #32, the muon VP in SE correction shown in Fig. 11, is not included as a separate item in our Table 1. It should already be automatically included in any QED value which has been rescaled from the QED of electronic deuterium by a simple mass replacement $m_e \rightarrow m_\mu$ [38]. The size of this item #32 can be estimated from the relationship found by Borie [39], that the ratio of hadronic to muonic VP is 0.66. With Karshenboim's value of item #30* [36] one would get $\Delta E(\#32) = -0.000024/0.66 \text{ meV} = -0.000036 \text{ meV}$.

Item #21, *higher-order correction to μ SE and μ VP*, is Borie's *muon Lamb shift, higher orders*, calculated in her Appendix C of Ref. [22]. This item includes item #12, *eVP loop in self-energy* $\alpha^2(Z\alpha)^4$, as explained on p. 131 of Ref. [3].²

The sum of items #12, #13, #21, #30*,³ and #31* agree well enough to justify taking the average, $-0.00178 \pm 0.00014 \text{ meV}$ as our choice.

Item #14, *hadronic VP*, is evaluated by Borie [22] (p. 5) as 0.013 meV, who assigns a 5% uncertainty to this estimate which is based on Refs. [39,40,17,41].

² There is a typo in footnote f of Tab. 1 in Ref. [3], where we wrote, item #12 "is part of #22" (instead of #21).

³ The asterisk * indicates that this item had not been considered for muonic hydrogen in Ref. [3].

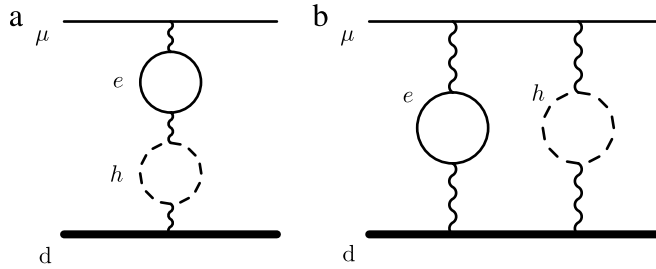


Fig. 10. Item #31*, the mixed eVP- and hadronic VP contribution, comes from the Uehling correction to the hadronic VP correction. See Fig. 6(c) in Karshenboim [36].

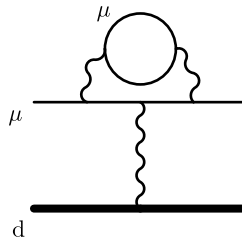


Fig. 11. Item #32, muon VP in SE contribution, is automatically included in a rescaled electronic deuterium QED value of higher-order SE contributions (see text).

Martynenko's value of 0.0129 meV [23], Tab. 1, row 31, agrees very nicely. They quote Refs. [40,42], and estimate the uncertainty to 5% as well.

The previous items #15 and #16 in Ref. [3] are higher-order corrections to the hadronic VP and have only been calculated for muonic hydrogen by Martynenko's group [43,44], where they are small (0.000047 meV and -0.000015 meV, respectively). It is expected that their magnitude will be similar in muonic deuterium. Hence these terms are included in the 5% uncertainty assigned to item #14.

Item #18 in Ref. [3] is the *recoil finite size* contribution in Borie [21,22]. According to Pachucki, this item #18, which was first calculated by Friar [45], should be discarded [46], as we did for muonic hydrogen in Ref. [3].

Item #17 is the Barker–Glover correction [47], termed *additional recoil* by Borie. This item includes the Darwin–Foldy (DF) term that arises from the Zitterbewegung of the nucleus. Different conventions are used in the literature [48–50] which has caused some confusion (see Appendix). As in the case of muonic hydrogen [3], we follow the “atomic physics” convention [50], also adopted by CODATA-2010 [4]. In this convention the DF term is a recoil correction of order $(Z\alpha)^4 m^3/M^2$ to the energy levels, and *not* a part of the rms charge radius. So, for a spin-1 nucleus such as the deuteron (as well as for the spin-0 ^4He nucleus) the DF term is absent [51]. In this way, the charge radii from muonic hydrogen [1,2] and deuterium [10] are directly comparable to the CODATA-2010 values [4], see Eqs. (26) and (27) therein. It is also the convention used in the most recent measurement of the H–D isotope shift [13,14] which is the origin of the difference of the squared rms radii of the deuteron and the proton given in Eq. (4). Note that the DF term is nonzero in the case of hydrogen and muonic hydrogen because the proton has spin 1/2 (see [3], item #17 in Tab. 1 therein).

Item #28[†] is the *rad. (only eVP) RC* $\propto (Z\alpha)^5$ labeled “new” in Ref. [3]. For definiteness, we enumerate it as item #28[†]. It is the sum of three individual parts which sum up to 0.000093 meV in Ref. [28], Eq. (46b).

Martynenko's row 26 of Tab. I in Ref. [23], *recoil corr. to VP of order* $\alpha(Z\alpha)^5$ (*seagull term*) is only the seagull term from the three terms evaluated by Jentschura, taken from Ref. [27], Eq. (29). We take the full result from Ref. [28], Eq. (46b).

Item #24 are radiative recoil corrections of order $\alpha(Z\alpha)^5$ and $(Z^2\alpha)(Z\alpha)^4$, first introduced for μp by Pachucki [18], Eq. (51), based on Ref. [52]. Borie writes (p. 9 of Ref. [22]) that these terms correspond to

Tab. 9 and two additional terms from Tab. 8 of the review of Eides et al. [41]. The sum is -0.00302 meV for μ d. Martynenko et al. (Ref. [23], row 27 of Tab. 1, and Eq. (71)), on the other hand, evaluate only the terms from Tab. 9 of Eides [41], which gives -0.0026 meV. We use Borie's complete result.

Item #29*, the $\alpha^2(Z\alpha)^4 m$ contribution to the Lamb shift, is new and has not been considered for muonic hydrogen in Ref. [3]. We keep enumerating the items, making this item #29* (see footnote 3).

Martynenko gives this as the sum of rows 8 and 11 in Tab. 1 of [23], *relativistic and two-loop VP corrections of order $\alpha^2(Z\alpha)^4$ in 1st and 2nd order PT*. They sum up to $-0.0002 + 0.0004 = 0.0002$ meV. Karshenboim calculated the complete correction of this order, with recoil corrections included and calls it $eVP2$ in Tab. VIII of Ref. [36]. Their value of 0.000203 meV replaces Martynenko's rows 8 and 11 [38].

Numerically this item #29* is of little practical importance, because it is so tiny: 0.000173 meV in μ p, and 0.000203 meV in μ d. Of course, the calculation of this term was an important confirmation that previously uncalculated higher-order terms are not responsible for the proton radius discrepancy. It is very reassuring that the two different approaches of Martynenko [23] and Karshenboim [36] give the same result. Interestingly, there is no such an agreement for the cases of muonic helium-3 and -4 ions. In view of our recent measurements in muonic helium-3 and -4 [53], this disagreement may deserve further study, even though the size of the terms is small compared to the overall uncertainty.

The sum of all contributions without explicit nuclear structure dependence summarized in Table 1 amounts to

$$\Delta E_{\text{rad.}-\text{indep.}}^{\text{LS}} = 228.77356 \pm 0.00075 \text{ meV.} \quad (8)$$

3.2. Radius-dependent contributions to the Lamb shift

The radius-dependent contributions to the Lamb shift [24,22,30] are listed in Table 2. Generally, the finite size of the nucleus affects mainly the S states whose wave function is nonzero at the origin, where the nucleus resides. The main finite size contributions to the nS states have been given to order $(Z\alpha)^6$ by Friar [45]

$$\Delta E_{\text{fin. size}} = \frac{2\pi Z\alpha}{3} |\Psi(0)|^2 \left[\langle r^2 \rangle - \frac{Z\alpha m_r}{2} \langle r^3 \rangle_{(2)} + (Z\alpha)^2 (F_{\text{REL}} + m_r^2 F_{\text{NREL}}) \right]. \quad (9)$$

Here, $\Psi(0)$ denotes the muon wave function at the origin, $\langle r^2 \rangle$ is the rms charge radius of the nucleus, and $\langle r^3 \rangle_{(2)}$ is its "Friar moment".⁴ As detailed in Section 3.3 there is no contribution from the Friar moment due to a cancellation with part of the inelastic deuteron "polarizability" contributions.

In Eq. (9), F_{REL} and F_{NREL} contain various moments of the nuclear charge distribution, see Ref. [45], and in particular the Appendix E therein for analytic expressions for some simple model charge distributions.

The leading order finite size effect, item (r1) in Table 2, is the first term in Eq. (9). It originates from the one-photon exchange with a deuteron form factor insertion shown in Fig. 12 and is proportional to the rms charge radius of the deuteron, $\langle r_d^2 \rangle$.

For (r2), the radiative correction $\alpha(Z\alpha)^5$, we chose Martynenko's value: The equations for the calculation of this term are given in [57]. Borie [22], Tab. 14 uses Eq. (10) of Ref. [57] which gives the total radiative correction of order $\alpha(Z\alpha)^5$, i.e. the sum of Eqs. (7) and (9) in Ref. [57]. Martynenko [23], in contrast, uses Eq. (9) of Ref. [57], stating that the additional polarization correction, Eq. (7) in Ref. [57], which is included in Eq. (10), cancels with a part of the (inelastic) deuteron polarizability contribution. The finite size correction to the Lamb shift of order $(Z\alpha)^6$ has first been calculated by Friar [45], see in particular Appendix E therein. Both Borie [22] (p. 30) and Martynenko [24] (Eq. (33)) follow Friar [45] and evaluate this contribution as the sum of two terms which we list separately:

⁴ $\langle r^3 \rangle_{(2)}$ has been coined "third Zemach moment" by Friar [45]. To avoid confusion with the "Zemach radius" r_Z that appears in the finite size effect in the 2S hyperfine splitting (Section 4.3) we adopt the term "Friar moment" as recently suggested by Karshenboim [56].

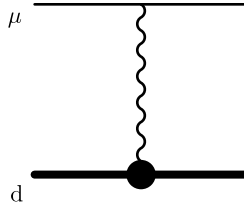


Fig. 12. Item (r1), the leading nuclear finite size correction stems from a one-photon interaction with a deuteron form factor insertion, indicated by the thick dot.

The first one, (r3), has an explicit $\langle r_d^2 \rangle$ dependence, while the second one, (r3'), is usually evaluated for an exponential charge distribution, since a model-independent evaluation of this term is prohibitively difficult [22]. These terms (r3) and (r3') which arise from Ref. [45] consider third-order perturbation theory in the finite size potential correction and relativistic corrections of the Schrödinger wave functions. There are corrections of the two-photon exchange (see Section 3.3) of the same order $(Z\alpha)^6$, but these are of different origin.

Small differences between the formulas given by Borie [22] and Martynenko [24] result in values for (r3') of 0.0033 meV and 0.0029 meV, respectively. For example, the term $\langle r^2 \rangle \langle \ln(\mu r) \rangle$, which is part of F_{REL} in Eq. (9),⁵ is attributed to (r3) and (r3') by Martynenko and Borie, respectively. Following our usual procedure one obtains an average $\Delta E(\text{r3}') = 0.0031(2)$ meV. However, two further considerations prompted us to increase this uncertainty by a factor of three: The value of (r3') depends on the model of the charge distribution, and both Borie and Martynenko used an exponential one. For comparison, the worst case assumption of a uniform charge distribution with $r_d = 2.130(10)$ fm [11] gives $\Delta E(\text{r3}') = 0.0036$ meV. More importantly, it is not clear if (r3') is (partially) canceled by a part of the inelastic $(Z\alpha)^6$ contributions, similar to the cancellation of the $(Z\alpha)^5$ Friar term, explained in Section 3.3. This can however only be answered by a dedicated calculation [38]. We adopt $\Delta E(\text{r3}') = 0.0031(6)$ meV and assume that this conservative uncertainty estimate covers model dependence and “higher-order” moments of the charge distribution as well as possible cancellations.

The items (r4) and (r5) do not depend on the shape of the deuteron charge distribution [22,38]. The two-loop vacuum polarization corrections (r6) and (r7) are only given by Martynenko [24].

A correction to the $2P_{1/2}$ level (r8) is given by Borie [22]. Item (r8) shifts the $2P_{1/2}$ level “upwards” (less bound). This *increases* the energy difference between the 2S and $2P_{1/2}$ levels, which explains the positive sign of this contribution in Table 2. At the same time, this term *decreases* the fine structure ($2P_{3/2} - 2P_{1/2}$ energy difference) and is hence listed as item (f10) with a negative sign in Table 5.

The total radius-dependent contribution to the Lamb shift yields

$$\Delta E_{\text{rad.,-dep.}}^{\text{LS}} = -6.11025(28) r_d^2 \text{ meV/fm}^2 + 0.00310(60) \text{ meV.} \quad (10)$$

3.3. Two-photon exchange contribution to the Lamb shift

Historically, the two-photon exchange (TPE) contribution to the Lamb shift (LS) in muonic atoms has been considered the sum of the two parts displayed in Fig. 13 (a, b) and (c, d), respectively:

$$\Delta E_{\text{TPE}}^{\text{LS}} = \Delta E_{\text{Friar}}^{\text{LS}} + \Delta E_{\text{inelastic}}^{\text{LS}}. \quad (11)$$

The elastic “Friar moment” contribution, $\Delta E_{\text{Friar}}^{\text{LS}}$, also known as “third Zemach moment” $\langle r^3 \rangle_{(2)}$ contribution, shown in Fig. 13(a, b) is sensitive to the shape of the nuclear charge distribution, beyond the leading $\langle r^2 \rangle$ dependence discussed in Section 3.2. This part is traditionally parameterized as being proportional to the third power of the rms charge radius. The coefficient depends on the assumed

⁵ See e.g. Ref. [45] Eq. (43) or Ref. [22] p. 30.

Table 2
Coefficients of the **radius-dependent** contributions to the Lamb shift. Values are in meV/fm², except for r3'^e. KS: Källén–Sabry, VP: vacuum polarization, SOPT: second-order perturbation theory.

Contribution	Martynenko [24]	Borie [22] Tab. 14	Karshenboim [30] Tab. III	Our choice Value	Source
r1	Leading fin. size corr., $(Z\alpha)^4$	(27)	-6.0732	$\Delta E_{\text{FNS}}^{(0)}$ -6.07310	± 0.00010 Avg.
r2	Radiative corr., $\alpha(Z\alpha)^5$	(62), [23]	b_a	-0.000962	M
r3	Finite size corr. order $(Z\alpha)^6$	(33)	b_b	-0.002124	± 0.000004 Avg.
r4	Uehling corr. (+KS), $\alpha(Z\alpha)^4$	(28)	b_c	-0.01325	± 0.00025 Avg.
r5	One-loop VP in SOPT, $\alpha(Z\alpha)^4$	(29)	b_d	$\Delta E_{\text{FNS}}^{(2)}$ -0.020554	± 0.000067 Avg.
r6	Two-loop VP corr., $\alpha^2(Z\alpha)^4$	(30, 31)	b_e	$\Delta E_{\text{FNS}}^{(1)}$ -0.000105	M
r7	Two-loop VP in SOPT, $\alpha^2(Z\alpha)^4$	(32)		-0.000095	M
r8	Corr. to the $2P_{1/2}$ level		$b(2p_{1/2})$	$+0.0000606^c$	B
Sum					
r3'	Remaining order $(Z\alpha)^6$ [meV] ^d	(33)	Tab. 4	ΔE_{FNS} -6.11013	± 0.00028
Sum				0.00310	$\pm 0.00060^e$ meV Avg.
					$-6.11025(28)r_d^2 + 0.00310(60)$ meV

^a This value was published with a wrong sign in [23]. The term is from Eq. (9) in [57].

^b This value is obtained in [57], Eq. (10). For further explanations see Section 3.2.

^c The sign is explained in the text.

^d Belongs to r3. Depends on the charge distribution in a non-trivial way, see text.

^e Conservative estimate of the uncertainty including model dependence, see text.

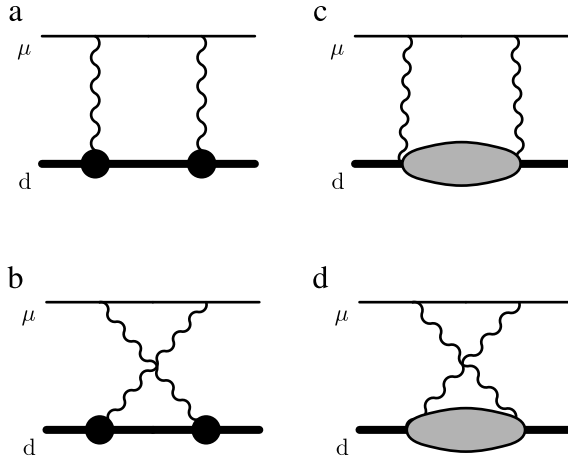


Fig. 13. (a) + (b) Elastic $\Delta E_{\text{Friar}}^{\text{LS}}$, and (c) + (d) inelastic $\Delta E_{\text{inelastic}}^{\text{LS}}$ two-photon exchange (TPE) contribution. The thick dots in (a) indicate deuteron form factor insertions. The blob in (c) and (d) represents all possible excitations of the nucleus. The elastic part (a) + (b) is canceled by a part of the inelastic (polarizability) contribution of (c) + (d) [55,58], just like for electronic deuterium [59,60].

radial charge distribution. For example, Borie gives $\langle r^3 \rangle_{(2)} = 4.0(2) r^3$, where $r = \sqrt{\langle r^2 \rangle}$. For μd , the Friar (3rd Zemach) moment contribution amounts to ~ 0.43 meV [22].

The inelastic part, $\Delta E_{\text{inelastic}}^{\text{LS}}$, frequently termed “nuclear polarizability contribution” is shown in Fig. 13(c, d). It stems from virtual excitations of the nucleus due to the exchange of two photons with the muon. The inelastic contributions are notoriously the least well-known theory contributions and limit the extraction of the charge radius from laser spectroscopy of the Lamb shift.

Early calculations of the contribution from the deuteron polarizability, i.e. the inelastic part $\Delta E_{\text{inelastic}}^{\text{LS}}$ displayed in Fig. 13(c, d) include Fukushima et al. [61], 1.24 meV, Lu and Rosenfelder [62], 1.45 ± 0.06 meV, and Leidemann and Rosenfelder [63], 1.500 ± 0.025 meV. The latter value has been used extensively in the literature.

3.3.1. Modern determinations of $\Delta E_{\text{TPE}}^{\text{LS}}$

Recently, several works have revisited the TPE contributions to the Lamb shift in μd . Table 3 lists the contributions to $\Delta E_{\text{TPE}}^{\text{LS}}$ obtained by Pachucki (2011) [55], Friar (2013) [60], Carlson et al. (2014) [64], the TRIUMF/Hebrew University group in Hernandez et al. (2014) [58], and Pachucki and Wienczek (2015) [65].

As it will turn out that the uncertainty in $\Delta E_{\text{TPE}}^{\text{LS}}$ is by far the largest uncertainty in the determination of r_d from the μd data, we next summarize the main features of these papers. We identify missing and incorrect terms in the original papers. The detailed compilation in Table 3 allows us to obtain the reliable average given in Eq. (17).

In his 2011 paper [55], Pachucki calculated the nuclear structure corrections to the Lamb shift in muonic deuterium using the AV18 potential for the deuteron and obtained $\Delta E_{\text{TPE}}^{\text{LS}} = 1.680(16)$ meV. Moreover, he confirmed that for μd , similar to electronic deuterium [59,60], the elastic “Friar moment” contribution of order $(Z\alpha)^5$, $\Delta E_{\text{Friar}}^{\text{LS}}$ (Fig. 13(a, b)) is canceled by a part of the inelastic two-photon (polarizability) contributions, $\Delta E_{\text{inelastic}}^{\text{LS}}$ (Fig. 13(c, d)). The reason for this cancellation is that the deuteron binding energy of 2.2 MeV is small compared to the muon mass.⁶

Pachucki [55] includes both the elastic and inelastic TPE contribution of the proton, but not the neutron. For the proton, he rescaled the full proton TPE contribution calculated for muonic

⁶ For muonic hydrogen, in contrast, the first excited state of the nucleus (proton) is the Δ resonance with an excitation energy of 300 MeV. Hence there is no such cancellation between elastic and inelastic TPE contributions in μp .

Table 3

Deuteron structure contributions to the Lamb shift in muonic deuterium. Values are in meV. For source 4, the N^3LO^\dagger calculation by Hernandez et al. [58] we use their value from the rightmost two columns of their Tab. 3 that differs most from their “AV18” value. Their terms $\delta_{Z1}^{(1)}$, $\delta_{Z3}^{(1)}$, and δ_{Zem} (Friar term) are not listed because they cancel (see text). Items with a diamond \diamond are corrected from the published values, see footnotes.

Item	Contribution	Pachucki [55] AV18	Friar [60] ZRA	Hernandez et al. [58] AV18 N^3LO^\dagger		Pach.& Wienczek [65] AV18	Carlson et al. [64] data	Our choice value source	
	Source	1	2	3	4	5	6		
p1	Dipole	1.910 $\delta_0 E$	1.925 Leading C1	1.907	1.926 $\delta_0^{(2)} E$	1.910 $\delta_0 E$		1.9165 \pm 0.0095	3-5
p2	Rel. corr. to p1, longitudinal part	-0.035 $\delta_R E$	-0.037 Subleading C1	-0.029	-0.030 $\delta_R^{(2)} E$	-0.026 $\delta_R E$			
p3	Rel. corr. to p1, transverse part			0.012	0.013 $\delta_T^{(2)} E$				
p4	Rel. corr. to p1, higher-order					0.004 $\delta_{HO} E$			
sum	Total rel. corr., p2+p3+p4	-0.035	-0.037	-0.017	-0.017	-0.022		-0.0195 \pm 0.0025	3-5
p5	Coulomb distortion, leading	-0.255 $\delta_{C1} E$				-0.255 $\delta_{C1} E$			
p6	Coul. distortion, next order	-0.006 $\delta_{C2} E$				-0.006 $\delta_{C2} E$			
sum	Total Coulomb distortion, p5+p6	-0.261		-0.262	-0.264 $\delta_C^{(2)} E$	-0.261		-0.2625 \pm 0.0015	3-5
p7	El. monopole excitation	-0.045 $\delta_{Q0} E$	-0.042 C0	-0.042	-0.041 $\delta_{Q0}^{(2)} E$	-0.042 $\delta_{Q0} E$			
p8	El. dipole excitation	0.151 $\delta_{Q1} E$	0.137 Retarded C1	0.139	0.140 $\delta_{Q1}^{(2)} E$	0.139 $\delta_{Q1} E$			
p9	El. quadrupole excitation	-0.066 $\delta_{Q2} E$	-0.061 C2	-0.061	-0.061 $\delta_{Q2}^{(2)} E$	-0.061 $\delta_{Q2} E$			
sum	Tot. nuclear excitation, p7+p8+p9	0.040	0.034 C0 + ret.-C1 + C2	0.036	0.038 $\delta_Q^{(2)} E$	0.036		0.0360 \pm 0.0020	2-5
p10	Magnetic	-0.008 $\diamond \delta_M E$	-0.011 M1	-0.008	-0.007 $\delta_M^{(2)} E$	-0.008 $\delta_M E$		-0.0090 \pm 0.0020	2-5
SUM.1	Total nuclear (corrected)	1.646	1.648 ^a	1.656	1.676	1.655		1.6615 \pm 0.0103	
p11	Finite nucleon size		0.021 Retarded C1 f.s.	0.020 \diamond	0.021 $\diamond \delta_{FS}^{(2)} E$	0.020 $\delta_{FS} E$			
p12	n-p charge correlation		-0.023 pn correl. f.s.	-0.017	-0.017 $\delta_{FS}^{(2)} E$	-0.018 $\delta_{FS} E$			
sum	p11+p12		-0.002	0.003	0.004	0.002		0.0010 \pm 0.0030	2-5
p13	Proton elastic 3rd Zemach moment	0.043(3) $\delta_P E$	0.030 $(r_p^3)_{(2)}^{pp}$	0.027(2)	$\delta_{pol}^{N_p}$ [64]	0.043(3) $\delta_P E$	0.028(2) ΔE^{bnd}	0.0289 \pm 0.0015 Eq.(13) ^d	6
p14	Proton inelastic polarizab.								
p15	Neutron inelastic polarizab.								
p16	Proton & neutron subtraction term								
sum	Nucleon TPE, p13+p14+p15+p16	0.043(3)	0.030	0.027(2)		0.059(9)		-0.0098 \pm 0.0098 Eq.(15) ^e	
SUM.2	Total nucleon contrib.	0.043(3)	0.028	0.030(2)		0.061(9)		0.0471 \pm 0.0101 f	
	Sum, published	1.680(16)	1.941(19)	1.690(20)		1.717(20)	2.011(740)		
	Sum, corrected		1.697(19) ^e	1.714(20) ^f		1.707(20) ^g	1.748(740) ^h	1.7096 \pm 0.0147	

^aCorrected from -0.016 meV, see Ref. [65] below Eq. (45).^bThe Coulomb distortion contribution p5+p6 of -0.263 meV (our choice) has been added to Friar's sum of 1.911 meV to make the numbers comparable.^cCorrected from +0.015 meV [70, 71].^dRescaled from the muonic hydrogen values from Refs. [66, 74]. See text.^eRescaled from the muonic hydrogen value from Ref. [74]. See text.^fSee text.^gCorrections: p5+p6, p14+p15+p16. Items p3+p4 (higher-order corr. to p1) would increase this value by another ~ 0.015 meV.^hCorrections: p13, p16. Item p11 updated from 0.015 meV^c.ⁱCorrection: p16.^jCorrections: p5+p6.

hydrogen [66], $\Delta E(2S) = -0.0369(24)$ meV, with a reduced mass ratio to correct for the larger wave function overlap in μd ,

$$\zeta = (m_r^{\mu d} / m_r^{\mu p})^3 = 1.1685. \quad (12)$$

This gives a value of 0.043(3) meV for our items p13 + p14.

Pachucki's value for the magnetic contribution (p10) was found to be wrong by a factor of two in Ref. [58] and was corrected in Pachucki's later work [65].

Friar (2013) used the zero-range approximation (ZRA) [60] which allows for a systematic derivation of all terms. Friar finds very good agreement with the results of Pachucki [55] despite the simplicity of the ZRA. The cancellation between elastic and inelastic TPE contributions is observed in ZRA, too.⁷ Friar noted that a nucleon finite size contribution of 0.029 meV should be added that had not been included in Ref. [55]. Friar's value of $\Delta E_{TPE}^{LS} = 1.941 \pm 1\%$ meV seems at first glance to be in serious disagreement with Pachucki's value [55]. The difference is however mainly caused by the Coulomb distortion (p5 + p6) of -0.263 meV which should be included in every calculation [67]. Including further items in Table 3 like the nucleon polarizability contribution p14 + p15, and the nucleon subtraction term p16 results in a “corrected value” of 1.697 meV. Higher-order corrections to the dipole contribution (p3 and p4) can account for the remaining difference to the other model calculations and “our avg.”

In their 2014 paper [58] the TRIUMF/Hebrew University group performed an independent calculation using two parameterizations of the deuteron potential: AV18 one the one hand, and nucleon–nucleon (NN) forces from chiral effective field theory (χ EFT) up to order N^3LO and with various cutoffs, on the other. As in their work on muonic helium-4 [68,69] they added higher-order relativistic corrections, corrected the magnetic term, and added the intrinsic neutron

⁷ Friar's paper [60] gives a very good understanding about the nature of this cancellation.

polarizability [70]. They also introduced the reduced-mass-dependence in higher-order terms, while the earlier Ref. [55] had worked in the limit of infinite nuclear mass for all terms. The nuclear mass dependence for all terms was then further refined in Ref. [65].

Ref. [58] observed the cancellation of elastic and inelastic contribution for the muonic deuterium case explicitly: The sum of terms $\delta_{Z1}^{(1)} + \delta_{Z3}^{(1)} = -0.424(3)$ meV⁸ in Ref. [58] cancels very nicely with elastic Friar (“3rd Zemach”) contribution $\Delta E_{\text{Friar}}^{\text{LS}} = 0.433(21)$ meV of the deuteron as calculated by Borie, see Ref. [22] p. 7.

Averaging over their results from AV18 and N³LO they obtained a value of $\Delta E_{\text{TPE}}^{\text{LS}} = 1.690(20)$ meV. The apparently good agreement with Pachucki’s value [55] may however be accidental as it arises from the cancellation of many small differences [58,70]. Again, adding omitted items (p13 and p16) results in very good agreement with all other sums in Table 3. Note that the 4th column in our Table 3 (“Source 4”) is that value from Tab. 3 of Ref. [58], columns “N³LO-EM” and “N³LO-EGM”, which deviates most from their AV18 result. This is an attempt to be rather conservative when determining “our average” following Eq. (6).

According to Bacca [70,71], their values for $\delta_{\text{NS}}^{(2)}$ (our item p11) should be updated to +0.020 meV and +0.021 meV from the published value of +0.015 meV [58].

The 2015 paper by Pachucki and Wienczek [65] updated Pachucki’s results from 2011 (Ref. [55]), again using the AV18 potential. Among other things, they included the finite size of the nucleons, and the intrinsic elastic and inelastic two-photon exchange with individual nucleons. They corrected their magnetic interaction term, and derived the correct mass dependence of the TPE correction and its consistent separation with the so-called pure recoil correction. Their total TPE contribution of order $(Z\alpha)^5$ is 1.717 ± 0.020 meV. Item p16 must be added to obtain a “corrected value” in very good agreement with all other determinations.

Complementary to the calculations using various deuteron potentials [55,60,58,65], Carlson et al. [64], in 2014, determined the TPE contributions with minimal model dependence using measured elastic and inelastic electron–deuteron scattering data and dispersion relations. Their model-independent calculation yields 2.01(74) meV, confirming the numbers given by [55,60,58] albeit with a much larger uncertainty. This uncertainty stems from the uncertainty in the data and can be improved significantly when new data from the Mainz MAMI and MESA facilities becomes available [64].

The several contributions to their sum cannot be easily equated with individual items p1...p16 listed in Table 3, so we do not quote their individual contributions, with one important exception. Carlson et al. [64] note that the proton and neutron intrinsic polarizabilities of 0.028(2) meV (our items p14 + p15) should be added to the earlier results of Pachucki [55] and Friar [60]. Such a correction is already included in the later paper by Hernandez et al. [58].

On the other hand, the value of Carlson et al. [64] should be corrected [67,72] for Coulomb distortion (p5 + p6) of −0.263 meV. Then the central value becomes 1.748 meV, in even better agreement with the (corrected) values from nuclear models [55,60,58,65]. Note that this correction corresponds to 1/3 of their quoted uncertainty and may hence look absurd. But the uncertainty quoted in Ref. [64] originates almost exclusively from the plane wave Born approx. (PWBA) term and may be reduced by at least a factor of 4 with new data from a planned experiment in Mainz [64]. The good agreement between the corrected central value and all other (corrected) values makes one wonder if the uncertainty in Ref. [64] is maybe somewhat conservative.

The “Thomson term” is a recoil correction that has first been calculated in Ref. [64]. It has received some attention [67,72,46,70] in the discussion of our Table 3, and the conclusion was that this term is indeed correctly added to the sum of the contributions in the dispersion-relation treatment of Ref. [64]. The other calculations [55,60,58,65] have correctly *not* included such a term, because the cancellation between elastic and (part of the) inelastic contributions to the polarizability will eliminate this Thomson term (as well as other similar recoil-like terms) in such a “nuclear Hamiltonian approach”. All further recoil corrections of order $(Z\alpha)^5$ to the Lamb shift in muonic deuterium are then included in the “pure recoil corrections”, item #22 in Table 1.

⁸ The sign convention in Ref. [58] is opposite to the one used here.

3.3.2. Comparison of terms and further corrections

An earlier version of the present manuscript was sent to the authors of Refs. [55,60,64,58,65] and other experts in the field. The ensuing insightful discussions resolved several discrepancies between the published values of $\Delta E_{\text{TPE}}^{\text{LS}}$ and revealed that some further corrections should be included.

Table 3 lists in chronological order the modern determinations of $\Delta E_{\text{TPE}}^{\text{LS}}$ using various nuclear models, and scattering data. As usual, we calculate an “average” following our Eq. (6) and consider the spread of values in the uncertainty.

Items **p1 through p10** contain the nuclear contributions, and the various calculations are in good agreement.

It is satisfying to note that the dominant dipole term, item p1, is in very good agreement for the three models used: AV18, ZRA, and $N^3\text{LO } \chi\text{EFT}$. We average the results using “modern” potentials [58,65] and take the agreement of the ZRA result as an indication that the ZRA results for the smaller terms are likely to be accurate on the few μeV level and can hence be used in “our average”.

Items p2..p4 are relativistic corrections to p1. The two most recent works [58,65] include higher-order relativistic corrections so we consider only these works in the average.

There is consensus that the Coulomb distortion contribution (p5 + p6) should be included in *all* calculations. Adding our average of -0.263 meV to the results of Friar [60] and Carlson et al. [64] removes most of the discrepancy between all published values.

Nuclear excitation corrections p7..p9 cancel to some degree. Our average includes the results from ZRA [60] and the most recent AV18 and $N^3\text{LO}$ models [58,65].

The magnetic contribution p10 from Ref. [55] has been corrected in the later work [65]. We average over the other results.

Items **p11 through p16** are the nucleon contributions.

Item p11 from the TRIUMF/Hebrew University group ($\delta_{\text{NS}}^{(2)}$ in Ref. [58]) has been updated to $+0.020\text{ meV}$ and $+0.021\text{ meV}$ [70,71], further improving the agreement with Refs. [60,65].

After some discussions, consensus has been reached that several nucleon contributions should be included [70,46,73,72,67]: The elastic Friar (3rd Zemach) term of the proton (p13), the inelastic proton and neutron contributions (p14 + p15), and the subtraction terms from both the proton and the neutron (p16) are therefore included in our sum. In principle, the elastic Friar term of the neutron should be included too, but it is small enough to be neglected [60,65,72].

We follow the suggestion of Birse and McGovern [72] who obtain these values as follows:

Item p13, the elastic Friar (3rd Zemach) moment contribution of the *proton* to the Lamb shift in μd is obtained from the values of the elastic and the non-pole Born term calculated for muonic hydrogen (μp) [72].

Both, the elastic term in μp , and the non-pole term in μp , have been obtained by Carlson and Vanderhaeghen from scattering data using dispersion relations [66]. Their value for the elastic term, ΔE^{el} , amounts to $0.0295 \pm 0.0013\text{ meV}$.⁹ Their value for the non-pole Born term for μp is -0.0048 meV (see footnote 9). The sum of these two terms, rescaled with ζ from Eq. (12) yields for p13, the elastic Friar moment contribution of the proton to the Lamb shift in muonic deuterium, the value

$$\Delta E_{\text{Friar}}^{\text{LS}}(\text{p}) = 0.0289 \pm 0.0015\text{ meV}. \quad (13)$$

The inelastic proton and neutron polarizabilities p14 and p15 have been calculated from deuteron data and dispersion relations by Carlson et al. [64]. Their result for the sum p14 + p15 amounts to

$$\Delta E_{\text{inelastic}}^{\text{LS}}(\text{p}) + \Delta E_{\text{inelastic}}^{\text{LS}}(\text{n}) = 0.028 \pm 0.002\text{ meV} \quad (14)$$

which is the value we adopt. Hernandez et al. [58] used the value $0.027(2)\text{ meV}$ from the same Ref. [64]. This number is, however, only an estimate using numbers rescaled from muonic hydrogen, whereas our choice Eq. (14) is calculated from deuteron data, and the value in Eq. (14) should be used [67].

Finally, the contribution from the “subtraction term” of the nucleon polarizabilities has to be considered, too [72,67]. Birse and McGovern have calculated the subtraction term for the inelastic

⁹ The sign convention in Ref. [66] is opposite to the one used here.

TPE of the proton in muonic *hydrogen*, $\Delta E_{\text{sub}} = -0.0042 \pm 0.0010$ meV,¹⁰ using chiral perturbation theory [74]. This value is in good agreement with the value $\Delta E_{\text{sub}}^{\text{subt}} = -0.0053 \pm 0.0019$ meV (see footnote 9) from Carlson and Vanderhaeghen [66] which was however obtained from a particular model of the proton form factor and an older value of the proton magnetic polarizability [72]. For the deuteron, we hence adopt the former value, double it assuming that the proton and neutron contributions are approximately the same [72], and rescale with ζ from Eq. (12) to yield p16 for muonic deuterium

$$\Delta E_{\text{sub}}^{\text{LS}}(\text{p}) + \Delta E_{\text{sub}}^{\text{LS}}(\text{n}) = -0.0098 \pm 0.0098 \text{ meV.} \quad (15)$$

Here we have assigned a 100% uncertainty.

3.3.3. Our choice

Summing all values in Table 3, and adding the uncertainties from (the spreads of) our averaging in quadrature, gives

$$\Delta E_{\text{TPE}}^{\text{LS}}(\text{simple}) = 1.7096 \pm 0.0147 \text{ meV.} \quad (16)$$

This uncertainty is smaller than the published uncertainties in all original papers [55,60,64,58,65]. Hence we increase conservatively the uncertainty in our average to the 0.020 meV obtained by the two most recent model calculations [58,65].

The total TPE contribution of order $(Z\alpha)^5$ to the Lamb shift in muonic deuterium¹¹ is hence

$$\Delta E_{\text{TPE}}^{\text{LS}}(\text{final}) = 1.7096 \pm 0.0200 \text{ meV.} \quad (17)$$

Further rounding is deferred to Eq. (18).

The uncertainty of the TPE contribution is by far the dominant one, and it limits severely the accuracy of the deuteron rms charge radius obtained from laser spectroscopy of the Lamb shift in muonic deuterium.

3.4. Total Lamb shift in muonic deuterium

Collecting the radius-independent (mostly) QED contributions listed in Table 1 and summarized in Eq. (8), the radius-dependent contributions listed in Table 2 and summarized in Eq. (10), and the complete two-photon (polarizability) contribution $\Delta E_{\text{TPE}}^{\text{LS}}$ from Eq. (17), we obtain for the $2S - 2P$ energy difference in muonic deuterium

$$\begin{aligned} \Delta E(2S - 2P_{1/2}) &= 228.77356(75) \text{ meV} + 0.00310(60) \text{ meV} - 6.11025(28) r_d^2 \text{ meV/fm}^2 \\ &\quad + 1.70960(2000) \text{ meV} \\ &= 230.486(20) \text{ meV} - 6.1103(3) r_d^2 \text{ meV/fm}^2 \end{aligned} \quad (18)$$

where in the last step we have rounded the values to reasonable accuracies.

One should note that the uncertainty of 0.020 meV from the nuclear structure corrections $\Delta E_{\text{TPE}}^{\text{LS}}$, Eq. (17), is about 30 times larger than the combined uncertainty of all radius-independent terms summarized in Table 1, and 15 times larger than the uncertainty in the $\langle r^2 \rangle$ coefficient (which amounts to 0.0013 meV). A further improvement of the nuclear structure corrections in light muonic atoms is therefore desirable.

4. 2S hyperfine splitting

4.1. Fermi and Breit contributions

The interaction between the magnetic moment of the nucleus with the magnetic field induced by the lepton gives rise to shifts and splittings of the energy levels termed hyperfine effects. In classical

¹⁰ The sign convention in Ref. [74] is opposite to the one used here.

¹¹ Note that non-perturbative Coulomb corrections of higher-order in $(Z\alpha)$ have been accounted here, whereas the pure recoil part of the TPE has been separately given in Table 1 #22.

electrodynamics, the interaction between the magnetic moments μ_d and μ_μ of deuteron and muon, respectively, is described by [41]

$$H_{\text{HFS}}^{\text{classical}} = -\frac{2}{3} \mu_d \cdot \mu_\mu \delta(\mathbf{r}) \quad (19)$$

where $\delta(\mathbf{r})$ is the delta-function in coordinate space. A similar Hamiltonian to the one in Eq. (19) can be derived in quantum field theory from the one-photon exchange diagram. Using the Coulomb wave function, this gives rise in first-order perturbation theory to an energy shift for muonic deuterium nS -states of [22]

$$\begin{aligned} E_{\text{HFS}}(F) &= \frac{4(Z\alpha)^4 m_r^3}{3n^3 m_\mu m_d} (1 + \kappa)(1 + a_\mu) \frac{1}{2} \left[F(F+1) - \frac{11}{4} \right] \\ &= \frac{1}{3} \Delta E_{\text{Fermi}} \left[F(F+1) - \frac{11}{4} \right] \end{aligned} \quad (20)$$

where ΔE_{Fermi} is the Fermi splitting, m_d is the deuteron mass, F is the total angular momentum, κ and a_μ are the deuteron and muon anomalous magnetic moments, respectively.

The Fermi splitting

$$\begin{aligned} \Delta E_{\text{Fermi}} &= \frac{2(Z\alpha)^4 m_r^3}{n^3 m_\mu m_d} (1 + \kappa)(1 + a_\mu) \\ &= \frac{3}{2} \beta_D (1 + a_\mu) \end{aligned} \quad (21)$$

with

$$\beta_D = \frac{4(Z\alpha)^4 m_r^3}{3n^3 m_\mu m_d} (1 + \kappa) \quad (22)$$

is the main contribution to the HFS, (h1) in Table 4. The value Borie gives on p. 19 of Ref. [22] is

$$\Delta E_{\text{Fermi}}^{\text{B}} = 6.14298 \text{ meV}. \quad (23)$$

It already includes the correction $\Delta E_{\mu\text{AMM}}$ (h4) due to the muon anomalous magnetic moment (μAMM). However, Borie's value $\Delta E_{\text{Fermi}}^{\text{B}} = 6.14298 \text{ meV}$ is not correct. Since ΔE_{Fermi} depends only on fundamental constants [4], we have recalculated it following Eq. (21), and obtain a value of

$$\Delta E_{\text{Fermi}} = 6.14308 \text{ meV} \quad (24)$$

which differs from Borie's, but coincides with Martynenko's value of Ref. [15]

$$\begin{aligned} \Delta E_{\text{Fermi}}^{\text{M}} &= 6.1431 \text{ meV} \\ &= 6.1359 \text{ meV}_{\text{h1}} + 0.0072 \text{ meV}_{\text{h4}}. \end{aligned} \quad (25)$$

Here, the two terms in the second line are, respectively, the Fermi splitting excluding the contribution of the anomalous magnetic moment of the muon, (h1), and the μAMM correction, (h4), which Martynenko calculates separately.

The Breit term ΔE_{Breit} (h2) corrects for relativistic and binding effects accounted for in the Dirac–Coulomb wave function but excluded in the Schrödinger wave function. Both, Martynenko and Borie, calculated the Breit correction term to be

$$\Delta E_{\text{Breit}} = 0.0007 \text{ meV}. \quad (26)$$

4.2. Vacuum polarization (VP) and self-energy (SE) contributions

On p. 21 of Ref. [22], Borie provides the values for ϵ_{VP1} (h8) and ϵ_{VP2} (h5). The values we used are the ones for a point-like nucleus. In Section 4.3 we give a correction due to the finite size, which is given by (h25, h26). The corresponding terms from Martynenko and Borie agree.

(h7) is neglected by Martynenko as pointed out on p. 21 in [22]. The origin of the difference between Martynenko and Borie in (h9) is not clear. In this case we take the average. (h9b) is a correction in third order perturbation theory which is only given by Martynenko.

Table 4

All contributions to the **2S hyperfine splitting (HFS)** in muonic deuterium. The item numbers *hi* in the first column follow the entries in Tab. 3 of Ref. [3]. For Martynenko, numbers #1–#15 refer to rows in Tab. I of Ref. [15], whereas numbers in parentheses refer to equations therein. Borie [22] gives the values as *coefficients* to be multiplied with the sum of (*h1* + *h4*). We list the resulting values in meV. AMM: anomalous magnetic moment, PT: perturbation theory, VP: vacuum polarization, SOPT: second order perturbation theory, TOPT: third order perturbation theory. All values are in meV (meV/fm for *h20*).

Contribution	Martynenko [15]	Borie [22]	Our choice
h1	Fermi splitting, $(Z\alpha)^4$	#1, (6)	
h4	μ AMM corr., $\alpha(Z\alpha)^4$	#2, (7)	
Sum		6.14298	p. 19 6.14308 Eq. (24)
h2	Breit corr., $(Z\alpha)^6$	#3, (8)	p. 19 0.00069 B
h5	eVP in 2nd-order PT, $\alpha(Z\alpha)^5 (\epsilon_{VP2})$	#4, (23)	p. 21 0.0207 M
h7	Two-loop corr. to Fermi-energy (ϵ_{VP2})	Neglected	p. 21 0.00016 B
h8	One-loop eVP in 1γ int., $\alpha(Z\alpha)^4 (\epsilon_{VP1})$	#4, (12)	p. 21 0.0134 M
h9	Two-loop eVP in 1γ int., $\alpha^2(Z\alpha)^4 (\epsilon_{VP1})$	#5, (16), (29–32)	p. 21 0.0003 Avg.
h9b	VP contr. in TOPT	#6, (33)	0.00004 M
h12	μ VP (sim. to ϵ_{VP})	#9, (48)	p. 21 0.00025 ^a B
h13	Vertex, $\alpha(Z\alpha)^5$	incl. in <i>h13</i>	
h14	Higher-order corr. of (<i>h13</i>), part with $\ln(\alpha)$	–0.00059	p. 19 incl. in <i>h17b</i>
h17b	Radiative nucl. fn. size corr., $\alpha(Z\alpha)^5$	–0.00004	p. 19 –0.00004 B
h18	Hadron VP, α^6	#13, (71–74)	–0.0005 M
h19	Weak interact. contr.	#10, (50)	p. 19 0.00016 B
h20	Fin. size (Zemach) corr. to ΔE_{Fermi} , $(Z\alpha)^5$	#10, (50)	p. 21 0 [75]
h23	Recoil corr. to fin. size	[32] ^b	p. 22 –0.04539 <i>r_Z</i>
Sum	(<i>h20</i> + <i>h23</i>)	#7, (46)	0.0015 ±0.0007 M
h22a	Deuteron polarizability, $(Z\alpha)^5$	#14 using [80]	0.2121 M
h22b	Deuteron internal polarizability, $(Z\alpha)^5$	#15 using [81]	0.0105 M
Sum	(<i>h22a</i> + <i>h22b</i>)	0.2226	±0.0049 p. 22 ±0.0042 ±0.0025 M
h24	eVP + nucl. struct. corr., α^6	#8, (47)	0.0019 M
h25	eVP corr. to fin. size (sim. to ϵ_{VP2})		p. 21 –0.00068 ^d B
h26	eVP corr. to fin. size (sim. to ϵ_{VP1})		p. 21 –0.00068 B
h27	Nucl. struct. corr., $\alpha(Z\alpha)^5$	#11, (55)	0.0008 M
h27b	Nucl. struct. in SOPT	#12, (59)	–0.0069 M
Sum		6.39880	±0.00490 6.39680 ± 0.00494 –0.04539 <i>r_Z</i>

^a This value is $3\alpha^2/4 \approx 3.993385 \times 10^{-5}$ of the Fermi splitting, (*h1* + *h4*), see Eq. (28) and text, as well as p. 21 of Ref. [22].
^b The published value for the sum of items *h20* + *h23* is -0.1163 ± 0.0010 meV [15]. For the separation into items *h20* and *h23* see text.
^c Calculated from Eq. (21), including the factor $(1 + a_\mu)$. According to Martynenko, this factor should be omitted in the 2γ amplitudes with point vertices [32].
^d Difference of two terms in Borie [22]. See text.

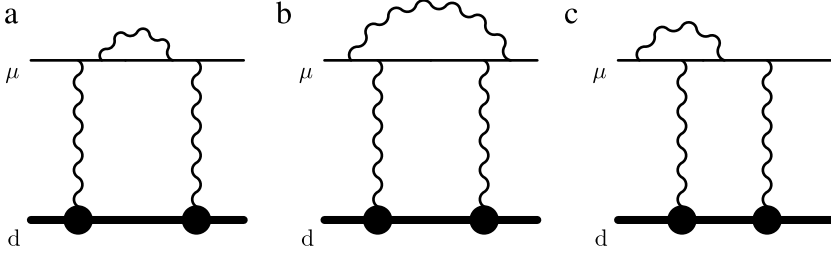


Fig. 14. Item (h17b), the radiative nuclear finite size correction $\alpha(Z\alpha)^5$ is composed of (a) μ SE with nuclear structure (b) spanning photon contribution, also referred to as jellyfish diagram, and (c) the vertex correction which results in two terms. Item (h17b) also contains the diagrams where the exchange photon lines are crossed. This figure corresponds to Fig. 7 from Martynenko [15].

The μ VP contribution $\Delta E_{\mu\text{VP}}$ (h12) is given by Martynenko as

$$\Delta E_{\mu\text{VP}}^{\text{M.}} = 0.0002 \text{ meV}. \quad (27)$$

Borie included this contribution in the vertex term ΔE_{vertex} (h13) as pointed out on p. 21 in [22]. However, in the same paragraph Borie states that the value of $\Delta E_{\mu\text{VP}}^{\text{B.}}$ is $3\alpha^2/4 \simeq 3.993385 \times 10^{-5}$ of her Fermi splitting $\Delta E_{\text{Fermi}}^{\text{B.}}$, whereby we obtain

$$\Delta E_{\mu\text{VP}}^{\text{B.}} = 0.00025 \text{ meV} \quad (28)$$

which is what we use.

Martynenko gives a value for a term called radiative nuclear finite size correction $\alpha(Z\alpha)^5$ (h17b). It is composed of four terms (see Fig. 14), μ SE with nuclear structure, spanning photon contribution (a.k.a. “jellyfish diagram”) and two vertex correction terms, so it should also include (h13). Their sum yields -0.0005 meV . We think that (h14) is an additional term, only calculated by Borie. So we add this to ‘our choice’.

The hadron VP ΔE_{hVP} (h18) results equal for both, Martynenko and Borie:

$$\Delta E_{\text{hVP}}^{\text{M.,B.}} = 0.0002 \text{ meV}. \quad (29)$$

There is no considerable contribution from weak interaction [75].

4.3. Zemach radius

The Bohr–Weisskopf effect [76] is the main finite size correction to the 2S hyperfine splitting. It is also called the Zemach term [77], $\Delta E_{\text{Zemach}}^{\text{HFS}}$, and is listed as item (h20) in our summary. The Zemach term is usually parameterized as [78]

$$\Delta E_{\text{Zemach}}^{\text{HFS}} = -\Delta E_{\text{Fermi}} 2(Z\alpha) m_r r_Z \quad (30)$$

using the so-called Zemach radius of the nucleus [78]

$$\begin{aligned} r_Z &= \int d^3r \int d^3r' r' \rho_E(\mathbf{r}) \rho_M(\mathbf{r} - \mathbf{r}') \\ &= -\frac{4}{\pi} \int_0^\infty \frac{dq}{q^2} (G_E(q^2) G_M(q^2) - 1). \end{aligned} \quad (31)$$

This convolution of charge $\rho_E(\mathbf{r})$ and magnetization $\rho_M(\mathbf{r})$ distribution comes from the fact that the finite charge distribution alters the muon’s wave function at the origin.

Diagrammatically, the Zemach correction (h20) to the HFS, $\Delta E_{\text{Zemach}}^{\text{HFS}}$, is the elastic part of the two-photon exchange contribution to the 2S HFS, just like the Friar correction to the Lamb shift Fig. 13(a, b) [18].

A recoil correction to the elastic TPE, (h23), is considered here, too. It is somewhat parallel to the item #22 of the Lamb shift, termed *rel. RC* ($Z\alpha$)⁵ listed in Table 1.

The inelastic part of the TPE correction to the 2S HFS, $\Delta E_{\text{inelastic}}^{\text{HFS}}$, is topic of the next Section 4.4.

Borie gives a value of $\epsilon_{\text{Zemach}} = -0.007398 \text{ fm}^{-1} r_Z$ (Ref. [22], p. 22). Her Zemach contribution is hence (Eq. (30), Ref. [22], p. 23 top)

$$\Delta E_{\text{Zemach}}^{\text{HFS}} (\text{Borie}) = -0.04545 r_Z \text{ meV/fm.} \quad (32)$$

Note that the coefficient

$$-0.04545 = \frac{3}{2} \beta_D (1 + a_\mu) \epsilon_{\text{Zemach}} \quad (33)$$

explicitly includes the factor $(1 + a_\mu)$.

Using $r_Z = 2.593 \pm 0.016 \text{ fm}$ from Ref. [78] Borie's value for the Zemach contribution to the 2S HFS amounts to

$$\Delta E_{\text{Zemach}}^{\text{HFS}} (\text{Borie}) = -0.11782 \pm 0.00074 \text{ meV.} \quad (34)$$

Borie mentions that nuclear recoil corrections (our item (h23)) are important, but have not been included (Ref [22], p. 22, bottom).

Martynenko calculates the *nuclear structure correction* α^5 from the deuteron electromagnetic current that involves the form factors F_1 , F_2 , and F_3 which can be related to the measured charge, magnetic and quadrupole form factors of the deuteron, $G_E(q^2)$, $G_M(q^2)$ and $G_Q(q^2)$, see Eq. (37) in Ref. [15]. Using the parameterization of G_E , G_M and G_Q from Ref. [79], Martynenko obtains a value of $-0.1163 \pm 0.0010 \text{ meV}$ (Ref. [15], Tab. 1 item #7, Eq. (46)).

This value is the sum of the Zemach term, item (h20), as calculated by Borie, but includes recoil corrections to the finite size effect, (h23) [32]. The separation of these two contributions is not unique [32], but if one adopts the canonical definition of the Zemach radius in terms of the form factors G_E and G_M as given in Eq. (31), one can separate Martynenko's sum into

$$\begin{aligned} \Delta E_{\text{Zemach+RC}}^{\text{HFS}} (\text{Martynenko}) &= -0.1163 \text{ meV} \pm 0.0010 \text{ meV} \\ &= (-0.1178 \text{ meV}_{\text{h20}} + 0.0015 \text{ meV}_{\text{h23}}) \pm 0.0010 \text{ meV.} \end{aligned} \quad (35)$$

Here the item (h20) was calculated using the Zemach radius $r_Z = 2.5959 \text{ fm}$ [32], obtained by numerical integration of the parameterization of the deuteron form factors from Ref. [79]. This Zemach radius is in excellent agreement with the value $r_Z = 2.593 \pm 0.016 \text{ fm}$ from Ref. [78] used by Borie [22]. A small difference arises from Martynenko's observation that the factor $(1 + a_\mu)$ in Eq. (21) should not be included for the 2γ amplitudes with point vertices [32].

Rewriting the -0.1178 meV of (h20) as

$$\Delta E_{\text{Zemach}}^{\text{HFS}} (\text{Martynenko}) = -0.0453934 r_Z \text{ meV/fm} \quad (36)$$

makes the dependence on the Zemach radius explicit. Putting the nuclear recoil corrections back in, the combined Zemach (h20) and recoil (h23) corrections evaluated by Martynenko (Eq. (35)) become

$$\Delta E_{\text{Zemach+RC}}^{\text{HFS}} = -0.0453934 r_Z \text{ meV/fm}_{\text{h20}} + (0.0015 \pm 0.0007) \text{ meV}_{\text{h23}} \quad (37)$$

which we adopt. The total uncertainty of 0.0010 meV given by Martynenko is then the sum of the uncertainty in the Zemach radius $\delta r_Z = 0.016 \text{ fm}$, corresponding to 0.0007 meV , and the uncertainty of (h23) given above.

4.4. Nuclear polarizability contributions to the 2S HFS

The polarizability contribution to the 2S hyperfine splitting in muonic deuterium, $\Delta E_{\text{TPE}}^{\text{HFS}}$, has only recently been calculated for the first time by the group of Martynenko [15]. They obtain the polarizability term in two parts:

First, the *deuteron polarizability contribution* $\Delta E_{\text{TPE}}^{\text{HFS}}(\text{deuteron})$ (h22a) is obtained from the analytic expressions derived in zero range approximation for electronic deuterium by Khriplovich and Milstein [80]. This part takes into account the virtual excitation of a deuteron made from point nucleons.

Second, the much smaller *internal deuteron polarizability contribution* $\Delta E_{\text{int. d-pol.}}$ (h22b), which accounts for the excitation of the individual nucleons (proton and neutron) inside the deuteron. This part is estimated based on the results for muonic hydrogen [81].

Summing these two up yields

$$\Delta E_{\text{tot. d-pol.}}^{\text{M.}} = 0.2121(42) \text{ meV} + 0.0105(25) \text{ meV} = 0.2226(49) \text{ meV} \quad (38)$$

with a generous uncertainty that accounts also for the fact that the original derivation [80] was for electronic, and not for muonic deuterium.

Eq. (38) is also the value quoted by Borie. As pointed out by Borie, Ref. [22] p. 22, it is not clear whether the ‘elastic’ contribution of the two-photon exchange diagrams is taken into account.

As for the Lamb shift, the polarizability term for the 2S HFS is the one with by far the largest uncertainty.

4.5. Further corrections to the 2S HFS

Several further corrections are considered by either Martynenko or Borie (h24, h25, h26, h27, and h27b):

Martynenko calculates a mixed term which includes eVP and a nuclear structure correction (h24)

$$\Delta E_{\text{eVP+nucl.struct.}}^{\text{M.}} = 0.0019 \text{ meV} \quad (39)$$

as well as two further nuclear structure contributions (h27, h27b):

$$\Delta E_{\text{nucl.str.corr.}}^{\text{M.}} = 0.0008 \text{ meV} \quad (40)$$

$$\Delta E_{\text{nucl.str.SOPT}}^{\text{M.}} = -0.0069 \text{ meV}. \quad (41)$$

Borie gives finite size corrections (h25, h26) to the eVP terms ϵ_{VP1} and ϵ_{VP2} , both contributing -0.00068 meV . These are obtained by calculating the difference of ϵ_{VP1} and ϵ_{VP2} with a point size nucleus compared to the ones when considering a finite size ([22], p. 21). It is not yet clear whether the nuclear structure contributions from Martynenko are complementary to the ones of Borie. We should remark that item (h27b) is quite large and does not seem to be included in Borie’s calculations. The apparent agreement of Borie’s and Martynenko’s total 2S HFS is a result of many small terms omitted by one author or the other, and therefore rather coincidental.

For now we refrain from assigning a large uncertainty to this item h27b, but an independent calculation, or at least an estimate of its accuracy, would certainly be helpful.

4.6. Total 2S hyperfine splitting

Hence, collecting all terms, but separating out the deuteron polarizability correction Eq. (38) as it is the dominant source of uncertainty, we can write the total 2S HFS in muonic deuterium as

$$\begin{aligned} \Delta E_{\text{HFS}}^{\text{th}} &= 6.17420(73) \text{ meV} + 0.22260(490) \text{ meV} - 0.04539 r_z \text{ meV/fm} \\ &= 6.39680(494) \text{ meV} - 0.04539 r_z \text{ meV/fm}. \end{aligned} \quad (42)$$

The large uncertainty in the polarizability corrections to the 2S HFS will prevent a determination of the deuteron Zemach radius from the measured transitions in muonic deuterium [10]. An improved calculation of the polarizability terms is therefore highly desirable.

Using the Zemach radius $r_z = (2.593 \pm 0.016) \text{ fm}$ [78] we get:

$$\Delta E_{\text{HFS}}^{\text{th}} = 6.27910(495) \text{ meV} \quad (43)$$

to be compared to the muonic deuterium measurement [10]. Alternatively, a precise measurement of the 2S HFS in μd , together with the Zemach radius [78], could be used to accurately determine the polarizability contributions.

Such a number may serve as a benchmark for accurate lattice calculations.

5. 2P fine structure

The contributions to the $2P_{3/2} - 2P_{1/2}$ fine structure splitting in muonic deuterium are displayed in Table 5.

The main contributions to the fine structure have only been calculated by Borie [22] and Martynenko's group [23,24]. For the latter, we refer to the more recent paper Ref. [24]. The values agree in both papers.

As always, Borie starts from the Dirac equation, which has to be corrected for recoil effects. This sum of entries (f1) + (f2) has to be compared to Martynenko's leading term (f3), corrected for relativistic effects (f4) which are automatically included in the Dirac equation. The result of both approaches agree reasonably well and we adopt the average 8.83894 ± 0.00016 meV.

The relativistic recoil correction of order $\alpha(Z\alpha)^4$, (f5), has been calculated including all recoil corrections of order m/M by Karshenboim [30]. This value thus supersedes [38] the values obtained by Borie [22] and Martynenko [23,24].

The Källén–Sabry term, item (f6), agrees nicely among all authors. Karshenboim et al. have evaluated some higher-order $\alpha^2(Z\alpha)^4 m$ contributions with great accuracy [36] which we list as (f7a), (f7d), and (f7e). These terms originate from the same graphs as the Lamb shift items #11, #12, and #30*, shown in Figs. 6, 7 and 9, respectively.

Contributions from the anomalous magnetic moment of the muon in second (f8) and higher (f9) orders have been calculated by Borie and Martynenko et al., and their sums agree.

A finite size correction to the $2P_{1/2}$ state (f10) is included, too. This term is the same term as item (r8) of the $\langle r^2 \rangle$ -dependent contributions to the Lamb shift, but with the opposite sign (see discussion in Section 3.2). We evaluate (r8) for the deuteron radius from Eq. (5) and obtain for our choice of the item (f10) $-0.000606 \langle r^2 \rangle = -0.000274 \pm 6 \cdot 10^{-8}$ meV.

Summing up we obtain as our choice for the $2P_{3/2} - 2P_{1/2}$ fine structure splitting in muonic deuterium

$$\Delta E_{fs}(2P_{3/2} - 2P_{1/2}) = 8.86412(16) \text{ meV.} \quad (44)$$

6. 2P levels

The various 2P levels displayed in Fig. 1 are separated by the 2P fine structure treated in Section 5, and further split by the 2P hyperfine splitting caused by the magnetic hyperfine interaction and the electric quadrupole interaction. The Breit–Pauli Hamiltonian can be displayed in matrix form as a sum of the magnetic HFS matrix and the quadrupole interaction matrix:

$$\begin{aligned}
 M_{\text{Breit-Pauli}} &= \begin{pmatrix} -1.381777 & 0 & -0.126405 & 0 & 0 \\ 0 & 0.690889 & 0 & -0.199864 & 0 \\ -0.126405 & 0 & 8.161148 & 0 & 0 \\ 0 & -0.199864 & 0 & 8.582931 & 0 \\ 0 & 0 & 0 & 0 & 9.285903 \end{pmatrix} \text{ meV} \\
 &\quad \text{magnetic HFS} \\
 &+ \begin{pmatrix} 0 & 0 & 0.613872 & 0 & 0 \\ 0 & 0 & 0 & -0.194123 & 0 \\ 0.613872 & 0 & 0.434073 & 0 & 0 \\ 0 & -0.194123 & 0 & -0.347258 & 0 \\ 0 & 0 & 0 & 0 & 0.086815 \end{pmatrix} \text{ meV} \\
 &\quad \text{quadrupole int.} \\
 &= \begin{matrix} 2P_{1/2}^{F=1/2} & 2P_{1/2}^{F=3/2} & 2P_{3/2}^{F=1/2} & 2P_{3/2}^{F=3/2} & 2P_{3/2}^{F=5/2} \\ \begin{pmatrix} -1.381777 & 0 & 0.487467 & 0 & 0 \\ 0 & 0.690889 & 0 & -0.393988 & 0 \\ 0.487467 & 0 & 8.595220 & 0 & 0 \\ 0 & -0.393988 & 0 & 8.235672 & 0 \\ 0 & 0 & 0 & 0 & 9.372718 \end{pmatrix} \end{matrix} \text{ meV.} \quad (45)
 \end{aligned}$$

Table 5
Contributions to the **2P fine structure**. The items (f7a), (f7d), and (f7e) originate from the same graphs as the Lamb shift items #11, #12, and #30*, respectively. VP: vacuum polarization, AMM: anomalous magnetic moment, KS: Källén–Sabry. All values are in meV.

	Contribution [24] Tab. 2	Martynenko [22]	Borie	Karshenboim	Our choice	
f1	Dirac		8.86430			
f2	Recoil		−0.02521			
f3	Contrib. of order $(Z\alpha)^4$	8.83848				
f4	Contrib. of order $(Z\alpha)^6$ and $(Z\alpha)^6 m_1/m_2$	0.00030				
Sum	(f1 + f2) or (f3 + f4)	8.83878	8.83909		8.83894	± 0.00016
f5	eVP correction (Uehling), $\alpha(Z\alpha)^4$	0.00575	0.00575	0.0057361	[30] Tab. IV	0.0057361
f6	2nd order eVP corr. (KS), $\alpha^2(Z\alpha)^4$	0.00005	0.00005	0.0000501	[36] Tab. IX "eVP2"	0.0000501
f7a	$\alpha^2(Z\alpha)^4 m$, like #11			0.0000127	[36] Tab. IX (a)	0.0000127
f7d	$\alpha^2(Z\alpha)^4 m$, like #12			0.0000991	[36] Tab. IX (d)	0.0000991
f7e	$\alpha^2(Z\alpha)^4 m$, like #30*			0.0000012	[36] Tab. IX (e)	0.0000012
f8	AMM (second order)		0.01949			
f9	AMM (higher orders)		0.00007			
Sum	Total AMM (f8 + f9)	0.01957	0.01956		0.019565	± 0.000005
f10	Finite size	−0.00028	−0.00027		−0.000274	Avg. a
	Sum	8.86387	8.86419		8.86412	± 0.00016

^a This is item (f8), evaluated for the deuteron radius from Eq. (5), see text.

Table 6

Elements of the transition matrix (Eq. (45)) obtained from two unnumbered tables on p. 24 and 25 in Ref. [22]. See also Ref. [82]. The various quantities are explained in the text.

j	j'	Energy
Magnetic HFS		
1/2	1/2	$(\beta'_D/6)(2 + x_d + a_\mu)[- \delta_{F,1/2} + 1/2 \delta_{F,3/2}]$
3/2	3/2	$\Delta E_{fs} + (\beta'_D/4)(4 + 5x_d - a_\mu) \times$ $[-1/6 \delta_{F,1/2} - 1/15 \delta_{F,3/2} + 1/10 \delta_{F,5/2}]$
3/2	1/2	$(\beta'_D/48)(1 + 2x_d - a_\mu)[- \sqrt{2} \delta_{F,1/2} - \sqrt{5} \delta_{F,3/2}]$
Quadrupole interaction		
1/2	1/2	0
3/2	3/2	$\epsilon_Q [\delta_{F,1/2} - 4/5 \delta_{F,3/2} + 1/5 \delta_{F,5/2}]$
3/2	1/2	$\epsilon_Q [\sqrt{2} \delta_{F,1/2} - 1/\sqrt{5} \delta_{F,3/2}]$

Table 7

Input parameters for the transition matrix. We recalculated Borie's values, but use our fine structure (see Section 5) and an updated value of the quadrupole moment Q [83] for ϵ_Q , see Eq. (49).

	Borie [22]	Our value
β_D	4.0906 meV	4.0906259 meV
β'_D	4.0922 meV	4.0922253 meV
ϵ_Q	0.43439 meV	0.434073(46) meV
x_d	0.0248	0.0247889
a_μ		0.00116592
ΔE_{fs}	8.86419 meV	8.86412(16) meV

It attains off-diagonal elements from mixing of levels with the same total angular momentum F , but different total muon angular momentum j [82,18,35,22], as shown in Table 6. Note that the diagonal terms of the quadrupole interaction lead to a change in the order of the $2P_{3/2}$ levels (see also Fig. 1).

We follow Borie's treatment [22], see also Pachucki [18] and Jentschura [35], but use our value for the $2P$ fine structure $\Delta E_{fs}(2P_{3/2} - 2P_{1/2}) = 8.86412(16)$ meV from Section 5, Eq. (44), as well as a more recent value of the deuteron quadrupole moment

$$Q = 0.285783 (30) \text{ fm}^2 \quad (46)$$

from Ref. [83], or, equivalently, $Q = 7.33945(77) \cdot 10^{-24} / \text{meV}^2$, using $\hbar c = 197.3269718(44) \text{ MeV fm}$ [4].

The numerical values of the quantities used in Table 6 are given in Table 7. In brief, β_D is defined in Eq. (22). For the $2P$ levels,

$$\beta'_D = \beta_D(1 + \epsilon_{2P}) \quad (47)$$

has to be used which contains the Uehling correction required for levels with $\ell > 0$ (see p. 25 and Eq. (12) in Ref. [22]). For muonic deuterium,

$$\epsilon_{2P} = 0.000391. \quad (48)$$

The quadrupole moment of the deuteron enters in the hyperfine splitting via the quadrupole interaction, see Borie [22], pp. 24 and 25.

$$\epsilon_Q = \frac{\alpha Q}{2} \frac{(\alpha Z m_r)^3}{24} (1 + \epsilon_{2P}), \quad (49)$$

where Q the quadrupole moment of the deuteron and ϵ_{2P} is given in Eq. (48).

Diagonalizing the matrix Eq. (45) results in shifts of the $2P(F = 1/2)$ and $2P(F = 3/2)$ levels by

$$\begin{aligned} \Delta_{1/2} &= 0.02376 \text{ meV} \quad \text{and} \\ \Delta_{3/2} &= 0.02052 \text{ meV}, \end{aligned} \quad (50)$$

respectively, as displayed in Fig. 1. The resulting energies of the various 2P sublevels are termed 'Borie reevaluated' and summarized in Table 8.

Very recently, an independent calculation of the 2P level energies by Martynenko [84] yielded somewhat different results, albeit well within the experimental uncertainty. The differences are taken into account in "Our value" in Table 8.

7. Summary

In summary, we have compiled all known contributions to the Lamb shift, the 2P fine structure, and the 2S and 2P hyperfine splittings, from QED and nuclear structure contributions.

For the Lamb shift, the QED contributions in Table 1 show good agreement between the four (groups of) authors. A problem with our item #2 from Ref. [23] was identified and resolved by the authors. Ultimately, the uncertainty of these "pure QED" terms in Table 1 is sufficiently good.

For the radius-dependent terms in Table 2 we find good agreement between the authors, too. Some terms have however been calculated by only one group. A small term ($r3'$) may deserve further attention.

The main limitation for the Lamb shift, and hence the deuteron charge radius to be extracted from the upcoming data, originates from the two-photon exchange contribution to the Lamb shift in μd . Here, a superficial inspection of the six modern values published in five papers since 2011 [55,60,64,58,65] vary between 1.68 and 2.01 meV, suggesting an uncertainty as large as 0.3 meV.

The term-by-term comparison of the individual contributions in Table 3 revealed that the agreement is in fact much better. Fruitful discussions with the authors of these papers and other experts in the field revealed missing terms and resulted in updated values of some individual terms. It is very reassuring that vastly different approaches give results in excellent agreement, when corrected for missing terms: zero-range approximation, modern nuclear models like AV18 (from two groups of authors) and χEFT -inspired NN-forces up to N^3LO order, and dispersion relations using electron–deuteron scattering data. Our average, 1.709 ± 0.020 meV is a reliable prediction for the deuteron polarizability contribution to the Lamb shift in μd .

For the 2S-HFS, several nuclear structure contributions have so far only been calculated by one group [15]: These are items (h22a), (h22b), and (h27b) in Table 4, which are rather large, and their uncertainties dominate the theoretical uncertainty for the 2S-HFS. This uncertainty will prevent us from obtaining a meaningful value of the Zemach radius of the deuteron from the measurement of the 2S-HFS in μd . An improved calculation of these items is therefore desirable.

For the 2P fine- and hyperfine splittings we collect all terms from the various authors, recalculate the matrix elements of the Breit–Pauli Hamiltonian with updated values of the 2P fine structure and the deuteron quadrupole moment. Diagonalizing this matrix Eq. (45) we obtain the 2P level energies, and their uncertainties. We compare these with an independent calculation from Ref. [84].

Acknowledgments

We are grateful to S. Bacca, M. Birse, E. Borie, M. Eides, J.L. Friar, M. Gorchtein, A.P. Martynenko, J. McGovern, K. Pachucki, and M. Vanderhaeghen for their careful reading of earlier versions of the manuscript and their very valuable remarks and insightful discussions in particular of the issues concerning the nuclear polarizability contributions to the Lamb shift discussed in Section 3.3. S. Karshenboim is acknowledged for helpful remarks on QED theory in general. We acknowledge support from the European Research Council (ERC) through StG. #279765 and the Swiss National Science Foundation Projects No. 200021L_138175 and No. 200020_159755.

Appendix. The Darwin–Foldy term

The Darwin–Foldy term, which is part of the Barker–Glover corrections (our item #17 in Table 1) has historically been subject of different definitions.

Table 8

2P levels from fine- and hyperfine splitting. All values are in meV relative to the $2P_{1/2}$ level. The column ‘Borie reevaluated’ is calculated in this work following the treatment of Borie and contains an updated value of the quadrupole moment Q from Eq. (46) as well as our value of the fine structure ($2P_{3/2} - 2P_{1/2}$ energy splitting) $\Delta E_{fs} = 8.86412(16)$ meV from Eq. (44). Uncertainties arise from Q and ΔE_{fs} .

	Borie [22]	Borie reevaluated	Martynenko [84]	Our value
$2P_{1/2}^{F=1/2}$	−1.4056	−1.40554(1)	−1.40534	−1.40544(10)
$2P_{1/2}^{F=3/2}$	0.6703	0.67037(1)	0.67031	0.67034(3)
$2P_{3/2}^{F=1/2}$	8.6194	8.61898(17)	8.62002	8.61950(55)
$2P_{3/2}^{F=3/2}$	8.2560	8.25619(16)	8.25618	8.25619(16)
$2P_{3/2}^{F=5/2}$	9.3728	9.37272(16)	9.37183	9.37228(47)

Pachucki and Karshenboim [51] argue that the DF term originates from the Zitterbewegung of the nucleus and is hence absent for a spin-1 nucleus such as the deuteron (as well as for the spin-0 ^4He nucleus).

Khriplovich, Milstein and Sen’kov [49] argue that the DF term must be made a part of the rms charge radius to be consistent with electron scattering. In this case, the DF term is *not* absent for spin-1 nuclei such as the deuteron.

Friar, Martorell and Sprung [48] have emphasized that the DF-term can be alternatively considered as part of a recoil correction of order $1/M^2$, or as the energy shift due to a part of the mean-square radius of the nuclear charge distribution. They advocate the second choice but admit that the first choice has to be used for the proton because “it is unfortunately far too late to change these conventions for the hydrogen atom”. They recommend, however, to not extend the hydrogen atom conventions to other nuclei.

Jentschura has discussed the situation in some breadth [50] and concluded that the DF term should indeed be considered a contribution to the atomic energy levels, supporting the “atomic physics” convention of Ref. [51]. The DF term is hence absent for the deuteron.

This “atomic physics” convention, in which the DF term is *not* a part of the rms charge radius, but rather a recoil correction of order $(Z\alpha)^4 m^3/M^2$ to the energy levels, is the convention used in CODATA-2010 [4], see Eqs. (26) and (27) therein. It is also the convention used in the most recent measurement of the H–D isotope shift [13,14] which is the origin of the difference of the squared rms radii of the deuteron and the proton given in Eq. (4). Moreover, it is the convention used for the proton radius in muonic hydrogen [3].

Therefore, to be able to directly compare the numerical values of the proton and deuteron rms charge radii obtained in electronic and muonic atoms, one must follow the “atomic physics” convention [51,14,50,4], which is what we do.

References

- [1] R. Pohl, A. Antognini, F. Nez, F.D. Amaro, F. Biraben, J.M.R. Cardoso, D.S. Covita, A. Dax, S. Dhawan, L.M.P. Fernandes, A. Giesen, T. Graf, T.W. Hänsch, P. Indelicato, L. Julien, C.-Y. Kao, P. Knowles, E.-O.L. Bigot, Y.-W. Liu, J.A.M. Lopes, L. Ludhova, C.M.B. Monteiro, F. Mulhauser, T. Nebel, P. Rabinowitz, J.M.F. dos Santos, L.A. Schaller, K. Schuhmann, C. Schwob, D. Taqq, J.F.C.A. Veloso, F. Kottmann, Nature 466 (2010) 213.
- [2] A. Antognini, F. Nez, K. Schuhmann, F.D. Amaro, F. Biraben, J.M.R. Cardoso, D.S. Covita, A. Dax, S. Dhawan, M. Diepold, L.M.P. Fernandes, A. Giesen, T. Graf, A.L. Gouvea, T.W. Hänsch, P. Indelicato, L. Julien, C.-Y. Kao, P. Knowles, F. Kottmann, E.-O.L. Bigot, Y.-W. Liu, J.A.M. Lopes, L. Ludhova, C.M.B. Monteiro, F. Mulhauser, T. Nebel, P. Rabinowitz, J.M.F. dos Santos, L.A. Schaller, C. Schwob, D. Taqq, J.F.C.A. Veloso, J. Vogelsang, R. Pohl, Science 339 (2013) 417.
- [3] A. Antognini, F. Kottmann, F. Biraben, P. Indelicato, F. Nez, R. Pohl, Ann. Phys. 331 (2013) 127, arXiv:1208.2637.
- [4] P.J. Mohr, B.N. Taylor, D.B. Newell, Rev. Modern Phys. 84 (2012) 1527.
- [5] I. Sick, Phys. Lett. B 576 (1–2) (2003) 62–67, arXiv:nucl-ex/0310008.
- [6] J.C. Bernauer, P. Aschenbach, C. Ayerbe Gayoso, R. Böhm, D. Bosnar, L. Debenjak, M.O. Distler, L. Doria, A. Esser, et al., Phys. Rev. Lett. 105 (2010) 242001, arXiv:1007.5076.
- [7] F. Biraben, Eur. Phys. J. Spec. Top. 172 (2009) 109, arXiv:0809.2985 (atom-ph).
- [8] R. Pohl, R. Gilman, G.A. Miller, K. Pachucki, Annu. Rev. Nucl. Part. Sci. 63 (2013) 175, arXiv:1301.0905.
- [9] C.E. Carlson, Prog. Part. Nucl. Phys. 82 (2015) 59, arXiv:1502.05314.
- [10] CREMA Collaboration, to be published.
- [11] I. Sick, D. Trautmann, Phys. Lett. B 375 (1996) 16.

- [12] I. Sick, D. Trautmann, *Nuclear Phys. A* 637 (1998) 559–575.
- [13] C.G. Parthey, A. Matveev, J. Alnis, R. Pohl, T. Udem, U.D. Jentschura, N. Kolachevsky, T.W. Hänsch, *Phys. Rev. Lett.* 104 (2010) 233001.
- [14] U.D. Jentschura, A. Matveev, C.G. Parthey, J. Alnis, R. Pohl, T. Udem, N. Kolachevsky, T.W. Hänsch, *Phys. Rev. A* 83 (2011) 042505.
- [15] R.N. Faustov, A.P. Martynenko, G.A. Martynenko, V.V. Sorokin, *Phys. Rev. A* 90 (2014) 012520.
- [16] G. Carboni, *Lett. Nuovo Cimento* 7 (1973) 160.
- [17] E. Borie, G.A. Rinker, *Rev. Modern Phys.* 54 (1982) 67.
- [18] K. Pachucki, *Phys. Rev. A* 53 (1996) 2092–2100.
- [19] E. Borie, *Phys. Rev. A* 71 (2005) 032508.
- [20] E. Borie, *Phys. Rev. A* 72 (2005) 0522511.
- [21] E. Borie, *Ann. Phys.* 327 (2012) 733.
- [22] E. Borie, Lamb shift in light muonic atoms—Revisited, 2014, arXiv:1103.1772-v7 [physics.atom-ph].
- [23] A.A. Krutov, A.P. Martynenko, *Phys. Rev. A* 84 (2011) 052514.
- [24] A. Martynenko, A. Krutov, R. Shamsutdinov, *Phys. At. Nucl.* 77 (2014) 786–794.
- [25] E. Uehling, *Phys. Rev.* 48 (1935) 55–63.
- [26] P. Indelicato, *Phys. Rev. A* 87 (2013) 022501. arXiv:1210.5828 (physics.atom-ph).
- [27] U.D. Jentschura, *Phys. Rev. A* 84 (2011) 012505.
- [28] U.D. Jentschura, B.J. Wundt, *Eur. Phys. J. D* 65 (2011) 357.
- [29] S.G. Karshenboim, V.G. Ivanov, E.Y. Korzinin, V.A. Shelyuto, *Phys. Rev. A* 81 (2010) 060501(R).
- [30] S.G. Karshenboim, V.G. Ivanov, E.Y. Korzinin, *Phys. Rev. A* 85 (2012) 032509.
- [31] A. Krutov, A. Martynenko, G. Martynenko, R. Faustov, *J. Exp. Theor. Phys.* 120 (2015) 73.
- [32] A. Martynenko, private communication, 2015.
- [33] G. Källén, A. Sabry, *Dan. Mat. Fys. Medd.* 29 (17) (1955).
- [34] S.G. Karshenboim, E.Y. Korzinin, V.G. Ivanov, V.A. Shelyuto, *JETP Lett.* 92 (2010) 8.
- [35] U.D. Jentschura, *Ann. Phys.* 326 (2011) 500.
- [36] E.Y. Korzinin, V.G. Ivanov, S.G. Karshenboim, *Phys. Rev. D* 88 (2013) 125019.
- [37] E. Borie, *Helv. Phys. Acta* 48 (1975) 671.
- [38] S.G. Karshenboim, private communication, 2015.
- [39] E. Borie, *Z. Phys. A* 302 (1981) 187.
- [40] J. Friar, J. Martorell, D. Sprung, *Phys. Rev. A* 59 (1999) 4061.
- [41] M.I. Eides, H. Grotch, V.A. Shelyuto, *Phys. Rep.* 342 (2001) 63–261.
- [42] R. Faustov, A. Martynenko, *EPJdirect C* 6 (1999) 1.
- [43] A.P. Martynenko, R.N. Faustov, *Phys. At. Nucl.* 63 (2000) 845.
- [44] A.P. Martynenko, R.N. Faustov, *Phys. At. Nucl.* 64 (2001) 1282.
- [45] J.L. Friar, *Ann. Phys.* 122 (1979) 151–196.
- [46] K. Pachucki, private communication, 2015.
- [47] W. Barker, F. Glover, *Phys. Rev.* 99 (1955) 317.
- [48] J. Friar, J. Martorell, D. Sprung, *Phys. Rev. A* 56 (1997) 4579.
- [49] I.B. Khriplovich, A.I. Milstein, R.A. Sen'kov, *Phys. Lett. A* 221 (1996) 370.
- [50] U.D. Jentschura, *Eur. Phys. J. D* 61 (2011) 7.
- [51] K. Pachucki, S.G. Karshenboim, *J. Phys. B* 28 (1995) L221.
- [52] K. Pachucki, *Phys. Rev. A* 52 (1995) 1079. <http://dx.doi.org/10.1103/PhysRevA.52.1079>.
- [53] A. Antognini, F. Nez, F.D. Amaro, F. Biraben, J.M.R. Cardoso, D.S. Covita, A. Dax, S. Dhanwan, L.M.P. Fernandes, A. Giesen, T. Graf, T.W. Hänsch, P. Indelicato, L. Julien, C.-Y. Kao, P. Knowles, F. Kottmann, E.-O.L. Bigot, Y.-W. Liu, J.A.M. Lopes, L. Ludhova, C.M.B. Monteiro, F. Mulhauser, T. Nebel, P. Rabinowitz, J.M.F. dos Santos, L.A. Schaller, K. Schuhmann, C. Schwob, D. Taqq, J.F.C.A. Veloso, R. Pohl, *Can. J. Phys.* 89 (2010) 47.
- [54] U.D. Jentschura, *Phys. Rev. A* 84 (2011) 012505.
- [55] K. Pachucki, *Phys. Rev. Lett.* 106 (2011) 193007.
- [56] S.G. Karshenboim, E.Y. Korzinin, V.A. Shelyuto, V.G. Ivanov, *Phys. Rev. D* 91 (2015) 073003.
- [57] M.I. Eides, H. Grotch, *Phys. Rev. A* 56 (1997) R2507–R2509.
- [58] O. Hernandez, C. Ji, S. Bacca, N.N. Dinur, N. Barnea, *Phys. Lett. B* 736 (2014) 344.
- [59] J. Friar, G. Payne, *Phys. Rev. A* 56 (1997) 5173.
- [60] J.L. Friar, *Phys. Rev. C* 88 (2013) 034003.
- [61] Y. Fukushima, M. Yahiro, M. Kamimura, *Phys. Rev. A* 46 (1992) 6894–6902.
- [62] Y. Lu, R. Rosenfelder, *Phys. Lett. B* 319 (1993) 1;
- [62] Y. Lu, R. Rosenfelder, *Phys. Lett. B* 333 (1994) 564. (erratum).
- [63] W. Leidemann, R. Rosenfelder, *Phys. Rev. C* 51 (1995) 427–430.
- [64] C.E. Carlson, M. Gorchtein, M. Vanderhaeghen, *Phys. Rev. A* 89 (2014) 022504.
- [65] K. Pachucki, A. Wienczek, *Phys. Rev. A* 91 (2015) 040503(R). arXiv:1501.07451 (physics.atom-ph).
- [66] C.E. Carlson, M. Vanderhaeghen, *Phys. Rev. A* 84 (2011) 020201(R). arXiv:1101.5965 (hep-ph).
- [67] M. Gorchtein, private communication, 2015.
- [68] C. Ji, N. Nevo Dinur, S. Bacca, N. Barnea, *Phys. Rev. Lett.* 111 (2013) 143402.
- [69] C. Ji, N. Nevo Dinur, S. Bacca, N. Barnea, *Few-Body Syst.* 55 (2014) 917.
- [70] S. Bacca, private communication, 2015.
- [71] O. Hernandez, Nuclear structure corrections in muonic deuterium (Master's thesis), University of Manitoba, 2015, URL <http://hdl.handle.net/1993/30748>.
- [72] M.C. Birse, J.A. McGovern, private communication, 2015.
- [73] E. Borie, private communication, 2015.
- [74] M.C. Birse, J.A. McGovern, *Eur. Phys. J. A* 48 (2012) 120. arXiv:1206.3030 (hep-ph).
- [75] M.I. Eides, *Phys. Rev. A* 85 (2012) 034503.
- [76] A. Bohr, V.F. Weisskopf, *Phys. Rev.* 77 (1950) 94–98.

- [77] A.C. Zemach, *Phys. Rev.* 104 (1956) 1771–1781.
- [78] J. Friar, I. Sick, *Phys. Lett. B* 579 (2004) 285.
- [79] D. Abbott, et al., *Eur. Phys. J. A* 7 (2000) 421.
- [80] I.B. Khriplovich, A.I. Milstein, *JETP* 98 (2) (2004) 181–185.
- [81] R.N. Faustov, A.P. Martynenko, *Phys. Rev. A* 67 (2003) 052506.
- [82] S.J. Brodsky, R.G. Parsons, *Phys. Rev.* 163 (1967) 134–146.
- [83] M. Pavanello, W.-C. Tung, L. Adamowicz, *Phys. Rev. A* 81 (2010) 042526.
- [84] R.N. Faustov, A.P. Martynenko, G.A. Martynenko, V.V. Sorokin, *Phys. Rev. A* 92 (2015) 052512. [arXiv:1508.06109v2](https://arxiv.org/abs/1508.06109v2) [hep-ph].

F. Abbreviations

Table F.1.: Abbreviations. Here are listed and explained the abbreviations and expressions used throughout this thesis.

ADC	Analog-to-digital converter
APD	Avalanche photo diode. Short for LAAPD.
BSM	Beyond Standard Model – this term summarizes all effects not described by the SM
CODATA	COmmittee on DATA for Science and Technology – A committee which compiles theory and experimental data by a least squares adjustment in order to provide a reliable set of fundamental constants.
CREMA	Charge Radius Experiment with Muonic Atoms – an international collaboration performing laser spectroscopy experiments on muonic atoms.
CT	Cyclotron trap
DAQ	Data Acquisition
event	The signals which are recorded by various detectors during an EVG.
EVG	Event gate, is initialized upon the detection of a muon.
e VP	electron vacuum polarization
FF	Form factor
FS	Fine structure
FWHM	Full width at half maximum
happening	A single signal from a detector is called happening.
HFS	Hyperfine structure
LAAPD	Large area avalanche photo diode. In this thesis often just termed APD

LS	Lamb shift, defined as the energy difference of the $2S_{1/2}$ and the $2P_{1/2}$ state. However, the term Lamb shift transition is used for any transition between a 1S and a 2P state.
LSA	Least squares adjustment
LSM	Line shape model, the function which is used to determine the positions of the measured Lamb shift transitions.
LTW	Laser time window, the time window in which the muon stop volume is illuminated by the laser
MEC	Muon extraction channel
MIDAS	A data acquisition system developed at PSI and TRIUMF.
MPQ	Max Planck Institute of Quantum Optics
μ VP	Muon vacuum polarization
PSC	A large solenoid in the MEC, originally a part of a phase-space compressor scheme. That is where the term PSC comes from.
PSI	Paul Scherrer Institute
QED	Quantum electrodynamics
rms	root mean square, is the quadratic mean.
ROOT	A modular scientific software framework. It is used by the CREMA collaboration for the data analysis.
SM	Standard Model
TDC	Time-to-digital converter
TPE	Two-photon exchange
tidiness	An electron quality parameter used in the analysis
WFD	Waveform digitizer

List of Figures

1.1. $n=2$ states of muonic helium-3	4
1.2. Leading Lamb shift contributions in ordinary hydrogen	5
2.1. Muon beamline	11
2.2. Muon detection	13
2.3. Pictures of target, cavity, and detection system.	15
2.4. The multipass cavity	16
2.5. Light distribution inside the multipass cavity	18
2.6. X-ray and electron detection system	19
2.7. The laser system	21
2.8. Thin disk oscillator	22
2.9. Beam trace and mirror array of thin disk amplifier	23
3.1. Interfering paths in an atomic system.	27
3.2. Detection geometry for the QI effect	32
3.3. ϕ dependence	33
3.4. The quantum interference effect	35
3.5. Laser pulse energy vs. frequency.	37
4.1. Particle identification via waveform trace analysis	45
4.2. APD spectrum, energy cut	46
4.3. Coincidences	48
4.4. Exemplary delayed electron cuts	49
4.5. Second muon identification	51
4.6. Laser time and power in Run 2079	52
4.7. Pulse energy vs. event number in Run 2079	53
4.8. Laser time vs. delay to previous LON event	53
4.9. Xdele time spectrum of 1 st transition	55
4.10. Xdele time spectrum of 2 nd and 3 rd transition	56
4.11. Laser time vs. frequency.	57
4.12. Exponentially saturating Lorentzian.	59

4.13. LSM fit to the $2S_{1/2}^{F=1} - 2P_{3/2}^{F=2}$ transition.	61
4.14. LSM fit to the $2S_{1/2}^{F=0} - 2P_{3/2}^{F=1}$ and $2S_{1/2}^{F=1} - 2P_{1/2}^{F=1}$ transition	62
5.1. Uehling term	66
5.2. One- and two-photon exchange in nuclear structure	67
6.1. Helion charge radii	75
6.2. Charge radius difference of the He isotopes -3 and -4	76
A.1. Laser light in APD B9	80
A.2. Offset between laser light in B9 and E0	80
A.3. Raw energy spectrum of APD A3 in run 1944	81
A.4. Prompt X-ray spectrum, jumps in calibration	83
A.5. Prompt X-ray spectrum, corrected calibration	83
A.6. Raw pulse energies at the output of the Ti:Sa oscillator in run 2054	85
B.1. $n=2$ energy levels of the helium-3 ion.	87
C.1. ^3He circulation system	90

List of Tables

3.1. Systematic effects in the $\mu^3\text{He}^+$ experiment	25
3.2. Quantum interference: rule of thumb applied to CREMA measurements	28
3.3. Quantum interference effect in the CREMA experiments	34
3.4. Zeeman shift in the $\mu^3\text{He}^+$ Lamb shift transitions	39
4.1. Coincidence cuts	49
4.2. XDele cuts for different electron classes	50
4.3. Fit results: Line shape model	60
5.1. 2P levels from fine- and hyperfine splitting	72
B.1. The Lamb shift transitions in $\mu^3\text{He}^+$	87
F.1. Abbreviations	153

Bibliography

- [1] W. E. Lamb and R. C. Retherford. ‘Fine structure of the hydrogen atom by a microwave method’. *Phys. Rev.* **72**, 241 (1947).
- [2] P. Kusch and H. M. Foley. ‘The magnetic moment of the electron’. *Phys. Rev.* **74**, 250 (1948).
- [3] T. Udem, R. Holzwarth, and T. W. Hansch. ‘Optical frequency metrology’. *Nature* **416**, 233 (2002).
- [4] C. G. Parthey, A. Matveev, J. Alnis, et al. ‘Improved measurement of the hydrogen 1S–2S transition frequency’. *Phys. Rev. Lett.* **107**, 203001 (2011).
- [5] A. Matveev, C. G. Parthey, K. Predehl, et al. ‘Precision measurement of the hydrogen 1s-2s frequency via a 920-km fiber link’. *Phys. Rev. Lett.* **110**, 230801 (2013).
- [6] R. Pohl, A. Antognini, F. Nez, et al. ‘The size of the proton’. *Nature* **466**, 213 (2010).
- [7] A. Antognini, F. Nez, K. Schuhmann, et al. ‘Proton structure from the measurement of 2S-2P transition frequencies of muonic hydrogen’. *Science* **339**, 417 (2013).
- [8] P. J. Mohr, D. B. Newell, and B. N. Taylor. ‘CODATA recommended values of the fundamental physical constants: 2014*’. *Rev. Mod. Phys.* **88**, 035009 (2016).
- [9] I. Sick. ‘Problems with the proton radii’. *Prog. Part. Nucl. Phys.* **67**, 473 (2012).
- [10] R. Pohl, R. Gilman, G. A. Miller, et al. ‘Muonic hydrogen and the proton radius puzzle’. *Ann. Rev. Nucl. Part. Sci.* **63**, 175 (2013). arXiv 1301.0905 [physics.atom-ph].
- [11] Antognini, A., Schuhmann, K., Amaro, F. D., et al. ‘Experiments towards resolving the proton charge radius puzzle’. *EPJ Web of Conferences* **113**, 01006 (2016).

- [12] C. E. Carlson. ‘The proton radius puzzle’. *Prog. Part. Nucl. Phys.* **82**, 59 (2015).
- [13] R. Pohl, F. Nez, L. M. P. Fernandes, et al. ‘Laser spectroscopy of muonic deuterium’. *Science* **353**, 669 (2016).
- [14] U. D. Jentschura, A. Matveev, C. G. Parthey, et al. ‘Hydrogen-deuterium isotope shift: From the 1S-2S-transition frequency to the proton-deuteron charge-radius difference’. *Phys. Rev. A* **83**, 042505 (2011).
- [15] T. Nebel, F. Amaro, A. Antognini, et al. ‘The Lamb-shift experiment in muonic helium’. *Hyp. Interact.* **212**, 195 (2012).
- [16] H. Collard, R. Hofstadter, E. B. Hughes, et al. ‘Elastic electron scattering from tritium and helium-3’. *Phys. Rev.* **138**, B57 (1965).
- [17] C. Ottermann, G. Köbschall, K. Maurer, et al. ‘Elastic electron scattering from ^3He and ^4He ’. *Nuclear Physics A* **436**, 688 (1985).
- [18] A. Amroun, V. Breton, J.-M. Cavedon, et al. ‘ ^3H and ^3He electromagnetic form factors’. *Nuclear Physics A* **579**, 596 (1994).
- [19] I. Angeli. ‘Table of nuclear root mean square charge radii’. *International nuclear data committee, INDC (HUN)—033* (1999).
- [20] I. Sick. ‘Elastic electron scattering from light nuclei’. *Prog. Part. Nucl. Phys.* **47**, 245 (2001).
- [21] I. Angeli and K. Marinova. ‘Table of experimental nuclear ground state charge radii: An update’. *Atomic Data and Nuclear Data Tables* **99**, 69 (2013).
- [22] D. Shiner, R. Dixon, and V. Vedantham. ‘Three-Nucleon Charge Radius: A Precise Laser Determination Using ^3He ’. *Phys. Rev. Lett.* **74**, 3553 (1995).
- [23] G. Carboni, G. Gorini, G. Torelli, et al. ‘Precise measurement of the $2S_{1/2} - 2P_{3/2}$ splitting in the $(\mu^{-4}\text{He})^+$ muonic ion’. *Nuclear Physics A* **278**, 381 (1977).
- [24] M. Diepold. *The Lamb shift in muonic helium ions*. Ph.D. thesis Ludwig-Maximilians-Universität (2015).
- [25] J. J. Krauth, M. Diepold, B. Franke, et al. ‘Theory of the $n=2$ levels in muonic deuterium’. *Ann. Phys.* **366**, 168 (2016). [arXiv:1506.01298].

- [26] E. C. Kemble and R. D. Present. ‘On the breakdown of the coulomb law for the hydrogen atom’. *Phys. Rev.* **44**, 1031 (1933).
- [27] E. Uehling. ‘Polarization effects in the positron theory’. *Phys. Rev.* **48**, 55 (1935).
- [28] H. A. Bethe. ‘The electromagnetic shift of energy levels’. *Phys. Rev.* **72**, 339 (1947).
- [29] G. Brown and C. Lee. *Hans Bethe and his physics*. World Scientific. ISBN 9789812774507 (2006).
- [30] G. Newton, D. A. Andrews, and P. J. Unsworth. ‘A Precision Determination of the Lamb Shift in Hydrogen’. *Phil. Trans. R. Soc. A* **290**, 373 (1979).
- [31] S. R. Lundeen and F. M. Pipkin. ‘Measurement of the Lamb shift in hydrogen, $n=2$ ’. *Phys. Rev. Lett.* **46**, 232 (1981).
- [32] S. R. Lundeen and F. M. Pipkin. ‘Separated Oscillatory Field Measurement of the Lamb Shift in H, $n = 2$ ’. *Metrologia* **22**, 9 (1986).
- [33] S. H. Neddermeyer and C. D. Anderson. ‘Note on the nature of cosmic-ray particles’. *Phys. Rev.* **51**, 884 (1937).
- [34] F. B. Dittus. *Experimentelle Untersuchung ueber Bildung und Zerfall myonischer Heliumionen im metastabilen 2S-Zustand*. Ph.D. thesis ETH Zurich, Switzerland (1985).
- [35] M. Seidel, S. Adam, A. Adelmann, et al. ‘Production of a 1.3 MW Proton Beam at PSI’. *IPAC10* page 1309 (2010).
- [36] M. Olivo, E. Mariani, and J. Sherman. ‘The PSI 870 keV high intensity Cockcroft–Walton preinjector’. *Review of Scientific Instruments* **63** (1992).
- [37] L. M. Simons. ‘Die Zyklotronfalle’. *Phys. Bl.* **48**, 261 (1992).
- [38] P. DeCecco, P. Hauser, D. Horvath, et al. ‘A new method to produce a negative muon beam of keV energies’. *Nucl. Inst. Meth. A* **394**, 287 (1997).
- [39] H. Anderhub, F. Kottmann, H. Hofer, et al. ‘Formation of the lightest muonic atoms in low density gases’. *Physics Letters B* **60**, 273 (1976).
- [40] K. A. Olive et al. ‘Review of Particle Physics’. *Chin. Phys.* **C38**, 090001 (2014).
- [41] M. Mühlbauer, H. Daniel, F. Hartmann, et al. ‘Frictional cooling: Experimental results’. *Hyp. Interact.* **119**, 305 (1999).

- [42] J. Vogelsang, M. Diepold, A. Antognini, et al. ‘Multipass laser cavity for efficient transverse illumination of an elongated volume’. *Opt. Express* **22**, 13050 (2014).
- [43] J. Krauth. *A monitoring system for the light distribution in a multipass cavity at the μHe^+ Lamb shift experiment*. Master’s thesis Ludwig-Maximilian-University Munich, Germany (2014).
- [44] L. Ludhova, F. D. Amaro, A. Antognini, et al. ‘Planar LAAPDs: temperature dependence, performance, and application in low-energy X-ray spectroscopy’. *Nucl. Inst. Meth. A* **540**, 169 (2005).
- [45] L. M. P. Fernandes, F. D. Amaro, A. Antognini, et al. ‘Characterization of large area avalanche photodiodes in X-ray and VUV-light detection’. *Journal of Instrumentation* **2**, P08005 (2007).
- [46] T. Nebel. *The Lamb Shift in Muonic Hydrogen*. Ph.D. thesis Ludwig-Maximilians-Universität, München (2010).
- [47] A. Antognini, K. Schuhmann, F. D. Amaro, et al. ‘Thin-disk Yb:YAG oscillator-amplifier laser, ASE, and effective Yb:YAG lifetime’. *IEEE J. Quant. Electr.* **45**, 993 (2009).
- [48] K. Schuhmann, A. Antognini, K. Kirch, et al. ‘Thin-disk laser for the measurement of the radii of the proton and the alpha-particle’. *Advanced Solid-State Lasers Congress* page ATu3A.46 (2013).
- [49] K. Schuhmann, M. A. Ahmed, A. Antognini, et al. ‘Thin-disk laser multi-pass amplifier’. *Proc. SPIE* **9342**, 93420U (2015).
- [50] A. Giesen, H. Hügel, A. Voss, et al. ‘Scalable concept for diode-pumped high-power solid-state lasers’. *Appl. Phys. B* **58**, 365 (1994).
- [51] B. Naar. ‘*Contribution to the muonic helium Lamb shift experiment: Frequency calibration of the laser system*’. Bachelor Thesis, Delft University of Technology, Delft, 2014.
- [52] M. Horbatsch and E. A. Hessels. ‘Shifts from a distant neighboring resonance’. *Phys. Rev. A* **82**, 052519 (2010).
- [53] R. C. Brown, S. Wu, J. V. Porto, et al. ‘Quantum interference and light polarization effects in unresolvable atomic lines: Application to a precise measurement of the $^6,7\text{Li}$ D_2 lines’. *Phys. Rev. A* **87**, 032504 (2013).

- [54] D. C. Yost, A. Matveev, E. Peters, et al. ‘Quantum interference in two-photon frequency-comb spectroscopy’. *Phys. Rev. A* **90**, 012512 (2014).
- [55] P. Amaro, B. Franke, J. J. Krauth, et al. ‘Quantum interference effects in laser spectroscopy of muonic hydrogen, deuterium, and helium-3’. *Phys. Rev. A* **92**, 022514 (2015).
- [56] T. Udem. ‘2S-nP Cross Damping’. Internal report (unpublished) (2014).
- [57] H. A. Bethe and E. E. Salpeter. *Quantum Mechanics of One and Two Electron Atoms*. Springer (1957), Berlin (1957).
- [58] I. I. Sobel’man. *Atomic Spectra and Radiative Transitions*. Number 12 in Springer Series on Atoms and Plasmas. Springer–Verlag, Berlin second edition. ISBN 3-540-54518-2 (1992).
- [59] P. A. M. Dirac. ‘The quantum theory of the emission and absorption of radiation’. *Proceedings of the Royal Society of London A: Mathematical, Physical and Engineering Sciences* **114**, 243 (1927).
- [60] R. Loudon. *The Quantum Theory of Light*. Oxford University Press. ISBN 9780191589782 (2000).
- [61] P. Amaro, F. Fratini, L. Safari, et al. ‘Quantum interference shifts in laser spectroscopy with elliptical polarization’. *Phys. Rev. A* **92**, 062506 (2015).
- [62] C. J. Foot. *Atomic Physics (Oxford Master Series in Atomic, Optical and Laser Physics)*. Oxford University Press, USA 1 edition. ISBN 0198506961 (2005).
- [63] D. Meschede. *Optics, Light and Lasers*. Teubner Studienbücher. Vieweg+Teubner Verlag. ISBN 3-527-40364-7 (2008).
- [64] G. Y. Korenman, V. N. Pomerantsev, and V. P. Popov. ‘Collisional shift and broadening of the $2p$ - $2s$ spectral lines in muonic helium ions’. *Phys. Rev. A* **88**, 032503 (2013).
- [65] M. Diepold, L. M. P. Fernandes, J. Machado, et al. ‘Improved x-ray detection and particle identification with avalanche photodiodes’. *Review of Scientific Instruments* **86**, 053102 (2015).
- [66] J. Böcklin. ‘Suche nach dem metastabilen 2S–Zustand im myonischen Wasserstoff bei tiefen Gasdrucken’. *Ph.D. thesis ETHZ Nr.* **7161** (1982).

- [67] A. Antognini, F. Kottmann, F. Biraben, et al. ‘Theory of the 2S-2P Lamb shift and 2S hyperfine splitting in muonic hydrogen’. *Ann. Phys.* **331**, 127 (2013). [arXiv:1208.2637].
- [68] M. Diepold, J. J. Krauth, B. Franke, et al. ‘Theory of the Lamb shift and Fine Structure in $(\mu^4\text{He})^+$ ’ (2016). Submitted. [arXiv:1606.05231].
- [69] B. Franke, J. J. Krauth, et al. ‘Theory of the n=2 levels in $\mu^3\text{He}^+$ ’. To be submitted.
- [70] E. Borie. ‘Lamb shift in light muonic atoms – Revisited’. arXiv: 1103.1772-v7 [physic.atom-ph] (2014).
- [71] G. A. Miller. ‘Proton polarizability contribution: Muonic hydrogen Lamb shift and elastic scattering’. *Phys. Lett. B* **718**, 1078 (2013).
- [72] M. C. Birse and J. A. McGovern. ‘Proton polarisability contribution to the Lamb shift in muonic hydrogen at fourth order in chiral perturbation theory’. *Eur. Phys. J. A* **48**, 120 (2012). [arXiv:1206.3030 (hep-ph)].
- [73] J. M. Alarcón, V. Lensky, and V. Pascalutsa. ‘Chiral perturbation theory of muonic-hydrogen Lamb shift: polarizability contribution’. *The European Physical Journal C* **74**, 2852 (2014).
- [74] N. Nevo Dinur, C. Ji, S. Bacca, et al. ‘Nuclear structure corrections to the Lamb shift in and $\mu^3\text{He}^+$ and $\mu^3\text{H}$ ’. *Phys. Lett. B* **755**, 380 (2016).
- [75] O. J. Hernandez, N. Nevo Dinur, C. Ji, et al. ‘Update on nuclear structure effects in light muonic atoms’. *Hyperfine Interactions* **237**, 158 (2016). [arXiv:1604.06496].
- [76] C. E. Carlson, M. Gorchtein, and M. Vanderhaeghen. ‘Two-photon exchange correction to $2S - 2P$ splitting in muonic helium’. ArXiv:1611.06192v1 [nucl-th].
- [77] M. I. Eides, H. Grotch, and V. A. Shelyuto. ‘Theory of light hydrogenlike atoms’. *Phys. Rep.* **342**, 63 (2001).
- [78] A. Bohr and V. F. Weisskopf. ‘The influence of nuclear structure on the hyperfine structure of heavy elements’. *Phys. Rev.* **77**, 94 (1950).
- [79] J. L. Friar and I. Sick. ‘Zemach moments for hydrogen and deuterium’. *Phys. Lett. B* **579**, 285 (2004).
- [80] F. Kottmann. private communication (2014).

- [81] J. L. Friar and G. L. Payne. ‘Nuclear corrections to hyperfine structure in light hydrogenic atoms’. *Phys. Rev. C* **72**, 014002 (2005).
- [82] I. Sick. ‘Zemach radius of ^3He and ^4He ’. *Phys. Rev. C* **90**, 064002 (2014).
- [83] K. Pachucki. ‘Theory of the Lamb shift in muonic hydrogen’. *Phys. Rev. A* **53**, 2092 (1996).
- [84] P. C. Dunn, S. B. Kowalski, F. N. Rad, et al. ‘ ^3He magnetic form factor’. *Phys. Rev. C* **27**, 71 (1983).
- [85] G. A. Retzlaff and D. M. Skopik. ‘ ^3He charge form factors by nuclear recoil detection’. *Phys. Rev. C* **29**, 1194 (1984).
- [86] R. van Rooij, J. S. Borbely, J. Simonet, et al. ‘Frequency metrology in quantum degenerate helium: Direct measurement of the $2^3S_1 \rightarrow 2^1S_0$ transition’. *Science* **333**, 196 (2011).
- [87] P. Cancio Pastor, L. Consolino, G. Giusfredi, et al. ‘Frequency metrology of helium around 1083 nm and determination of the nuclear charge radius’. *Phys. Rev. Lett.* **108**, 143001 (2012).
- [88] V. Patkóš, V. A. Yerokhin, and K. Pachucki. ‘Higher-order recoil corrections for triplet states of the helium atom’. *Phys. Rev. A* **94**, 052508 (2016).
- [89] V. Patkóš, V. A. Yerokhin, and K. Pachucki. ‘Higher-order recoil corrections for singlet states of the helium atom’. *Phys. Rev. A* **95**, 012508 (2017).
- [90] M. Herrmann, M. Haas, U. Jentschura, et al. ‘Feasibility of coherent xuv spectroscopy on the $1S - 2S$ transition in singly ionized helium’. *Phys. Rev. A* **79**, 052505 (2009).
- [91] K. S. E. Eikema. ‘Precision deepUV Ramsey-comb spectroscopy of H_2 and prospects for $1S$ - $2S$ excitation of He-ions’. Talk at ECT* Workshop on the Proton Radius Puzzle (2016).
- [92] D. Tucker-Smith and I. Yavin. ‘Muonic hydrogen and MeV forces’. *Phys. Rev. D* **83**, 101702 (2011).
- [93] R. Gilman. ‘Studying the proton "radius" puzzle with μp elastic scattering’. *AIP Conf. Proc.* **1563**, 167 (2013).

- [94] A. Beyer, L. Maisenbacher, K. Khabarova, et al. ‘Precision spectroscopy of $2S$ – nP transitions in atomic hydrogen for a new determination of the Rydberg constant and the proton charge radius’. *Physica Scripta* **2015**, 014030 (2015).

Acknowledgements

This thesis would not have been possible without the valuable support of many to whom I would like to express my gratitude.

First of all, I would like to thank Prof. Hänsch for the possibility to make my PhD in his department at the Max-Planck-Institute of Quantum Optics. He created an excellent research atmosphere, with all the required freedom and excellent conditions to realize all kind of ideas. I am also very thankful for the great time at the various group seminars at Schloss Ringberg, which is a unique and inspiring place.

Second, I would like to thank Randolph Pohl, my advisor, for his guidance and support, the fruitful discussions and inspirations. It is a great pleasure to work in his group. He is a great teacher and always has an open ear for questions and worries.

I am grateful to Beatrice Franke. She has been PostDoc in our group for more than two years, we shared the same office, had shifts together at PSI, and motivated each other to do sports as an important compensation for the daily intellectual work. Furthermore she is a great person to talk to, not only for physics topics. I would like to thank her also for proofreading my thesis.

Marc Diepold, who did the analysis of the muonic helium-4 data, for answering many many questions about the data analysis software, for debugging my code and for the support in general.

I would like to thank Aldo Antognini, who invited us several times during the beamtime to his apartment for dinner. He worked like crazy to get the experiment running, even though he always has many other projects to do at the same time. His ability to spread his good mood to those around him is admirable.

Franz Kottmann, for sharing his inexhaustible knowledge regarding muonic atoms, for his advice and support, as well as for very valuable comments and proofreading my

thesis.

Karsten Schuhmann, for his support regarding my questions about the laser setup.

Savely Karshenboim, for the insightful discussions about the Lamb shift theory in muonic atoms, about Feynman diagrams, polarizability and other topics which are all very difficult to handle for a poor experimentalist.

I would like to thank Lothar Maisenbacher for the great company and discussions at innumerable coffee breaks and for the great time we shared at several conferences as e.g. in Jerusalem and Trento.

The Hänsch group, for the great time at MPQ, in the group seminars at Tegernsee, the skiing, the high-precision physics environment, the discussions and much more.

The CREMA collaboration, it was a great pleasure to be part of the muonic helium project, and to contribute as part of an extraordinary team, which achieved remarkable results.

The PSI workshop, the Hallendienst, and the accelerator group, for their support and a nearly uninterrupted beam.

Our technicians Karl (Charlie) Linner, Wolfgang Simon, as well as our electrical engineer Helmut Brückner for their support.

Gabriele Gschwendtner, Ingrid Hermann, and Anita Van Loon-Govaerts, for their administrative support.

Last but not least,
I would like to thank my parents, my sister, and my brothers
for their trust and support.

Curriculum Vitae

Julian Krauth

Max Planck Institute of Quantum Optics
Hans-Kopfermann-Str. 1
85748 Garching
Germany
mail: julian.krauth@mpq.mpg.de

Education

- | | |
|-------------|---|
| Since 2014 | Max Planck Institute of Quantum Optics, Garching
PhD in physics: <i>The Lamb shift of the muonic helium-3 ion and the helion charge radius.</i> |
| 2011 – 2014 | Ludwig-Maximilians-Universität München (Master of Science)
Master's thesis at the Max Planck Institute of Quantum Optics: <i>A monitoring system for the light distribution in a multipass cavity at the μHe^+ Lamb shift experiment.</i> |
| 2008 – 2011 | Ludwig-Maximilians-Universität München (Bachelor of Science)
Bachelor's thesis at the Institute of Biomolecular Optics: <i>Flourescence spectroscopy of a DPP compound in combination with α-synuclein aggregates.</i> |
| 1998 – 2007 | Ganztagsgymnasium Osterburken
High School (Abitur) |

Talks

- 2016 **New insights into the proton radius puzzle (PRP) and nuclear structure from muonic deuterium**
PSI2016 Physics of fundamental Symmetries and Interactions, Villigen, Switzerland.
- 2016 **The size of the deuteron and its implications for the PRP**
ECT* Workshop on the proton radius puzzle, Trento, Italy.
- 2016 **Charge radii from hydrogen-like muonic atoms**
PSAS International Conference, Jerusalem, Israel.
- 2015 **Current Status of the Proton Radius Puzzle**
DPG spring meeting, Heidelberg, Germany.
- 2014 **The muonic helium Lamb shift experiment**
Particle physics colloquium of the Paul Scherrer Institute, Villigen, Switzerland.

Posters

- 2015 **Problems with charge radii**
ACFC2015 - 591. WE-Heraeus-Seminar on Astrophysics, Clocks, and Fundamental Constants, Bad Honnef, Germany.
- 2014 **The multipass cavity of the μHe^+ Lamb shift experiment**
EXA2014 - International Conference on Exotic Atoms and Related Topics, Vienna, Austria.

Publications

- [10] *Measurement of the Lamb shift in the muonic helium-3 ion and the helion charge radius*
Julian J. Krauth, *et al.* (CREMA collaboration)
Will contain the content of this thesis.
- [9] *Theory of the $n=2$ levels in muonic helium-3*
Beatrice Franke, **Julian J. Krauth**, Aldo Antognini, Marc Diepold, Franz Kottmann, and Randolph Pohl
In preparation, App. D of this thesis.

- [8] *Deuteron charge radius and Rydberg constant from spectroscopy data in atomic deuterium*
 Randolph Pohl, François Nez, Thomas Udem, Aldo Antognini, Axel Beyer, Hélène Fleurbaey, Alexey Grinin, Theodor W. Hänsch, Lucile Julien, Franz Kottmann, **Julian J. Krauth**, Lothar Maisenbacher, Arthur Matveev, and François Biraben
Metrologia **54** (2017) L1-L10, doi:10.1088/1681-7575/aa4e59. [arXiv:1607.03165].
- [7] *Theory of the Lamb shift and Fine Structure in $(\mu^4\text{He})^+$*
 Marc Diepold, Beatrice Franke, **Julian J. Krauth**, Aldo Antognini, Franz Kottmann, and Randolph Pohl
 Submitted to and under review in *Annals of Physics*. [arXiv:1606.05231].
- [6] *Experiments towards resolving the proton charge radius puzzle*
 A. Antognini, K. Schuhmann, F. D. Amaro, P. Amaro, M. Abdou-Ahmed, F. Biraben, T.-L. Chen, D. S. Covita, A. J. Dax, M. Diepold, L. M. P. Fernandes, B. Franke, S. Galtier, A. L. Gouvea, J. Götzfried, T. Graf, T. W. Hänsch, M. Hildebrandt, P. Indelicato, L. Julien, K. Kirch, A. Knecht, F. Kottmann, **J. J. Krauth**, Y.-W. Liu, J. Machado, C. M. B. Monteiro, F. Mulhauser, F. Nez, J. P. Santos, J. M. F. dos Santos, C. I. Szabo, D. Taqqu, J. F. C. A. Veloso, A. Voss, B. Weichelt, and R. Pohl
EPJ Web of Conferences **113** (2016) 01006, doi:10.1051/epjconf/201611301006. [arXiv:1509.03235].
- [5] *Theory of the $n=2$ levels in muonic deuterium*
Julian J. Krauth, Marc Diepold, Beatrice Franke, Aldo Antognini, Franz Kottmann, and Randolph Pohl
Annals of Physics **366** (2016) 168–196, doi:10.1016/j.aop.2015.12.006. [arXiv:1506.01298].
- [4] *Quantum interference effects in laser spectroscopy of muonic hydrogen, deuterium, and helium-3*
 Pedro Amaro, Beatrice Franke, **Julian J. Krauth**, Marc Diepold, Filippo Fratini, Laleh Safari, Jorge Machado, Aldo Antognini, Franz Kottmann, Paul Indelicato, Randolph Pohl, and José Paulo Santos
Physical Review A **92** (2015) 022514, doi:10.1103/PhysRevA.92.022514. [arXiv:1506.02734].
- [3] *Improved x-ray detection and particle identification with avalanche photodiodes*
 Marc Diepold, Luis M. P. Fernandes, Jorge Machado, Pedro Amaro, Marwan

Abdou-Ahmed, Fernando D. Amaro, Aldo Antognini, François Biraben and Tzu-Ling Chen, Daniel S. Covita, Andreas J. Dax, Beatrice Franke, Sandrine Galtier, Andrea L. Gouvea, Johannes Götzfried, Thomas Graf, Theodor W. Hänsch, Malte Hildebrandt, Paul Indelicato, Lucile Julien, Klaus Kirch, Andreas Knecht, Franz Kottmann, **Julian J. Krauth**, Yi-Wei Liu, Cristina M. B. Monteiro, Françoise Mulhauser Boris Naar, Tobias Nebel, François Nez, José Paulo Santos, Joaquim M. F. dos Santos, Karsten Schuhmann, Csilla I. Szabo, David Taqqu, João F. C. A. Veloso, Andreas Voss, Birgit Weichelt, and Randolph Pohl

Review of Scientific Instruments **86** (2015) 053102, doi:10.1063/1.4921195. [arXiv:1505.06879].

- [2] *Multipass laser cavity for efficient transverse illumination of an elongated volume*
Jan Vogelsang, Marc Diepold, Aldo Antognini, Andreas Dax, Johannes Götzfried, Theodor W. Hänsch, Franz Kottmann, **Julian J. Krauth**, Yi-Wei Liu, Tobias Nebel, François Nez, Karsten Schuhmann, David Taqqu, and Randolph Pohl
Optics Express **22** (2014) 13050–13062, doi:10.1364/OE.22.013050. [arXiv:1506.03028].

- [1] *Anle138b: a novel oligomer modulator for disease-modifying therapy of neurodegenerative diseases such as prion and Parkinson's disease*
Jens Wagner, Sergey Ryazanov, Andrei Leonov, Johannes Levin, Song Shi, Felix Schmidt, Catharina Prix, Francisco Pan-Montojo, Uwe Bertsch, Gerda Mitteregger-Kretzschmar, Markus Geissen, Martin Eiden, Fabienne Leidel, Thomas Hirschberger, Andreas A. Deeg, **Julian J. Krauth**, Wolfgang Zinth, Paul Tavan, Jens Pilger, Markus Zweckstetter, Tobias Frank, Mathias Bähr, Jochen H. Weishaupt, Manfred Uhr, Henning Urlaub, Ulrike Teichmann, Matthias Samwer, Kai Bötzel, Martin Groschup, Hans Kretzschmar, Christian Griesinger, and Armin Giese
Acta Neuropathologica **125** (2013) 795–813, doi:10.1007/s00401-013-1114-9.